

**FEDERAL UNIVERSITY OF SAO CARLOS**  
**EXACT AND TECHNOLOGY SCIENCES CENTER**  
**GRADUATE PROGRAM IN CHEMICAL ENGINEERING**

**Desalination by Capacitive Deionization: Development of New Electrodes  
and Process Optimization**

RAFAEL LINZMEYER ZORNITTA

São Carlos -SP

2019

**FEDERAL UNIVERSITY OF SAO CARLOS**  
**EXACT AND TECHNOLOGY SCIENCES CENTER**  
**GRADUATE PROGRAM IN CHEMICAL ENGINEERING**

**Desalination by Capacitive Deionization: Development of New Electrodes  
and Process Optimization**

Ph.D. thesis presented to the Chemical Engineering Graduation Program of the Federal University of São Carlos as part of the requirements to obtain the title of Doctor in Chemical Engineering, in the field of Research and Development of Chemical Processes

RAFAEL LINZMEYER ZORNITTA

São Carlos

2019

MEMBROS DA BANCA EXAMINADORA DA DEFESA DE TESE DE RAFAEL LINZMEYER ZORNITTA APRESENTADA AO PROGRAMA DE PÓS-GRADUAÇÃO EM ENGENHARIA QUÍMICA DA UNIVERSIDADE FEDERAL DE SÃO CARLOS, EM 18 DE FEVEREIRO DE 2019.


BANCA EXAMINADORA:

  
Luis Augusto Martins Ruotolo  
**Orientador, UFSCar**

  
Janaina Fernandes Gomes  
**UFSCar**

  
Hudson Giovani Zanin  
**UNICAMP**

  
Lucia Helena Mascaro Sales  
**UFSCar**

  
Aparecido dos Reis Coutinho  
**UNIMEP**

**Dedico este trabalho com amor aos meus pais Nelson Zornitta e Celia Rita Linzmeyer Zornitta, e minha irmã Vanessa L. Z. Silvati que sempre acreditaram em mim e foram parte essencial desta conquista.**

## ACKNOWLEDGMENTS

I would like to thank first to my parents Nelson Zornitta and Celia R. L. Zornitta for all the support, dedication, and life lessons they have taught me. I thank my father for being the most intelligent and brilliant person I have ever met in my life, a worthy, persevering, and inspiring man. To my mother, for all the strength showed during difficult times, all the patience, calm, dedication, and for helping me during difficult decisions. Both have always gave their best to provide me everything. I am grateful forever, and very proud of having you as my parents.

I thank to my sister Vanessa Linzmeyer Zornitta Silvati, my brother in law Elias Silvati Junior, and my niece Valentina L. Z. Silvati for supporting me, especially my sister who was an example of strength and dedication to achieve her goals.

I thank to Prof. Dr. Luis Augusto for his guidance, dedication, passion for science, and help during many years working together that culminated in a strong friendship.

To my friend Dr. Julio Lado that was part of important discussions and suggestions assisting with the improvement of the project. To my friends from Malaga University, especially Dr. Francisco J. García-Mateos who assisted me during the three months that I stayed in Malaga, being part active of discussions and providing suggestions to the project.

To my friends I have made during my one year internship in Germany, especially Dr. Thiago M. Amaral, Dr. Juhan Lee, MSc. Öznil Budak, MSc. Pattarachai Srimuk, Dr. Aslan Mesut who have always actively assisted me with ideas, discussions, and friendship.

To Prof. Dr. Francisco Nogueira for the discussions and ideas that were very important on the analysis of the prepared materials.

To all of my friends from the Laboratory for Environmental Technologies (LATEA) laboratory who have always assisted me when I needed.

To Prof. Dr. Peter Hammer for the discussions and suggestions about XPS analyses.

To Jéssica A. Oliveira and EMBRAPA for the nitrogen adsorption, thermogravimetric, and zeta potential analyses.

To Structural Characterization Laboratory – UFSCar for the scanning and transmission electron microscopy analyses. To Brazilian Bioethanol Science and Technology Laboratory (CTBE) for providing the lignin.

To Prof. Ernest Urquieta-González for the nitrogen adsorption analyses.

To the Department of Chemical Engineering of UFSCar, to all the employees, especially the technician Dr. Alyne Veroli for all the assistance during the project.

To Malaga University and the group of “Tecnología de Residuo y del Medio Ambiente” (TERMA), and to Prof. Dr. José Rodríguez-Mirasol.

To the Leibniz Institute for New Materials (INM) from Germany, especially to Prof. Dr. Volker Presser for the discussions, suggestions, and assistance during my one year internship and to Eduardo Artz for his continuous support.

To the Graduate Program in Chemical Engineering from UFSCar.

To the São Paulo Research Foundation (FAPESP, processes 2015/26593-3 and 2016/24684-4) for the PhD and Research Internship Abroad scholarships. To Carolina Foundation for the international researcher scholarship.

To FAPESP and the National Council for Scientific and Technological Development (CNPq) for the financial support (FAPESP processes 2015/16107-4 e 2017/19838-5).

To the Coordination for the Improvement of Higher Education Personnel (CAPES) for the financial support to the Graduate Program in Chemical Engineering from UFSCar.

I thank also to all who directly or indirectly assisted me to complete this work. Thank you very much.

## RESUMO EXPANDIDO

O objetivo principal deste trabalho de doutorado foi a preparação de carvões ativados de alta performance para a dessalinização de águas salobras por meio da tecnologia de deionização capacitiva (DIC). Os precursores para a preparação dos carvões ativados foram a polianilina e a lignina. A polianilina, além de ser fácil de se sintetizar, seu monômero é de baixo custo, enquanto a lignina possui custo ainda mais baixo e não requer nenhum pré-tratamento adicional. A escolha destes precursores foi baseada na composição elementar, estrutura molecular e disponibilidade. Após a obtenção dos carvões ativados, estes materiais foram utilizados para a preparação dos eletrodos empregados no processo de dessalinização. Estudou-se também diferentes configurações desses eletrodos (simétricos, assimétricos e com membrana) e formas de operação (*single-pass* e batelada). O desempenho na dessalinização foi avaliado aplicando-se diferentes potenciais de célula. Os materiais e eletrodos obtidos foram caracterizados quanto às suas propriedades texturais, grupos superficiais e capacitância, e avaliados quanto ao seu desempenho na dessalinização por meio da capacidade de eletrossorção, eficiência de carga, cinética e consumo energético específico.

Os eletrodos preparados com carvão ativado de lignina (LK) apresentaram elevada área superficial específica (ASE) e volume de micro/mesoporos que proporcionaram uma elevada capacitância em solução de sal concentrada. Contudo, quando esses eletrodos foram dispostos de forma simétrica constatou-se uma redução da capacidade de dessalinização ao longo dos ciclos de eletrossorção/dessorção. Este comportamento foi associado a degradação do eletrodo positivo e revelou a importância do potencial de carga zero, associado à presença de grupos funcionais nos eletrodos. Desta forma, utilizou-se duas estratégias baseadas na assimetria de eletrodos para estabilizar a capacidade e a eficiência de carga do eletrodo: assimetria de massa e assimetria de material. A primeira forma de assimetria foi capaz de estabilizar o eletrodo, porém causou uma redução da capacidade de eletrossorção. Por outro lado, a assimetria de material não só estabilizou a capacidade e a eficiência de carga dos eletrodos por mais de 100 ciclos, mas também maximizou a capacidade de eletrossorção aplicando-se um potencial de célula menor do que o usualmente utilizado, o que teve um impacto na redução do consumo energético.

Os carvões ativados de polianilina foram denominados PAC e foram preparados partindo-se do polímero dopado com diferentes ânions (Cl<sup>-</sup>, p-toluenosulfonato, dodecilbenzenosulfonato e poliestirenosulfonato), os quais tiveram impacto sobre as

propriedades texturais, grupos superficiais, e desempenho eletroquímico do carvão ativado obtido. Demonstrou-se que é possível customizar o PAC em termos de ASE, volume de poros, condutividade e capacitância através do emprego de diferentes ânions dopantes. Os eletrodos de PAC foram empregados com sucesso na dessalinização por DIC, atingindo elevadas capacidades de eletrossorção e proporcionando um baixo consumo energético específico. O PAC que apresentou melhor desempenho foi aquele obtido a partir da polianilina dopada com p-toluenosulfonato (PAC/PTS), o qual foi empregado posteriormente na otimização da configuração dos eletrodos. Para tanto, duas técnicas foram aplicadas: modificação química da superfície do eletrodo e utilização de membrana íon seletiva. Apesar da primeira técnica ter causado uma redução do consumo energético de dessalinização, a capacidade de eletrossorção também diminuiu devido à redução da ASE do material de eletrodo. Por outro lado, a utilização da membrana íon seletiva além de aumentar a capacidade, reduziu o consumo energético específico.

Neste trabalho, propôs-se também uma nova metodologia de análise da capacidade de dessalinização levando em conta não somente a capacidade, mas também as cinéticas de eletrossorção e dessorção do sistema. Demonstrou-se que, apesar da capacidade de eletrossorção ser uma condição necessária para a dessalinização, ela não é suficiente para garantir o sucesso do processo. Eletrodos com capacidades baixas, mas com cinéticas rápidas, podem proporcionar uma capacidade de dessalinização maior, uma vez que mais ciclos de eletrossorção podem ser operados em um mesmo intervalo de tempo.

Visando aumentar ainda mais a capacidade de eletrossorção do PAC/PTS, descobriu-se que a temperatura de carbonização da polianilina, que é uma etapa anterior à sua ativação, exerce grande influência sobre as propriedades texturais e capacitivas dos materiais. Juntamente com temperatura de carbonização estudou-se os efeitos da proporção de KOH e precursor de carbono e a temperatura de ativação. Demonstrou-se que baixas temperaturas de carbonização (< 600 °C) causam um aumento surpreendente da ASE e de volume de poros e um mecanismo de carbonização/ativação foi proposto com base em diversas caracterizações estruturais. Uma condição de síntese otimizada do PAC/PTS levou à maximização tanto da ASE quanto do volume de poros, o que se refletiu na obtenção de um valor elevado de capacitância e uma capacidade de eletrossorção dentre as maiores já relatadas na literatura de deionização capacitiva para um eletrodo simétrico de carbono.

**Palavras chave:** deionização capacitiva, eletrossorção, dessalinização, polímero condutor, lignina, carvão ativado.



## ABSTRACT

The main aim of this PhD thesis was the preparation of high performance activated carbons employed as electrodes for water desalination by capacitive deionization technology (CDI). The precursors used for the activated carbon preparation were lignin and polyaniline (PAni). Besides being easily synthesized, PAni is obtained from a low-cost precursor, while the lignin is a no-cost precursor and demands no treatments prior activation. The choice of these precursors were based on their elemental composition, molecular structure, and availability. After the activated carbon synthesis, they were prepared as electrodes for the desalination process. Different configurations (symmetrical, asymmetrical, and with membrane) and operational conditions (single-pass and batch) were studied. The desalination performance was evaluated under different cell potentials. The materials and electrodes were characterized in terms of their textural properties, functional surface groups, and capacitance, and then the desalination performance was evaluated in terms of electrosorption, charge efficiency, kinetics, and specific energy consumption.

The electrodes prepared with lignin activated carbon (LK) had high specific surface area (SSA) and micro/mesoporous volume, providing high capacitance values in concentrated salt solution. However, when these electrodes were employed for water desalination in symmetrical configuration, it was observed a reduction on the desalination capacity along with the electrosorption/desorption cycle number. This behavior was assigned to the positive electrode degradation and revealed the importance of the potential of zero charge ( $E_{PZC}$ ), which is related to the presence of functional surface groups. Therefore, it was employed two different strategies based on electrode asymmetry to stabilize the capacity and charge efficiency of the electrodes: asymmetry of mass and material. The asymmetry of mass was capable of stabilizing the electrode, but caused a reduction on the electrosorption capacity. On the other hand, asymmetry of material not only stabilized capacity and charge efficiency for more than 100 cycles, but also maximized the electrosorption capacity applying a cell potential ( $E_{cell}$ ) lower than the typical values, which had an impact on the specific energy reduction.

The polyaniline activated carbons were labeled as PAC, and were obtained from the polymer doped with different anions ( $Cl^-$ , p-toluenesulfonate, dodecylbenzenesulfonate, and polystyrenesulfonate), which had a strong effect on the textural properties, functional surface groups, and electrochemical performance of the PAC. It was demonstrated that it is possible to customize PAC in terms of SSA, pore volume, conductivity, and capacitance by employing different doping anions. The PAC electrodes were successfully used as electrodes on the CDI

desalination process, reaching high salt adsorption capacity (SAC) and low specific energy consumption. The PAC derived from polyaniline doped with p-toluenesulfonate (PAC/PTS) presented the best CDI performance, and its performance was optimized using different electrode configurations. In this regard, two techniques were used: chemical electrode surface modification, and use of ion exchange membranes. Although the first technique caused reduction on the specific energy consumption, the SAC was also reduced due to the decrease of its SSA. On the other hand, the use of ion exchange membrane increased SAC, and reduced the specific energy consumption.

In this work, a new method to analyze the desalination capacity was proposed taking into account not only SAC, but also electrosorption/desorption kinetic. Despite SAC is a necessary condition for desalination, it was demonstrated that it is not enough to assure the high desalination performance. Electrode with low SAC, but with fast electrosorption/desorption kinetic, can provide high desalination capacity since more desalination cycles may be carried out at the same time interval.

In order to enhance even further the SAC of PAC/PTS, we found out that carbonization temperature, which is the stage right before the carbon activation, plays a fundamental role on the textural and capacitive properties of the electrode material. It was also studied the effect of the activation temperature and KOH/carbon weight ratio. We showed that low carbonization temperatures (<600 °C) cause remarkable increase on the SSA, and pore volume. A carbonization/activation mechanism was proposed based on several structural characterizations. An optimized synthesis condition for PAC/PTS led to the maximization of both SSA, and pore volume, resulting in high capacitance values, and a SAC value among the highest presented on CDI literature for symmetrical electrodes.

**Keywords:** capacitive deionization, electrosorption, desalination, conducting polymer, lignin, activated carbon.

## SUMMARY

<b>1. Chapter 1 – Introduction</b> .....	1
1.1 Broad context .....	1
1.2 Desalination technologies.....	2
1.2.1 Multi-stage flash distillation .....	2
1.2.2 Reverse osmosis.....	2
1.2.3 Electrodialysis.....	3
1.3.CDI Technology .....	4
1.4.Thesis outline.....	7
1.5.Objectives.....	9
<b>2. Chapter 2 -Charge and potential balancing for optimized capacitive deionization using lignin-derived, low-cost activated carbon</b> .....	13
2.1.Introduction.....	14
2.2.Experimental description.....	15
2.2.1. Materials.....	15
2.2.2. Lignin activation.....	15
2.2.3. Electrode preparation.....	16
2.2.4. Materials characterization.....	16
2.2.5. Electrochemical characterization.....	17
2.2.6. Desalination experiments.....	18
2.3.Results.....	19
2.3.1. Material characterization.....	19
2.3.2. Basic electrochemical characterizations in aqueous 1 M NaCl.....	23
2.3.3. Desalination performance in aqueous 10 mM NaCl: Symmetric electrode configuration.....	25
2.3.4. Desalination performance in aqueous 10 mM NaCl: Asymmetric electrode configuration.....	29
2.4.Conclusions.....	34
<b>3. Chapter 3 – High-performance activated carbon from polyaniline for capacitive deionization</b> .....	43
3.1.Introduction.....	43
3.2.Experimental.....	46
3.2.1. Materials.....	46
3.2.2. Polyaniline synthesis.....	46
3.2.3. Polyaniline carbonization and activation.....	46
3.2.4. Preparation of CDI electrodes.....	47
3.2.5. Material characterization.....	47
3.2.6. Electrochemical characterization.....	48
3.2.7. Electrosorption experiments.....	49
3.3.Results and discussion.....	50
3.3.1. Polymerization and activation.....	50
3.3.2. Characterizations.....	51
3.3.2.1.FTIR.....	51
3.3.2.2.Morphology.....	52
3.3.2.3.Elemental analysis and surface groups.....	53

3.3.2.4. Textural properties.....	56
3.3.2.5. Electrochemical characterizations.....	59
3.3.3. Electrosorption experiments.....	64
3.4. Conclusions.....	70
<b>4. Chapter 4 – Simultaneous analysis of electrosorption capacity and kinetics for CDI desalination using different electrode configurations.....</b>	<b>83</b>
4.1. Introductions.....	83
4.2. Experimental .....	89
4.2.1. Materials.....	89
4.2.2. Polyaniline synthesis.....	89
4.2.3. PAC/PTS preparation and surface treatment.....	89
4.2.4. Electrode preparation and characterization.....	90
4.2.5. Electrosorption experiments.....	91
4.3. Results and discussion.....	92
4.3.1. Activated carbon characterization.....	92
4.3.2. Electrochemical characterization.....	92
4.3.3. Electrosorption.....	93
4.3.4. Simultaneous analysis of SAC, $k_e$ , and $k_d$ using the OSR approach.....	97
4.4. Conclusions.....	100
<b>5. Chapter 5 – Optimized polyaniline-derived carbon electrodes for capacitive deionization.....</b>	<b>107</b>
5.1. Introduction.....	107
5.2. Experimental .....	109
5.2.1. Materials.....	109
5.2.2. Polyaniline synthesis, activation, and electrode preparation.....	110
5.2.3. Material characterization.....	111
5.2.4. Electrochemical characterization.....	111
5.2.5. Electrosorption.....	112
5.3. Results and discussion.....	113
5.3.1. Characterizations.....	115
5.3.2. Mechanism of activation of the carbonized precursors.....	121
5.3.3. Textural properties.....	122
5.3.4. Electrochemical characterization.....	124
5.3.5. Desalination.....	126
5.3.5.1. Influence of carbonization conditions.....	126
5.3.5.2. Influence of activation conditions.....	128
5.3.5.3. Influence of the activating agent.....	130
5.4. Conclusion.....	130
<b>6. Chapter 6 – General discussion, conclusions, and suggestions for future works ....</b>	<b>147</b>
6.1. Specific surface area, pore volume, and pore size distribution.....	147
6.2. Surface groups.....	148
6.3. Asymmetry vs. MCDI .....	148
6.4. Materials development.....	149
6.5. Metrics for CDI evaluation.....	149
6.6. Summary.....	149
6.7. Suggestions for future works.....	150
<b>7. Chapter 7 – Academic production.....</b>	<b>152</b>

7.1.Publications.....	152
7.1.1. First author.....	152
7.1.2. Co-author.....	152
7.2.Conferences.....	153
7.2.1. Presenter.....	153
7.2.2. Published in the proceedings.....	154
7.3.Patents.....	155

## LIST OF TABLES

<b>Table 2.1.</b> Elemental analysis and yield of the carbon samples (all values in mass%).....	20
<b>Table 2.2.</b> SSA, total pore volume ( $V_{total}$ ), micropore volume ( $V_{mic}$ ), and average pore diameter ( $d_{50}$ ) of LC, LK, and AC obtained by nitrogen gas sorption at -196 °C.....	22
<b>Table 2.3.</b> Charge efficiency with and without leakage current, energy consumption, and salt adsorption capacity (SAC) for LK and AC electrodes with different configurations. For all data, the discharge half cycle was carried out at 0 V.....	30
<b>Table A2.1.</b> SAC obtained using different carbon materials in CDI literature.....	39
<b>Table 3.1.</b> Elemental analysis and atomic composition of the near surface region obtained by XPS for PAC doped with different anions.....	55
<b>Table 3.2.</b> Textural properties of the PAC doped with different anions, including the commercial activated carbon reference (CAC).....	57
<b>Table 3.3.</b> Capacitance values determined from CV curves, charge-discharge and EIS measurements.....	59
<b>Table 3.4.</b> EIS parameters from the Nyquist plot and the modified Randle equivalent circuit.....	62
<b>Table 3.5.</b> Electrosorption parameters $Q_E$ , $\eta$ , SAC, and $k_1$ , of the PAC and CAC electrodes.....	66
<b>Table 3.6.</b> SAC obtained using different carbon materials in a CDI process.....	69
<b>Table A3.1.</b> Polymerization yield for PANi doped with different anions.....	79
<b>Table A3.2.</b> Yield of pre-carbonization and activation of PANi doped with different anions.	80
<b>Table A3.3.</b> $D_c$ based on the charge-discharge experiments.....	80

<b>Table 4.1.</b> SAC, kinetic constants, $Q_E$ , and $\eta$ for CDI carried out using different PAC and mPAC electrode configurations and applied voltages.....	96
<b>Table 4.2.</b> Parameters used to calculate <i>OSR</i> for the different electrode configurations, considering an operational time of one day.....	98
<b>Table 4.3.</b> <i>OSR</i> values reported for different electrode materials.....	100
<b>Table 5.1.</b> PANi carbonization ( $Y_{CP}$ ), activation ( $Y_{PAC}$ ) and total ( $Y_T$ ) yields.....	114
<b>Table 5.2.</b> Elemental analysis of PANi/PTS and their carbonization and activation products, weight percentage of PTS, and ratio between the oxygen from PTS and total oxygen content ( $O_{PTS}/O$ ).....	117
<b>Table 5.3.</b> $SSA_{BET}$ , $SSA_{DFT}$ , total volume of pores ( $V_{total}$ ), volume of micropores ( $V_{mic}$ ), percentage of mesopores ( $\%V_{mes}$ ), and average pore diameter ( $d_{50}$ ) obtained from the N <sub>2</sub> adsorption/desorption isotherms.....	123
<b>Table 5.4.</b> Capacitance calculated from the cyclic voltammograms at 1 mV/s in 200 mM NaCl, and converted deionization capacity ( $D_c$ ).....	125
<b>Table 5.5.</b> <i>mSAC</i> , <i>OSR</i> , charge-efficiency and specific energy consumption for the activated carbon electrodes in 600 ppm NaCl. $E_{cell} = 1.2$ V. <i>tSAC</i> was calculated for 5 mM NaCl...	127
<b>Table A5.1.</b> Surface elemental composition obtained from the XPS survey and surface groups determined from the deconvoluted O1s high resolution XPS.....	139
<b>Table A5.2.</b> Electrosorption kinetics constant and desorption time ( $t_D$ ).....	139
<b>Table A5.3.</b> <i>mSAC</i> of different electrode materials for water desalination using CDI.....	139
<b>Table A5.4.</b> Values of $E_0$ and $E_{PZC}$ for the activated carbon electrodes.....	140

## LIST OF FIGURES

<b>Figure 1.1.</b> Scheme of the water desalination using .....	3
<b>Figure 1.2.</b> Scheme of the CDI water desalination.....	5
<b>Figure 1.3.</b> One of the possible structures for lignin.....	8
<b>Figure 2.1.</b> Scanning electron micrographs of (A) lignin, (B) LC, (C) LK, and (D) commercial AC (MSP-20).....	20

- Figure 2.2** (A) Thermogravimetry of LK and AC in an argon atmosphere. (B) Coupled TGA-MS plotting the ionic current vs. temperature for  $m/z$ : 28, 32, and 44 of LK. (C) Raman spectra of LK and AC. (D) Cumulative pore size distribution of LC, LK, and AC obtained from nitrogen gas sorption at  $-196\text{ }^{\circ}\text{C}$ . The corresponding isotherms can be found in the Appendix..... 21
- Figure 2.3.** Electrochemical characterization of LK and AC in aqueous 1 M NaCl. (A) Cyclic voltammograms at 5 mV/s and (B) corresponding capacitance values at 5-500 mV/s. (C) Galvanostatic charge/discharge profiles and (D) corresponding capacitance values at specific currents of 0.1-10 A/g..... 24
- Figure 2.4.** Electrochemical stability limits for LK and AC in aqueous 1 M NaCl (S-value analysis)..... 24
- Figure 2.5.** Salt adsorption capacity (SAC) and charge efficiency varying with cycles at different cell potentials for (A) LK and (B) commercial AC. (C) Conductivity profile for the 10<sup>th</sup> cycle at 1.0 V and 1.2 V and (D) electrode potential distribution for the sample LK. WE: working electrode; CE: counter electrode;  $E_0$ : short-circuit potential..... 26
- Figure 2.6.** Scheme of the co-ion effect when  $E_{PZC}$  is on the negative potential window (A), the negative and positive electrodes present  $E_{PZC}$  on their potential window (B), and the negative and positive electrodes present the  $E_{PZC}$  out of the potential window (C).  $E_{PZC}$  values obtained from the lowest capacitance value using EIS measurement for LK and AC electrodes (D)..... 28
- Figure 2.7.** Data for the 1LK:2LK electrode configuration in aqueous 10 mM NaCl. (A) Salt adsorption capacity and charge efficiency. (B) Electrode potential distribution for several CDI cycles..... 30
- Figure 2.8.** (A) Salt adsorption capacity, (B) charge efficiency, and (D) potential distribution for the asymmetric LK and AC electrodes..... 32
- Figure 2.9.** Data for the LK:AC electrode configuration at 1.0 V and 1.1 V in aqueous 10 mM NaCl: (A) Long-term SAC and charge efficiency. (B) Potential distribution. (C) Conductivity profile. (D) Kinetic plot..... 33
- Figure 2.10.** Kinetic data analysis for CDI half-cycles. (A) Conductivity profile and (B) the corresponding kinetic plot for adsorption and desorption data..... 34

<b>Figure A2.1.</b> Coupled TGA-MS plotting the ionic current vs. temperature for m/z: 28, 32, and 44 of AC (MSP-20).....	39
<b>Figure A2.2.</b> Nitrogen gas sorption isotherms of LK, LC, and AC recorded at -196 °C .....	40
<b>Figure A2.3.</b> Galvanostatic charge/discharge profiles for LK and AC at 10 A/g.....	40
<b>Figure A2.4.</b> Electrode potential distribution for the sample AC. WE: working electrode; CE: counter electrode; $E_0$ : short-circuit potential; $E_{PZC}$ : potential of zero charge.....	41
<b>Figure A2.5.</b> pH values measured during the desalination experiment using symmetrical LK electrodes at a cell potential of 1.0 V, 1.1 V and 1.2 V.....	41
<b>Figure 3.1.</b> Infrared spectra of PANi doped with different anions (A) and schematic representation of the anion doping: (B) $Cl^-$ , (C) $PTS^-$ , (D) $DBS^-$ , and (E) $PSS^-$ .....	52
<b>Figure 3.2.</b> SEM images of (A) PAC/ $Cl^-$ , (B) PAC/ $PTS^-$ , (C) PAC/ $DBS^-$ , and (D) PAC/ $PSS^-$ .....	53
<b>Figure 3.3.</b> Deconvoluted high resolution XPS C 1s, O 1s, N 1s, Cl 2p and S 2p spectra of PAC/ $Cl^-$ , PAC/ $PTS^-$ , PAC/ $DBS^-$ and PAC/ $PSS^-$ .....	56
<b>Figure 3.4.</b> (A) Isotherms of $N_2$ adsorption-desorption; (B) PSD. Inset: Relative cumulative pore volume distribution ( $V/V_T$ ).....	57
<b>Figure 3.5.</b> Scheme of micelle formation prior to PANi/ $DBS^-$ polymerization.....	58
<b>Figure 3.6.</b> (A) Cyclic voltammeteries of PAC and CAC electrodes. Scan-rate: 1.0 mV/s; electrolyte: NaCl 0.2 mol/ L; (B) capacitance as a function of the potential scan rate.....	60
<b>Figure 3.7.</b> Nyquist plot (A) and capacitance as a function of the frequency (B) for PAC and CAC electrodes. (C) Modified Randle equivalent circuit. Electrolyte: NaCl 0.2 mol/L; potential: 0.0 V; AC amplitude: 10 mV.....	62
<b>Figure 3.8.</b> SAC of PAC and CAC electrodes for desalination at 1.2 V (A) and 1.4 V (B).....	66
<b>Figure 3.9.</b> ASAR vs. SAC for PAC/ $PTS^-$ and CAC at 1.2 and 1.4 V.....	67
<b>Figure A3.1.</b> Scheme of a CDI device: (A) electrosorption and (B) regeneration.....	81
<b>Figure A3.2.</b> Charge-discharge profiles obtained for the different carbon materials at a charge density of 0.4 mA/cm <sup>2</sup> .....	81



<b>Figure A3.3.</b> Circuit fitting for the PAC doped with $\text{Cl}^-$ (A) $\text{PTS}^-$ (B) $\text{DBS}^-$ (C) $\text{PSS}^-$ (D) CAC (E) and the equivalent circuit used for the fitting (F).....	82
<b>Figure 4.1.</b> Electrosorption/desorption curves described by the pseudo-first order model for the PAC-PTS electrodes (20 mg/g $SAC_m$ and pseudo-first order constants of $k_e = 0.0055 \text{ s}^{-1}$ and $k_d = 0.0090 \text{ s}^{-1}$ for electrosorption and desorption, respectively).....	87
<b>Figure 4.2.</b> (A) Plot of $m_{sr}$ against $t_e$ ( $t_{op} = 5 \text{ h}$ ), and (B) $SAC$ comparison considering $t_{e-99\%}$ and $t_{e-opt}$ in a simulated CDI process lasting 5 h. Parameters: $SAC_m = 20 \text{ mg/g}$ , $k_e = 0.0055 \text{ s}^{-1}$ , and $k_d = 0.0090 \text{ s}^{-1}$ .....	89
<b>Figure 4.3.</b> Zeta potential as a function of pH for PAC and mPAC.....	92
<b>Figure 4.4.</b> (A) Voltammograms for the $\text{PAC}^-$ and $\text{mPAC}^+$ electrodes at $1 \text{ mV s}^{-1}$ , and (B) capacitance as a function of the scan rate. Electrolyte: $0.2 \text{ mol/L NaCl}$ .....	93
<b>Figure 4.5.</b> (A) Electrosorption and desorption performances of $\text{PAC}^-(-) \parallel (+)\text{PAC}^-$ , $\text{PAC}^-(-) \parallel (+)\text{mPAC}^+$ , and $\text{mPAC}^+(-) \parallel (+)\text{PAC}^-$ in $600 \text{ mg/L NaCl}$ at $1.2 \text{ V}$ , and schematic representations of co-ion repulsion and counterion adsorption for symmetric (B) and asymmetric configurations (C and D).....	94
<b>Figure 4.6.</b> Plot of $SAC$ against time for the MCDI and symmetric CDI, carried out at $1.2 \text{ V}$ and $1.4 \text{ V}$ in $600 \text{ mg/L NaCl}$ .....	97
<b>Figure 4.7.</b> Plots of $m_{sr}$ against $t_{e-opt}$ for the symmetric and asymmetric CDI and MCDI.....	98
<b>Figure 5.1.</b> SEM images of the PANi/PTS (A), $\text{C}_5$ (B), $\text{C}_5\text{A}_{85}\text{K}_4$ (C), and $\text{C}_{8.5}\text{A}_{85}\text{K}_4$ .....	116
<b>Figure 5.2.</b> (A) XRD patterns for PANi/PTS, $\text{C}_4$ , $\text{C}_5$ and $\text{C}_{8.5}$ samples, (B) turbostratic structure, and (C) graphitic structure .....	116
<b>Figure 5.3.</b> TGA (A), and dTGA (B) of PANi and their carbonization products.....	118
<b>Figure 5.4.</b> FTIR of PANi and their carbonization products (A), and high resolution deconvoluted O1s XPS spectra of $\text{C}_4$ and $\text{C}_5$ (B).....	120
<b>Figure 5.5.</b> Nitrogen adsorption-desorption isotherms (A), and PSD (B) of polyaniline activated carbon obtained under different activation conditions. The isotherms and PSD for $\text{C}_5$ and $\text{C}_{8.5}$ are shown in	
<b>Figure A5.3</b> .....	122

<b>Figure 5.6.</b> (A) Cyclic voltammeteries recorded at 1 mV/s and (B) capacitance at different scan-rates. Electrolyte concentration: 200 mM NaCl.....	125
<b>Figure 5.7.</b> SAC (A) and $m_{sr}$ (B) against time obtained using the electrode materials prepared at different values of $T_C$ . Desalination conditions: 600 mg/L NaCl, 1.2 V.....	126
<b>Figure 5.8.</b> SAC (A) and $m_{sr}$ (B) against time for the electrodes prepared with carbons activated at different conditions. 600 mg/L NaCl, 1.2 V.....	129
<b>Figure 5.9.</b> SAC (A) and OSR (B) against time for C <sub>5</sub> A <sub>85</sub> K <sub>4</sub> and C <sub>5</sub> A <sub>85</sub> KC. 600 mg/L NaCl, $E_{cell} = 1.2$ V.....	130
<b>Figure A5.1.</b> SEM images of C <sub>4</sub> (A) and C <sub>8.5</sub> (B).....	140
<b>Figure A5.2.</b> TEM micrographs of C <sub>4</sub> (A), C <sub>5</sub> (B), C <sub>8.5</sub> (C), C <sub>5</sub> A <sub>85</sub> K <sub>4</sub> (D), and C <sub>8.5</sub> A <sub>85</sub> K <sub>4</sub> (E).....	141
<b>Figure A5.3.</b> XPS survey spectrum for C <sub>4</sub> (A) and C <sub>5</sub> (B), deconvoluted high resolution XPS C1s for C <sub>4</sub> (C) and C <sub>5</sub> (E), and N1s for C <sub>4</sub> (D) and C <sub>5</sub> (F).....	142
<b>Figure A5.4.</b> Nitrogen adsorption-desorption isotherms (A), and PSD (B) for C <sub>5</sub> and C <sub>8.5</sub> . Observation: The open isotherm observed for C <sub>5</sub> was reproducible, including using different equipment, and was ascribed to the presence of very narrow slit pores or bottle shaped pores. In this case, N <sub>2</sub> molecules at 77 K move very slowly that the adsorption is kinetically limited.....	143
<b>Figure A5.5.</b> CVs recorded at 1 mV/s in 200 mM NaCl for the electrodes prepared with the activated carbons obtained under different activation conditions.....	143
<b>Figure A5.6.</b> Conductivity profile for the electrodes prepared with PANi carbonized at different temperatures.....	144
<b>Figure A5.7.</b> $mSAC$ vs. $SSA_{BET}$ for PAC electrodes. Experimental conditions: 1.2 V, 600 mg/L NaCl.....	144
<b>Figure A5.8.</b> Conductivity profile and $E_{cell}$ vs. time for C <sub>5</sub> A <sub>6.5</sub> K <sub>4</sub> . Concentration: 600 mg/L NaCl.....	145
<b>Figure A5.9.</b> Normalized capacitance vs. electrode potential for PAC electrodes obtained at different activation temperatures (A), and low $K/C$ (B). The values of capacitance were measure in 600 mg/L NaCl by EIS at 0.01 Hz.....	145

## NOMENCLATURE

ASAR	Average salt adsorption rate	[mg/g.s]
$C_s$	Specific capacitance	[F/g]
$C_{CD}$	Average capacitance obtained from charge-discharge	[F/g]
$C_{CV}$	Average capacitance obtained from CV	[F/g]
$C_{EIS}$	Average capacitance obtained from EIS	[F/g]
$D_c$	Converted deionization capacity	[mg/g]
$D_{H_3O^+}$	Diffusion coefficient of hydronium	[m <sup>2</sup> /s]
$D_{OH^-}$	Diffusion coefficient of hydroxyl	[m <sup>2</sup> /g]
$E_0$	Short circuit potential	[V]
$E_{cell}$	Cell potential	[V]
$E_{cell-regeneration}$	Cell potential of regeneration	[V]
$E_{CE}$	Counter electrode potential	[V]
$E_{kT}$	Specific energy removal per molecule	[kT]
$E_{PZC}$	Potential of zero charge	[V]
$E_{WE}$	Working electrode potential	[V]
F	Faraday constant	[C/mol]
I	Current	[A]
$I_d$	Discharge current	[A]
K/C	KOH/carbon weight ratio	[-]
$k_B$	Boltzmann constant	[m <sup>2</sup> /kg.s <sup>2</sup> .K]
mSAC	Maximum SAC	[mg/g]
$m_{sr}$	Mass of salt removed	[mg]
OSR	Optimized salt removal	[mg/day]
$Q_E$	Charge efficiency	[Ω]
$R_{CT}$	Charge transfer resistance	[ohm]
SAC	salt adsorption capacity	[mg/g]
SSA	Specific surface area	[m <sup>2</sup> /g]
$t_e$	Electrosorption time	[s]
$t_d$	Desorption time	[s]

$t_{e-opt}$	Optimized electrosorption time	[s]
tSAC	Theoretical SAC	[mg/g]
W	Warburg element	[ $\Omega$ ]
$Y_{AC}$	Yield of activated carbon	[-]
$Y_C$	Yield of carbonized carbon	[-]
$Y_T$	Total yield	[-]

### GREEK LETTERS

$\eta$	Specific energy consumption	[J/mg]
$\varepsilon$	Capacitance efficiency	[-]
$\nu$	Scan-rate	[mV/s]
$\omega$	Angular frequency	[-]
$\sigma$	Conductivity	[ $\mu\text{S}/\text{cm}$ ]

### ACRONYMS

AEM	Anion exchange membrane
BET	Brunauer-Emmett-Teller
CDI	Capacitive deionization
CEM	Cation exchange membrane
CV	Cyclic voltammetry
DBS	Dodecylbenzenesulfonate
DFT	Density functional theory
DLC	Electric double layer
ED	Electrodialysis
EDLC	Electric double layer capacitor or supercapacitor
GCPL	Galvanostatic charge/discharge cycling with potential limitation
HCDI	Hybrid capacitive deionization
iCDI	Inverse capacitive deionization
LK	Lignin activated carbon
MCDI	Membrane capacitive deionization

MFD	Multi-stage flash distillation
mPAC	Surface modified PAC
NFDFT	Non-local density functional theory
NMP	n-Metilpyrrolidone
PAC	Polyaniline activated carbon
PAni	Polyaniline
PAni/PTS	Polyaniline doped with PTS
PTFE	Polytetrafluoroethylene
PVDF	Polyvinylidene fluoride
PSD	Pore size distribution
PSS	Polystyrenesulfonate
PTS	para-Toluenesulfonate
QSDFT	Quenched solid density functional theory
RED	Reverse electrodialysis
RO	Reverse osmosis
T <sub>A</sub>	Activation temperature
T <sub>C</sub>	Carbonization temperature

## CHAPTER 1

### INTRODUCTION

#### 1.1. Broad context

The XXI century has been known not only by the scientific and technological breakthroughs, but also by many environmental challenges. One of them is the access to drinkable water, which has become a serious problem even in countries that had never suffered of water scarcity. While the Fortune Magazine declared that water will possibly be as important for the XXI century as petroleum was in the XX century, the United Nations reported that around 4 billion people are potentially water scarce, and this number may rise up to 6 billion until 2050.[1,2]

The access of water is not only important for providing water for human consumption, but also plays a fundamental role on the human development, since agriculture and industry depends on fresh water for their development. Indeed, agriculture and industry represent ~69% and ~20% of the total water consumption, respectively.[3] Therefore, the only alternative to develop many regions suffering with water scarcity is the use of different technologies to provide water.

Although there are plenty of water reservoirs on Earth, the water distribution is still the main drawback. It is estimated that 97.5% of water is stored in the oceans, while the 2.5% left is divided in glaciers/snow covers (1.72%), groundwater (0.75%), lakes and rivers (0.0075%), and soil/air water (0.023%).[4] Only this 2.5% is fresh water and can be used direct for human and animal consumption or agricultural and industrial purposes, since the high salt concentration in seawater demands high energy consumption for desalination.

The most accessible fresh water reservoirs are groundwater, lakes, rivers, and soil/air water. Despite of groundwater be more abundant than the other water sources, it is usually contaminated with low salt concentrations (brackish water). An example is underground of the Brazilian semi-arid region, which it is estimated that it can provide 19.5 m<sup>3</sup>/year of water without risk of exhaustion. However, the presence of brackish due to the long exposure of water to the crystalline rocks [5] demand new desalination technologies to provide drinking water for human, animal, and agricultural consumption, thus contributing to the economic and social development of the semi-arid.

## **1.2. Desalination technologies**

The most well established technologies employed for water desalination are the multi-stage flash distillation (MFD), reverse osmosis (RO), and electrodialysis (ED). Among these technologies, RO is still the most used all over the world, and many advances regarding reduction on energy consumption, and improvements on water recovery were achieved. In the next sections, it will be described the main characteristics of these desalination technologies.

### **1.2.1. Multiple stage flash distillation (MFD)**

Flash distillation is a thermal process in which heat is used at low pressure to evaporate concentrated salt water, and then condensate it again to yield pure water. A more advanced distillation technique is the multiple stage flash distillation, in which the condensation energy is reused to reduce the overall energy demand. Semiat (2008) estimates that the MFD energy consumption is between 15-58 kWh/m<sup>3</sup>. [6]

The MFD is based on the flash distillation process. The seawater is evaporated by reducing the pressure and increasing the water temperature. The reduction on the energy consumption is achieved by the back warming of the feedwater provided by the heat of the evaporated water that is condensing. Therefore, the temperature of the incoming water increases, reducing the energy required to evaporate it.

The distillation has been employed in large-scale plants to desalinate seawater. Advances in the technology, such as the use of membrane distillation may prolong the life time of this technology, however, its high energy requirements turns this technology only feasible in countries where the energy cost is not a hindrance, such as Saudi Arabia.

### **1.2.2. Reverse osmosis**

Reverse osmosis is one of the most used desalination technologies in the world, being largely employed in countries such as the United States of America, Spain and Israel. [7–9] It is based on a pressure-driven separation process in which an external pressure, higher than the osmotic, forces the saline stream to flow through a water permeable membrane, resulting in brine and purified water streams. Although RO is a recognized high demanding energy process, recent advances on minimizing fouling and concentration polarization, and maximization of permeate flux and energy recovery reduced RO energy consumption from 12 kWh/m<sup>3</sup> in the 1970s to less than 2 kWh/m<sup>3</sup> in 2006. [10,11]

On the other hand, problems such as membrane fouling is still a drawback regarding to this technology. Moreover, the water obtained after the desalination process is extremely diluted, and unhealthy. Hence, after desalination, the water has to be hardened to make it drinkable. The water recovery for RO, which is the ratio between pure water and brine, may reach 70-80% for brackish water (salt concentration < 10 g/L of water) and 35-60% for seawater.

In the Brazilian context, in accordance with the Association of Brazilian Geographers, in 2004 there were more than 3000 RO units in the semiarid region of Brazil employed for water desalination. Unfortunately, most part of the systems were not working properly due to bad use and lack of maintenance.

### 1.2.3. Electrodialysis

The reverse electrodialysis (RED) is also a membrane-based separation process, however, in this case, the driven force for ions separation is an electric field developed when a high voltage is applied between two electrodes in a desalination cell, as show in **Fig. 1.1**. Hydronium and hydroxyl are formed on the anode and cathode, respectively, and based on the principle of electroneutrality, a counterbalance must be established, forcing the chloride through the anion exchange membrane (AEM) to the anode chamber, while sodium cations move through the cation exchange membrane (CEM) to the cathode chamber. Pure water is obtained in the middle chamber.

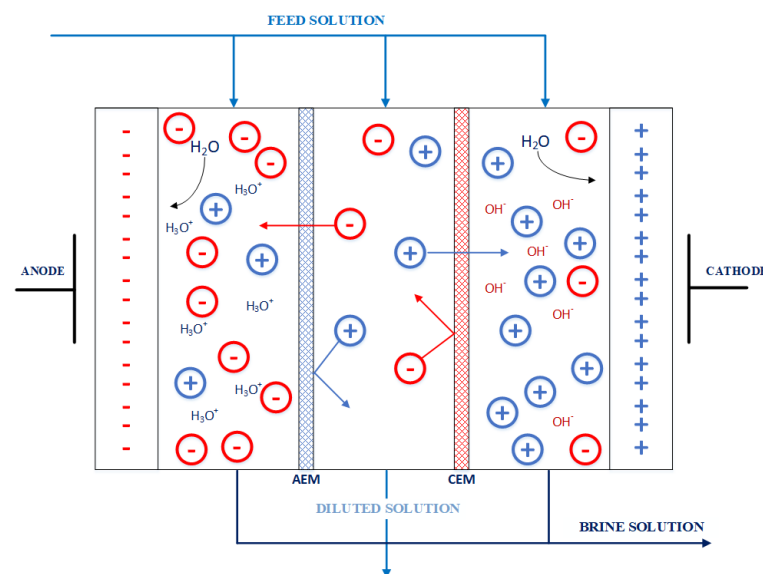


**Figure 1.1.** Scheme of the water desalination using ED. (Source: The author)



The ED is effective for water desalination achieving 75-98% of TDS removal. Furthermore, by reversing the polarity (reverse ED), it is possible to clean the membranes reducing fouling and incrustation. The water recovery in this system may be as high as 94%. [7] However, the upper concentration limit to operate ED is around 5000 mg TDS/L. Beyond this concentration, the energy consumption is high ( $> 2.5 \text{ kWh/m}^3$ ) and do not compete with other technologies. [12]

### 1.3. CDI technology

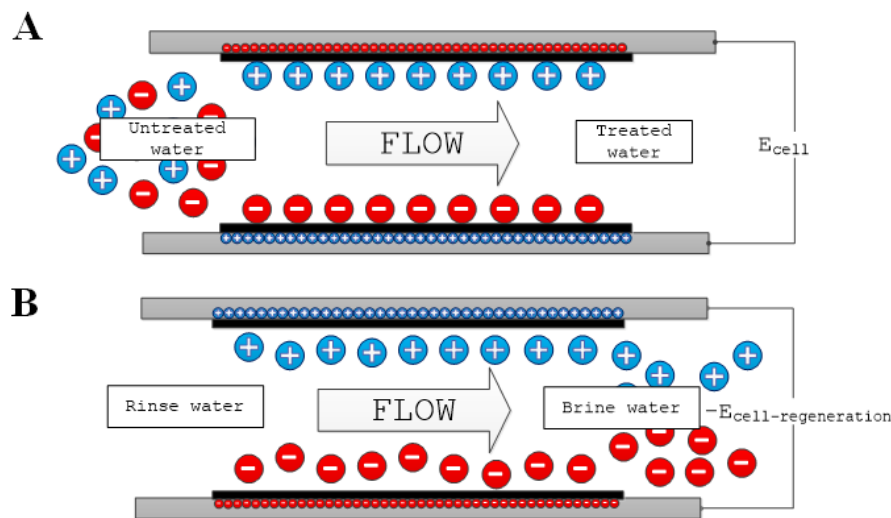
In the beginning of this century, a new technology called capacitive deionization (CDI) emerged as an alternative for water desalination. Although Caudle *et al.* (1966) and Johnson and Newman (1973) [13,14] introduced its main concept a long time ago, its ascension occurred in the middle of 1990s due to the work of Farmer *et al.* (1995) using carbon aerogels as CDI electrodes. [15] This technology presents some advantages over their competitors, such as low energy consumption, ease assembly and maintenance, and use of environmentally friendly materials. Furthermore, CDI fills the gap of being a cost-effective technology for small systems where the salt content is low. There are different situations in which a small unit easy to reallocate is required. For instance, to prevent transportation costs in rural areas for agriculture, the water treatment has to be carried out on site, where usually electricity is not available. That is the case for brackish groundwater desalination in rural areas.

CDI is based on the same concept of the electric double layer capacitors (EDLC), in which a pair of electrodes are polarized and the ions present in an electrolytic solution are attracted and stored in the electric double layer (EDL). Unlike the EDLC, the CDI interest is on the outflow solution obtained after the electrodes polarization. Fig. 1.2 shows a scheme of the desalination process using CDI. The electrolytic solution is fed to the CDI cell, and a cell potential ( $E_{cell}$ ) is applied between a pair of electrodes. Cations are attracted to the negatively charged electrode, and are stored on the EDL, while the same happens with anions on the positively charged electrode (Fig. 1.2A). After a while, the electrode becomes saturated and must be regenerated (Fig. 1.2B). This is easily accomplished by short circuiting the electrodes ( $E_0$ ), or by applying an inverse regeneration cell potential ( $E_{cell-regeneration}$ ) (typical values are in between -0.1 V to -0.4 V). [16,17]

The low energy consumption of CDI results from the low  $E_{cell}$  required for water desalination when high charge efficiencies are achieved. The charge efficiency is the ratio

between the total charge supplied and the amount of ions removed. Therefore, as close as unit the charge efficiency is, the more effective is the desalination process. Besides, as CDI is a capacitive technology, part of the energy used for the electrosorption process can be recovered, which reduces even more the total energy consumption.[18,19] On the other hand, it has also been demonstrated that there are many sources for energy losses, such as by ohmic resistance, electrode degradation, water splitting, and irreversible faradaic reactions.[20,21] Having this in mind, many researchers follow investigating new electrode materials and new cells designs to optimize the CDI process.

**Figure 1.2.** Scheme of the CDI water desalination. (Source: Zornitta *et al.*[17])



The challenge of finding electrode materials that fulfills all the requirements for the CDI process is still on course. Most part of the works on CDI literature is based on studying new materials, and finding new correlations between the electrode material properties and CDI performance. The main requirements for a good CDI electrode are:[22,23]

- (1) High specific surface area (SSA) available for electrosorption. Although there is a relationship between SSA, and salt adsorption capacity (SAC), it was demonstrated that the surface area accessible for electrosorption is much lower than the actual surface area;
- (2) Good chemical and electrochemical electrode stability, since the electrodes must run for thousands of cycles;
- (3) Fast electrosorption/desorption kinetics, which can be limited by the pore size and electrode thickness of the electrode (other operational variables, such as electrolyte concentration are not considered here);

- (4) Good wettability (or hydrophilicity), which is closely related to the presence of polar surface groups on the electrode;
- (5) High conductivity of the electrode material, ensuring low potential drop across the electrode, and low energy dissipation, which could reduce the electrode charge efficiency;
- (6) Low-cost, abundance, and environmentally friendly materials are desired for large-scale desalination plants.

Taking into account those characteristics, carbon electrodes have been largely used for CDI since it fulfills most part of these requirements. Different forms of carbons have already been employed as electrodes for water desalination, such as carbon nanotubes,[24] graphene,[25,26] carbon cloths,[27] carbon sponges,[28] activated carbons,[29] carbide-derived carbons,[30] and carbon aerogel.[31] Most of these materials present promising results in terms of SAC, but many are not cost-effective, such as carbon nanotubes and graphene, besides they are not easy to synthesize, which hinders their use in large-scale applications.

Recently, new approaches for CDI emerged, such as hybrid CDI (HCDI), which aims to overcome one of the main drawbacks in CDI desalination: the oxidation of the positive electrode, which is the main impeditive for long-term operations of CDI cells. Although cells potentials lower than 1.23 V may prevent water splitting, they can cause irreversible reactions occurring on the carbon surface.[32] Therefore, the employ of more stable positive electrode materials has been proposed, such as battery electrode materials.[33,34] Unlike the capacitive process, in which the ions are adsorbed on the EDL, battery electrodes undergo faradaic reactions in which ions are intercalated inside of the material structure. The main advantage of this process is the high selectivity for cations or anions, which avoids the waste of charge used for co-ions repulsion, instead of using it for counterion electrosorption. This approach is even more interesting if one consider that the effect of co-ion repulsion is much more pronounced as the concentration increases.[35] The results presented so far showed remarkable desalination capacity, reaching values far higher than pure CDI. For instance, some authors reported a desalination capacity as high as 120.0 mg/g using Prussian blue ( $\text{FeFe}(\text{CN})_6$ ) as anode in a CDI cell, with low energy consumption.[34]

On one hand, the HCDI shows much higher desalination capacity than usual activated carbon electrodes, but on the other hand, one of the great advantages of using capacitive systems is the fast response to the desalination process. Indeed, the main difference between a supercapacitor and a battery is their specific power and specific energy. While batteries have

higher specific energy, supercapacitors can deliver much higher power rates.[36] This is also of paramount importance since CDI desalination is carried out in cycles of electrosorption and desorption and the faster the cycle, more salt can be removed.

As a counterpart for battery electrode materials, improvements using low-cost activated carbons may provide very high SAC, high electrosorption/desorption kinetic and long-term stability. For instance, the use of ion selective membranes not only is reported to prevent co-ions repulsion, but also hinders electrode oxidation caused by dissolved oxygen present in the electrolyte solution.[32] In this context, ion selective membranes can both improve charge efficiency and electrode stability of carbon electrodes. The CDI process in which membranes are employed is known as MCDI.

Typically, most of the low-cost CDI electrodes are prepared from activated carbon derived from low-cost precursors, such as activated carbon derived from sugar cane bagasse fly ash,[37] starch,[38] silk cocoon,[39] cotton,[28] biomass,[40,41] and plenty of commercial activated carbons.[17,29,42] However, when used without any modification (e.g. nitrogen or hydrogen treatment, post CO<sub>2</sub> activation, etc.) these materials do not perform well, and typical values of SAC are lower than 10 mg of salt removed per g of carbon. Therefore, the cost of preparation of these carbons still do not compensate their SAC. In this scenario, it is still important to search for low-cost CDI electrodes with improved desalination capacity, low energy consumption, and long-term stability.

#### **1.4. Thesis outline**

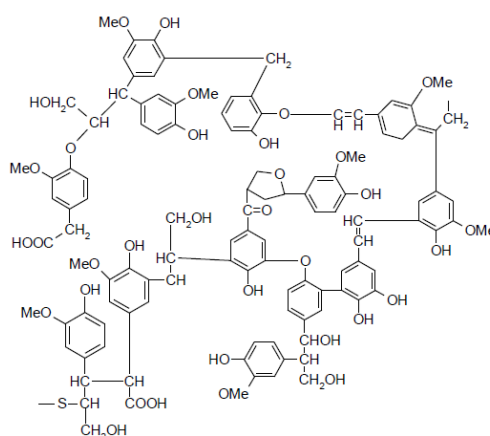
As discussed so far, there is still a search for new high-performance and low-cost materials for CDI. This thesis focuses on developing new activated carbons to be employed as electrode based on the low-cost of the precursor (aniline and lignin), simplicity and efficacy of the activation method, high SSA and pore volume, and high capacitance. Simultaneously, it was also investigated some strategies (asymmetry and membrane) to improve the electrode performance, by reducing the co-ion repulsion effect, electrode degradation, and optimizing the desalination performance by taking into account the electrosorption/desorption kinetic.

In Chapter 2, lignin is introduced as a low-cost precursor for activated carbon since it is an abundant waste from cellulose plants. We also estimate that the amount of lignin can grow significantly with the advent of the second-generation ethanol production. Considering that lignin (Fig. 3) is mostly composed by carbon (>60 wt.%), and oxygen (>30 wt.%), it a good candidate as precursor to obtain activated carbon. Lignin activated carbon is known by the high

SSA and capacitance in the EDLC literature.[43] In this work, lignin activated carbon (LK) is used as electrode for CDI and compared with commercial activated carbon electrodes.

In Chapter 3, aniline is used to synthesize the PANi, which is employed as precursor to prepare activated carbons. PANi-derived activated carbon has been reported as electrode material for supercapacitors due to its high SSA, large pore volumes, and high nitrogen content, thus providing high capacitance. The main advantages of PANi is the low-cost of the monomer, easy preparation, high nitrogen content (~15 wt.%), and the possibility of modifying the precursor by changing the doping anion used for the PANi synthesis.

**Figure 1.3.** One of the possible structures for lignin (Source: Norgren and Edlung [44])



The use of PANi dopants as templates is another interesting characteristic of this precursor. It has already been demonstrated that carbonized PANi develops unique pore size distribution (PSD), and electric properties depending on the anion used as dopant.[45] In Chapter 3, dopant anions are not only used as templates for the carbonized carbon but instead for the activated carbon. The advantage of the activation is to enlarge the carbon pores increasing the SSA, and pore volume. Therefore, the characteristics of the activated carbons are investigated in a CDI desalination process.

In Chapter 4, the PAC desalination performance (SAC and charge efficiency) are further improved by employing ion exchange membranes or chemical surface modification. Both techniques are intended to reduce the deleterious effect caused by co-ion repulsion. Furthermore, it is introduced a new methodology to evaluate the carbon performance, by taking into account not only the SAC, but also electrosorption/desorption kinetic.

In Chapter 5, it is carried out a comprehensive study of the PANi doped with p-toluenesulfonate (PANi/PTS) activation, taking into account the carbonization and activation temperatures ( $T_C$  and  $T_A$ ), and the KOH/carbon weight ratio ( $K/C$ ). Unlike the investigation

carried out in Chapter 3, in which  $T_A$ ,  $T_C$ , and  $K/C$  were maintained constant, in this chapter these variables are deeply investigated for PAC/PTS, and a new mechanism for carbonization/KOH activation is proposed. The desalination performance is correlated with the PAC/PTS properties in order to better understand the role of textural properties and surface groups on the electrosorption process.

In Chapter 6, a general discussion about the results obtained in this thesis is provided. It is enlightened the specific characteristics of the carbon materials, and their influence on the electrodes performance for CDI desalination. Suggestions for future works are also provided in this chapter.

### 1.5. Objectives

The aim of this work is to obtain high performance electrodes for water desalination by capacitive deionization. In order to accomplish this aim, the following specific objectives are established:

- (1) Preparation of low-cost electrodes using as activated carbon precursor the lignin. Lignin activation carbon (LK) is prepared using KOH as activation agent, which is known to develop high SSA, and pore volume. Aiming to improve electrode stability and desalination performance, different electrode configurations were studied (symmetry and asymmetry of mass and material).
- (2) In order to obtain activated carbon with high SAC, it is studied the use of PANi as activated carbon precursor, and the effect of their doping anions on the obtained activated carbons. Their performance as CDI electrodes is investigated through desalination process.
- (3) The carbonization and activation temperature, as well as the KOH/carbon weight ratio are studied in order to maximize the specific surface area, pore volume, and nitrogen content on the PAC, and to improve their electrode performance in a CDI desalination process.
- (4) Aiming to reduce the effect of co-ion repulsion, and reduce electrode degradation on the desalination process, it is studied the use of ion exchange membranes, and the surface chemical modification of the PAC materials.
- (5) A new metric for CDI desalination performance is studied in which the electrode capacity, and the electrosorption/desorption kinetic are taken into account.

## References

- [1] S. Tully, Water, water everywhere today companies like France's Suez are rushing to privatize water, already a \$400 billion global business. They are betting that H<sub>2</sub>O will be to the 21st century what oil was to the 20th, *Fortune Mag.* (2000).
- [2] WWAP (United Nations World Water Assessment Programme)/UN-Water. 2018. The United Nations World Water Development Report 2018: Nature-based solutions for water, UNESCO, Paris, 2018. [www.unesco.org/open-access/](http://www.unesco.org/open-access/).
- [3] A.J. Philippi, M.A. Romero, B.G. Collet, *Curso de Gestão Ambiental*, Editora Manole, Barueri, SP, 2004.
- [4] I.A. Shiklomanov, *World water resources a new appraisal and assessment for the 21st century*, Unesco, Paris, 1998.
- [5] T.M. Soares, S.N. Duarte, Ê.F.D.F. Silva, Destinação de águas residuárias provenientes do processo de dessalinização por osmose reversa, *Rev. Bras. Eng. Agrícola e Ambient.* 10 (2006) 730–737.
- [6] R. Semiat, *Critical Review Energy Issues in Desalination Processes*, 42 (2008) 8193–8201.
- [7] T. Younos, K.E. Tulou, *Overview of Desalination Techniques*, (2005) 3–10.
- [8] A. Tenne, Sea water desalination in Israel: planning, coping with difficulties, and economic aspects of long-term risks, *Water Auth. State Isr.* (2010) 1–13.
- [9] G.L. Meerganz von Medeazza, “Direct” and socially-induced environmental impacts of desalination, *Desalination*. 185 (2005) 57–70. doi:10.1016/j.desal.2005.03.071.
- [10] K.P. Lee, T.C. Arnot, D. Mattia, A review of reverse osmosis membrane materials for desalination-Development to date and future potential, *J. Memb. Sci.* 370 (2011) 1–22. doi:10.1016/j.memsci.2010.12.036.
- [11] R.L. Stover, Seawater reverse osmosis with isobaric energy recovery devices, *Desalination*. 203 (2007) 168–175. doi:10.1016/j.desal.2006.03.528.
- [12] M. a. Anderson, A.L. Cudero, J. Palma, Capacitive deionization as an electrochemical means of saving energy and delivering clean water. Comparison to present desalination practices: Will it compete?, *Electrochim. Acta.* 55 (2010) 3845–3856. doi:10.1016/j.electacta.2010.02.012.
- [13] D.D. Caudle, J.H. Tucker, J.L. Cooper, B.B. Arnold, A. Papastamataki, *Electrochemical demineralization of water with carbon electrodes*, 1966.
- [14] A.M. Johnson, J. Newman, *Desalting by Means of Porous Carbon Electrodes*, *J. Electrochem. Soc.* 118 (1971) 510. doi:10.1149/1.2408094.
- [15] J.C. Farmer, D. V Fix, R.W. Pekala, J.F. Poco, G. V Mack, *The Use of Capacitive Deionization with Carbon Aerogel Electrodes to Remove Inorganic Contaminants from Water*, *Low Lev. Waste Conf.* (1995).
- [16] P.M. Biesheuvel, R. Zhao, S. Porada, A. van der Wal, *Theory of membrane capacitive*

- deionization including the effect of the electrode pore space, *J. Colloid Interface Sci.* 360 (2011) 239–248. doi:10.1016/j.jcis.2011.04.049.
- [17] R.L. Zornitta, J.J. Lado, M.A. Anderson, L.A.M. Ruotolo, Effect of electrode properties and operational parameters on capacitive deionization using low-cost commercial carbons, *Sep. Purif. Technol.* 158 (2016) 39–52. doi:10.1016/j.seppur.2015.11.043.
- [18] P. Długołęcki, A. van der Wal, Energy recovery in membrane capacitive deionization., *Environ. Sci. Technol.* 47 (2013) 4904–10. doi:10.1021/es3053202.
- [19] J.E. Dykstra, S. Porada, A. van der Wal, P.M. Biesheuvel, Energy consumption in capacitive deionization – Constant current versus constant voltage operation, *Water Res.* 143 (2018) 367–375. doi:10.1016/j.watres.2018.06.034.
- [20] A. Hemmatifar, J.W. Palko, M. Stadermann, J.G. Santiago, Energy breakdown in capacitive deionization, *Water Res.* 104 (2016) 303–311. doi:10.1016/j.watres.2016.08.020.
- [21] T. Kim, J. Yu, C. Kim, J. Yoon, Hydrogen peroxide generation in flow-mode capacitive deionization, *J. Electroanal. Chem.* 776 (2016) 101–104. doi:10.1016/j.jelechem.2016.07.001.
- [22] Y. Oren, Capacitive deionization (CDI) for desalination and water treatment — past, present and future (a review), *Desalination.* 228 (2008) 10–29. doi:10.1016/j.desal.2007.08.005.
- [23] S. Porada, R. Zhao, a. van der Wal, V. Presser, P.M. Biesheuvel, Review on the science and technology of water desalination by capacitive deionization, *Prog. Mater. Sci.* 58 (2013) 1388–1442. doi:10.1016/j.pmatsci.2013.03.005.
- [24] H. Li, Y. Gao, L. Pan, Y. Zhang, Y. Chen, Z. Sun, Electrosorptive desalination by carbon nanotubes and nanofibres electrodes and ion-exchange membranes, *Water Res.* 42 (2008) 4923–4928. doi:10.1016/j.watres.2008.09.026.
- [25] H. Li, L. Zou, L. Pan, Z. Sun, Novel graphene-like electrodes for capacitive deionization., *Environ. Sci. Technol.* 44 (2010) 8692–7. doi:10.1021/es101888j.
- [26] W. Shi, H. Li, X. Cao, Z.Y. Leong, J. Zhang, T. Chen, H. Zhang, H.Y. Yang, Ultrahigh Performance of Novel Capacitive Deionization Electrodes based on A Three-Dimensional Graphene Architecture with Nanopores, *Sci. Rep.* 6 (2016) 18966. doi:10.1038/srep18966.
- [27] C. Kim, P. Srimuk, J. Lee, S. Fleischmann, M. Aslan, V. Presser, Influence of pore structure and cell voltage of activated carbon cloth as a versatile electrode material for capacitive deionization, *Carbon N. Y.* 122 (2017) 329–335. doi:10.1016/j.carbon.2017.06.077.
- [28] G.X. Li, P.X. Hou, S.Y. Zhao, C. Liu, H.M. Cheng, A flexible cotton-derived carbon sponge for high-performance capacitive deionization, *Carbon N. Y.* 101 (2016) 1–8. doi:10.1016/j.carbon.2015.12.095.
- [29] M. Aslan, M. Zeiger, N. Jackel, I. Grobelsek, D. Weingarth, V. Presser, Improved capacitive deionization performance of mixed hydrophobic / hydrophilic activated carbon electrodes, *J. Phys. Condens. Matter.* 28 (2016) 114003. doi:10.1088/0953-8984/28/11/114003.



- [30] S. Porada, L. Weinstein, R. Dash, a van der Wal, M. Bryjak, Y. Gogotsi, P.M. Biesheuvel, Water desalination using capacitive deionization with microporous carbon electrodes., *ACS Appl. Mater. Interfaces*. 4 (2012) 1194–9. doi:10.1021/am201683j.
- [31] G. Rasines, P. Lavela, C. Macías, M. Haro, C.O. Ania, J.L. Tirado, Electrochemical response of carbon aerogel electrodes in saline water, *J. Electroanal. Chem.* 671 (2012) 92–98. doi:10.1016/j.jelechem.2012.02.025.
- [32] A. Omosebi, X. Gao, J. Landon, K. Liu, Asymmetric electrode configuration for enhanced membrane capacitive deionization, *ACS Appl. Mater. Interfaces*. 6 (2014) 12640–12649. doi:10.1021/am5026209.
- [33] J. Lee, S. Kim, C. Kim, J. Yoon, Hybrid capacitive deionization to enhance the desalination performance of capacitive techniques, *Energy Environ. Sci.* 7 (2014) 3683–3689. doi:10.1039/c4ee02378a.
- [34] L. Guo, R. Mo, W. Shi, Y. Huang, Z.Y. Leong, M. Ding, F. Chen, H.Y. Yang, A Prussian blue anode for high performance electrochemical deionization promoted by the faradaic mechanism, *Nanoscale*. 9 (2017) 13305–13312. doi:10.1039/c7nr03579a.
- [35] R. Zhao, P.M. Biesheuvel, a. van der Wal, Energy consumption and constant current operation in membrane capacitive deionization, *Energy Environ. Sci.* 5 (2012) 9520. doi:10.1039/c2ee21737f.
- [36] X. Cai, M. Peng, X. Yu, Y. Fu, D. Zou, Flexible planar/fiber-architected supercapacitors for wearable energy storage, *J. Mater. Chem. C*. 2 (2014) 1184–1200. doi:10.1039/c3tc31706d.
- [37] J.J. Lado, R.L. Zornitta, F.A. Calvi, M.I. Tejedor-Tejedor, M.A. Anderson, L.A.M. Ruotolo, Study of sugar cane bagasse fly ash as electrode material for capacitive deionization, *J. Anal. Appl. Pyrolysis*. 120 (2016) 389–398. doi:10.1016/j.jaap.2016.06.009.
- [38] T. Wu, G. Wang, Q. Dong, F. Zhan, X. Zhang, S. Li, H. Qiao, J. Qiu, Starch Derived Porous Carbon Nanosheets for High-Performance Photovoltaic Capacitive Deionization, *Environ. Sci. Technol.* 51 (2017) 9244–9251. doi:10.1021/acs.est.7b01629.
- [39] L. Zhang, Y. Liu, T. Lu, L. Pan, Cocoon derived nitrogen enriched activated carbon fiber networks for capacitive deionization, *J. Electroanal. Chem.* 804 (2017) 179–184. doi:10.1016/j.jelechem.2017.09.062.
- [40] A.M. Dehkoda, N. Ellis, E. Gyenge, Effect of activated biochar porous structure on the capacitive deionization of NaCl and ZnCl<sub>2</sub> solutions, *Microporous Mesoporous Mater.* 224 (2016) 217–228. doi:10.1016/j.micromeso.2015.11.041.
- [41] S. Porada, F. Schipper, M. Aslan, M. Antonietti, V. Presser, T.P. Fellingner, Capacitive Deionization using Biomass-based Microporous Salt-Templated Heteroatom-Doped Carbons, *ChemSusChem*. 8 (2015) 1823. doi:10.1002/cssc.201500696.
- [42] T. Kim, J. Yoon, Relationship between capacitance of activated carbon composite electrodes

- measured at a low electrolyte concentration and their desalination performance in capacitive deionization, *J. Electroanal. Chem.* 704 (2013) 169–174. doi:10.1016/j.jelechem.2013.07.003.
- [43] B. Yu, Z. Chang, C. Wang, The key pre-pyrolysis in lignin-based activated carbon preparation for high performance supercapacitors, *Mater. Chem. Phys.* 181 (2016) 187–193. doi:10.1016/j.matchemphys.2016.06.048.
- [44] M. Norgren, H. Edlund, Lignin: Recent advances and emerging applications, *Curr. Opin. Colloid Interface Sci.* (2014). doi:10.1016/j.cocis.2014.08.004.
- [45] N. Gavrilov, I.A. Pasti, M. Vujkovic, J. Travas-Sejdic, G. Ciric-Marjanovic, S. V. Mentus, High-performance charge storage by N-containing nanostructured carbon derived from polyaniline, *Carbon N. Y.* 50 (2012) 3915–3927. doi:10.1016/j.carbon.2012.04.045.

## **CHAPTER 2**

### **CHARGE AND POTENTIAL BALANCING FOR OPTIMIZED CAPACITIVE DEIONIZATION USING LIGNIN-DERIVED, LOW-COST ACTIVATED CARBON ELECTRODES**

Lignin-derived carbon is introduced as a promising electrode material for water desalination by using capacitive deionization (CDI). Lignin is a low-cost precursor that is obtained from the cellulose and ethanol industries, and we used carbonization and subsequent KOH activation to obtain highly porous carbon. CDI cells with a pair of lignin-derived carbon electrodes presented an initially high salt adsorption capacity but rapidly lost their beneficial desalination performance. To capitalize on the high porosity of lignin-derived carbon and to stabilize the CDI performance, we then used asymmetric electrode configurations. By using electrodes of the same material but with different thicknesses, the desalination performance was stabilized through reduction of the potential at the positive electrode. To enhance the desalination capacity further, we used cell configurations with different materials for the positive and negative electrodes. The best performance was achieved by a cell with lignin-derived carbon as a negative electrode and commercial activated carbon as a positive electrode. Thereby, a maximum desalination capacity of 18.5 mg/g was obtained with charge efficiency over 80% and excellent performance retention over 100 cycles. The improvements were related to the difference in the potential of zero charge between the electrodes. Our work shows that an asymmetric cell configuration is a powerful tool to adapt otherwise inappropriate CDI electrode materials.

#### **2.1. Introduction**

Capacitive deionization (CDI) is a promising technology for the treatment of brackish water (<10 g/L). The CDI process is based on the concept of the electric double layer (EDL) developed by applying a cell voltage (typically 1.0–1.2 V) to polarize a pair of parallel electrodes.[1] If a solution containing ions flows along the electrodes, cations and anions are attracted to and immobilized by the charged electrodes; as a consequence, the ion concentration of the out-flowing water stream decreases.[2] CDI consumes less energy than other technologies, and it offers the possibility of recovering parts of the invested energy for

electrosorption through electrode regeneration.[3, 4] To achieve high-performance desalination, the CDI electrode material should present a large pore volume accessible for ion electrosorption, high electrical conductivity, hydrophilicity, and chemical stability.[5] Usually, CDI electrodes are carbon-based materials, which have been explored in the forms of carbon nanotubes,[6, 7] mesoporous carbon,[8–10] and microporous carbons such as carbon felts,[11] carbide-derived carbon,[12] and carbon beads.[13] Some of these materials are expensive, and their synthesis may involve environmentally unfriendly procedures; for instance, the synthesis of carbide-derived carbons requires the use of halogens.[14]

The search for new low-cost precursors for the synthesis of electrode materials and carbon activation by simple methods is important to reduce the costs of CDI systems. Various low-cost precursors for CDI electrodes have been explored, including cotton-derived carbon sponge,[15] sugar cane bagasse fly ash,[16] polyaniline-derived activated carbon,[17] phenolic-resin derived activated carbon cloth,[18] and commercially available activated carbons.[19] Despite the improved salt adsorption capacity (SAC) and charge efficiency of these materials, few authors have investigated the long-term performance stability. A highly attractive candidate for a new low-cost precursor is lignin, which is obtained from natural sources and extracted during the manufacturing of cellulose by the Kraft process.[20] With the rise of biofuels, lignin has become available on an industrial level in large production because it is a byproduct of second-generation ethanol from the sugarcane bagasse.[21] Activated carbons derived from lignin have already been demonstrated to be attractive electrodes for supercapacitors,[22, 23] and hard carbon derived from lignin has been shown as an effective anode for lithium-ion batteries.[24] For the best of our knowledge, lignin-derived activated carbons have not been explored as an electrode material for CDI applications.

Two key performance metrics for the performance of CDI electrode materials are the desalination capacity and the corresponding charge efficiency.[25] Both parameters benefit from counterion electrosorption but not from co-ion electrodesorption. Therefore, the desalination process is strongly affected by the chemical charge of the surface functionalities at the interface between the carbon electrode and electrolyte. Whereas a positive chemical charge of the surface groups may enhance the desalination performance of the positive electrode, it lowers the performance if the material is used as the negative electrode.[26, 27] During long-term CDI operation, faradaic processes such as electrooxidation may further modify the electrode chemical charge; therefore, such processes must be considered upon evaluating the performance stability.[28] The presence of chemical charges may shift the potential of zero

charge ( $E_{PZC}$ ) of the electrode, causing co-ion expulsion and, consequently, reduce the ion removal capacity of the electrodes.[29] Different approaches have been employed to adjust the chemical charge, including electrochemical and chemical treatment of the electrode material[30] and the addition of conducting polymers with tailored surface charges.[31]

In this work, we introduce lignin-derived activation carbon as an attractive electrode material for CDI and demonstrate the importance of an asymmetric electrode configuration to optimize the performance and the long-term operation stability. The first approach for the asymmetric configuration varies the electrode thickness to reduce the potential of the positive electrode. Thereby, we discuss the potential distribution of the individual electrodes, the shift in the potential of zero charge, and the resulting performance stability. The second approach adopts carbon electrode materials with different  $E_{PZC}$  values to minimize co-ion expulsion and electrode oxidation on the positive electrode. We show enhanced desalination performance by controlling the potential distribution between the CDI electrodes composed of commercial activated carbon and our lignin-derived activated carbon.

## 2.2. Experimental description

### 2.2.1. Materials

Lignin was obtained from a pilot plant of the delignification process of sugar cane bagasse used for second-generation ethanol production at the Brazilian Bioethanol Science and Technology Laboratory (CTBE), located in Campinas, Brazil. The commercial activated carbon MSP-20 was purchased from the Kansai Coke and Chemical sand is denoted “AC”.

### 2.2.2. Lignin activation

Lignin was activated following a procedure adapted from Yu *et al.*[22] First, around 10 g of lignin was carbonized at 10 °C/min to 600 °C and kept at this temperature for 2 h in a vertical tubular furnace (Thermal Technology) under an argon atmosphere. The carbonized material is denoted “LC”. The material was then mixed with KOH pellets (Sigma–Aldrich) in a proportion of 1:3 (LC/KOH), mixed with a small amount of distilled water, and dried in an oven at 105 °C overnight. The dried material was then activated at 800 °C for 2 h at a heating rate of 10 °C/min. The resulting activated carbon material was neutralized with 0.5 M HCl (Sigma–Aldrich), washed with distilled water until neutral pH, and dried at 80 °C for 24 h. The activated carbon from lignin is denoted “LK”.

### 2.2.3. Electrode preparation

The electrodes of activated carbon were prepared by mixing 95 mass% activated carbon and 5 mass% polytetrafluoroethylene as a binder (PTFE, 60 mass% solution in water from Sigma–Aldrich). First, the activated carbon was mixed with ethanol (Sigma–Aldrich) until a homogeneous slurry was obtained. After adding PTFE, the mixture was kneaded until it became paste like and was then rolled out by a rolling machine (MTI HR01, MTI Corp.) to obtain free standing carbon electrode films with a thickness of  $(200\pm 20)$   $\mu\text{m}$ . The electrode films were dried in an oven filled with air at 2.0 kPa and 120 °C for 24 h. The CDI electrodes were prepared by punching carbon film discs with a diameter of 2.54 cm with corresponding masses of  $(54\pm 2)$  mg and  $(65\pm 3)$  mg for LK and AC, respectively. The electrodes for general electrochemical characterization had a diameter of 1.2 cm with corresponding masses of  $(12.2\pm 0.3)$  mg and  $(14.5\pm 0.4)$  mg for LK and AC, respectively.

### 2.2.4. Materials characterizations

The morphology of the carbon materials LC, LK, and AC was characterized by scanning electron microscopy (SEM) by using a JEOL JSM 7500F microscope operating at 3 kV. Nitrogen gas sorption at -196 °C was performed by using a Quantachrome iQ system to obtain the specific surface area (SSA) and pore size distribution (PSD). Prior to the measurements, the samples were dried at 250 °C for 10 h under vacuum conditions. The DFT SSA and PSD were calculated by using the ASiQwin software with quenched-solid density functional theory (QSDFT) assuming slit-shaped carbon pores.[63] The BET SSA was calculated by using the Brunauer–Emmett–Teller equation (BET) in the linear region of the isotherm (i.e., the relative pressure range of 0.05 to 0.30). The total pore volume ( $V_{total}$ ) was obtained from the cumulative pore size distribution, and the average pore size ( $d_{50}$ ) corresponds to the pore size in which the volume adsorbed is half of  $V_{total}$ .

Elemental analysis (CHNS) was performed with a Vario Micro Cube system from Elementar Analysensysteme. The reduction temperature was 850 °C, and the device was calibrated with sulfanilamide. Quantitative analysis of elemental oxygen was performed by using a rapid OXY cube oxygen analyzer at 1450 °C (Elementar Analysensysteme GmbH). Raman spectra were recorded with a Renishaw inVia microscope by using an Nd-YAG laser (wavelength: 532 nm; grating: 2400 lines/mm; spectral resolution: 1.2 /cm; numeric aperture: 0.75; power on the sample: 0.2 mW). The surface groups of the activated carbon samples were

also investigated by using thermogravimetric analysis in a mass spectrometer (STA449F3 Jupiter and QMS 403C Aëolos from Netzsch) under an inert atmosphere (argon; purity: 5.0).

### 2.2.5. Electrochemical characterization

Cyclic voltammetry (CV) and galvanostatic charge/discharge cycling with potential limitation (GCPL) were performed in an aqueous 1 M NaCl solution in a three-electrode cell with carbon as the counter electrode and the working electrode. The mass of the counter electrode was three times larger than that of the working electrode. Ag/AgCl was used as a reference electrode in all experiments. For all electrochemical measurements, we used a VSP300 potentiostat from Bio-Logic. Cyclic voltammograms were recorded at scan rates ( $v$ ) of 5 to 500 mV/s within a potential window of 0 to 0.6 V (vs. Ag/AgCl). The specific capacitance ( $C_S$  [F/g]) and the average capacitance ( $C_{CV}$  [F/g]) of the electrodes were calculated by using Equations (2.1) and (2.2):

$$C_S = \frac{I}{vm} \quad (2.1)$$

$$C_{CV} = \frac{\int_{V_1}^{V_2} I dV}{vm(V_2 - V_1)} \quad (2.2)$$

in which  $I$  is the current,  $V$  is the voltage,  $m$  is the mass of the active material in the working electrode, and  $V_1$  and  $V_2$  are the upper and lower values in the potential window. The GCPL measurements were performed with a specific current ranging from 0.1 to 10 A/g. The specific capacitance obtained by GCPL was calculated by using Equation (2.3):

$$C_{CD} = \frac{I_d \Delta t}{m \Delta U} \quad (2.3)$$

in which  $I_d$  is the discharge current,  $\Delta t$  is the discharge time, and  $\Delta U$  is the potential difference after discharge, subtracting the ohmic drop ( $IR_{drop}$ ). The lower and upper potentials limits were 0 and 0.6 V (vs. Ag/AgCl), respectively. The potential of zero charge ( $E_{PZC}$ ) was determined from electrochemical impedance spectroscopy (EIS) in potentiostatic mode by using 10 mm NaCl, a low frequency (10 mHz), and a 30 mV amplitude. A step potential of 50 mV was applied starting from -0.3 to +0.5 V. The capacitance ( $C_{EIS}$ ) was calculated by using Equation (2.4), in which  $\omega$  is the angular frequency and  $Z''$  is the imaginary component of the EIS spectrum. The values were normalized by the lowest measured capacitance.

$$C_{EIS} = \frac{1}{|\omega Z^n|} \quad (2.4)$$

Electrode stability was evaluated through S-value analysis.[47] We used data from the CV scans recorded at 1 mV/s in 1 M NaCl by varying the vertex potential in 50 mV increments. Scans towards positive potentials started at -0.1 V, finished at the vertex potential of +1.2 V. Scans towards negative potentials started at + 0.1 V, and finished at the vertex potential of - 1.8 V. The S-value was calculated for the positive and negative window by using Equations (2.5) and (2.6), in which  $Q_{pos}$  and  $Q_{neg}$  are the positive and negative charges provided to the electrodes. The second derivative ( $d^2S/dV^2$ ) was used as an indicator of electrode stability, by which the electrode was considered stable if  $d^2S/dV^2 < 5\%$ .

$$S_{pos} = \frac{Q_{pos}}{Q_{neg}} - 1 \quad (2.5)$$

$$S_{neg} = \frac{Q_{neg}}{Q_{pos}} - 1 \quad (2.6)$$

### 2.2.6. Desalination experiments

The CDI experiments were performed in a quasi single-pass process, the setup of which was previously described elsewhere.[19, 48] In short, the desalination unit was composed of two acrylic plates to which graphite current collectors were attached. The electrodes were placed on graphite current collectors and separated by a porous filter paper. The cell was tightly sealed by rubber gaskets. An Ag/AgCl reference electrode was placed close to the working electrode. During the desalination process, a peristaltic pump (Masterflex L/S Cole-Parmer) maintained the constant flow of a deaerated aqueous solution (10 mM NaCl) at 10 mL/min. A VSP300 potentiostat (Bio-Logic) provided a constant cell voltage (1.0, 1.1, or 1.2 V) during the electrosorption process and a set value of 0 V during the desorption. A conductivity probe (Metrohm) and a pH probe (WTW Multi 3510 IDS) continuously monitored the outlet stream of the CDI cell. The conductivity value was corrected by using the pH data [Eq. (2.7)] and the temperature and was then converted into salt concentration [mM] by using Equation (2.8) obtained prior to the experiment. Each experiment was performed until electrode saturation was reached.

$$\sigma_n = \sigma_m - \frac{e^2}{k_B T} \left( 10^{pH} \cdot N_A \cdot D_{H_3O^+} + \frac{10^{-14}}{10^{-pH}} \cdot N_A \cdot D_{OH^-} \right) \quad (2.7)$$



$$c_n = \left( \frac{\sigma_n - 4.5}{121.29} \right)^{\frac{1}{0.9826}} - 0.13 \quad (2.8)$$

in which  $\sigma_n$  is the corrected conductivity [mS/cm],  $\sigma_m$  is the measured conductivity,  $k_B$  is the Boltzmann constant ( $1.38 \cdot 10^{-23}$  m<sup>2</sup>/kg.s<sup>2</sup>.K),  $N_A$  is the Avogadro constant ( $6.022 \cdot 10^{23}$  mol<sup>-1</sup>),  $D_{H_3O^+}$  is the diffusion coefficient of a hydronium ion ( $9.3 \cdot 10^{-9}$  m<sup>2</sup>/s), and  $D_{OH^-}$  is the diffusion coefficient of a hydroxyl ion ( $5.3 \cdot 10^{-9}$  m<sup>2</sup>/s). The salt adsorption capacity (SAC), charge efficiency, rate of desalination, and energy consumption were calculated by using Equations (2.9), (2.10), (2.11), and (2.12).

$$SAC = \frac{VM_{NaCl} \int_{t_1}^{t_2} C(t) dt}{m_E} \quad (2.9)$$

$$\text{Charge efficiency (\%)} = 100 \cdot \frac{zFm_E SAC}{\int I_e dt} \quad (2.10)$$

$$\text{Rate} = \frac{\text{Capacity}}{t_{cap}} \quad (2.11)$$

$$E_{kT} = \frac{M_{NaCl} E_{cell} \int I_e dt}{m_{rem} RT} \quad (2.12)$$

in which  $V$  is the flow rate of the electrolytic solution,  $M_{NaCl}$  is the molecular mass of NaCl (58.4 g/mol),  $C$  is the variation in the salt concentration with time,  $t_1$  and  $t_2$  are the electrosorption time intervals,  $m_E$  is the mass of active material in the electrodes,  $z$  is the ion charge, and  $F$  is the Faraday constant (96485 C/mol). The current ( $I_e$ ) from Equation (2.10) is the total current measured during the electrosorption process, that is, in our experiments, the leakage current was not subtracted. This condition must be considered

## 2.3. Results

### 2.3.1. Material characterization

The morphologies of lignin, lignin-derived carbon (after carbonization; LC), and activated LC (labeled LK) are granular with particle sizes in the range of a few micrometers (Figure 2.1). Before carbonization, however, lignin has a rough surface and agglomerated particles (Figure 2.1a). After carbonization and activation, the surface of the particles is smoother with macropores similar to lignin-derived activated carbon reported in the literature (Figure 2.1b, c). [32] Commercially available activated carbon (AC) chosen for our study shows slightly larger primary particle sizes of approximately 10–15  $\mu\text{m}$  (Figure 2.1d).

Table 2.1 shows the elemental analysis and the yields after carbonization ( $Y_C$ ), after activation ( $Y_{AC}$ ), and the total yield ( $Y_T$ ). The contents of carbon and oxygen in lignin are relatively high (61 and 33 mass%, respectively), as lignin is an organic compound rich in oxygen-containing functional groups such as carbonyl, phenolic hydroxy, ether, and methoxy

groups.[33] After carbonization of lignin, we see a large mass loss (64 mass%) caused by the decomposition of the oxygen groups at high temperatures.[34,35] The carbon content of LC increases to 84 mass% and to approximately 90 mass% after activation (LK), whereas the hydrogen and oxygen contents decrease. The total yield of LK (~21 mass%) is comparable to that of other activated carbons derived from lignin by using different activation techniques and pore-structure development ( $Y_T=13\text{--}35$  mass%).[36]

**Figure 2.1.** Scanning electron micrographs of (A) lignin, (B) LC, (C) LK, and (D) commercial AC (MSP-20)

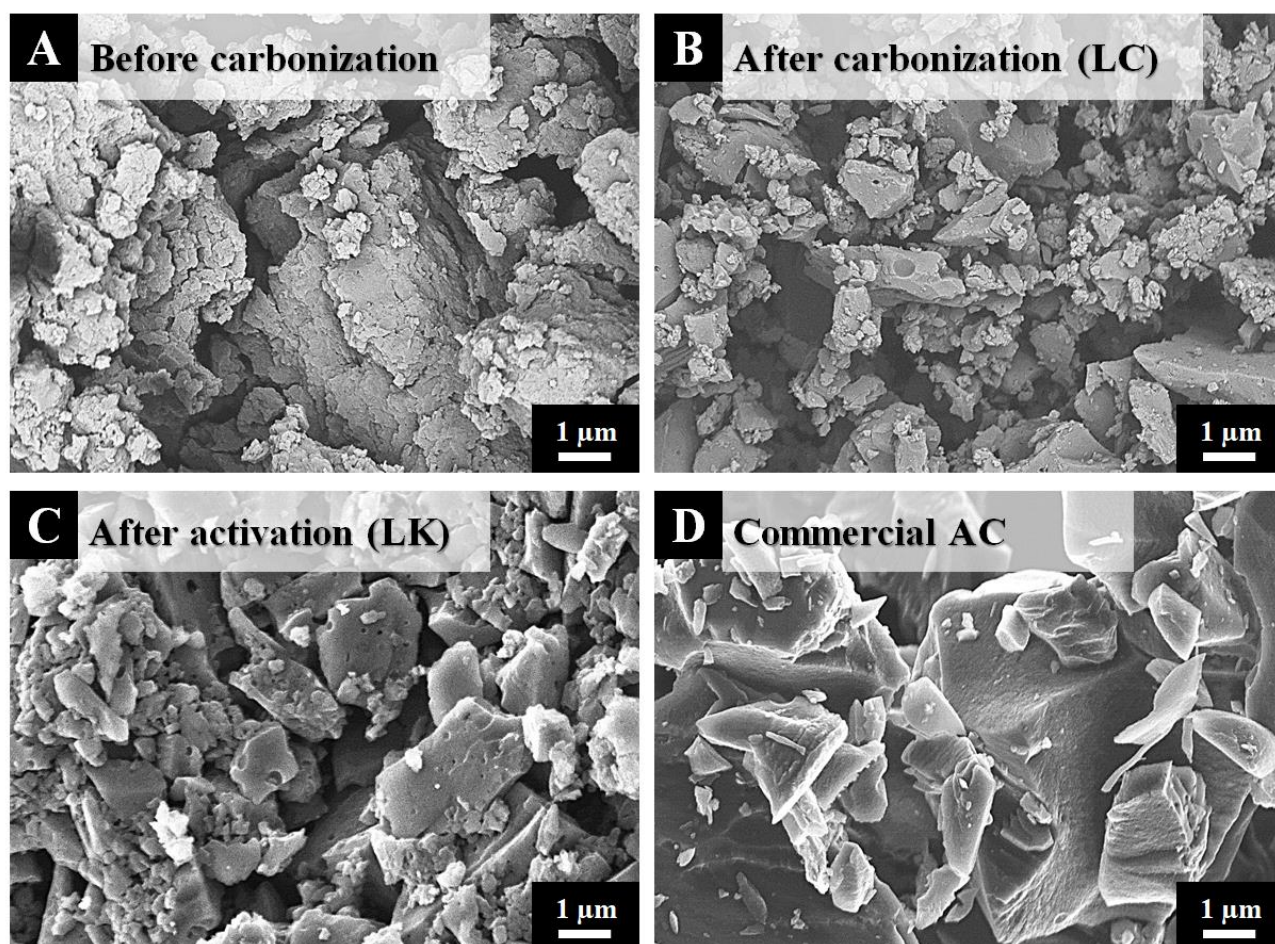


**Table 2.1.** Elemental analysis and yield of the carbon samples (all values in mass%)

	Lignin	LC	LK	AC
<b>Carbon</b>	61.0±0.3	86.1±0.1	88.2±2.2	95.8±0.6
<b>Nitrogen</b>	0.7±0.1	0.9±0.1	0.2±0.1	0.3±0.1
<b>Hydrogen</b>	5.9±0.1	3.0±0.1	1.1±0.1	0.5±0.1
<b>Oxygen</b>	32.5±1.3	10.0±0.3	10.5±0.1	3.4±0.1
<b>Yield (%)</b>		$Y_C = 36.5$	$Y_{AC} = 57.0$	
		$Y_T = 20.8$		

Thermogravimetric analysis coupled with mass spectrometry (TGA-MS) was performed under an inert gas atmosphere (argon) to evaluate the surface groups present in LK and AC. The results from TGA correlate well with those obtained by elemental analysis. After heating to 1000 °C, the mass losses are approximately 10 and 5 mass% for LK and AC, respectively (Figure 2.2a). At such a high temperature, the oxygen and hydrogen surface groups are released from the material.[34, 37] Analysis of LK by TGA-MS (Figure 2.2b) demonstrates that thermal degradation of the carboxylic groups occurs between 200 and 400 °C and that of the lactone groups occurs between 600 and 700 °C. Above 800 °C, the CO<sub>2</sub> signal ( $m/z=44$ ) is reduced owing to the reaction with carbon, the formation of carbonyl groups, and the release of CO ( $m/z=28$ ).[38, 38] The presence of oxygen groups on the surface of LK agrees with the high content of oxygen groups of lignin (Table 2.1). No variation in the O<sub>2</sub> signal ( $m/z=32$ ) is observed in the range of the analysis, which indicates that most of the decomposed oxygen reacts with carbon to form CO<sub>2</sub>. Analysis of AC by TGA-MS shows the release of CO<sub>2</sub>, which can also be ascribed to thermal degradation of carboxylic groups ( $m/z=44$ ; see Figure A2.1 in the Appendix).

The carbon structures of LK and commercially available AC were further characterized by using Raman spectroscopy (Figure 2.2c). For LK and AC, the D and G modes are located at Raman shifts of 1350 and 1593 cm<sup>-1</sup>, respectively. The D-mode indicates the presence of disordered carbon, whereas the G-mode is related to sp<sup>2</sup>-hybridized carbon atoms. The degree of carbon ordering can be estimated by the relative intensity of the D and G bands ( $I_D/I_G$ ).[22] The  $I_D/I_G$  values for LK and AC are almost identical (~0.90), which indicates that both materials have a similar degree of ordering of the incompletely graphitic carbon structure.[40, 41]

Nitrogen gas sorption analysis was performed to obtain the DFT specific surface areas (SSAs) and pore size distributions (PSDs) of LC, LK, and AC (Table 2.2). The type I isotherms for both carbons (Figure A2.2) are characteristic of microporous materials.[42] The cumulative PSD reveals that most pores are micropores (<2 nm) with a small contribution of mesopores.[43] The successful KOH activation of LC is demonstrated by the large increase in the pore volume from 0.13 g/cm<sup>3</sup> for LC to 1.04 g/cm<sup>3</sup> for LK and the large increase in the DFT SSA from 256 m<sup>2</sup>/g for LC to 1937 m<sup>2</sup>/g for LK.

**Figure 2.2** (A) Thermogravimetry of LK and AC in an argon atmosphere. (B) Coupled TGA-MS plotting the ionic current vs. temperature for  $m/z$ : 28, 32, and 44 of LK. (C) Raman spectra of LK and AC. (D) Cumulative pore size distribution of LC, LK, and AC obtained from nitrogen gas sorption at  $-196\text{ }^{\circ}\text{C}$ . The corresponding isotherms can be found in the Appendix

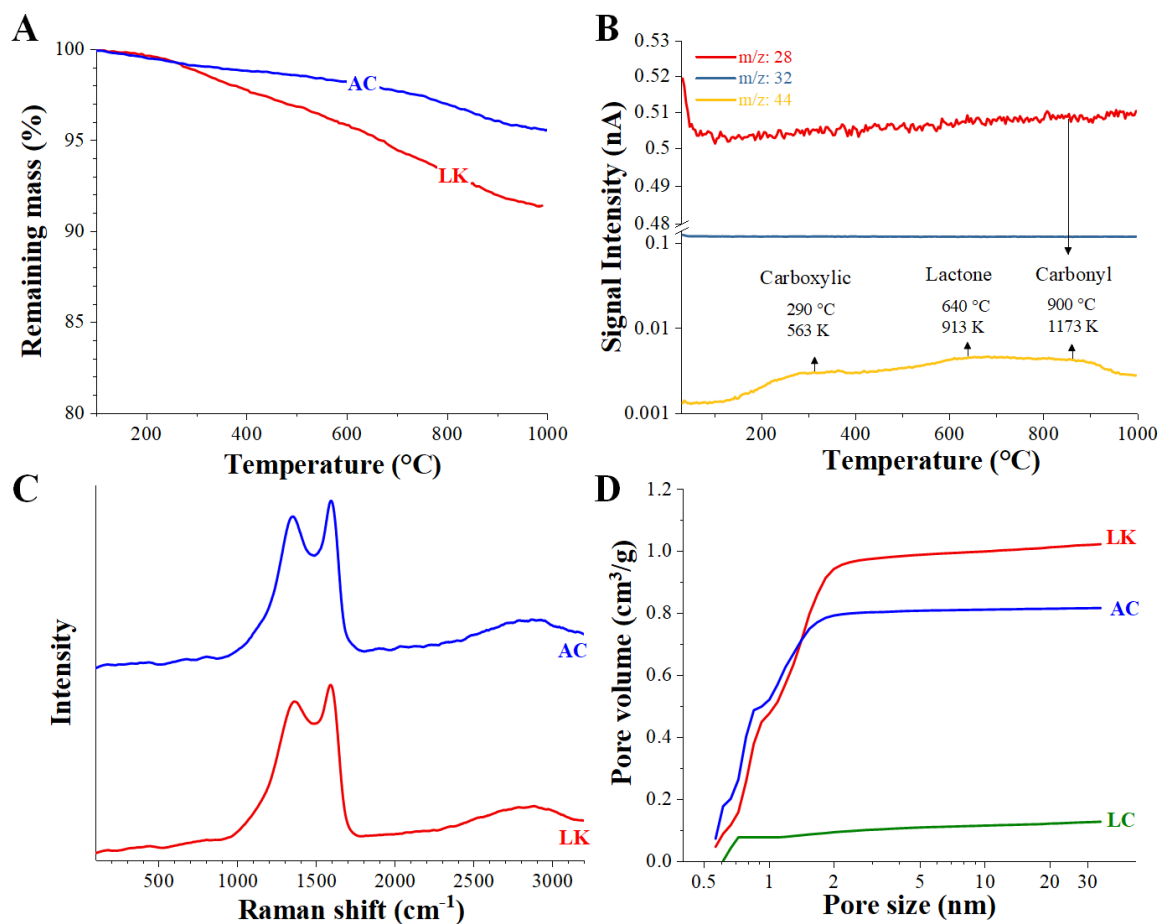
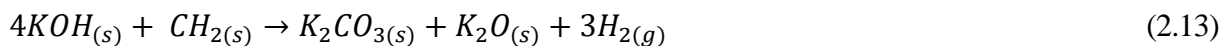


**Table 2.2.** SSA, total pore volume ( $V_{\text{total}}$ ), micropore volume ( $V_{\text{mic}}$ ), and average pore diameter ( $d_{50}$ ) of LC, LK, and AC obtained by nitrogen gas sorption at  $-196\text{ }^{\circ}\text{C}$

	DFT-SSA ( $\text{m}^2/\text{g}$ )	BET-SSA ( $\text{m}^2/\text{g}$ )	$V_{\text{total}}$ ( $\text{cm}^3/\text{g}$ )	$V_{\text{mic}}$ ( $\text{cm}^3/\text{g}$ )	$d_{50}$ (nm)
LC	256	249	0.13	0.09	0.85
LK	1937	1860	1.04	0.94	1.09
AC	1883	1838	0.82	0.79	0.80

Chemical activation of carbon by KOH to enhance the electrochemical performance is well known because of the high surface area and pore volume.[44] The reaction between the precursor and KOH is ascribed to the reaction of hydrogen carbonate present in LC with KOH to produce  $\text{K}_2\text{O}$  and  $\text{H}_2$ . Consequently, there is a decrease in the hydrogen content rather than

a decrease in the oxygen content, as observed from LC to LK (Table 2.1). Other reactions, such as the reactions of  $K_2CO_3$  and  $K_2O$  with carbon, may also occur and contribute to the enhancement in the porosity per Equations (2.13), (2.14), and (2.15).[45]



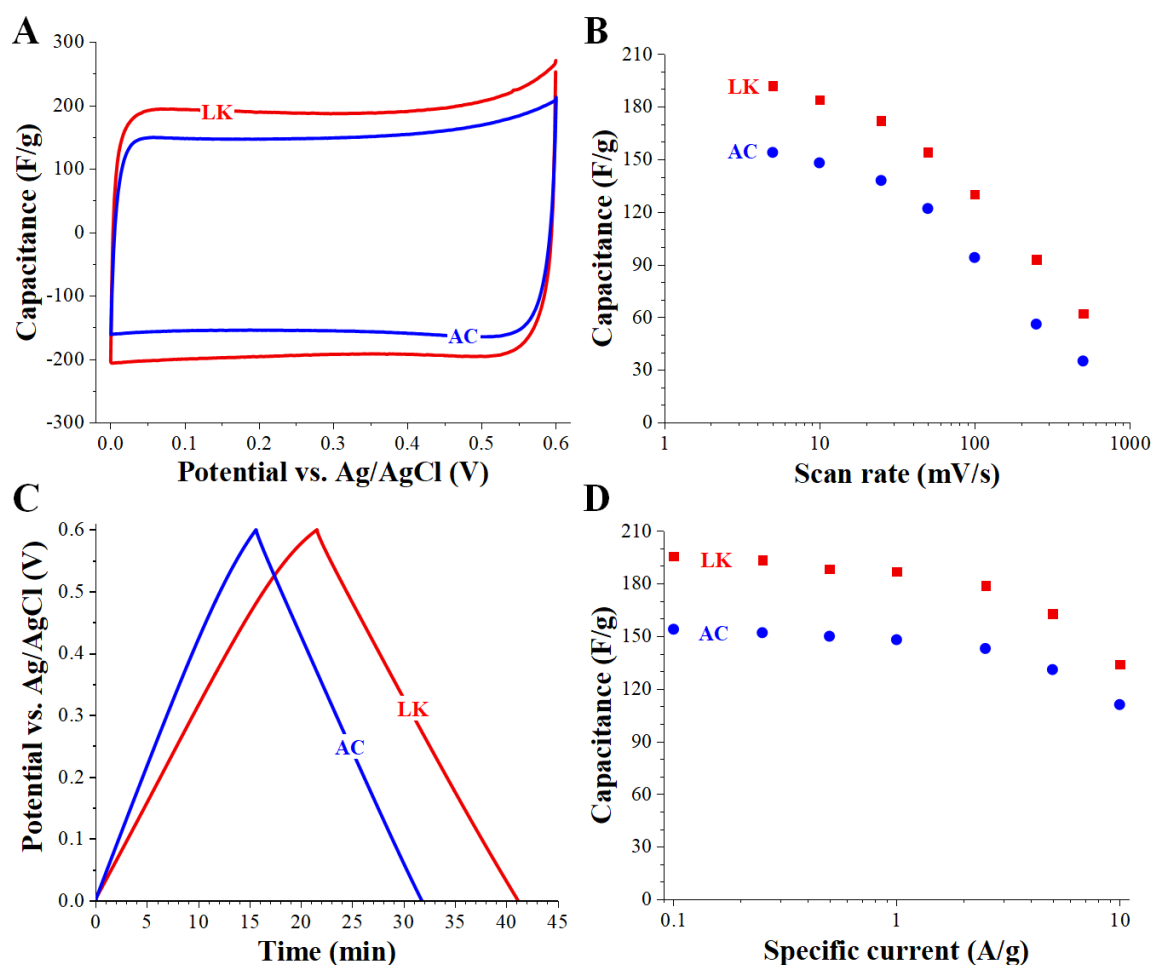
### 2.3.2. Basic electrochemical characterizations in aqueous 1 M NaCl

Electrochemical characterization [cyclic voltammetry (CV) and galvanostatic charge/discharge cycling with potential limitation (GCPL)] of LK and AC was performed in 1 M NaCl. This high salt concentration was chosen to avoid issues associated with ion depletion during the measurements.[19] The cyclic voltammograms (Figure 2.3a) show that both materials present quasi rectangular CV shapes, which are indicative of capacitive materials. Upon increasing the scan rate from 5 to 100 mV/s (Figure 2.3b), the capacitance of LK decreases from 192 to 130 F/g (~32%) and that of AC decreases from 154 to 94 F/g (~39 %). The fact that the capacitance of LK is higher than that of AC aligns well with the increased pore volume and surface area of the former (Table 2.2). The triangular GCPL profiles confirm near ideal behavior of an electrical double-layer capacitor (Figure 2.3c). In agreement with the CV data, from the GCPL data we obtained specific capacitances of 196 F/g for LK and 154 F/g for AC at 0.1 A/g with a coulombic efficiency of almost 100% for both electrodes. At a specific current of 10 A/g, although there is a significant increase in the ohmic drop (Figure A2.3), AC and LK retain 72% (111 F/g) and 68% (134 F/g) of their initial capacitance values, respectively (Figure 2.3d). The capacitance values of LK are promising if compared with other activated carbons from the literature.[46]

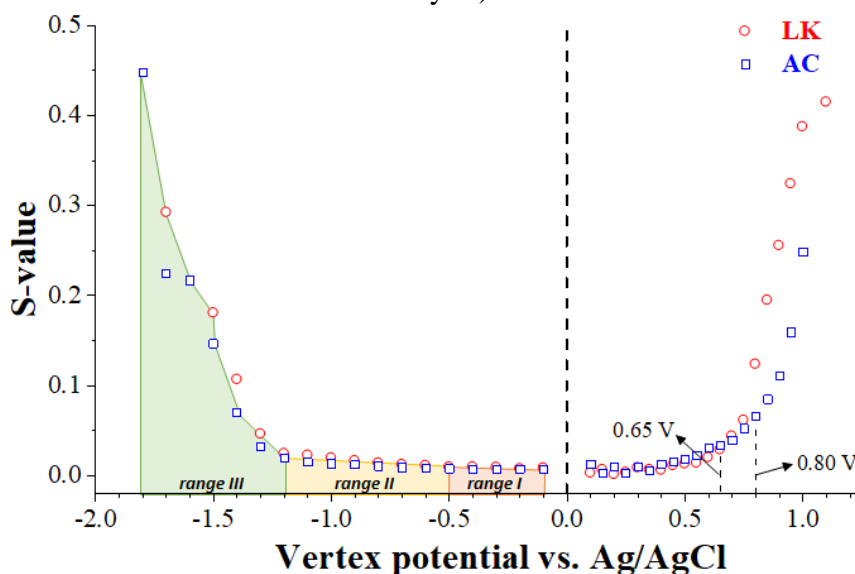
We then determined the electrochemical stability (S-value) window of the carbons (Figure 2.4). The basis for analyzing the S values was the CV data recorded at 1 mV/s at different potential limits.[47] Commonly, CDI experiments employ a fixed maximum cell voltage of 1.2 V; yet, each carbon may have a different onset for the electrochemical decomposition in the anodic and cathodic regimes. In the cathodic regime, both LK and AC present almost the same stability. Using the stability criterion of  $d^2S/dV^2$  (V=electrical potential) of Weingarth *et al.*,[47] the S-value varies only slightly, and the value of  $d^2S/dV^2$  remains below 5% at negative potentials from 0 to -0.5 V versus Ag/AgCl (region I, Figure 2.4).

At more negative values of -0.5 to -1.2 V (vs. Ag/AgCl), we observe a small linear increase in the S-value, which corresponds to reversible hydrogen formation and possible energy storage (region II, Figure 2.4).[48] The reversibility is finally lost below -1.2 V (vs. Ag/AgCl), and the  $d^2S/dV^2$  values exceed 5% (region III, Figure 2.4).[49] During positive polarization, the second derivative of the S-value exceeds the critical value of 5% at +0.65 and +0.80 V (vs. Ag/AgCl) for LK and AC, respectively. The increased irreversible faradaic charge loss aligns with oxidation reactions of the carbon electrodes and reactions of surface functional groups.[50–52] The slightly lower potential limit of LK aligns with the fact that its oxygen content is larger than that of AC (Table 2.1), in agreement with our previous work with heteroatom carbons.[53]

**Figure 2.3.** Electrochemical characterization of LK and AC in aqueous 1 M NaCl. (A) Cyclic voltammograms at 5 mV/s and (B) corresponding capacitance values at 5-500 mV/s. (C) Galvanostatic charge/discharge profiles and (D) corresponding capacitance values at specific currents of 0.1-10 A/g





**Figure 2.4.** Electrochemical stability limits for LK and AC in aqueous 1 M NaCl (S-value analysis)

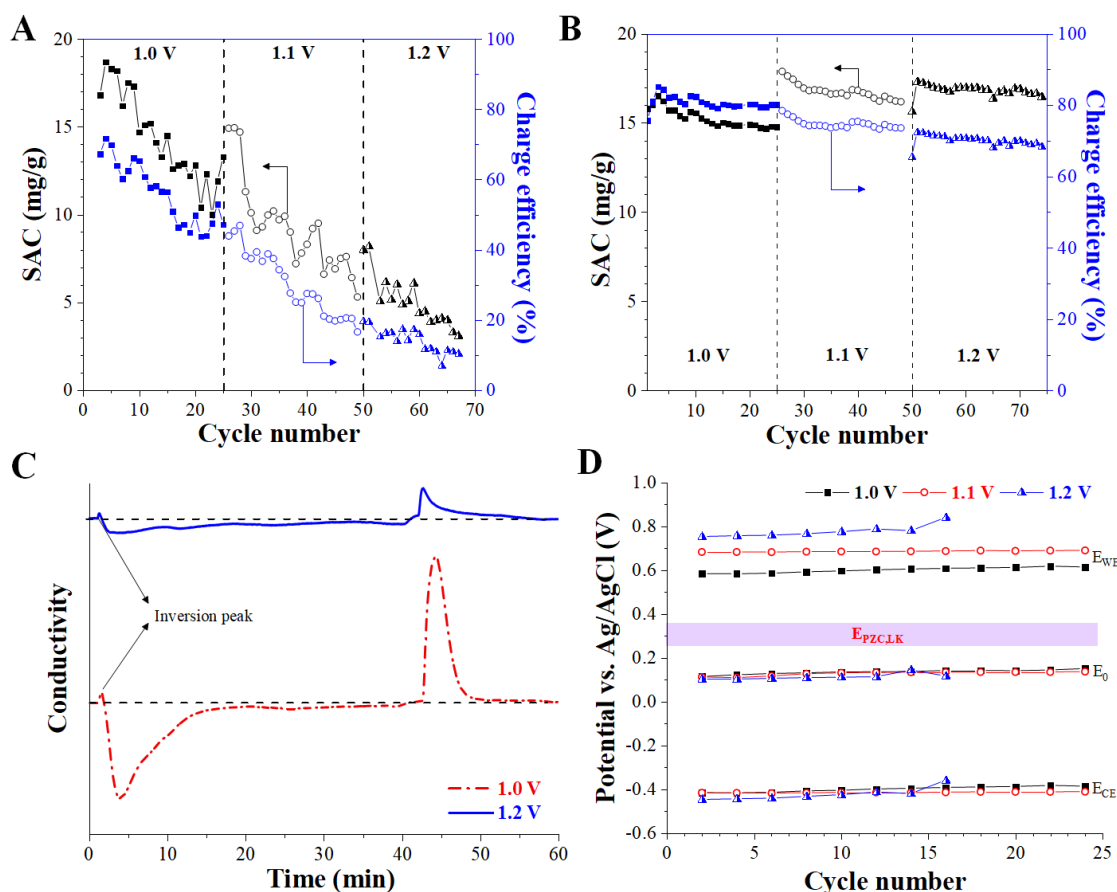
### 2.3.3. Desalination performance in aqueous 10 mM NaCl: Symmetric electrode configuration

We characterized the desalination performance and stability by using deaerated aqueous 10 mM NaCl through electrosorption/desorption experiments at cell voltages of 1.0, 1.1, and 1.2 V at ambient temperature. The first experiments were performed by using a symmetric electrode configuration, for which positive and negative electrodes with the same mass, size, and material were used. Figure 2.5a shows that regardless of the applied cell voltage, the salt adsorption capacity (SAC) and charge efficiency of the LK electrode decrease with the number of cycles. In contrast, AC electrodes provide stable desalination performance (Figure 2.5b). Figure 2.5c shows the conductivity profile of the 10th cycle for the LK electrode at cell voltages of 1.0 and 1.2 V. The presence of an inversion peak indicates that co-ions are repelled during electrode polarization. This effect relates to the positions of the  $E_{PZC}$ , which is strongly affected by the chemical charge of surface groups and the short-circuit potential ( $E_0$ ) at the positive and negative electrodes.[26, 27]

To understand better the difference in the performance and stability of LK and AC, in addition to the total cell voltage we must also consider the potential distribution of each electrode. Figure 2.5d plots each electrode potential and the short-circuit potential during electrode polarization for the LK electrode. We use the term “symmetrical electrodes” for cell configurations in which the electrodes have the same capacitance, area, mass, and  $E_{PZC}$ . This definition is important, as even electrodes of the same material with the same area and mass can present a different  $E_{PZC}$  value after electrochemical treatment. Upon applying a cell voltage of 1.0 V, the maximum working electrode potential ( $E_{WE}$ ) starts at approximately +0.59 V (vs.

Ag/AgCl) for the initial cycle and increases to +0.61 V (vs. Ag/AgCl) after 25 cycles. The same behavior is observed for the  $E_0$  potential (+0.11 to +0.15 V vs. Ag/AgCl). During constant voltage operation, the counter electrode potential ( $E_{CE}$ ) increases from -0.42 to -0.39 V (vs. Ag/AgCl) to balance the cell voltage of 1.0 V. After 25 cycles of operating the cell at 1.0 V, the cell voltage was increased to 1.1 V, and the potential over the working electrode is even higher starting at +0.68 V (vs. Ag/AgCl) and reaches +0.69 V (vs. Ag/AgCl) after 25 cycles. The maximum potentials of the positive electrode at each cycle are higher than the potential limits that we determined by analyzing the S-values.

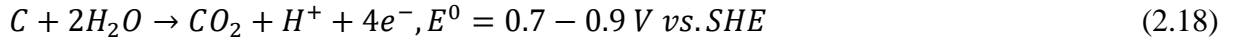
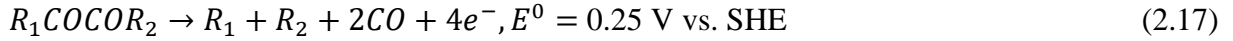
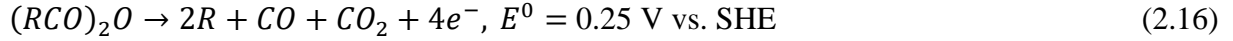
**Figure 2.5.** Salt adsorption capacity (SAC) and charge efficiency varying with cycles at different cell potentials for (A) LK and (B) commercial AC. (C) Conductivity profile for the 10<sup>th</sup> cycle at 1.0 V and 1.2 V and (D) electrode potential distribution for the sample LK. WE: working electrode; CE: counter electrode;  $E_0$ : short-circuit potential



High electrode potentials are known to cause electrode and performance degradation, water splitting, and carbon oxidation.[10, 50] There are several possible oxidation reactions of



carbon and surface groups ( $R_i$ ;  $i=1, 2$ ) that are relevant to the symmetrical LK configuration [Eqs. (2.16), (2.17), (2.18), (2.19), (2.20), (2.21),(2.22)]:[51, 54, 55]



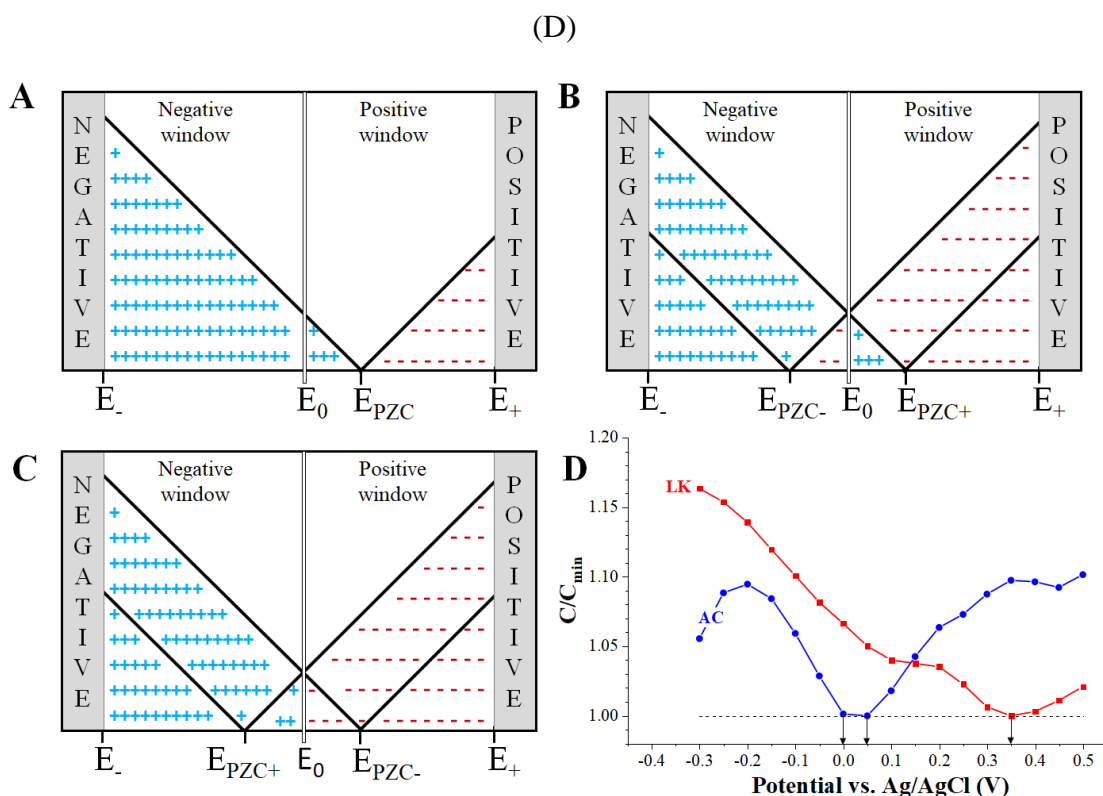
The oxidation reactions of the surface functional groups [Eqs. (2.16) and (2.17)] occur at low electrode potentials, which aligns with the low stability of LK at positive electrode potentials. Equations (2.18)–(2.22) show that oxidation of the carbon electrode is accompanied by pH changes during the desalination process, as observed for the symmetrical LK operation (Figure A2.5). A detailed analysis of the electrochemical reactions possibly occurring in CDI operation without membranes can be found in Refs. [50, 56].

Finally, upon applying a cell voltage of 1.2 V, the working electrode potential is already very high (0.75 V vs. Ag/AgCl) and exceeds 0.8 V (vs. Ag/AgCl) after only 16 cycles. After this point, we observe large pH fluctuations and the desalination capacity of the electrode decreases by more than 80%. Clearly, CDI operation with these cell parameters yields poor performance stability.

To illustrate further the differences between LK and AC, we show in Figure 2.6 the influence of  $E_{PZC}$  of the negative and positive electrodes in the context of co-ion expulsion (which does not contribute toward desalination) and counterion electrosorption.[57–59] Figure 2.6a depicts the case in which symmetrical electrodes have higher  $E_{PZC}$  values than  $E_0$  values (positive window). In this case, part of the charge at the positive electrode is used for electrosorption of the counter ions (anions), whereas some of the charge is also consumed for co-ion expulsion. For the negative electrode, most of the electrical charge contributes toward electrosorption of the cations (counter ions). In the scenario shown in Figure 2.6a, the value of  $E_{PZC}$  is higher than the value of  $E_0$  and the same behavior can be observed if the  $E_{PZC}$  value of the electrodes is lower than the  $E_0$  value (negative window). The only difference, in this case, is that the expulsion is caused at the negative electrode by anion expulsion. In Figure 2.6b, we

show the situation for asymmetrical electrodes with different values of  $E_{PZC}$ . The negative electrode has an  $E_{PZC}$  value within the negative window, and the positive electrode has an  $E_{PZC}$  value within the positive window. In this case, during electrode polarization, part of the charge at both electrodes will be consumed for co-ion expulsion. This asymmetrical configuration is the least desirable for the CDI process. In Figure 2.6c, the electrodes with different  $E_{PZC}$  values are placed more favorably: the electrode with an  $E_{PZC}$  value in the positive window is placed on the negative side, and the electrode with an  $E_{PZC}$  value in the negative window is placed on the positive side. In this case, most of the potential is beneficial for electrosorption of the counter ions during electrode polarization.

**Figure 2.6.** Scheme of the co-ion effect when  $E_{PZC}$  is on the negative potential window (A), the negative and positive electrodes present  $E_{PZC}$  on their potential window (B), and the negative and positive electrodes present the  $E_{PZC}$  out of the potential window (C).  $E_{PZC}$  values obtained from the lowest capacitance value using EIS measurement for LK and AC electrodes



To determine the  $E_{PZC}$  position for LK and AC, we performed electrochemical impedance spectroscopy (EIS) measurements at different electrode potentials. The corresponding capacitance was calculated from the EIS data by using Equation (2.4). Figure 2.6d shows the normalized capacitance values for LK and AC with a potential step of

50 mV. We used a low-frequency regime (10 mHz) to provide sufficient time for EDL formation. A low salt concentration of the solution (10 mM NaCl) was chosen, as the  $E_{PZC}$  value becomes more evident owing to the higher potential drop across the diffuse layer and because it corresponds with the target application of brackish water desalination.[26] As can be observed, the capacitance values are strongly influenced by the electrode potentials, forming a V-shaped curve in which the lowest capacitance value represents the  $E_{PZC}$ . The lowest capacitance value indicates that the entire surface charge of the electrode is compensated if the  $E_{PZC}$  potential is applied. We identified  $E_{PZC}$  values of +350 and +50 mV (vs. Ag/AgCl) for LK and AC, respectively.

The case depicted in Figure 2.6a aligns with the configuration of symmetrical electrodes of LK (Figure 2.5d) that show the presence of an inversion peak due to co-ion expulsion, whereas with AC the inversion peak is not observed. In the case of the AC material that we used, the  $E_{PZC}$  value is close to the  $E_0$  value, and negligible co-ion expulsion occurs (Figure A2.4). Co-ion expulsion commonly reduces the charge efficiency and the electrosorption capacity of the electrode. At the positively polarized LK electrode, oxidation reactions align with the measured performance deterioration. The higher potential stability of AC (Figure 2.4), however, effectively prevents an escalating performance decay within the cell voltage range up to 1.2 V. These data clearly show that the common use of a cell voltage of 1.2 V in the CDI community cannot be generalized for all carbons and all electrode configurations. The performance stability of symmetric and asymmetric CDI cell configurations remains an important research topic. It is important to investigate the long-term performance considering the electrochemical properties of electrodes after having reached a steady state.

#### **2.3.4. Desalination performance in aqueous 10 mM NaCl: Asymmetric electrode configuration**

CDI with a symmetric arrangement of the LK electrodes yielded poor desalination performance. To capitalize on the promising porosity and specific capacitance of the material, we investigated the performance upon using an asymmetric cell design. To do so, we first used the same material but with different electrode thicknesses. This strategy was previously investigated by Porada *et al.* regarding desalination capacity, efficiency, and kinetics but not considering performance stability.[60] The authors observed that the best CDI configuration for their carbon electrodes (PACMM 203) was a symmetric cell.[60] For our experiments labeled 1LK:2LK, we used two layers of the positive electrode, whereas on the negative

electrode, we only used one layer. The use of the higher thickness and consequently higher mass on the positive electrode provides a larger interface for ion electrosorption; therefore, the same amount of accumulated charge is afforded by a lower potential. The latter can be tailored in such a way that the maximum potential remains below the onset of electrode oxidation. Clearly, the electrochemical properties of the carbon (especially the  $E_{PZC}$  value) must be carefully considered for the cell design of a CDI system.[53]

Figure 2.7a shows the variation in the SAC along with the number of cycles for 1LK:2LK by using different cell voltages, and the performance values are provided in Table 2.3. The SACs at 1.0 and 1.1 V are practically constant throughout the cycles with values of 14–16 mg/g and corresponding charge efficiencies of 72–74 %. Compared to operation at a cell voltage of 1.1 V, the use of a cell voltage of 1.2 V yields more unstable and poorer performance with reduced charge efficiency (~62 %). Therefore, 1LK:2LK cells provide the most favorable desalination performance for a cell voltage of 1.1 V. Figure 2.7b shows the evolution of the potential distribution with the cycles during the electrosorption process. Compared to the symmetrical configuration (Figure 2.5d), we now observe a narrower potential window for the positive electrode, which explains the higher stability of the electrode during cycling.

**Figure 2.7.** Data for the 1LK:2LK electrode configuration in aqueous 10 mM NaCl. (A) Salt adsorption capacity and charge efficiency. (B) Electrode potential distribution for several CDI cycles

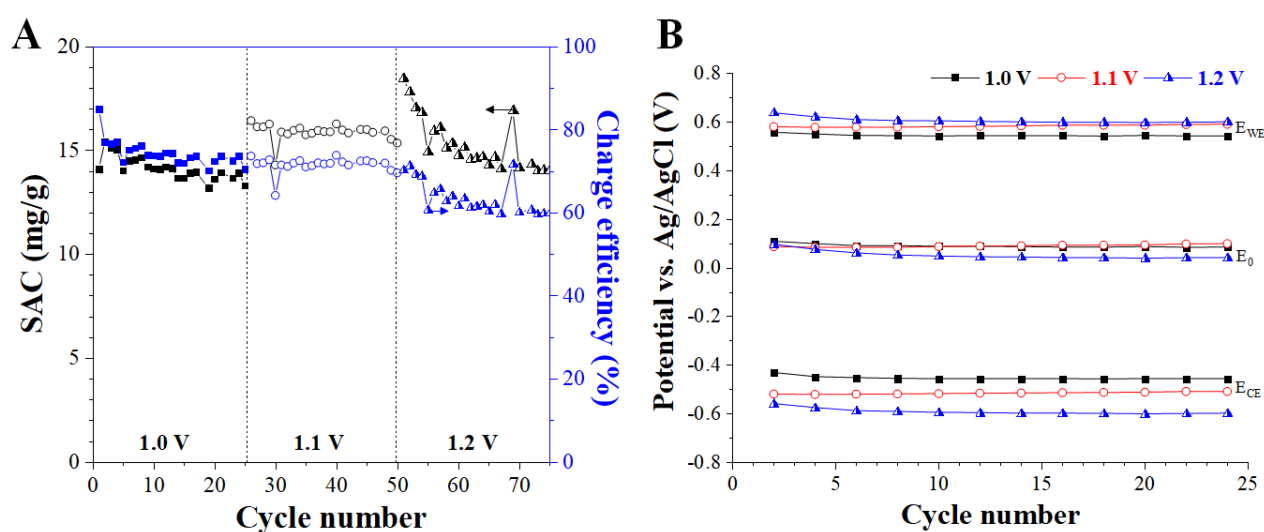


**Table 2.3.** Charge efficiency with and without leakage current, energy consumption, and salt adsorption capacity (SAC) for LK and AC electrodes with different configurations. For all data, the discharge half cycle was carried out at 0 V

Setup	Cell voltage (V)	Charge efficiency (%)		Energy consumption		SAC (mg/g)
		Without leakage current	With leakage current	(kT)	(kJ/g)	
LK:LK	1.0	53	47	60	2.5	13.3§
	1.1	27	17	184	7.8	5.3§
	1.2	19	10	295	12.5	3.1§
1LK:2LK	1.0	90±3	74±2	53±1	2.2±0.1	14.0±0.8 <sup>+</sup>
	1.1	85±2	72±1	60±1	2.6±0.2	16.0±0.2 <sup>+</sup>
	1.2	76±2	62±2	76±2	3.2±0.1	14.7±0.6 <sup>+</sup>
LK:AC	1.0	96±2	88±3	44±2	1.8±0.1	18.5±1.0 <sup>*</sup>
	1.1	86±3	76±4	56±3	2.4±0.1	16.7±1.2 <sup>*</sup>
	1.2	97±1	78±1	60±2	2.5±0.1	15.3±0.5 <sup>+</sup>
AC	1.0	92±3	80±2	48±1	2.0±0.1	15.3±0.5 <sup>+</sup>
	1.1	98±1	80±1	54±1	2.3±0.1	16.8±0.4 <sup>+</sup>
	1.2	-	75±1	62±1	2.6±0.1	16.8±0.3 <sup>+</sup>

§ Last value measured during the desalination process.

\* Average for 100 cycles.

<sup>+</sup> Average for 25 cycles.

Despite improved electrode stability and charge efficiency by using the 1LK:2LK configuration, the SAC was still below what the initial tests of the symmetric cell had indicated with initial SAC values up to 19 mg/g. Therefore, we explored a second type of asymmetric cell design: the use of different materials for the positive and negative electrodes. By combining LK and AC, our goal was to capitalize on different values of  $E_{PZC}$  without having to apply further chemical modifications to LK as previously explored, for example, by Omosebi *et al.*, [26] Gao *et al.*, [30] and Avraham *et al.*, [57] Owing to the position of  $E_{PZC}$ , the most favorable configuration in alignment to Figure 2.6 uses AC for the positive electrode and LK for the negative electrode. We investigated varying the desalination capacity (Figure 2.8a) and charge efficiency (Figure 2.8b) with the number of cycles by using LK:AC and AC:LK (negative and positive electrodes, respectively) at different cell voltages. For all cell voltages, LK:AC showed consistently high desalination capacities and charge efficiency values of 16.7–18.5 mg/g and 76–88%, respectively (Table 2.3). The stable performance with attractive desalination values of LK:AC aligns with the stable and beneficial potential distribution, as can be seen from Figure 2.8c. Yet, after 25 cycles, the charge efficiency for LK:AC at 1.2 V is the lowest among all three tested cell voltages with values below 80%. The performance of AC:LK at the same

cell voltages is much lower, with desalination capacities of approximately 6–12 mg/g and values for the charge efficiency of approximately 35–60 %. This reduction in capacity and charge efficiency is related to the unfavorable position of  $E_{PZC+}$  and  $E_{PZC-}$  in this configuration, which negatively impacts the effect of co-ion expulsion and reduces the ability of the system to adsorb counter ions effectively.

Having identified the asymmetric configuration LK:AC as the most promising setup, we further quantified the performance stability thereof. Figure 2.9 shows the desalination capacity and charge efficiency obtained for a long-term experiment performed at 1.0 and 1.1 V. Long-term experiments with a cell voltage of 1.2 V were not performed because of the lower charge efficiency seen from Figure 2.8b. Over 100 cycles at 1.0 V (Figure 2.9a), the average SAC of the electrodes remains at 18.5 mg/g with a charge efficiency higher than 80%. This value for the charge efficiency also contains the leakage current; upon removing the latter, the average charge efficiency would be 96% (Table 2.3). This is a very high value of the SAC and is comparable to the SACs of the best carbon electrodes in the CDI literature (Table A2.1). Upon increasing the cell voltage to 1.1 V, both the SAC and charge efficiency decrease during long-time operation. The final SAC in the 100th cycle after switching to 1.1 V is 15.4 mg/g. The performance stability is significantly improved by lowering the cell voltage. The potential distribution (Figure 2.9b) also remains practically constant throughout the cycles for 1.0 and 1.1 V, showing a stronger modification during the first cycles until an equilibrium is approached. A small inversion peak is observed upon using a cell voltage of 1.1 V (Figure 2.9c) possibly because the  $E_0$  value approaches the  $E_{PZC}$  value (+50 mV vs. Ag/AgCl) of the AC electrode.

We also observe a change in the desalination kinetics of the electrodes during the electrosorption process. Figure 2.9d shows the kinetic plot in which the rate [Eq. (2.11)] and the SAC are plotted on the x and y axes, respectively. Thereby, Figure 2.9d provides information about the characteristic time for maximum electrosorption performance. This analytical approach is a practical tool to characterize the desalination kinetics in the constant-potential mode, which can be achieved by one single experiment. Thereby, the kinetic plot differs from the so-called Kim–Yoon plot (also known as the CDI Ragone plot).[61] The graph also gives direct information on the half-cycle time that yields the maximum desalination rate and the corresponding desalination capacity. Using the diagonal lines in Figure 2.9d as a time reference, we see a significant change in the optimal operation point of the CDI electrodes. In the 10th cycle for a cell voltage of 1.0 V, the best operational time is close to 10 min, which

provides an adsorption capacity of approximately 11 mg/g at a rate of 1.3 mg/g.min. After 90 cycles, this time decreases, and the optimum point provides a desalination capacity of 7.5 mg/g at a rate of 1.4 mg/g.min. Using a cell voltage of 1.1 V, the best operational time increases (~15 min), with an adsorption capacity of 9 mg/g at a rate of 0.7 mg/g.min. Therefore, not only are the desalination capacity and charge efficiency affected by the higher cell voltage but the desalination rate is also affected. This characteristic is important, as CDI desalination operates in cycles and should be carefully designed to optimize the amount of salt removal during long-term operations.[62]

**Figure 2.8.** (A) Salt adsorption capacity, (B) charge efficiency, and (D) potential distribution for the asymmetric LK and AC electrodes

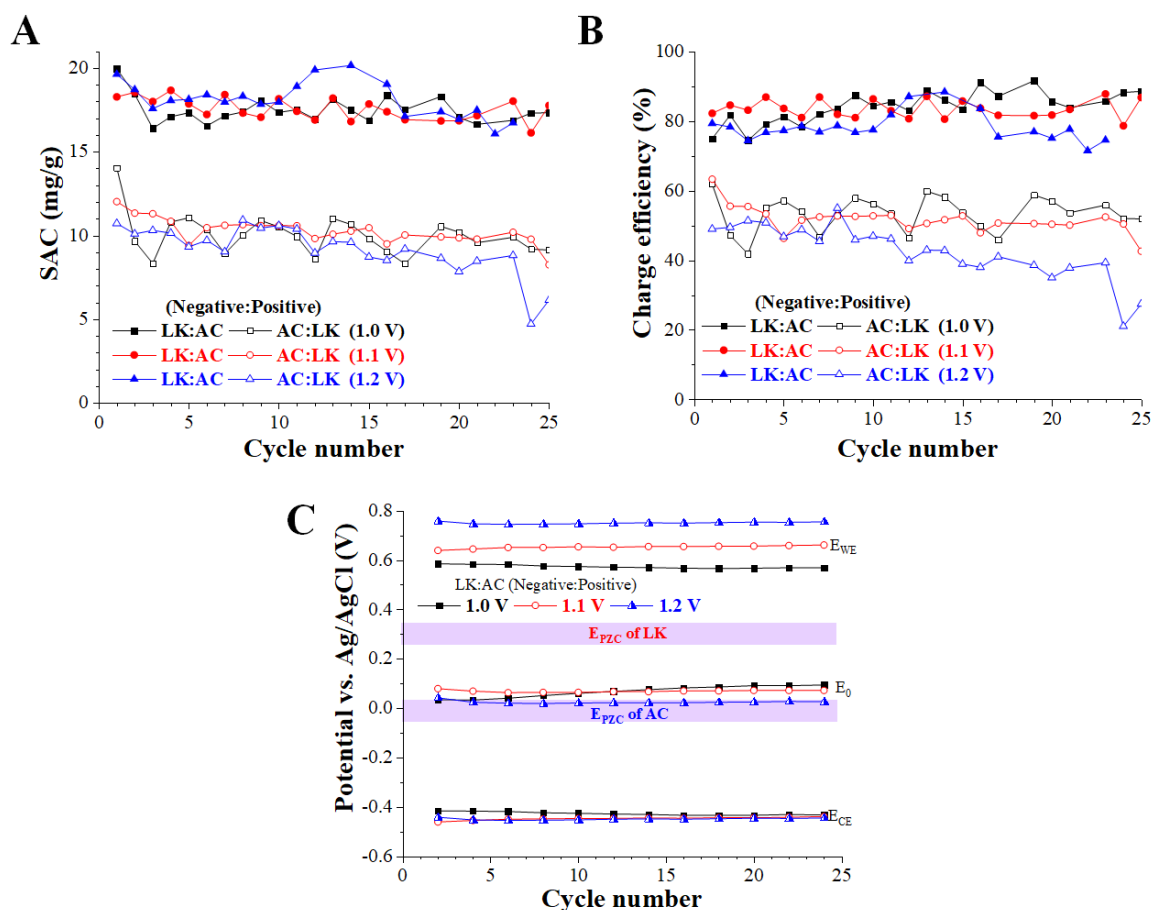
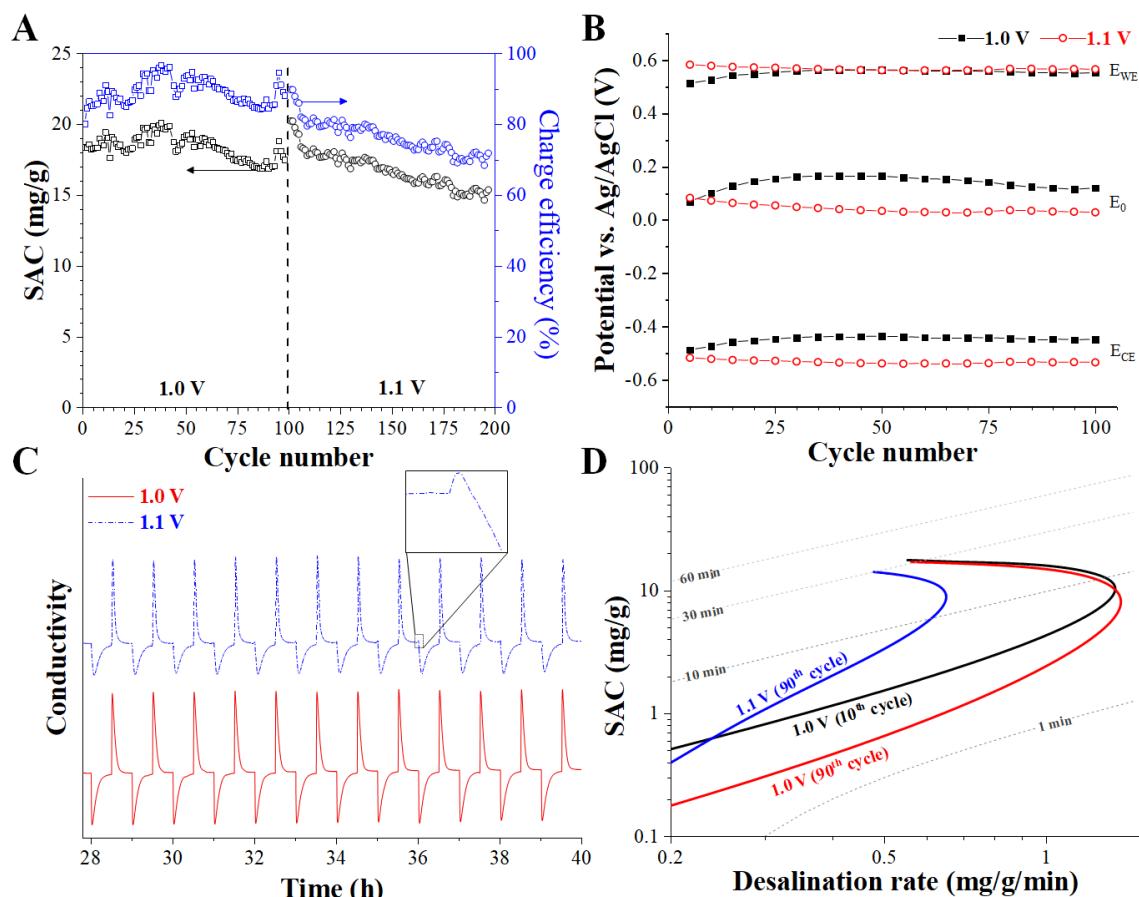


**Figure 2.9.** Data for the LK:AC electrode configuration at 1.0 V and 1.1 V in aqueous 10 mM NaCl: (A) Long-term SAC and charge efficiency. (B) Potential distribution. (C) Conductivity profile. (D) Kinetic plot



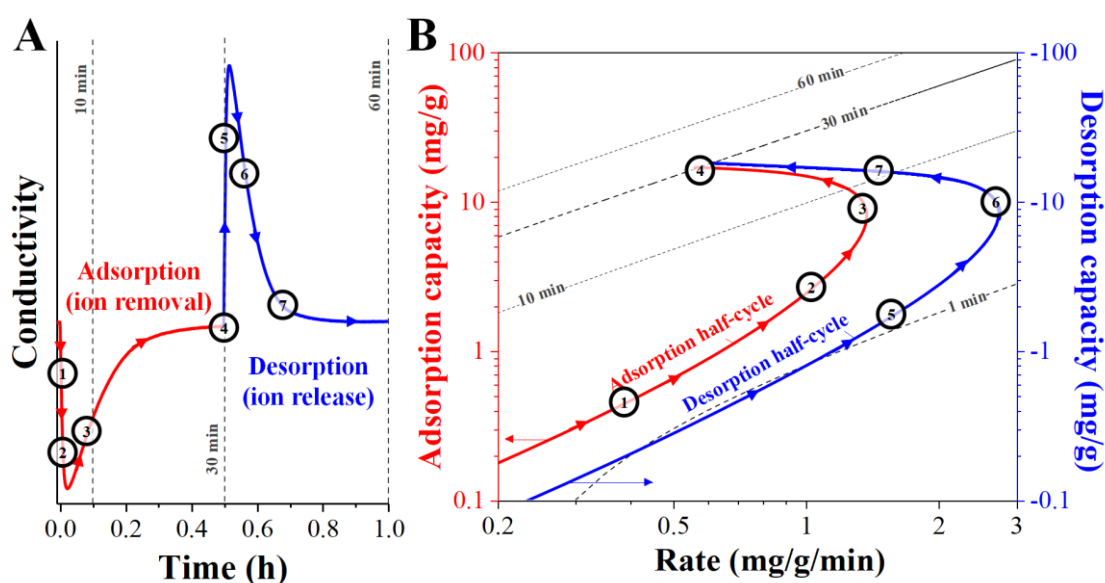
The correlation of the conductivity profile (Figure 2.9c) and the kinetic plot (Figure 2.9d) is exemplified in Figure 2.10. During the beginning of the electrosorption process (points 1 and 2), the adsorption capacity and rate increase with time. This initial process occurs quickly (close to 1 min), and soon the rate reaches a maximum (point 3). From this time forward, the electrosorption process effectively slows down until electrode saturation is approached (point 4). The path between points 3 and 4 takes more than half of the electrosorption time and corresponds to an increase in salt adsorption capacity from approximately 9 to 17 mg/g. The same pattern is observed for the desorption step, however with a faster rate. The faster desorption kinetics (maximum desalination rate is approximately two times faster) aligns with the high ion concentration inside the pores of the fully charged electrodes and the corresponding high ion mobility.

Finally, we calculated the energy required per NaCl ion removal ( $E_{kT}$ ) by using Equation (2.12) (Table 2.3). The energy consumption [kJ/g] was also calculated by multiplying



the Equation (2.12) by  $RT/M_{\text{NaCl}}$ , and the values are also provided in Table 2.3. For a cell potential of 1.0 V, the averages of  $E_{kT}$  over 100 cycles are  $(44 \pm 2)$  and  $(56 \pm 3)$  kT for 1.1 V and  $(60 \pm 2)$  kT for 1.2 V. The increase in the energy consumption per removed ion at higher cell voltages shows that, in general, it is desirable to operate CDI at lower voltages if the desalination capacity is sufficiently large. Values for  $E_{kT}$  using the LK:AC configuration are lower than those using AC as the positive and negative electrodes at 1.0 V (Table 2.3).

**Figure 2.10.** Kinetic data analysis for CDI half-cycles. (A) Conductivity profile and (B) the corresponding kinetic plot for adsorption and desorption data



## 2.4. Conclusions

In this work, we introduced lignin-derived activated carbon (LK) with a high surface area as an electrode material for capacitive deionization. Although providing a high specific capacitance, symmetric cells with LK as both the positive and negative electrodes showed poor performance stability. Therefore, we explored two ways to design an asymmetric cell, for which LK showed more beneficial performance. The first type of cell asymmetry varied the thickness of the positive and negative electrodes upon using LK for both electrodes. Thereby, the potential of the positive electrode was reduced and was maintained below values that would cause escalating electrode degeneration. Using this configuration, we obtained a desalination capacity of 14–16 mg/g and corresponding charge efficiency values of 62–74 %. The second type of asymmetric cell design used different electrode materials, which showed a different potential of zero charge. For that, we combined commercial activated carbon as a positive electrode with

LK as the negative electrode. This configuration yielded an improved charge efficiency (>80%), a high desalination capacity (~18.5 mg/g), and excellent performance stability over 100 cycles at a cell voltage of only 1.0 V. The desalination performance and the observed stability over 100 cycles are very encouraging, but commercial applications of CDI systems will require benchmarking of the long-term performance over significantly more cycles.

Our data show that CDI cell asymmetry (either by using different electrode masses or different electrode materials) is a powerful way to achieve improved desalination performance. The exact knowledge about the potential of zero charge and the electrode potential development during cell operation are crucial for the design of CDI systems with good performance stability. The widespread use of a cell voltage of 1.2 V for CDI, therefore, should not be blindly used, because this voltage window may already exceed the stability limit of one of the two electrodes.

## References

- [1] K. L. Yang, T. Y. Ying, S. Yiacoumi, C. Tsouris, E. S. Vittoratos, Electrosorption of Ions from Aqueous Solutions by Carbon Aerogel: An Electrical Double-Layer Model, *Langmuir* 2001, 17, 1961–1969.
- [2] “Electrochemical Demineralization of Water with Porous Electrodes of Large Surface Area”: J. W. Blair, G. W. Murphy in *Saline Water Conversion (Advances in Chemistry)*, American Chemical Society, Washington, DC, 1960, Vol. 27, pp. 206–223.
- [3] M. A. Anderson, A. L. Cudero, J. Palma, Capacitive Deionization as an Electrochemical Means of Saving Energy and Delivering Clean Water. Comparison to Present Desalination Practices: Will it Compete?, *Electrochim. Acta* 2010, 55, 3845–3856.
- [4] P. Długołęcki, A. van der Wal, Energy Recovery in Membrane Capacitive Deionization, *Environ. Sci. Technol.* 2013, 47, 4904–4910.
- [5] Y. Oren, Capacitive Deionization (CDI) for Desalination and Water Treatment – Past, Present and Future, *Desalination* 2008, 228, 10–29.
- [6] X. Z. Wang, M. G. Li, Y. W. Chen, R. M. Cheng, S. M. Huang, L. K. Pan, Z. Sun, Electrosorption of NaCl Solutions with Carbon Nanotubes and Nanofibers Composite Film Electrodes, *Electrochem. Solid-State Lett.* 2006, 9, E23–E26.
- [7] J. Yang, L. D. Zou, N. R. Choudhury, Ion-selective Carbon Nanotube Electrodes in Capacitive Deionisation, *Electrochim. Acta* 2013, 91, 11–19.
- [8] L. Zou, L. Li, H. Song, G. Morris, Using Mesoporous Carbon Electrodes for Brackish Water Desalination, *Water Res.* 2008, 42, 2340–2348.

- [9] C. Tsouris, R. Mayes, J. Kiggans, K. Sharma, S. Yiacoymi, D. DePaoli, S. Dai, Mesoporous Carbon for Capacitive Deionization of Saline Water, *Environ. Sci. Technol.* 2011, 45, 10243 –10249.
- [10] F. Duan, X. Du, Y. P. Li, H. B. Cao, Y. Zhang, Desalination Stability of Capacitive Deionization Using Ordered Mesoporous Carbon: Effect of oxygen-containing surface groups and pore properties, *Desalination* 2015, 376, 17– 24.
- [11] J. H. Lee, H. J. Ahn, D. Cho, J. I. Youn, Y. J. Kim, H. J. Oh, Effect of Surface Modification of Carbon Felts on Capacitive Deionization for Desalination, *Carbon Lett.* 2015, 16, 93– 100.
- [12] S. Porada, L. Weinstein, R. Dash, A. van der Wal, M. Bryjak, Y. Gogotsi, P. M. Biesheuvel, Water Desalination Using Capacitive Deionization with Microporous Carbon Electrodes, *ACS Appl. Mater. Interfaces* 2012, 4, 1194 –1199.
- [13] B. Krüner, P. Srimuk, S. Fleischmann, M. Zeiger, A. Schreiber, M. Asian, A. Quade, V. Presser, Hydrogen-Treated, Sub-micrometer Carbon Beads for Fast Capacitive Deionization with High Performance Stability, *Carbon* 2017, 117, 46–54.
- [14] S. Porada, L. Borchardt, M. Oschatz, M. Bryjak, J. S. Atchison, K. J. Keesman, S. Kaskel, P. M. Biesheuvel, V. Presser, Direct Prediction of the Desalination Performance of Porous Carbon Electrodes for Capacitive Deionization, *Energy Environ. Sci.* 2013, 6, 3700 – 3712.
- [15] G.-X. Li, P.-X. Hou, S.-Y. Zhao, C. Liu, H.-M. Cheng, A Flexible Cotton-derived Carbon Sponge for High-performance Capacitive Deionization, *Carbon* 2016, 101, 1–8.
- [16] J. J. Lado, R. L. Zornitta, F. A. Calvi, M. I. Tejedor-Tejedor, M. A. Anderson, L. A. M. Ruotolo, Study of Sugar Cane Bagasse Fly Ash as Electrode Material for Capacitive Deionization, *J. Anal. Appl. Pyrolysis* 2016, 120, 389–398.
- [17] R. L. Zornitta, F. J. García-Mateos, J. J. Lado, J. Rodríguez-Mirasol, T. Cordero, P. Hammer, L. A. M. Ruotolo, High-performance Activated Carbon from Polyaniline for Capacitive Deionization, *Carbon* 2017, 123, 318–333.
- [18] C. Kim, P. Srimuk, J. Lee, S. Fleischmann, M. Aslan, V. Presser, Influence of Pore Structure and Cell Voltage of Activated Carbon Cloth as a Versatile Electrode Material for Capacitive Deionization, *Carbon* 2017, 122, 329 –335.
- [19] M. Aslan, M. Zeiger, N. Jäckel, I. Grobelsek, D. Weingarth, V. Presser, Improved Capacitive Deionization Performance of Mixed Hydrophobic/Hydrophilic Activated Carbon Electrodes, *J. Phys. Condens. Matter* 2016, 28, 114003.

- [20] F. S. Chakar, A. J. Ragauskas, Review of Current and Future Softwood Kraft Lignin Process Chemistry, *Ind. Crops Prod.* 2004, 20, 131 –141.
- [21] F. Cotana, G. Cavalaglio, A. Nicolini, M. Gelosia, V. Coccia, A. Petrozzi, L. Brinchi, Lignin as Co-product of Second Generation Bioethanol Production from Ligno-Cellulosic Biomass, *Energy Procedia* 2014, 45, 52–60.
- [22] B. J. Yu, Z. Z. Chang, C. Y. Wang, The Key Pre-pyrolysis in Lignin-based Activated Carbon Preparation for High Performance Supercapacitors, *Mater. Chem. Phys.* 2016, 181, 187 –193.
- [23] L. J. Zhang, Y. Z. Jiang, L. W. Wang, C. Zhang, S. X. Liu, Hierarchical Porous Carbon Nanofibers as Binder-free Electrode for High-performance Supercapacitor, *Electrochim. Acta* 2016, 196, 189 –196.
- [24] H. J. Zhao, Q. J. Wang, Y. H. Deng, Q. Shi, Y. Qian, B. B. Wang, L. Lu, X. Q. Qiu, Preparation of Renewable Lignin Derived Nitrogen-doped Carbon Nanospheres as Anodes for Lithium-ion Batteries, *RSC Adv.* 2016, 6, 77143 – 77150.
- [25] R. Zhao, P. M. Biesheuvel, H. Miedema, H. Bruning, A. van der Wal, Charge Efficiency: A Functional Tool to Probe the Double-Layer Structure Inside of Porous Electrodes and Application in the Modeling of Capacitive Deionization, *J. Phys. Chem. Lett.* 2010, 1, 205 – 210.
- [26] A. Omosebi, X. Gao, J. Landon, K. Liu, Asymmetric Electrode Configuration for Enhanced Membrane Capacitive Deionization, *ACS Appl. Mater. Interfaces* 2014, 6, 12640 – 12649.
- [27] X. Gao, A. Omosebi, J. Landon, K. Liu, Surface Charge Enhanced Carbon Electrodes for Stable and Efficient Capacitive Deionization Using Inverted Adsorption-Desorption Behavior, *Energy Environ. Sci.* 2015, 8, 897 –909.
- [28] X. Gao, A. Omosebi, J. Landon, K. Liu, Dependence of the Capacitive Deionization Performance on Potential of Zero Charge Shifting of Carbon Xerogel Electrodes during Long-term Operation, *J. Electrochem. Soc.* 2014, 161, E159 –E166.
- [29] C. T. Hsieh, H. Teng, Influence of Oxygen Treatment on Electric Double-Layer Capacitance of Activated Carbon Fabrics, *Carbon* 2002, 40, 667 –674.
- [30] X. Gao, S. Porada, A. Omosebi, K.-L. Liu, P. M. Biesheuvel, J. Landon, Complementary Surface Charge for Enhanced Capacitive Deionization, *Water Res.* 2016, 92, 275– 282.
- [31] D. Lu, W. F. Cai, Y. Wang, Optimization of the Voltage Window for Long-term Capacitive Deionization Stability, *Desalination* 2017, 424, 53–61.

- [32] Z. Z. Chang, B. J. Yu, C. Y. Wang, Lignin-derived Hierarchical Porous Carbon for High-performance Supercapacitors, *J. Solid State Electrochem.* 2016, 20, 1405–1412.
- [33] J. W. Jeon, L. Zhang, J. L. Lutkenhaus, D. D. Laskar, J. P. Lemmon, D. Choi, M. I. Nandasiri, A. Hashmi, J. Xu, R. K. Motkuri, C. A. Fernandez, J. Liu, M. P. Tucker, P. B. McGrail, B. Yang, S. K. Nune, Controlling Porosity in Lignin-Derived Nanoporous Carbon for Supercapacitor Applications, *ChemSusChem* 2015, 8, 428–432.
- [34] W. L. Zhang, M. Z. Zhao, R. Y. Liu, X. F. Wang, H. B. Lin, Hierarchical Porous Carbon Derived from Lignin for High Performance Supercapacitor, *Colloids Surf. A* 2015, 484, 518–527.
- [35] X. F. Li, Q. Xu, Y. Fu, Q. X. Guo, Preparation and Characterization of Activated Carbon from Kraft Lignin via KOH Activation, *Environ. Prog. Sustainable Energy* 2014, 33, 519–526.
- [36] Suhas, P. J. M. Carrott, M. M. L. Ribeiro Carrott, Lignin – from Natural Adsorbent to Activated Carbon: A Review, *Bioresour. Technol.* 2007, 98, 2301–2312.
- [37] Q. Liu, S. Wang, Y. Zheng, Z. Luo, K. Cen, Mechanism Study of Wood Lignin Pyrolysis by Using TG-FTIR Analysis, *J. Anal. Appl. Pyrolysis* 2008, 82, 170–177.
- [38] W. Shen, Z. Li, Y. Liu, Surface Chemical Functional Groups Modification of Porous Carbon, *Recent Pat. Chem. Eng.* 2008, 1, 27–40.
- [39] M. Widmaier, B. Krüner, N. Jäckel, M. Aslan, S. Fleischmann, C. Engel, V. Presser, Carbon as Quasi-Reference Electrode in Unconventional Lithium-Salt Containing Electrolytes for Hybrid Battery/Supercapacitor Devices, *J. Electrochem. Soc.* 2016, 163, A2956–A2964.
- [40] M. A. Pimenta, G. Dresselhaus, M. S. Dresselhaus, L. G. Cancado, A. Jorio, R. Saito, Studying Disorder in Graphite-Based Systems by Raman Spectroscopy, *Phys. Chem. Chem. Phys.* 2007, 9, 1276–1291.
- [41] G. A. Zickler, B. Smarsly, N. Gierlinger, H. Peterlik, O. Paris, A Reconsideration of the Relationship Between the Crystallite Size  $L_a$  of Carbons Determined by X-ray Diffraction and Raman Spectroscopy, *Carbon* 2006, 44, 3239–3246.
- [42] M. Thommes, K. Kaneko, A. V. Neimark, J. P. Olivier, F. Rodriguez-Reinoso, J. Rouquerol, K. S. W. Sing, Physisorption of Gases, with Special Reference to the Evaluation of Surface Area and Pore Size Distribution (IUPAC Technical Report), *Pure Appl. Chem.* 2015, 87, 1051–1069.

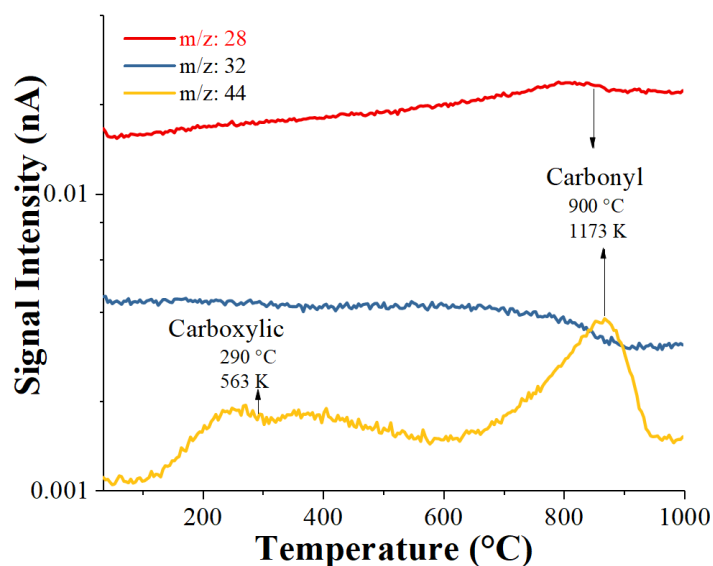
- [43] K. S. W. Sing, Reporting Physisorption Data for Gas/Solid Systems with Special Reference to the Determination of Surface Area and Porosity (Provisional), *Pure Appl. Chem.* 1982, 54, 2201 – 2218.
- [44] J. Wang, S. Kaskel, KOH Activation of Carbon-based Materials for Energy Storage, *J. Mater. Chem.* 2012, 22, 23710 – 23725.
- [45] J. Díaz-Terán, D. M. Nevskaja, J. L. G. Fierro, A. J. Lopez-Peinado, A. Jerez, Study of Chemical Activation Process of a Lignocellulosic Material with KOH by XPS and XRD, *Microporous Mesoporous Mater.* 2003, 60, 173 –181.
- [46] W. Gu, G. Yushin, Review of Nanostructured Carbon Materials for Electrochemical Capacitor Applications: Advantages and Limitations of Activated Carbon, Carbide-Derived Carbon, Zeolite-Templated Carbon, Carbon Aerogels, Carbon Nanotubes, Onion-Like Carbon, and Graphene, *Wiley Interdiscip. Rev.: Energy Environ.* 2014, 3, 424 – 473.
- [47] D. Weingarth, A. Foelske-Schmitz, R. Kütz, Cycle Versus Voltage Hold – Which is the Better Stability Test for Electrochemical Double Layer Capacitors?, *J. Power Sources* 2013, 225, 84–88.
- [48] J. Lee, P. Srimuk, K. Aristizabal, C. Kim, S. Choudhury, Y. C. Nah, F. Mücklich, V. Presser, Pseudocapacitive Desalination of Brackish Water and Seawater with Vanadium-Pentoxide-Decorated Multiwalled Carbon Nanotubes, *ChemSusChem* 2017, 10, 3611– 3623.
- [49] J. Lee, D. Weingarth, I. Grobelsek, V. Presser, Use of Surfactants for Continuous Operation of Aqueous Electrochemical Flow Capacitors, *Energy Technol.* 2016, 4, 75–84.
- [50] D. He, C. E. Wong, W. W. Tang, P. Kovalsky, T. D. Waite, Faradaic Reactions in Water Desalination by Batch-Mode Capacitive Deionization, *Environ. Sci. Technol. Lett.* 2016, 3, 222–226.
- [51] I. Cohen, E. Avraham, Y. Bouhadana, A. Soffer, D. Aurbach, Long Term Stability of Capacitive De-ionization Processes for Water Desalination: The Challenge of Positive Electrodes Corrosion, *Electrochim. Acta* 2013, 106, 91–100.
- [52] T. Kim, J. Yu, C. Kim, J. Yoon, Hydrogen Peroxide Generation in Flow-mode Capacitive Deionization, *J. Electroanal. Chem.* 2016, 776, 101 –104.
- [53] S. Porada, F. Schipper, M. Aslan, M. Antonietti, V. Presser, T.-P. Fellingner, Capacitive Deionization Using Biomass-based Microporous Salt-Templated Heteroatom-Doped Carbons, *ChemSusChem* 2015, 8, 1867 –1874.

- [54] M. He, K. Fic, E. Frackowiak, P. Novák, E. J. Berg, Ageing Phenomena in High-Voltage Aqueous Supercapacitors Investigated by *in situ* Gas Analysis, *Energy Environ. Sci.* 2016, 9, 623 –633.
- [55] J.-H. Lee, W.-S. Bae, J.-H. Choi, Electrode Reactions and Adsorption/Desorption Performance Related to the Applied Potential in a Capacitive Deionization Process, *Desalination* 2010, 258, 159 –163.
- [56] X. Dong, Y. Zhang, B. Ding, X. Hao, H. Dou, X. Zhang, Layer-by-Layer Self-Assembled Two-Dimensional MXene/Layered Double Hydroxide Composites as Cathode for Alkaline Hybrid Batteries, *J. Power Sources* 2018, 390, 208 –214.
- [57] E. Avraham, M. Noked, I. Cohen, A. Soffer, D. Aurbach, The Dependence of the Desalination Performance in Capacitive Deionization Processes on the Electrodes PZC *J. Electrochem. Soc.* 2011, 158, P168–P173.
- [58] E. Avraham, M. Noked, Y. Bouhadana, A. Soffer, D. Aurbach, Limitation of Charge Efficiency in Capacitive Deionization II. On the Behavior of CDI Cells Comprising Two Activated Carbon Electrodes, *J. Electrochem. Soc.* 2009, 156, P157 –P162.
- [59] E. Avraham, Y. Bouhadana, A. Soffer, D. Aurbach, Limitation of Charge Efficiency in Capacitive Deionization I. On the Behavior of Single Activated Carbon *J. Electrochem. Soc.* 2009, 156, P95–P99.
- [60] S. Porada, M. Bryjak, A. van der Wal, P. M. Biesheuvel, Effect of Electrode Thickness Variation on Operation of Capacitive Deionization, *Electrochim. Acta* 2012, 75, 148– 156.
- [61] T. Kim, J. Yoon, CDI Ragone Plot as a Functional Tool to Evaluate Desalination Performance in Capacitive Deionization, *RSC Adv.* 2015, 5, 1456 – 1461.
- [62] R. L. Zornitta, L. A. M. Ruotolo, Simultaneous Analysis of Electrosorption Capacity and Kinetics for CDI Desalination Using Different Electrode Configurations, *Chem. Eng. J.* 2018, 332, 33–41.
- [63] G. Y. Gor, M. Thommes, K. A. Cychosz, A. V. Neimark, Quenched Solid Density Functional Theory Method for Characterization of Mesoporous Carbons by Nitrogen Adsorption, *Carbon* 2012, 50, 1583 –1590.

## APPENDIX

**Table A2.1.** SAC obtained using different carbon materials in CDI literature

Authors	Material	[NaCl] (mg/L)	Cell voltage	SAC (mg/g)
Liu et al.	N-doped carbon nanospheres	500	1.2	13.7
Porada et al.	Salt-templated heteroatom-doped carbon	300	1.2	15.0
Xu et al.	N-doped graphene sponge	500	1.2	21.0
Zhao et al.	Hollow carbon nanospheres	500	1.4	13.0
Li et al.	Cotton-derived carbon sponge	500	1.2	16.1
Li et al.	Copolymer derived porous carbon	500	1.2	13.8
Xu et al.	Carbon spheres	500	1.2	15.8
Aslan et al.	Commercial activated carbon	300	1.2	13.1
Zornitta et al.	Polyaniline-derived activated carbon	600	1.2	14.3
This work	Lignin activated carbon and commercial activated carbon	585	1.0	18.5

**Figure A2.1.** Coupled TGA-MS plotting the ionic current vs. temperature for m/z: 28, 32, and 44 of AC (MSP-20)



**Figure A2.2.** Nitrogen gas sorption isotherms of LK, LC, and AC recorded at -196 °C

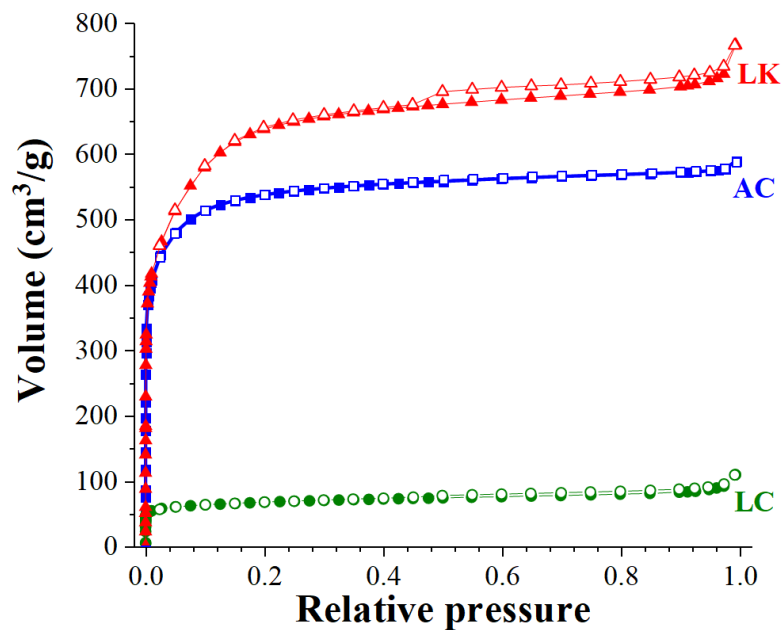


**Figure A2.3.** Galvanostatic charge/discharge profiles for LK and AC at 10 A/g

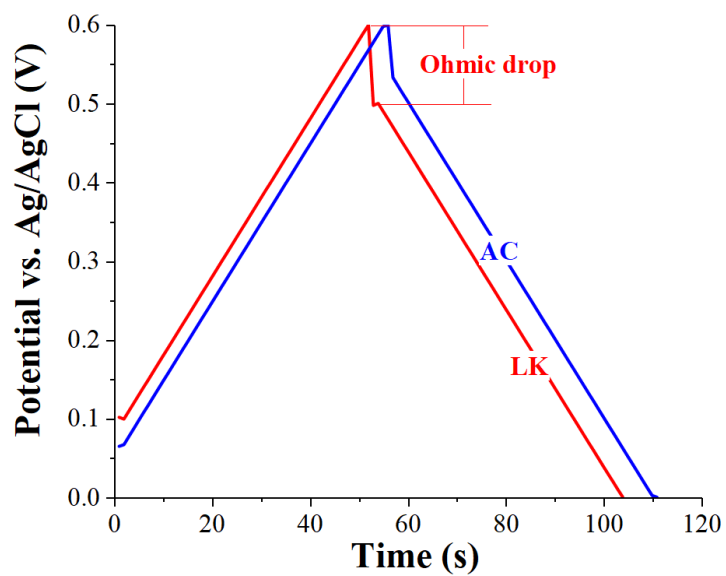


**Figure A2.4.** Electrode potential distribution for the sample AC. WE: working electrode; CE: counter electrode;  $E_0$ : short-circuit potential;  $E_{PZC}$ : potential of zero charge

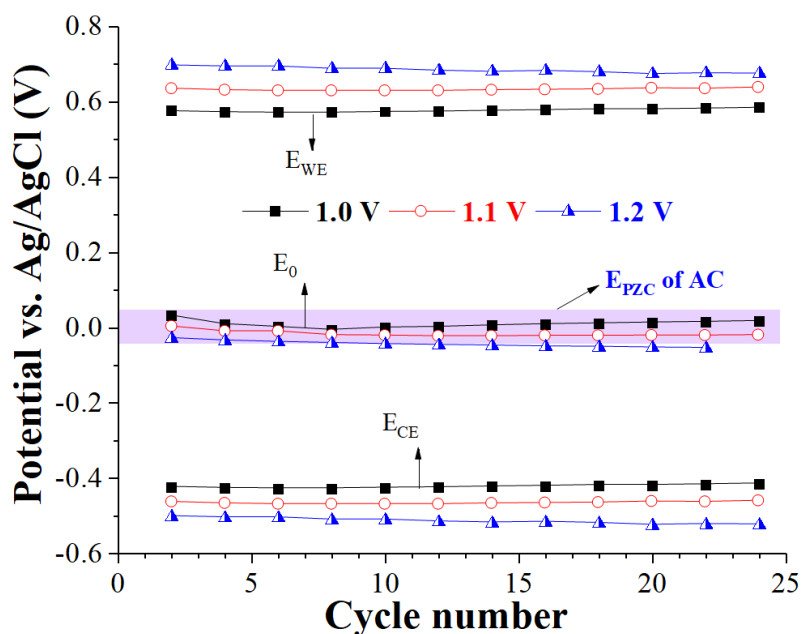
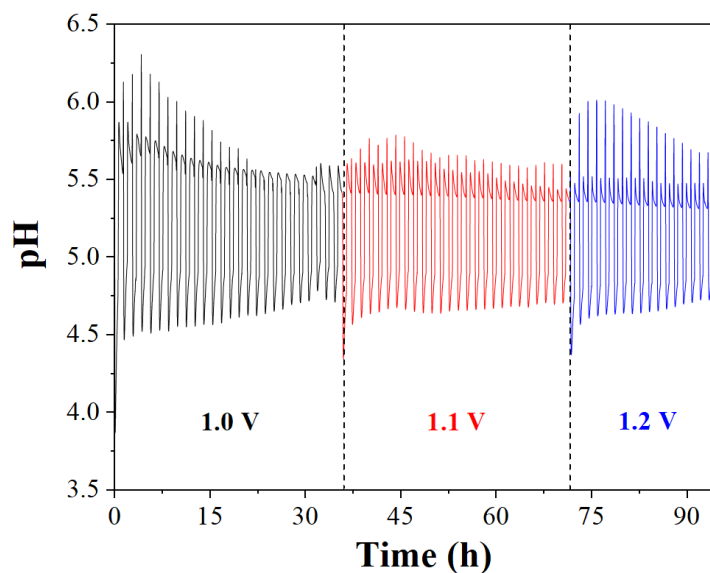


**Figure A2.5.** pH values measured during the desalination experiment using symmetrical LK electrodes at a cell potential of 1.0 V, 1.1 V and 1.2 V



**Appendix references:**

- [1] Y. Liu, T. Chen, T. Lu, Z. Sun, D. H. C. Chua, L. Pan *Electrochimica Acta*. 2015, 158, 403-409.
- [2] S. Porada, F. Schipper, M. Aslan, M. Antonietti, V. Presser, T.-P. Feller *ChemSusChem*. 2015, 8, 1867-1874.

- [3] X. Xu, Z. Sun, D. H. C. Chua, L. Pan *Scientific Reports*. 2015, 5, 11225.
- [4] S. Zhao, T. Yan, H. Wang, G. Chen, L. Huang, J. Zhang, L. Shi, D. Zhang *Applied Surface Science*. 2016, 369, 460-469.
- [5] G.-X. Li, P.-X. Hou, S.-Y. Zhao, C. Liu, H.-M. Cheng *Carbon*. 2016, 101, 1-8.
- [6] Y. Li, I. Hussain, J. Qi, C. Liu, J. Li, J. Shen, X. Sun, W. Han, L. Wang *Separation and Purification Technology*. 2016, 165, 190-198.
- [7] X. T. Xu, H. M. Tang, M. Wang, Y. Liu, Y. J. Li, T. Lu, L. K. Pan *Journal of Materials Chemistry A*. 2016, 4, 16094-16100.
- [8] M. Aslan, M. Zeiger, N. Jäckel, I. Grobelsek, D. Weingarh, V. Presser *Journal of Physics: Condensed Matter*. 2016, 28, 114003.
- [9] R. L. Zornitta, F. J. García-Mateos, J. J. Lado, J. Rodríguez-Mirasol, T. Cordero, P. Hammer, L. A. M. Ruotolo *Carbon*. 2017, 123, 318-333.

## CHAPTER 3

### HIGH-PERFORMANCE ACTIVATED CARBON FROM POLYANILINE FOR CAPACITIVE DEIONIZATION

Activated carbons prepared using polyaniline (PAni), a N-containing precursor, doped with different anions were successfully employed in this work as electrode materials for capacitive deionization. The aim of this research was to investigate the effect of chloride ( $\text{Cl}^-$ ), p-toluenesulfonate ( $\text{PTS}^-$ ), dodecylbenzene-sulfonate ( $\text{DBS}^-$ ) and polystyrenesulfonate ( $\text{PSS}^-$ ) as PAni dopants on the textural and electrochemical properties of PAni activate carbon (PAC) and evaluate their performance for desalination. It was demonstrated that textural PAC properties such as microporosity could be properly tuned, resulting in a suitable proportion of micro- and mesoporosity by using different doping anions. Furthermore, it was observed that the higher the oxygen content the higher the electrode hydrophilicity due to introduction of surface polar groups, as identified by XPS. These groups were found to be the most important variable influencing on the PAC electrosorption capacity and energy efficiency. The highest specific adsorption capacity (14.9 mg/g), along with the lowest specific energy consumption, was obtained using the PTS-doped PAC electrode. Considering its high capacity, low-cost and ease of synthesis, PAC/PTS seems to be a promising electrode for CDI.

#### 3.1. Introduction

Water scarcity as result of population growth and industrialization has become one of the major issues of the 21<sup>st</sup> century. Despite the large reserves of water still available on earth (e.g. seawater and groundwater), great part of this water does not meet quality standards for human consumption mainly due to the high concentration of salts. To make water drinkable, reverse osmosis (RO), electrodialysis (ED), and multi-effect distillation (MFD) can be employed for water desalination, although these technologies demand high energy consumption in large-scale applications.[1,2] In this context, CDI has emerged in the last few years as a low-cost technology that can be used to remove ions from brackish water (~10,000 mg/L), but consuming less energy than its main competitor, the RO.[2] CDI is based on the concept of charge storage in the electric double layer (EDL) developed when ions are attracted to a pair of porous carbon electrodes when an external voltage is applied. The low energy consumption of

CDI comes from the low voltage needed for the electrosorption process (typically 1.0 - 1.4 V) and the low required pressure when compared to RO. [3–5] After electrode saturation, the regeneration of the electrodes is achieved by short-circuiting the cell.[4,6] Another possibility is to invert the cell potential repelling the electrosorbed ions, thus reducing the time needed for electrode regeneration (Figure A3.1).[5]

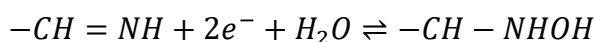
Despite the advantages presented by CDI relative to other well-established technologies like RO and ED, there are still challenging issues, such as electrode material, to be overcome in order to make this technology feasible for large-scale applications. The electrode material for CDI must have fast electrosorption kinetics and high adsorption capacity. A good candidate for electrode material to be used for CDI must have high specific surface area (SSA) available for electrosorption, high conductivity, good wettability, fast response to polarization, and chemical stability.[7] Carbon materials fit most of these requirements and have been intensively used as CDI electrodes, e.g., carbon aerogels, [3,8,9] mesoporous activated carbon,[4,10] microporous activated carbon,[11] carbon felts,[12] carbon fibers,[13] carbon nanotubes[14,15] and their modification using oxides[16,17] and conducting polymers.[18,19] Although there are many studies related to electrode materials for symmetrical membraneless CDI, the carbons showing the best performance, such as nitrogen doped graphene, are still too expensive and in many cases their preparations are not environmental friendly.[20]

Recently, nitrogen-doped activated carbons (N-doped AC) have been reported to enhance CDI electrode performance[21–24] mainly due to the (i) introduction of defects and distortion in the carbon matrix, facilitating the ion access to the surface area and increasing charge accumulation, (ii) enhancement of charge density due to the presence of nitrogen, which facilitates the charge-transfer process,[24,25] and (iii) introduction of surface groups responsible for pseudocapacitance.[21] CDI materials reported to exhibit the highest specific adsorption capacity (SAC) are N-doped graphene (21.9 mg/g),[21] N-doped graphene sponge (21 mg/g),[25] and N-doped cotton-derived carbon sponge (16.1 mg/g).[24] The most common approach to introduce N-groups into the carbon structure is the post-treatment with ammonia at high temperatures. However, this technique leads to a low nitrogen content and poor thermal stability.[26] Moreover, this process could become too expensive considering the precursor preparation followed by the activation with ammonia.

Nitrogen-containing precursors such as glucosamine hydrochloride,[23] polyacrylonitrile,[27] PANi[28–30] and polypyrrole[31] have become a low-cost alternative to

obtain N-doped AC dispensing the post-treatment. Among these materials, PANi find applications in different fields such as supercapacitors,[32] cation exchange,[33] and as additive to improve AC capacitance in CDI.[19,34] PANi presents high nitrogen-content (~15 wt.%), it is inexpensive, easily synthesized, and has a structure similar to graphite, which could facilitate the introduction of nitrogen-containing active sites inside the carbon matrix at high temperatures.[30,35] Furthermore, the PANi properties can be easily customized by varying the doping anion during the polymerization process.[36] The use of PANi as AC precursor has already been reported for different applications such as adsorption,[37] supercapacitors,[29,30,36,38–45] electrocatalysts,[35,41] and batteries;[45] however, to the best of our knowledge, PAC has never been used for CDI applications.

PAC has been considered a promising material for electrochemical applications due to its distinguished structural and textural characteristics. Recent studies have shown that depending on the precursor synthesis and activation method, PAC presents extremely high SSA,[37,44,45] high mesopore volume,[40] high capacitance,[29,43] good wettability[43], and long-term stability.[29,30] The presence of quaternary nitrogen in the carbon matrix can enhance the charge-transfer, thus improving the CDI electrode conductivity.[24,25] Moreover, the presence of pyridine- and pyrrole-like nitrogen groups is recognized as being responsible to create pseudocapacitance [21] and also to improve carbon wettability due to the redox reaction with water according to:[25,46]



In this scenario, the application of PAC as CDI electrodes seems to be promising and was the aim of this investigation. To the best of our knowledge, the use of PAC for CDI using PANi doped with different anions is reported for the first time. PANi was used as N-containing precursor to obtain a N-doped AC. Furthermore, the effect of the large (dodecylbenzenesulfonate, DBS<sup>-</sup>, and polystyrenesulfonate, PSS<sup>-</sup>) and small dopant anions (Cl<sup>-</sup> and p-toluenesulfonate, PTS<sup>-</sup>) on the textural properties of the obtained PAC was compared.

In order to understand the effect of different anions on the PAC electrode performance for desalination, PACs were characterized regarding to their SSA, pore size distribution (PSD), morphology, surface functional groups, electrochemical capacitance and charge-transfer resistance. The desalination performance was evaluated in terms of electrosorption kinetics, SAC, charge efficiency and specific energy consumption. The results confirmed the great

potential of this novel approach to explore the properties of PANi to obtain tailorable N-doped activated carbons for CDI electrodes.

## 3.2. Experimental

### 3.2.1. Materials

The monomer aniline (99% Sigma-Aldrich) was distilled prior to use for polymerization and maintained in amber bottle at low temperatures ( $< 3\text{ }^{\circ}\text{C}$ ) to prevent oxidation. Anion sources used as counter ions for polyaniline were hydrochloric acid (HCl, 36.5-38%, J.T. Baker), p-toluenesulfonic acid monohydrate (HPTS,  $\geq 98.5\%$ , Sigma-Aldrich), sodium dodecylbenzene-sulfonate (NaDBS, Sigma-Aldrich) and poly(4-styrenesulfonic acid) (HPSS, 18 wt.% solution in water, Sigma-Aldrich). The oxidant used for polymerization was ammonium persulfate (98%, Sigma-Aldrich). Polyvinylidene fluoride (PVDF, Sigma Aldrich) and n-methylpyrrolidone (NMP, 99.5%, Synth) were used as binder and solvent, respectively, for electrode preparation. Commercial activated carbon (CAC) YP-80F was purchased from Kuraray Corp., Japan.

### 3.2.2. Polyaniline Synthesis

PAni was chemically synthesized using the optimized conditions adapted from Jelmi *et al.*[47] Briefly, 10 mL of aniline (0.21 mol/L) was added at low temperature ( $\sim 3^{\circ}\text{C}$ ) and constant stirring to 500 mL solution containing 0.30 mol/L of the doping compounds (HCl, HPTS, NaDBS and HPSS). The polymerization started adding 85.9 mL of the oxidant solution ( $(\text{NH}_4)_2\text{S}_2\text{O}_8$  1.0 mol/L), dropped slowly into the monomer solution. The mixture was left to react for 24 h under stirring. After polymerization, the precipitated PANi doped with  $\text{Cl}^-$  and  $\text{PTS}^-$  were filtered, washed with acid solution (HCl and HPTS, respectively) and dried in oven at  $60\text{ }^{\circ}\text{C}$  for 24 h.[43] Regarding to PANi doped with  $\text{DBS}^-$ , 750 mL of acetone (99.5%, Synth) was added to the polymerization solution to precipitate the polymer particles, followed by filtration and washing with plenty of water and dried in oven at  $60\text{ }^{\circ}\text{C}$  for 24 h.[48,49] The particles of PANi doped with  $\text{PSS}^-$  were separated by leaving the polymerization solution in an oven for 24 h at  $60\text{ }^{\circ}\text{C}$  to evaporate the solvent.[50] The samples of PANi doped with the different anions were referred as PANi/Cl, PANi/PTS, PANi/DBS and PANi/PSS.

### 3.2.3. Polyaniline carbonization and activation

PAni was activated according to the procedure adapted from Yan *et al.*[29]. In this procedure, PANi was firstly carbonized in a tubular furnace (Thermo Scientific Lindberg Blue

M) at 850 °C at a heating rate of 10 °C/min for 2 h under N<sub>2</sub> atmosphere (150 mL/min). After carbonization, the samples were activated with KOH in a proportion of 1:4 (polymer:KOH, w/w) followed by heating at 850 °C for 1.5 h using the same heating rate and N<sub>2</sub> flow conditions of the carbonization process. The ratio 1:4 (w/w) of carbonized carbon to KOH was chosen based on previous studies reporting an increase of 41% of the SSA when the activation agent KOH was increased from 1:2 to 1:4.[43]

After carbonization, the activated carbon was washed with HCl 0.5 M and warm water until constant pH and then dried at 105 °C for 24 h. The samples were referred as PAC followed by the doping source of the PANi precursor: PAC/Cl, PAC/PTS, PAC/DBS and PAC/PSS.

### 3.2.4. Preparation of the CDI electrodes

Carbon electrodes were prepared by mixing 10 wt% of PVDF previously dissolved in NMP and 90 wt% of activated carbon. The slurry was kneaded and poured into a mold containing a graphite substrate. The mold was then placed into an oven at 80 °C for 12 h to remove all the solvent and form the carbon film.[5] The mass of the active material in the electrodes used in the desalination experiments was ~0.64 g.

### 3.2.5. Material Characterization

Doped PANi was characterized by Fourier transform infrared spectroscopy FTIR (Bruker Vertex 70 spectrophotometer) using the KBr pellet technique. Activated carbon morphology was analyzed by scanning electron microscope (SEM, JEOL JSM-840) using high voltages (20-25 kV) and depositing a gold layer to increase conductivity. SSA and PSD were investigated through N<sub>2</sub> adsorption/desorption at -196 °C using an Omnisorp 100cx (Coulter). The samples were prior outgassed for at least 8 h at 150 °C. The volume of micropores and the SSA were calculated from the N<sub>2</sub> isotherm using t-plot method and the Brunauer-Emmett-Teller (BET) equation, respectively. The mesopore volume was determined by the difference between the total pore volume of N<sub>2</sub> adsorbed at  $P/P_0 = 0.95$  and the micropore volume. The PSD between 1-20 nm was calculated using the density functional theory (DFT) method. X-Ray photoelectron spectroscopy analysis (XPS) was performed using a 5700C model Physical Electronics apparatus with Mg K $\alpha$  radiation (1253.6 eV). This technique was used for a quantitative analysis and determination of the chemical bonding structure of the PAC samples. The spectra were fitted without placing constraints using multiple Voigt profiles using the



CasaXPS software. The ultimate analysis of the samples were performed in a Leco CHNS-932 system, being the oxygen content calculated by difference.

### 3.2.6. Electrochemical characterization

Cyclic voltammetry (CV), galvanostatic charge-discharge, and electrochemical impedance spectroscopy (EIS) were performed in NaCl 0.2 mol/L using a three-electrode cell with carbon electrodes as working (2.5 cm x 2.5 cm) and counter electrode (2.5 cm x 3.0 cm). The reference electrode was Ag/AgCl in saturated KCl. A potentiostat Autolab PGStat 204 was used in all measurements.

CV was carried out at different scan-rates ( $v$ ): 1, 5, 10, 50, and 100 mV/s, in a potential window between -0.2 V and 0.5 V, which was previously determined to prevent redox reactions. The specific capacitance ( $C_S$ ) and the total specific capacitance ( $C_{CV}$ ) of the electrode (F/g), was calculated using Equations 3.1 and 3.2, respectively, where  $I$  is the current,  $m$  is the mass of the working electrode (g) and  $E_1$  and  $E_2$  are the low and high values of the potential window.

$$C_S = \frac{I}{vm} \quad (3.1)$$

$$C_{CV} = \frac{\int_{E_1}^{E_2} I dV}{vm(E_2 - E_1)} \quad (3.2)$$

The galvanostatic charge-discharge experiments were carried out at  $\pm 0.4$  mA/cm<sup>2</sup>. In this case, the specific capacitance ( $C_{CD}$ ) was calculated from the slope of the discharge curve using Equation 3.3, where  $I_d$  (A) is the discharge current,  $\Delta t$  (s) is the discharging time, and  $\Delta U$  is the potential drop during discharging (excluding  $IR_{drop}$ ). The inferior and superior electrode potential cutoffs used in these experiments were 0 V and 0.6 V, respectively.

$$C_{CD} = \frac{I_d \Delta t}{m \Delta U} \quad (3.3)$$

EIS measurements were carried out in the frequency range between 1 mHz and 100 kHz applying a potential of 0.0 V and an AC amplitude of 10 mV. Specific capacitance obtained from EIS ( $C_{EIS}$ ) was calculated using Equation 3.4, where  $\omega$  is the angular frequency and  $Z''$  is the imaginary part of the impedance spectrum. The fitting for the equivalent circuit was performed using the Metrohm Autolab NOVA v1.11 software.

$$C_{EIS} = \frac{1}{m|\omega Z''|} \quad (3.4)$$

### 3.2.7. Electrosorption experiments

The CDI experiments were used to evaluate the desalination performance in a batch experimental system. A detailed description of the CDI cell can be found in our previous work.[5] Briefly, the electrosorption unit cell consisted of two acrylic plates where carbon electrodes with dimensions of 10 cm x 5 cm were placed on titanium sheets used as current collectors. Two plastic meshes placed between the carbon electrodes provided a gap of 1.8 mm necessary for ensuring the electrolyte flow and preventing short circuit. Rubber gaskets sealed up the cell and all the components were assembled by nuts and bolts.

During desalination, a volume of 25 mL of NaCl 600 mg/L solution was pumped through the CDI cell using a peristaltic pump (Masterflex L/S Cole-Parmer) at a constant flow-rate of 26 mL/min. A potentiostat Autolab PGStat 204 supplied the constant cell potential (1.2 V or 1.4 V) during electrosorption and 0 V during desorption. The solution conductivity was measured online at the exit of the cell and it was recorded every 30 s using a conductivity meter (Mettler Toledo SevenCompact Conductivity). The conductivity was then converted to salt concentration using a linear relationship obtained prior to the experiment. Each electrosorption/desorption experiment was performed until no apparent conductivity variation was observed.

Salt adsorption capacity ( $SAC$ ), charge efficiency ( $Q_E$ ) and specific energy consumption ( $\eta$ ) were calculated using Equations 3.5-3.7, respectively, and used to evaluate the performance of the electrode in the desalination process.

$$SAC = \frac{(C_0 - C_t)V}{m_E} \quad (3.5)$$

$$Q_E = 100 \frac{zFV\Delta C}{\int I_e dt} \quad (3.6)$$

$$\eta = \frac{E_{cell} \int I dt}{m_{rem}} \quad (3.7)$$

In these Equations,  $C_0$  is the initial salt concentration (mg/L),  $C_t$  (mg/L) is the salt concentration at time  $t$ ,  $V$  is the volume of electrolyte (L),  $m_E$  is the mass of active material in both electrodes,  $z$  is the ion charge,  $F$  is the Faraday constant (96485 C/mol),  $E_{cell}$  is the cell voltage during electrosorption (V),  $m_{rem}$  is the mass of ions removed. The current ( $I_e$ ) in Equation 3.6 is the effective current used for electrosorption (subtracting the leakage current) while the current ( $I$ ) in Equation 3.7 is the total current applied to the cell.

### 3.3. Results and Discussion

#### 3.3.1. Polymerization and Activation

Table A3.1 shows the polymerization yield ( $Y_{PAni}$ ) calculated from the ratio of polyaniline/aniline (wt./vol.) for the solutions containing the different anions. The highest yield was achieved using  $PSS^-$  followed by  $DBS^-$  and  $PTS^-$ . This result can be explained by the high molecular weight of  $PSS^-$  (~ 75,000 g/mol), followed by  $DBS^-$  (348.5 g/mol) and  $PTS^-$  (172.2 g/mol). As the size of the anion gets smaller, the PAni final mass also decreases, reaching the lowest value for PAni/Cl. The polymerization process was adapted from the best yield conditions obtained by Jelmy *et al.*,[47] although the doping anion used in their work was the methanesulfonate. Nevertheless, it was possible to observe a high  $Y_{PAni}$  considering that for most of the experiments the final mass of PAni was close or even higher than the mass of aniline used for polymerization. For comparison, John *et al.*[51] synthesized PAni/PTS and obtained a  $Y_{PAni}$  of 91.4% with respect to aniline which is fairly close to the 82% achieved in this work.

Another way to estimate  $Y_{PAni}$  is to consider the ratio of the mass of the conducting polymer and the total mass of aniline plus the doping anion. In this case, the PAni/DBS yield only 26.7%, which is much lower than the 92.3% obtained by Shreepathi,[48] but this author used acidic DBS instead of the sodium salt used in this work. A possible explanation for the lower  $Y_{PAni}$  observed for PAni/DBS might be the high pH of the salt solution. The lower the pH the more protonated the PAni[52] and, consequently, there will be more doping sites for  $DBS^-$ . Therefore, it can be concluded that  $Y_{PAni}$  can be further optimized using different polymerization conditions.

After polymerization, the PAni powder was first carbonized and in a second step activated according to the methodology adapted from Yan *et al.*,[29] which describes the preparation of high SSA PAC/Cl for high performance supercapacitor. Table A3.2 displays the mass yield for the different materials obtained after carbonization ( $Y_C$ ), activation ( $Y_{AC}$ ), and the overall yield ( $Y_O$ ). It is interesting to notice that the sequence of  $Y_O$  for carbonization and activation is the opposite of the polymerization yield (Table A3.1). This could suggest that most part of the doping anion had been released during the carbonization or activation processes; therefore, the highest mass loss was obtained after the activation process of the PAni doped with the highest molar weight anion.

### 3.3.2. Characterizations

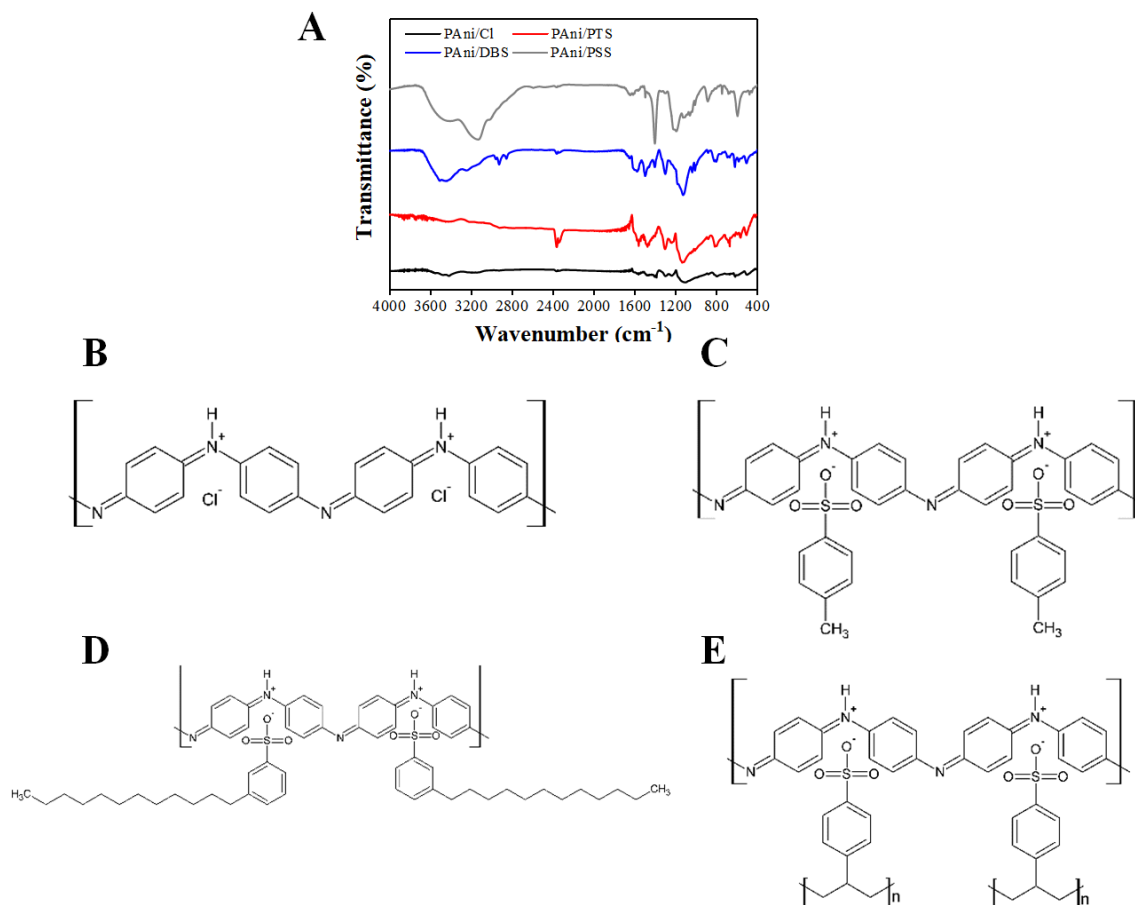
#### 3.3.2.1. FTIR

Prior carbonization and activation, FTIR was performed to investigate if PANi polymers have been successful doped and also to understand the bonding of PANi with the different anions.

Figure 3.1a shows the FTIR spectra. Despite of some similarity, each spectrum showed typical peaks related to the dopant structure. In all cases, PANi presented N-H stretching at  $\sim 3440\text{ cm}^{-1}$ , N-H bending in the range of  $1560\text{-}1640\text{ cm}^{-1}$ , C-C stretching at  $\sim 1100\text{ cm}^{-1}$ , C-C twisting at  $1235\text{ cm}^{-1}$ , C-N stretching of the benzenoid at  $1300\text{ cm}^{-1}$  and  $1407\text{ cm}^{-1}$ , C=C stretching of the benzenoid ring in the range of  $1477\text{-}1490\text{ cm}^{-1}$ , C=C stretching of the quinoid ring in the range of  $1585\text{-}1599\text{ cm}^{-1}$  and the N-H out-of-plane deformation at  $800\text{ cm}^{-1}$ . [51–54] The small peak observed between  $735\text{-}758\text{ cm}^{-1}$  for PANi/Cl indicates the presence of N-Cl, [55,56] confirming the PANi was doped by Cl<sup>-</sup>. For PANi/PTS, PANi/DBS and PANi/PSS the peaks between  $513\text{-}560\text{ cm}^{-1}$  and  $1130\text{-}1140\text{ cm}^{-1}$  indicate the presence of SO<sub>3</sub><sup>-</sup>, also confirming the doping. [51,53,54]

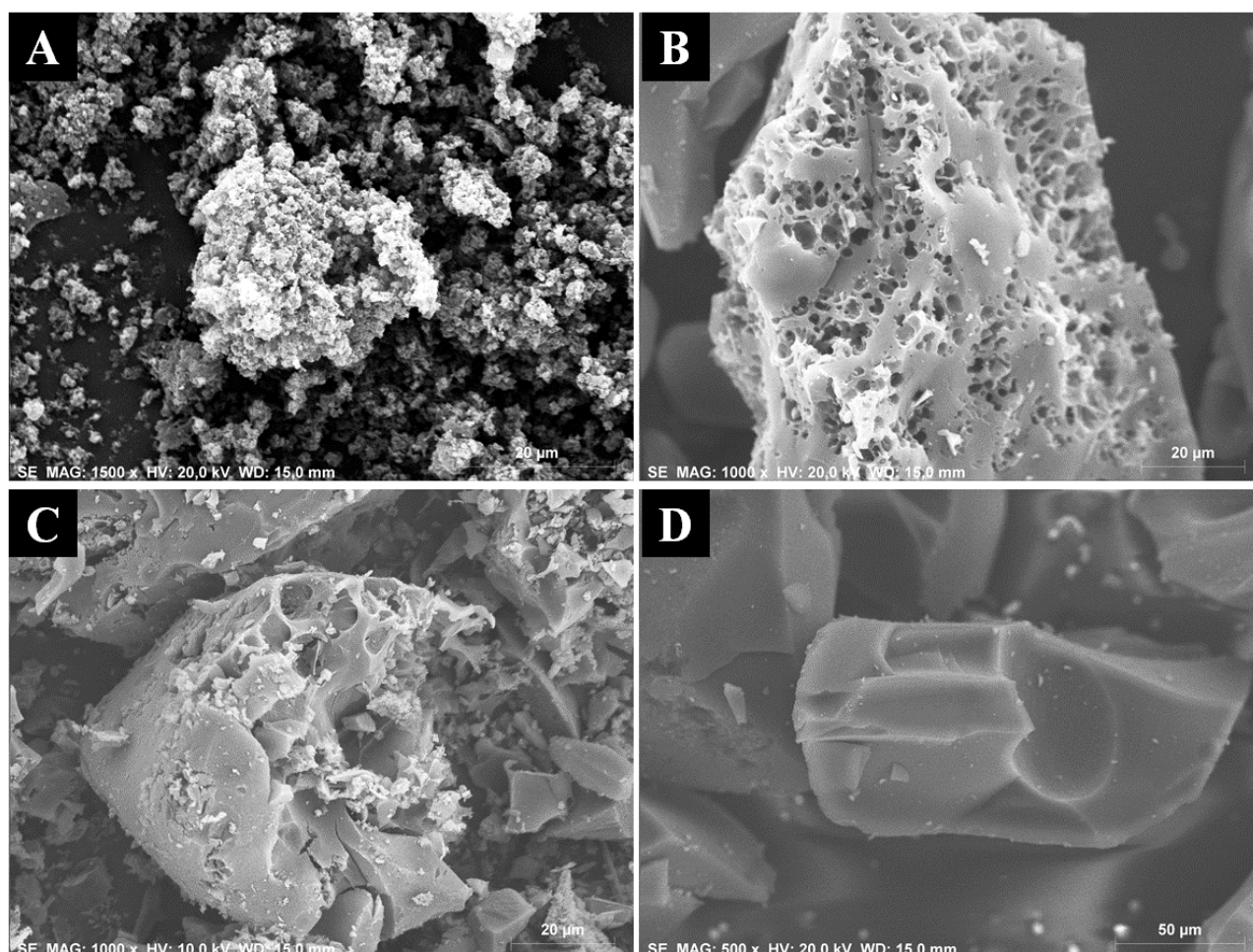
Figure 3.1a-d confirmed the PANi doping by different anions after polymerization. During oxidation, the nitrogen atoms between quinonoid and benzenoid rings are protonated and a positive charge emerged in the polymer backbone, which is compensated by the negative charge of the anion, characterizing the polymer doping. Depending on the polymerization conditions, PANi may be more or less oxidized, varying from leucoemeraldine (fully reduced) to pernigraniline (fully oxidized). Nevertheless, the emeraldine state (approximately 50% oxidized) is commonly obtained for the most of the synthesis conditions reported in literature. [48] The presence of quinonoid and benzenoid rings determined by FTIR is an evidence that the polymer has oxidized and reduced units, thus indicating an intermediate oxidation state between leucoemeraldine and pernigraniline. The oxidation state probably plays an important role on the polymerization yield because the doping level directly depends on the oxidation state. The higher the oxidation state the higher the doping. Moreover, the anion volume may cause steric hindrance and have influence on the doping process. [48]

**Figure 3.1.** Infrared spectra of PANi doped with different anions (A) and schematic representation of the anion doping: (B)  $\text{Cl}^-$ , (C)  $\text{PTS}^-$ , (D)  $\text{DBS}^-$ , and (E)  $\text{PSS}^-$



### 3.3.2.2. Morphology

The different morphologies obtained for doped PANi after carbonization and activation are shown in Figure 3.2. The size and shape of the AC particles varied according to the dopant employed. The PAC/Cl particles (Fig. 3.2a) were smaller and presented an irregular granular shape, similar to the morphology reported by Yan *et al.*[29]. The morphology of PAC/Cl retains the original morphology of the precursor PANi/Cl.[29] PAC/PTS and PAC/DBS (Fig. 3.2b and 3.2c) particles were larger and smoother than those of PAC/Cl, presenting also small cavities and sponge-like shape. PAC/PSS (Fig. 3.2d) also presents smooth surface, but unlike PAC/PTS and PAC/DBS, no cavities were observed. Similarly to PAC/Cl, the PAC/PSS also retains the same precursor morphology after carbonization and activation.[37] It is important to point out that the PANi morphology strongly depends on the method and solvent used for the synthesis [57] and the PAC characteristics depends directly on its precursor.[29]

**Figure 3.2.** SEM images of (A) PAC/Cl, (B) PAC/PTS, (C) PAC/DBS, and (D) PAC/PSS

### 3.3.2.3. Elemental analysis and surface groups

Elemental analysis and surface composition near the surface region (< 5 nm) obtained by quantitative XPS analysis, are presented in Table 3.1, including as reference one sample prepared without KOH activation, referred to PC/Cl. It can be observed that the PACs are mainly composed by carbon and oxygen. As expected, the oxygen content increased after activation with KOH since the hydroxyl ion present in KOH is a strong oxidant.[44]

The deconvoluted XPS core-level spectra of C 1s, shown in Figure 3.3, indicate that about 70% of the carbon is present in form of aromatic structures (component at 284.4 eV, ~60% of the peak area) and aliphatic C-H groups at 285.3 eV (~10%). The introduction of oxygen surface groups in the carbon matrix was reported to be beneficial for the process of electrosorption mainly due to the increase of wettability[58] and the displacement of the potential of zero-charge ( $E_{pzc}$ ) of the electrode.[59] The analysis of the fitted C 1s and O 1s

spectra showed that surface oxygen groups of carboxylic acid (-COOH), found at 289.3 eV for C 1s and 533.7 eV for O 1s, were present in all materials, however to a lower extent in PAC/DBS (Fig. 3). On the other hand, phenolic (C-OH) and/or ether (C-O-C) groups at 286.4 eV (C 1s) and 532.3 eV (O 1s) were most abundant in PAC/PTS and PAC/DBS, while carbonyl groups (C=O) at 287.9 eV (C 1s) and ~531 eV (O 1s) were present in all materials.[30,36] Finally, chemisorbed water was detected in all samples at about 535.5 eV (O 1s).[43] It has been suggested that carbonyl groups are electrochemically inert and their main effect is in the shift of the  $E_{pzc}$ . [60] In contrast, phenolic and carboxylic acid groups are responsible for a polar and thus hydrophilic behavior of the electrode.[61] Oxygen polar surface groups were observed in different amounts in PAC/PTS (7.3 at.%), PAC/PSS (6.1 at.%), PAC/DBS (5.6 at.%), and at lower level at PAC/Cl (4.9 at.%). These polar groups are important because they enhance hydrophilicity and wettability, which has a direct impact improving the electrode capacitance and performance for CDI since the access of water and ions to the active sites of the electrode will be facilitated, hence allowing better EDL formation.[58]

The presence of nitrogen surface groups in PAC introduced by the presence of nitrogen in the PANi precursor must also be considered due to the reasons aforementioned. However, according to Table 3.1, the content of nitrogen after activation was relatively low (<1 at.%). As an attempt to understand why the concentration of nitrogen was drastically reduced after activation, a XPS analysis of PANi/Cl after carbonization (PC/Cl) was performed. Table 3.1 indicates that the amount of nitrogen was significantly higher prior activation, indicating that KOH is probably eliminating N groups from the carbon matrix at high temperatures. This result is in accordance with those obtained by Zhu *et al.*, [44] which observed that during the pre-carbonization step at 500 °C the N groups were firstly released. Studying the activation at 700 °C and increasing the ratio of carbon and KOH from 1:2 to 1:4 (wt./wt.) these authors observed drastic reduction of the N content from 5.3 at. % to 0.9 at.%, which is a similar value found in this work. On the other hand, when the ratio of carbon and KOH was reduced to 1:1 (wt./wt.), Zhu *et al.* [44] observed an increase of the N content from 0.9 at.% to 5.3 at.%, indicating that KOH reacts preferentially with C atoms. Zhang *et al.* [43] also observed a reduction in N content when the ratio of carbonized PANi and KOH was increased from 1:2 to 1:4 during activation. It seems that the amount of KOH employed during the activation step plays an important role to control the amount of N-groups in the AC structure. On one hand, increasing the amount of KOH leads to high SSA and pore volume, [43,44] while it seems to eliminate N-groups.

The fitted N1s spectra (Fig. 3.3) shows that the most intense component of the PAC/Cl, PAC/PTS and PAC/PSS samples, located at 400.1 eV, is related to pyrrole and pyridine sites, while PAC/DBS presents pyridinic-like nitrogen structures (C=N-C) at 398.2 eV as the strongest contribution.[21] Furthermore, the high-energy tail of the N 1s spectra indicates the presence of traces of  $-N^+O^-/Cl^-$  structures at  $\sim 532$  eV, O-N=O groups ( $\sim 405$  eV) and possibly also quaternary nitrogen reported to be located at 401.4 eV. The first one is related, according to Figure 3.1, to a residual contribution of PANi doping sites, identified also in the Cl 2p (198.1 eV) and S 2p (168.7 eV) spectra (Fig. 3.3), while the O-N=O groups are probably formed during the KOH activation process. Evidence for the presence of traces of potassium in the samples was found in the tail of the C 1s spectra, showing the presence of the K  $2p_{3/2} / 2p_{1/2}$  spin-orbit pair at 293.3 eV and 295.7 eV, respectively. At this point, it is important to note that compared with other materials the PAC/PTS electrode showed the highest fraction of phenolic and/or ether groups (C 1s), pyrrole and pyridine nitrogen groups and residual  $-N^+O^-$  sites (N 1s), as well as the highest proportion of chemisorbed water (O 1s), suggesting a distinct nature of this material.

**Table 3.1.** Elemental analysis and atomic composition of the near surface region obtained by XPS for PAC doped with different anions

	Elemental analysis (at.%)					Surface elemental composition (at.%)				
	C	H	N	S	O	C 1s	N 1s	O 1s	S 2p	Cl 2p
<b>PAC/Cl</b>	87.9	0.66	0.88	0.08*	10.48	90.4	0.6	8.6	0.1	0.3
<b>PAC/PTS</b>	83.9	1.52	1.01	0.38	13.19	87.6	0.8	10.7	0.8	0.1
<b>PAC/DBS</b>	81.6	0.59	0.68	0.80	16.33	88.7	0.8	9.8	0.5	0.2
<b>PAC/PSS</b>	88.8	0.33	0.69	0.46	9.72	89.7	0.9	8.9	0.5	0.2
<b>PC/Cl</b>	-	-	-	-	-	86.4	5.5	7.8	0.1	0.2

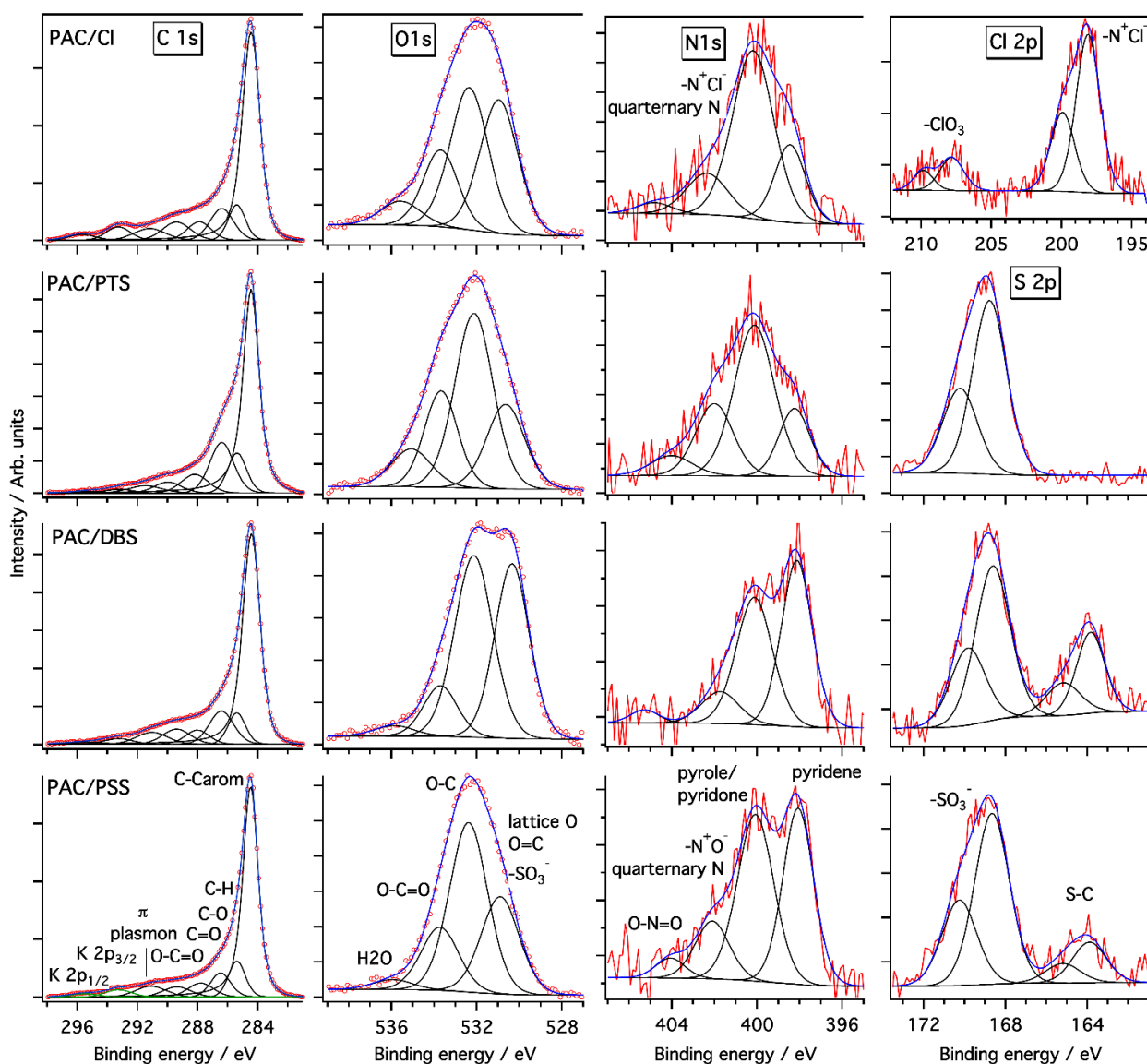
\* Under the precision of the equipment

Graphitic (or quaternary[21]) nitrogen is formed at high temperatures in a process that replaces carbon by nitrogen atoms in the activated carbon matrix, thus leading to an enhancement of the conductivity which could be improve the electrosorption process.[21,25,62] On the other hand, pyridine- and pyrrole-like nitrogen are located at the edge of the carbon matrix and are responsible for the pseudocapacitive effect which improves the total capacitance of the electrode and increases the SAC of the electrode.[62] Furthermore, the introduction of



N could generate defects inside the carbon matrix, such as the identified residual doping sites, which would increase the SSA and improve the ability of charge-transfer inside the carbon matrix.[22] In conclusion, it seems that the main contribution of nitrogen groups for all PACs would be the introduction of pseudocapacitance due to the presence of pyridine- and pyrrole-like nitrogen.

**Figure 3.3.** Deconvoluted high resolution XPS C 1s, O 1s, N 1s, Cl 2p and S 2p spectra of PAC/Cl, PAC/PTS, PAC/DBS and PAC/PSS



#### 3.3.2.4. Textural properties

Figure 3.4a shows the N<sub>2</sub> adsorption-desorption isotherms for the different PACs. All activated carbons have a type I isotherm according to IUPAC classification,[63] indicating the

predominance of microporous structure. The type H4 hysteresis of PAC/Cl and PAC/DBS at higher pressures ( $P/P_0 > 0.5$ ) indicates a considerable contribution of mesopores.

The pore size distribution (PSD) is shown in Figure 3.4b. In accordance with the isotherms, PAC/DBS showed most part of pores with diameters larger than 2 nm, confirming the predominance of mesopores in this material. According to the IUPAC classification, micropores are related to pore diameters lower than 2 nm, mesopores as pores between 2-50 nm, and macropores as pores beyond 50 nm.[63] Thus, PAC/DBS was the only material that could be classified as a mesoporous material while all other PACs present their main pore contributions under 2 nm.

**Figure 3.4.** (A) Isotherms of  $N_2$  adsorption-desorption; (B) PSD. Inset: Relative cumulative pore volume distribution ( $V/V_T$ )

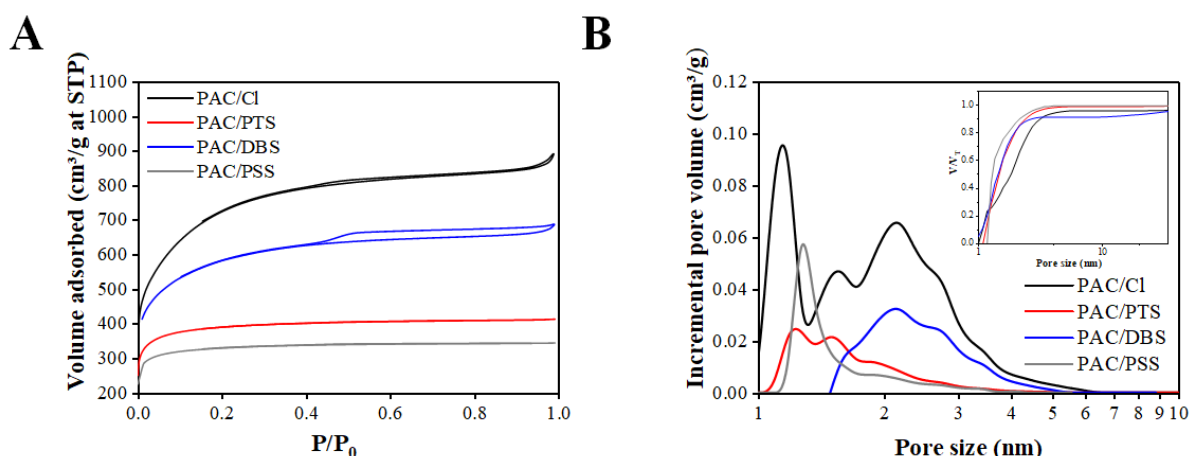


Table 3.2 displays the textural properties determined from nitrogen adsorption-desorption isotherms shown in Figure 3.4a. As previously hypothesized, the use of different dopants for PANi preparation had a strong effect on SSA, micropore ( $V_{mic}$ ) and mesopores ( $V_{mes}$ ) volumes of the PACs.

The PAC/Cl presented not only the highest value of SSA ( $2652 \text{ m}^2/\text{g}$ ), but also the highest volume of pores ( $1.38 \text{ cm}^3/\text{g}$ ) and 23% of mesopores. This value of SSA was even higher than that obtained by Yan *et al.*[29] ( $1976 \text{ m}^2/\text{g}$ ) using PANi/Cl synthesized under higher acid (1.0 mol/L) and lower oxidant (0.25 mol/L) concentrations. The value of SSA obtained in this work for PAC/Cl was also very close to that obtained by Qiu *et al.*[65] ( $2923 \text{ m}^2/\text{g}$ ) for a composite of PANi/Cl and carbon nanotubes prepared under the same activation conditions. This high SSA could be ascribed to pores generated by Cl volatilization in the carbonization

step at high temperature (850 °C), which was confirmed by the low content of chloride after carbonization (PC/Cl) or activation (PAC/Cl) (Table 3.1). The pore volume was further increased by the KOH activation, resulting in large SSA.

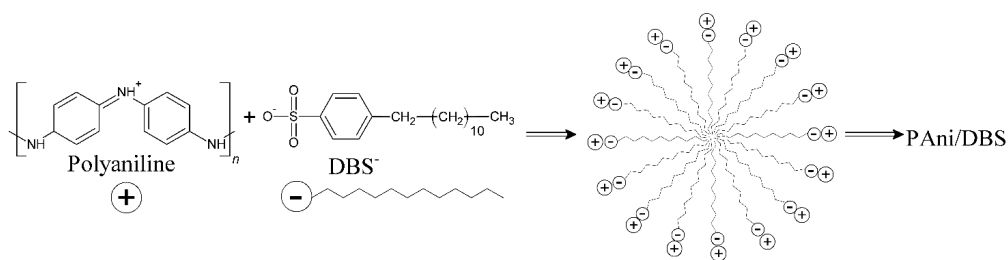
**Table 3.2.** Textural properties of the PAC doped with different anions, including the commercial activated carbon reference (CAC)

	SSA <sub>BET</sub> (m <sup>2</sup> /g)	V <sub>T</sub> (cm <sup>3</sup> /g)	V <sub>mic</sub> (cm <sup>3</sup> /g)	V <sub>mes</sub> (cm <sup>3</sup> /g)	% V <sub>mes</sub>
<b>PAC/Cl</b>	2652	1.38	1.06	0.32	23
<b>PAC/PTS</b>	1484	0.64	0.59	0.05	8
<b>PAC/DBS</b>	2041	1.05	0.44	0.61	58
<b>PAC/PSS</b>	1268	0.53	0.50	0.03	6
<b>CAC</b>	2107*	1.07	-	-	-

\* Data obtained from Aslan *et al.* [64]

Large SSA was also observed for PAC/DBS, however with a considerably higher mesopore volume fraction (~60%) which could be related to micelle formation during polymerization,[48] which would induce the formation of large pores after carbonization. Unlike the other anions used in this study, DBS<sup>-</sup> is a voluminous molecule with polar and non-polar sites, which allows micelle formation according to Figure 3.5. These micelles would act as a template for mesopore formation after carbonization.

**Figure 3.5.** Scheme of micelle formation prior to PANi/DBS polymerization



Differently of PAC/Cl and PAC/DBS, PAC/PTS and PAC/PSS showed lower SSA with a higher contribution of micropores. Although PTS<sup>-</sup> and especially PSS<sup>-</sup> are also large molecules, they are not likely to form a micelle structure and, consequently, high mesopore formation was not expected. These results emphasize the importance of PANi dopants as template agents defining the textural characteristic of activated carbons. Although Gavrillov *et*

*al.*[36] have studied carbonized PANi doped with 3,5-dinitrosalicylic and 5-sulfosalicylic acid for supercapacitors,[36] their influence as a template for activated carbons have yet not been explored. Moreover, in contrast with this work, the values of SSA obtained by Gavrilov *et al.*[36] (300-500 m<sup>2</sup>/g) were significantly lower, which demonstrates the importance of the activation step. Even so, Gavrilov *et al.* also observed the important effect of the dopants on the pore structure, SSA and nitrogen content of the carbonized PANi.

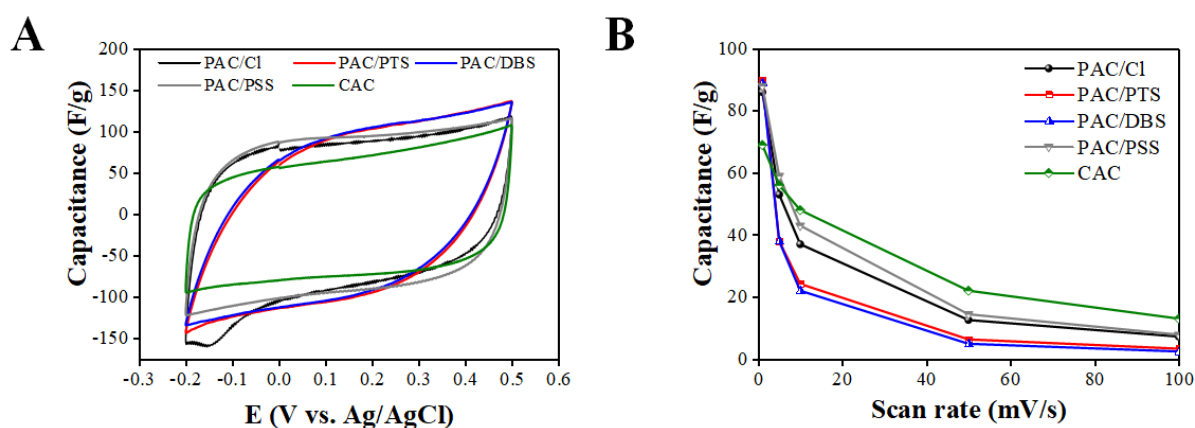
### 3.3.2.5. Electrochemical characterizations

As a first attempt to compare the different electrodes, cyclic voltammetry experiments were performed in order to analyze the capacitance and kinetics of the carbon electrodes. In this case, a more concentrated electrolyte was used in order to prevent any ion diffusion limitation and allow the comparison with other results reported in literature. Figure 3.6a shows the CVs measured at 1.0 mV/s in NaCl 0.2 mol/L, which is the typical concentration used in CDI literature for electrochemical characterizations. At this scan rate, the CVs for PAC/Cl, PAC/PSS and CAC showed a quasi-rectangular shape, characteristic of capacitive and easily polarized materials.[8,66] This characteristic could also be observed for PAC/PTS and PAC/DBS, however with some resistivity indicated by the distortion of the CV curve.[66] Table 3.3 displays the specific capacitance ( $C_{cv}$ ) values calculated using Equation 3.2. Surprisingly, all PACs exhibited similar capacitances (85-90 F/g), although the carbons presented distinguished characteristics. For instance, despite the highest SSA and percentage of mesopores of PAC/Cl and PAC/DBS, the electrode capacitances were quite similar to PAC/PTS and PAC/PSS, which are mostly composed by micropores. In this case, the surface groups probably played the most important role determining the capacitance of the electrodes. PAC/PTS and PAC/PSS had the major contribution of oxygen polar surface groups (phenol, ether and carboxylic groups), which probably enhanced the electrode wettability. In addition, PAC/PSS had major contribution of pseudocapacitive nitrogen surface groups. On the other hand, the CAC presented the lowest value of capacitance despite of its good capacitive behavior. It is also important to point out that the highest capacitance obtained in this study was very close to those obtained by other authors in literature. For instance, using similar electrolyte, Rasines *et al.*[6,67] obtained values of capacitance at 0.5 mV/s of 84 F/g and 97 F/g using nitrogen-doped carbon aerogel and carbon black-modified mesoporous, respectively. These values were very close to 90 F/g obtained for PAC/PTS at scan-rate of 1.0 mV/s.

**Table 3.3.** Capacitance values determined from CV curves, charge-discharge and EIS measurements

	$C_{cv}$ (F/g)	$C_{cd}$ (F/g)	$C_{eis}$ (F/g)
<b>PAC/Cl</b>	87	69.3	121.5
<b>PAC/PTS</b>	90	121.0	122.9
<b>PAC/DBS</b>	89	118.6	125.0
<b>PAC/PSS</b>	88	108.4	113.9
<b>CAC</b>	69	84.5	80.0

**Figure 3.6.** (A) Cyclic voltammograms of PAC and CAC electrodes. Scan-rate: 1.0 mV/s; electrolyte: NaCl 0.2 mol/L; (B) capacitance as a function of the potential scan rate



CVs at different scan-rates were also carried out in order to observe the effect of mass transfer for different electrodes (Fig. 3.6b). As expected, the faster the scan rate the lower capacitance due to a diffusion limited ion transfer to the electric double layer.[8] The capacitance drop for PAC/Cl, PAC/PSS, and CAC was less pronounced when compared to the sharp drop in capacitance observed for PAC/PTS and PAC/DBS. Besides the mass transfer resistance, another possible explanation for this trend could be the higher surface conductivity of PAC/Cl, PAC/PSS, and CAC electrodes, which have a direct effect on the electric field developed in the polarized electrode. Accordingly, the higher the electrode resistivity the lower the electric field; therefore, the lower the capacitance when the scan rate is faster. Consequently, PAC/PTS and PAC/DBS, which were the most resistive electrode, showed the highest capacitance drop.

Galvanostatic charge-discharge experiments were performed applying a current density of 0.4 mA/cm<sup>2</sup> (or ~0.13 A/g). The charge-discharge curves (Fig. A3.2) displays that

PAC/PSS and CAC showed a very triangular shape which indicates good reversibility and low  $IR_{drop}$  (0.02 V for both electrodes).[21,68] PAC/PTS and PAC/DBS showed the highest  $IR_{drop}$  (0.09 V and 0.12 V, respectively) compared with PAC/Cl (0.06 V). These results are in agreement with conclusions obtained from the CV analysis regarding to the shape of the voltammograms and confirm that PAC/PSS and CAC can be easily polarized, while PAC/DBS is the most resistive electrode. The  $IR_{drop}$  is a combination of different resistances in series including the contact between electrode and current collector, solution resistance, electrode resistivity and diffusion resistance.[68] Considering that all charge-discharge measurements were performed in the same three-electrode cell, it can be concluded that the difference in the  $IR_{drop}$  results from the major contribution of the electrode resistivity and ion diffusion resistance in the carbon matrix.

Although the capacitance determined from charge-discharge ( $C_{CD}$ ) experiments were higher than the calculated from  $C_{CV}$  (except for PAC/Cl), the trend in capacitance observed for the different electrodes using the two techniques was the same. As in the CV experiments, PAC/PTS showed highest capacitance, followed by PAC/DBS and PAC/PSS. This result indicates that PAC/PTS would be the best material in terms of charge storage.

Differently of the other techniques, EIS measurements allow to evaluate both capacitance and series resistances in the electrode cell. The Nyquist plots obtained using EIS measurements for PACs and CAC are displayed in Figure 3.7a. The shape of the curves are typical of electrochemical supercapacitors [69] and present two main regions: (1) the charge-transfer region that is ascribed to the double-layer capacitance, represented by the semi-circle observed at high-frequencies and limited by the material conductivity and electrosorption kinetics and (2) mass-transfer controlled region, represented by the linear line obtained at low-frequencies.[70] Using the Nyquist plot, it is possible to measure the electric contact resistance ( $R_{\Omega}$ ) of the electrode (current collector and electrolyte resistances) and the charge-transfer resistance ( $R_{CT}$ ), which is an intrinsic property of the AC electrode. The value of  $R_{\Omega}$  and  $R_{CT}$  are obtained from the first and second intersection of the semi-circle with the abscissa, respectively.[70] The values of the resistances are displayed in Table 3.4. As expected, all values of  $R_{\Omega}$  were very similar because the same three-electrode cell was used for all EIS measurements. On the other hand, the values of  $R_{CT}$  were quite different and express the differences in textural and electrochemical properties of the electrode materials. For instance, the  $R_{CT}$  for PAC/DBS was 11-times higher than PAC/PSS. This trend is in agreement CV and charge-discharge results. Thus, despite the high SSA and mesoporosity of PAC/DBS, these

properties were not enough to compensate the effect of its low conductivity. In contrast, PAC/PSS had the lowest SSA and mesopore ratio, and even so, presented a capacitance similar to other PACs. Similar trends were also observed by Xiong *et al.*[71] studying a PANi composite for supercapacitors.

Comparing the  $R_{CT}$  values in Table 3.4 with those reported in literature, e.g., 4.58  $\Omega$  for a N-doped copolymer,[62] it can be verified that the values obtained in this work are relatively high, except for PAC/PSS (2.3  $\Omega$ ).

**Figure 3.7.** Nyquist plot (A) and capacitance as a function of the frequency (B) for PAC and CAC electrodes. (C) Modified Randle equivalent circuit. Electrolyte: NaCl 0.2 mol/L; potential: 0.0 V; AC amplitude: 10 mV

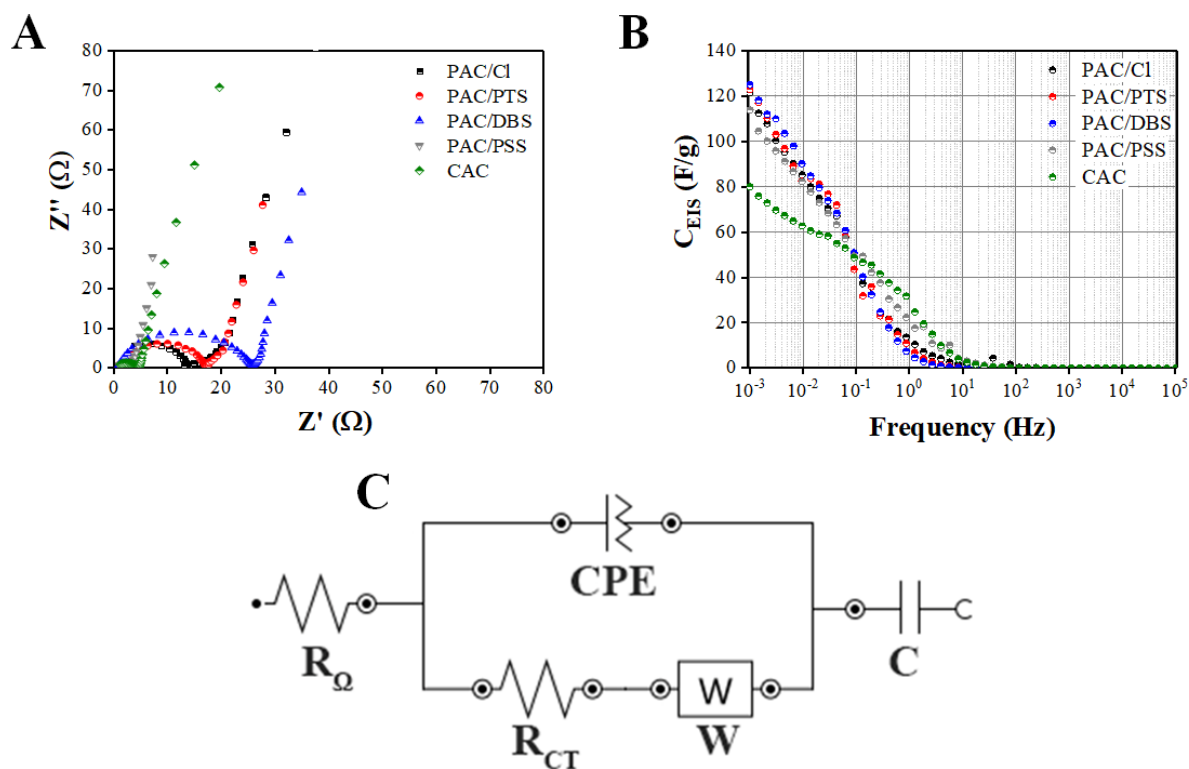


**Table 3.4.** EIS parameters from the Nyquist plot and the modified Randle equivalent circuit

	$R_{\Omega}$ ( $\Omega$ )	$R_{CT}$ ( $\Omega$ )	$A_0$ (mS)	$Q^0$ ( $\mu\text{S}\cdot\text{s}^N$ )	$N$	$C_C^*$ (mF/g)	$C_d$ (F/g)
PAC/Cl	0.71	14.7	260	1.23	0.86	0.02	162.0
PAC/PTS	0.95	16.5	790	226	0.82	2.10	174.7
PAC/DBS	0.86	25.1	1000	139	0.84	1.64	156.3
PAC/PSS	0.79	2.3	2170	320	0.75	0.58	125.7
CAC	0.80	4.0	1520	484	0.65	0.59	82.0

\* $C_C$  was calculated based on the values of  $R_{CT}$ ,  $Q^0$  and  $N$

A method widely used to describe the resistive and capacitive components of carbon electrode is the equivalent circuit fitting the Nyquist plots. The modified Randle equivalent circuit shown in the Figure 3.7c was successfully used to fit all plots of Figure 3.7a, as can be verified in Figure A3.3. The values of  $R_Q$  and  $R_{CT}$  were identical with those already presented in Table 3.4. The *CPE* element was used because in double layer capacitors a perfect semicircle ascribed to an ideal capacitor is seldom observed. The non-ideality of the double layer capacitor is typical of electrochemical charging processes and may be related to the non-uniformity of electrode thickness, variation of the microscopic charge-transfer rate, adsorption processes, or surface roughness.[72] The values of  $Q^0$  and  $N$  were obtained from the *CPE* impedance described by Equation 3.8, which is a modification of the Equation 3.4:

$$Z'' = \frac{1}{(j\omega)^N Q^0} \quad (3.8)$$

In this Equation,  $j$  is the imaginary number,  $N$  is a constant in the range of  $0 \leq N \leq 1$  and  $Q^0$  ( $S \cdot s^N$ ) has the numerical value of admittance at  $\omega = 1 \text{ rad s}^{-1}$ . When  $N = 1$ ,  $Q^0 = C_{EIS}$  and the Equation 3.9 becomes exactly the same Equation 3.4. However, as can be observed in Table 3.4,  $N$  was always lower than unit, reaching the lowest value for CAC. In order to obtain the capacitance associated to the *CPE* ( $C_C$ ), Equation 3.9 [73] was used in which  $m_{WE}$  is the mass of the working electrode.

$$C_C = \frac{(Q^0)^{\frac{1}{N}} (R_{CT})^{\frac{(1-N)}{N}}}{m_{WE}} \quad (3.9)$$

The  $C_C$  is the capacitance at the interface electrolyte/electrode at high frequencies,[74,75] while the capacitance of the capacitor element ( $C_d$ ) in the equivalent circuit is associated to the capacitance developed inside the micropores of the carbon electrode.[74,76] According to Table 3.4, it can be observed that PAC/PTS has the highest values of  $C_C$  and  $C_d$  among the electrodes studied; which  $C_d$  represents the main contribution to the total electrode capacitance.

Another component used to describe the EIS spectra is the Warburg element ( $W$ ), which is a diffusion element used to describe the effect of ion migration in the interior of pores of the carbon film.[74,77] The Warburg element was associated in series with the  $R_{CT}$  because



the Warburg region is located between the semicircle and the spike in the Nyquist plot.[78] The element  $A_0$  displayed in Table 3.4 was obtained from the circuit fitting for the Warburg element and represent the admittance, which is the inverse of the Warburg impedance. The higher  $A_0$  the higher the conductivity for the ion diffusion inside the pores. According to Table 3.4, while PAC/PSS showed the highest admittance (or the lowest Warburg resistance), PAC/Cl showed the lowest values.

Figure 3.7b shows the capacitance obtained using EIS measurements as function of frequency. At high frequencies, there was a predominance of the ohmic resistance, and the capacitances of the electrode materials were very low. This is expected since the ions do not have enough time to reach the pores and be stored in the EDL. As the frequency decreases they are able to reach the micropores, thus increasing significantly the capacitance, which reaches a maximum value at the lowest frequency.[79]

### 3.3.3. Electrosorption experiments

Desalination experiments were performed in a batch operational mode at different cell voltages ( $E_{\text{cell}}$ ). The electrode performance at 1.2 V and 1.4 V (Fig. 3.8a and b, respectively) is displayed in terms of specific adsorption capacity (SAC) against time for PAC and CAC electrodes. It can be observed that an increase of the applied voltage from 1.2 V to 1.4 V led to an increase of the SAC for PAC/PTS, PAC/PSS, and CAC electrodes. This enhancement can be ascribed to an EDL thickness reduction at higher voltages, which prevents the EDL to overlap, and consequently, increases the ions storage in the micropores.[80] In contrast, for PAC/Cl and PAC/DBS electrodes, SAC decreased applying 1.4 V, what could suggest the occurrence of Faradaic reactions that interfere in the conductivity measurement due to the release of new ionic species (Fig. 3.8b).[5] The generation of protons due to water electrolysis or carbon electrode oxidation has been often reported in the CDI literature.[81–86] In addition, the occurrence of certain species such as  $\text{H}_2\text{O}_2$  or  $\text{ClO}_3^-$  has been also identified in electrosorption experiments. In these studies, the likelihood of inducing Faradaic reactions has been demonstrated to rise with the increase of the applied cell potential. Moreover, higher concentrations of these species were found when higher cell voltages were applied, producing, as a consequence, a more disruptive effect on the conductivity measurements.[87]

The different response of these electrodes to the application of relatively high voltages (1.4 V) could be attributed to two main causes: (i) the cell setup could introduce a series of resistances between the pair of electrodes such as the electric contact current between

collector/substrate, flowing channel, and electrolyte resistivity. These resistances could be responsible for a potential drop throughout the cell and this would reduce the electrode potential preventing in this fashion the occurrence of faradaic reactions.[25,88] (ii) Another hypothesis is based on the electrode electrochemical stability and the shifting of the electrode potential due to the presence of certain surface groups that might avoid or promote the occurrence of faradaic reactions.[5] In this sense, Cohen *et al.*[84] and Lado *et al.*[87] showed how the presence of surface oxygen groups shifted the anode potential of the carbon electrodes inducing the oxidation of the carbon electrode, proton generation and pH drop.

In the present study, all the experiments were performed using the same CDI cell configuration and, consequently, cell resistances were always the same. Therefore, considering that PAC/PTS, PAC/PSS and CAC showed higher electrochemical stability at higher cell voltages, the authors attribute the differences in SAC to the potential shifting that induced the occurrence of faradaic reactions.

Comparing the values of capacitance shown in Table 3.3 with SAC values from Table 3.5, it can be observed that only the charge-discharge technique was able to predict the electrosorption trend in terms of SAC, i.e.,  $C_{CD, PTS} > C_{CD, PSS} > C_{CD, DBS} > C_{CD, CAC} > C_{CD, Cl}$  and, consequently,  $SAC_{PTS} > SAC_{PSS} > SAC_{DBS} > SAC_{CAC} > SAC_{Cl}$ . These results suggest that this technique would be rather used to predict the performance of the carbon electrodes for CDI. Although CV capacitance (and  $C_{EIS}$  as well) has been frequently used to predict the electrode performance in CDI, in this case this technique failed. Surprisingly, PAC/Cl had the worst electrosorption performance despite its high surface area (Table 3.2), which can be explained by the lower content of polar oxygen groups (Table 3.1). As discussed in section 3.3.2.3, polar oxygen groups play a paramount influence on the electrode wettability and, consequently, on the electrode performance.

The kinetic constant of pseudo first order ( $k_l$ ) of the process carried out using the different electrodes was evaluated by the fitting of the electrosorption curves (Fig. 3.8). PAC/Cl was by far the electrode that showed the lowest SAC but with fast electrosorption kinetics, which can probably be ascribed to its high conductivity (Table 3.4), and large exposed area (Fig. 3.2a). This same trend was also observed for CAC, which presented the highest conductivity among all ACs and displayed the highest  $k_l$  at 1.2 V. On the other hand, the lowest value of SAC observed for PAC/Cl can be attributed to the deficiency of polar surface groups (phenol, ether and carboxylic), which increases hydrophobicity (low wettability) and thus prevent the access of ions to the micropores. Furthermore, its lowest pyrrole- and pyridinic-

like nitrogen content (Table 3.1 and Fig. 3.3) prevents pseudocapacitive processes, which would contribute to the lowest value of SAC of PAC/Cl. All other PAC electrodes showed similar values of SAC ranging from 12 to 15 mg/g. It is interesting to note that despite the high SSA and mesopore ratio of PAC/DBS, the highest content of polar and pseudocapacitive surface groups of PAC/PTS and PAC/PSS, respectively, seems to provide easy access to the electrosorption sites, which resulted in the best performance of these electrodes in terms of SAC.[58] In the case of PAC/PTS, a clear evidence of its hydrophilicity is the high proportion of chemisorbed water demonstrated by its O1s XPS spectra. Therefore, the synergetic effect of different material characteristics such as active surface groups, electric properties and texture might be responsible for determining the electrode performance.

**Figure 3.8.** SAC of PAC and CAC electrodes for desalination at 1.2 V (A) and 1.4 V (B)

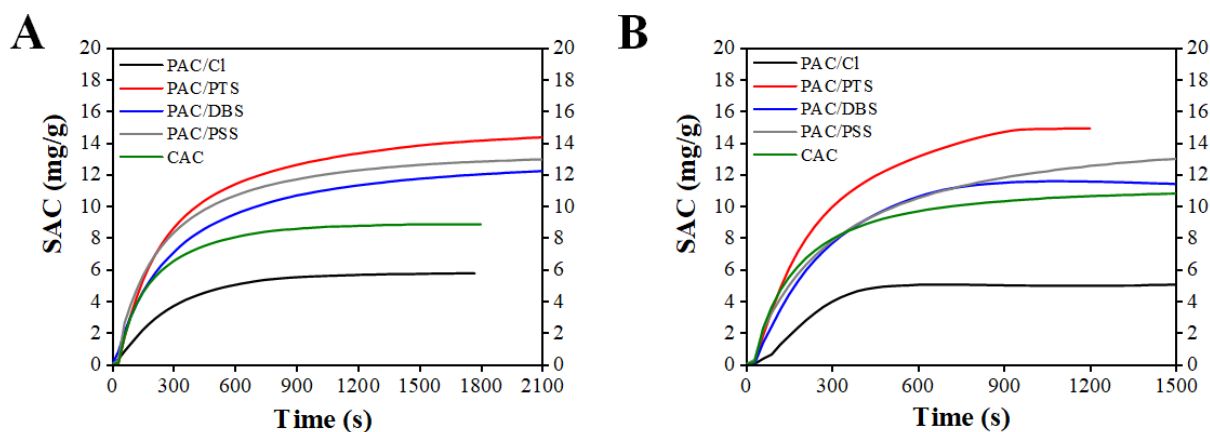
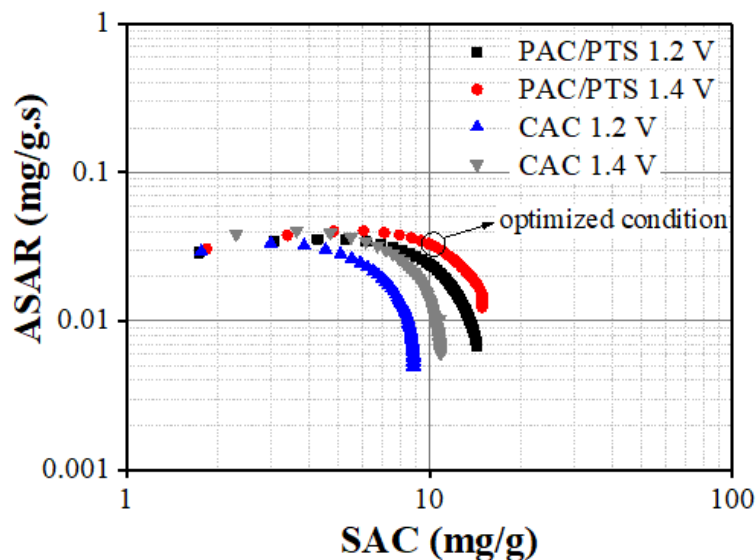


**Table 3.5.** Electrosorption parameters  $Q_E$ ,  $\eta$ , SAC, and  $k_1$ , of the PAC and CAC electrodes

$E_{cell}$	Electrode	SAC (mg/g)	$k_1$ ( $\times 10^{-3} s^{-1}$ )	$Q_E$ (%)	$\eta$ (J/mg)
1.2 V	PAC/Cl	5.8	3.3	44.5	6.9
	PAC/PTS	14.3	2.6	81.3	3.8
	PAC/DBS	12.6	2.1	74.1	7.6
	PAC/PSS	13.1	2.7	86.2	4.1
	CAC	8.9	4.4	69.7	4.2
1.4 V	PAC/Cl	5.1	5.2	32.8	12.0
	PAC/PTS	14.9	3.8	89.6	4.2
	PAC/DBS	11.7	3.9	71.5	5.1
	PAC/PSS	13.7	2.3	84.5	5.2
	CAC	10.9	4.1	73.0	4.7

The electrosorption kinetics is another important characteristic that influences the operation of a CDI cell. As the desalination process presupposes several electrosorption and regeneration cycles, the water recovery is directly affected by the time required for sorption and desorption. CDI Ragone Plot is widely applied as important tool to evaluate simultaneously the kinetics and electrosorption capacity by using the average salt adsorption rate (ASAR) and SAC, respectively. According to Figure 3.9, PAC/PTS presents the highest values of SAC compared to CAC. The points displayed in Figure 3.9 represent a complete electrosorption cycle indicating how SAC and ASAR varied with time. The curves displaced in the upper-right corner of the Ragone plot indicates the better electrode performance.[89] Although both electrodes display slightly similar electrosorption kinetics, PAC/PTS outperforms CAC in terms of capacity, especially at 1.4 V. The optimized condition using PAC/PTS was achieved for SAC 9.9 mg/g and ASAR 0.033 mg/g.s at 1.4 V, after 5 min of the beginning of the electrosorption process.

**Figure 3.9.** ASAR vs. SAC for PAC/PTS and CAC at 1.2 and 1.4 V



Besides SAC and the Ragone plot, the desalination process was also evaluated regarding to charge efficiency ( $Q_E$ ) and specific energy consumption ( $\eta$ ), which are parameters that indicate whether the charge supplied to the CDI system has being effectively used for the electrosorption process and how much energy is required per mass of salt removed (Equation 3.7), respectively. In order to properly evaluate  $Q_E$ , only the current effectively used for electrosorption was used in Equation 3.6, i.e., the leakage current, which is a parasitic process

commonly associated to redox reactions, was subtracted from the total current.[23,58,90] In the case of  $\eta$ , the leakage current was considered since it contributes to the overall energy consumption.

Table 3.5 shows the values of  $Q_E$  and  $\eta$  obtained for the NaCl electrosorption at different cell voltages using the PAC and CAC electrodes. In all cases, the values of  $Q_E$  were lower than the 100% valid for an ideal system in which the entire charge supplied by the external source is used for ion separation of monovalent salts such as NaCl. However, due to energy losses, faradaic reactions,[91] and the presence of co-ions,[92] this value hardly reaches more than 90%.

Interestingly, PAC/PTS showed an increase in  $Q_E$  when  $E_{cell}$  was increased from 1.2 V to 1.4 V, confirming a minor contribution of faradaic reactions to the total current of this electrode. PAC/PSS and PAC/DBS had only a small drop in  $Q_E$  (2-3%), in contrast with the PAC/Cl that showed a strong decrease (12%). The charge efficiency drop observed for PAC/Cl is in accordance with the decrease of the SAC values when the applied voltage was raised from 1.2 to 1.4 V and it supports the hypothesis that faradaic reactions is the main process explaining the SAC reduction. In addition, the CDI process carried out using PAC/Cl at 1.4 V demanded almost twice more energy than at 1.2 V, which can be attributed not only to faradaic reactions but also to resistive dissipation (heat loss).[93]

Surprisingly, PAC/DBS showed a simultaneous decrease of  $Q_E$  and  $\eta$  when the cell voltage was increased. One could think that a charge efficiency drop would lead to the increase of the energy consumption, however, higher values of leakage current were measured at 1.2 V (11.2 mA) than at 1.4 V (6.4 mA), which explains the reduction of the energy consumption when the cell voltage was increased. On contrary, for CAC electrode,  $Q_E$  and  $\eta$  increased with the cell voltage, indicating that despite of the efficient use of the supplied charge to remove ions, the increase of the leakage current at 1.4 V (from 3.2 mA at 1.2 V to 3.9 mA at 1.4 V) lead to an increase of  $\eta$ . Concerning PAC/PTS, only a slight increase of  $\eta$  was observed at 1.4 V, suggesting an improved stability of this electrode material.

Another way to analyze the effect of the cell voltage on the electrode performance was proposed by Kim *et al.*[94] (Equation 3.10). Using this method, the capacitance can be obtained from charge-discharge experiments to estimate the highest value of SAC ( $D_c$ ). The ratio between the values of SAC, determined from the electrosorption experiments, and  $D_c$  is referred as capacitance efficiency ( $\varepsilon$ ).

$$D_c = 1000 \frac{C_{CD} \cdot E_{cell} \cdot M_w}{4 \cdot F} \quad (3.10)$$

In Equation 3.10,  $D_c$  is in mg/g and  $M_w$  is the molecular weight of NaCl (58.5 g/mol). As can be observed in Table A3.3, the capacitance overestimate the SAC values in all cases, what was expected since the experiments of charge-discharge were carried out in a more concentrated solution (0.2 mol/L NaCl). Moreover, capacitance measurements consider that all current have been effectively used for electrosorption, excluding the leakage current. The same reason supports the increase of  $D_c$  values when the applied voltage was boosted due to since the negative effect of the faradaic reactions on charge efficiency and SAC values were not considered by this parameter. This argument was clearly appreciated in the case of PAC/Cl electrodes, where the increase of the cell voltage led to contradictory trends. Thus, while  $D_c$  values accompanied the applied potential increment, the drop in SAC values are supported by the previous results that suggested the occurrence of faradaic reactions as the cause of the salt electrosorption decay. These factors led to the lowest  $\epsilon$  value displayed by PAC/Cl (45.9% at 1.2 V and 34.6% at 1.4 V). The same trend was observed for PAC/DBS, which exhibited low  $\epsilon$  at 1.4 V (46.4%), indicating the occurrence of faradaic reactions at this cell voltage. On the other hand, PAC/PSS and PAC/PTS showed a good correlation between  $D_c$  and SAC (58-67%). Regarding PAC/PSS, the values of SAC seems to be boosted by its high conductivity (low  $R_{CT}$ ) and pseudocapacitive surface groups, therefore this material achieved almost 70% of the value of predicted by the capacitance ( $D_c$ ).

Interestingly, except for CAC, in all cases the application of 1.4 V resulted in lower  $\epsilon$ , even for PAC/PTS. Despite the higher values of SAC observed using PAC/PTS at 1.4 V, this enhancement was not proportional to the difference estimated by  $D_c$ . This suggests that despite of SAC enhancement after increasing the voltage from 1.2 V to 1.4 V, the values of SAC were still underestimated, probably due to a minor contribution of faradaic reactions. As a final remark, CAC, unlike the other electrodes, experienced a capacitance efficiency improvement at 1.4 V, suggesting that CAC presents higher electrochemical stability at high cell voltages than the PAC electrodes. The results suggest that capacitance efficiency analysis seems to be a useful tool for estimating the faradaic reactions effect on the CDI performance at different cell voltages.

In summary, PAC/PTS gathered most of the best results required for CDI: high salt electrosorption capacity (14-15 mg/g), high charge efficiency (81-90%), and low energy consumption (3.8-4.2 J/mg). Finally, Table 3.6 compares PAC/PTS with values of SAC obtained by other authors employing different electrode materials (most of them, N-doped carbon) under similar operational conditions. The comparison reveals that PAC/PTS is among

the best electrodes regarding the electrosorption capacity, although the SAC reported for N-doped graphene electrodes surpasses the PAC/PTS; however, PANi can be easily prepared and the low-cost of the monomer with respect to the graphene materials makes PAC/PTS a promising material for CDI applications.

**Table 3.6.** SAC obtained using different carbon materials in a CDI process

Authors	Electrode material	Salt concentration (mg/L)	Cell voltage (V)	SAC (mg/g)
Gu <i>et al.</i> , 2014[21]	N-doped graphene	500	2.0	21.9
Liu <i>et al.</i> , 2015[22]	N-doped nanofiber graphene	500	1.2	11.6
Liu <i>et al.</i> , 2015[95]	N-doped carbon nanospheres	500	1.2	13.7
Porada <i>et al.</i> , 2015[23]	N-doped biomass	300	1.2	15.0
Xu <i>et al.</i> , 2015[25]	N-doped graphene	500	1.2	12.8
Xu <i>et al.</i> , 2015[96]	N-doped graphene sponge	500	1.2	21.0
Xu <i>et al.</i> , 2015[97]	Graphene sponge	500	1.2	14.6
Kumar <i>et al.</i> , 2016[9]	Carbon aerogel	500	1.2	10.5
Zhao <i>et al.</i> , 2016[68]	Hollow carbon nanospheres	500	1.4	13.0
Li <i>et al.</i> , 2016[24]	N-doped carbon sponge	500	1.2	16.1
Li <i>et al.</i> , 2016[62]	N-doped copolymer	500	1.2	13.8
Shi <i>et al.</i> , 2016[98]	Three-dimensional graphene	500	1.2	12.4
		500	1.6	17.1
This work	PAC/PTS	600	1.2	14.3
		600	1.4	14.9

### 3.4. Conclusions

In this study, new activated carbon materials have been prepared using PANi doped with different anions as precursor. By the best of our knowledge, this was the first time that different dopant anions were used as template to prepare high-performance electrodes for CDI. Structural analysis of the PAC characteristics such as morphology, SSA, conductivity and surface groups were highly dependent on the anion used for PANi doping.

Although one of the initial ideas of using PANi as precursor was to obtain an activated carbon with high nitrogen content, the activation using KOH at high temperature removed most

part of it. On the other hand, the high oxygen content in the PACs, mainly in PAC/PTS, seemed to play the most important role improving the PAC wettability by the introduction of surface polar groups such as phenolic and carboxylic groups.

Regarding to electrosorption process, PAC/PTS, PAC/PSS, and PAC/DBS showed similar removal efficiencies, while PAC/Cl presented by far the lowest value of SAC. Although PAC/PTS presented low specific surface area and mesopore ratio among the electrodes, the values of SAC (14.3 mg/g at 1.2 V and 14.9 mg/g at 1.4 V),  $Q_E$  (81.9% and 89.6% at 1.2 V and 1.4 V, respectively), and  $\eta$  (3.8 J/mg at 1.2 V) outperformed those for all the other electrodes due to its high polar surface group content. Considering simplicity and low-cost preparation of PAC/PTS, it can be considered as very promising candidate for large-scale CDI applications.

## References

- [1] M.A. Anderson, A.L. Cudero, J. Palma, Capacitive deionization as an electrochemical means of saving energy and delivering clean water. Comparison to present desalination practices: Will it compete?, *Electrochim. Acta.* 55 (2010) 3845–3856. doi:10.1016/j.electacta.2010.02.012.
- [2] F.A. AlMarzooqi, A.A. Al Ghaferi, I. Saadat, N. Hilal, Application of Capacitive Deionisation in water desalination: A review, *Desalination.* 342 (2014) 3–15. doi:10.1016/j.desal.2014.02.031.
- [3] D.V. Fix, Capacitive deionization of  $\text{NH}_4\text{ClO}_4$  solutions with carbon aerogel electrodes, 26 (1996) 1007–1018.
- [4] C. Tsouris, R. Mayes, J. Kiggans, K. Sharma, S. Yiacoumi, D. DePaoli, Mesoporous carbon for capacitive deionization of saline water, *Env. Sci Technol.* 45 (2011) 10243–10249. doi:10.1021/es201551e.
- [5] R.L. Zornitta, J.J. Lado, M.A. Anderson, L.A.M. Ruotolo, Effect of electrode properties and operational parameters on capacitive deionization using low-cost commercial carbons, *Sep. Purif. Technol.* 158 (2016) 39–52. doi:10.1016/j.seppur.2015.11.043.
- [6] G. Rasines, P. Lavela, C. Macías, M.C. Zafra, J.L. Tirado, C.O. Ania, Mesoporous carbon black-aerogel composites with optimized properties for the electro-assisted removal of sodium chloride from brackish water, *J. Electroanal. Chem.* 741 (2015) 42–50. doi:10.1016/j.jelechem.2015.01.016.



- [7] Y. Oren, Capacitive deionization (CDI) for desalination and water treatment — past, present and future (a review), *Desalination*. 228 (2008) 10–29. doi:10.1016/j.desal.2007.08.005.
- [8] G. Rasines, P. Lavela, C. Macías, M. Haro, C.O. Ania, J.L. Tirado, Electrochemical response of carbon aerogel electrodes in saline water, *J. Electroanal. Chem.* 671 (2012) 92–98. doi:10.1016/j.jelechem.2012.02.025.
- [9] R. Kumar, S.S. Gupta, S. Katiyar, V.K. Raman, S.K. Varigala, T. Pradeep, A. Sharma, Carbon aerogels through organo-inorganic co-assembly and their application in water desalination by capacitive deionization, *Carbon N. Y.* 99 (2016) 375–383. doi:10.1016/j.carbon.2015.12.004.
- [10] C.-L. Yeh, H.-C. Hsi, K.-C. Li, C.-H. Hou, Improved performance in capacitive deionization of activated carbon electrodes with a tunable mesopore and micropore ratio, *Desalination*. 367 (2015) 60–68. doi:10.1016/j.desal.2015.03.035.
- [11] S. Porada, L. Weinstein, R. Dash, A. van der Wal, M. Bryjak, Y. Gogotsi et al., Water desalination using capacitive deionization with microporous carbon electrodes., *ACS Appl. Mater. Interfaces*. 4 (2012) 1194–9. doi:10.1021/am201683j.
- [12] J.-H. Lee, H.-J. Ahn, D. Cho, J.-I. Youn, Y.-J. Kim, H.-J. Oh, Effect of surface modification of carbon felts on capacitive deionization for desalination, *Carbon Lett.* 16 (2015) 93–100. doi:10.5714/CL.2015.16.2.093.
- [13] Z.H. Huang, M. Wang, L. Wang, F. Kang, Relation between the charge efficiency of activated carbon fiber and its desalination performance, *Langmuir*. 28 (2012) 5079–5084. doi:10.1021/la204690s.
- [14] X.Z. Wang, M.G. Li, Y.W. Chen, R.M. Cheng, S.M. Huang, L.K. Pan et al., Electrosorption of NaCl Solutions with Carbon Nanotubes and Nanofibers Composite Film Electrodes, *Electrochem. Solid-State Lett.* 9 (2006) E23. doi:10.1149/1.2213354.
- [15] L. Yang, Z. Shi, W. Yang, Enhanced capacitive deionization of lead ions using air-plasma treated carbon nanotube electrode, *Surf. Coatings Technol.* 251 (2014) 122–127. doi:10.1016/j.surfcoat.2014.04.012.
- [16] J.J. Lado, J.J. Wouters, M.I. Tejedor-Tejedor, M.A. Anderson, E. Garcia-Calvo, Asymmetric Capacitive Deionization Utilizing Low Surface Area Carbon Electrodes Coated with Nanoporous Thin-Films of Al<sub>2</sub>O<sub>3</sub> and SiO<sub>2</sub>, *J. Electrochem. Soc.* 160 (2013) E71–E78. doi:10.1149/2.094308jes.
- [17] K. Laxman, M.T.Z. Myint, H. Bourdoucen, J. Dutta, Enhancement in ion adsorption

- rate and desalination efficiency in a capacitive deionization cell through improved electric field distribution using zinc oxide nanorods coated activated carbon cloth electrodes., *ACS Appl. Mater. Interfaces*. (2014) 6–13. doi:10.1021/am501041t.
- [18] Y.-J. Kim, J.-H. Choi, Improvement of desalination efficiency in capacitive deionization using a carbon electrode coated with an ion-exchange polymer., *Water Res.* 44 (2010) 990–6. doi:10.1016/j.watres.2009.10.017.
- [19] C. Yan, L. Zou, R. Short, Polyaniline-modified activated carbon electrodes for capacitive deionisation, *Desalination*. 333 (2014) 101–106. doi:10.1016/j.desal.2013.11.032.
- [20] L. Weinstein, R. Dash, *Capacitive Deionization: Challenges and Opportunities*, (2013) 34–37.
- [21] X. Gu, Y. Yang, Y. Hu, M. Hu, J. Huang, C. Wang, Nitrogen-doped graphene composites as efficient electrodes with enhanced capacitive deionization performance, *RSC Adv.* 4 (2014) 63189–63199. doi:10.1039/C4RA11468J.
- [22] Y. Liu, X.T. Xu, T. Lu, Z. Sun, D.H.C. Chua, L.K. Pan, Nitrogen-doped electrospun reduced graphene oxide-carbon nanofiber composite for capacitive deionization, *RSC Adv.* 5 (2015) 34117–34124. doi:10.1039/C5RA00620A.
- [23] S. Porada, F. Schipper, M. Aslan, M. Antonietti, V. Presser, T.P. Fellingner, Capacitive Deionization using Biomass-based Microporous Salt-Templated Heteroatom-Doped Carbons, *ChemSusChem*. 8 (2015) 1823. doi:10.1002/cssc.201500696.
- [24] G.X. Li, P.X. Hou, S.Y. Zhao, C. Liu, H.M. Cheng, A flexible cotton-derived carbon sponge for high-performance capacitive deionization, *Carbon N. Y.* 101 (2016) 1–8. doi:10.1016/j.carbon.2015.12.095.
- [25] X. Xu, L. Pan, Y. Liu, T. Lu, Z. Sun, Enhanced capacitive deionization performance of graphene by nitrogen doping, *J. Colloid Interface Sci.* 445 (2015) 143–150. doi:10.1016/j.jcis.2015.01.003.
- [26] P. Chen, T.Y. Xiao, Y.H. Qian, S.S. Li, S.H. Yu, A nitrogen-doped graphene/carbon nanotube nanocomposite with synergistically enhanced electrochemical activity, *Adv. Mater.* 25 (2013) 3192–3196. doi:10.1002/adma.201300515.
- [27] X. Yang, D. Wu, X. Chen, R. Fu, Nitrogen-enriched nanocarbons with a 3-D continuous mesopore structure from polyacrylonitrile for supercapacitor application, *J. Phys. Chem. C*. 114 (2010) 8581–8586. doi:10.1021/jp101255d.
- [28] M. Trchová, E.N. Konyushenko, J. Stejskal, J. Kovářová, G. Čirić-Marjanović, The

- conversion of polyaniline nanotubes to nitrogen-containing carbon nanotubes and their comparison with multi-walled carbon nanotubes, *Polym. Degrad. Stab.* 94 (2009) 929–938. doi:10.1016/j.polymdegradstab.2009.03.001.
- [29] J. Yan, T. Wei, W. Qiao, Z. Fan, L. Zhang, T. Li et al., A high-performance carbon derived from polyaniline for supercapacitors, *Electrochem. Commun.* 12 (2010) 1279–1282. doi:10.1016/j.elecom.2010.06.037.
- [30] L. Li, E. Liu, J. Li, Y. Yang, H. Shen, Z. Huang et al., A doped activated carbon prepared from polyaniline for high performance supercapacitors, *J. Power Sources.* 195 (2010) 1516–1521. doi:10.1016/j.jpowsour.2009.09.016.
- [31] A.B. Fuertes, T.A. Centeno, Mesoporous carbons with graphitic structures fabricated by using porous silica materials as templates and iron-impregnated polypyrrole as precursor, *J. Mater. Chem.* 15 (2005) 1079–1083. doi:10.1039/b416007j.
- [32] E. Frackowiak, V. Khomenko, K. Jurewicz, K. Lota, F. Béguin, Supercapacitors based on conducting polymers/nanotubes composites, *J. Power Sources.* 153 (2006) 413–418. doi:10.1016/j.jpowsour.2005.05.030.
- [33] R.L. Zornitta, G. Pincelli, L.A.M. Ruotolo, Modificação do polímeros condutor polianilina para uso como trocador catiônico, *Quim. Nov.* 37 (2014) 1459–1464.
- [34] C. Yan, L. Zou, R. Short, Single-walled carbon nanotubes and polyaniline composites for capacitive deionization, *Desalination.* 290 (2012) 125–129. doi:10.1016/j.desal.2012.01.017.
- [35] P. Wu, Gang; More, Karren L.; Johnston, Christina M.; Zelenay, High-Performance Electrocatalysts for Oxygen Reduction Derived from Polyaniline, Iron, and Cobalt, *Science* (80-. ). 322 (2011) 443–448. doi:10.1126/science.1200832.
- [36] N. Gavrilov, I.A. Pasti, M. Vujkovic, J. Travas-Sejdic, G. Ciric-Marjanovic, S. V. Mentus, High-performance charge storage by N-containing nanostructured carbon derived from polyaniline, *Carbon N. Y.* 50 (2012) 3915–3927. doi:10.1016/j.carbon.2012.04.045.
- [37] Y. Jia, J. Jiang, K. Sun, Pyrolysis of polyaniline-poly(styrene sulfonate) hydrogels to prepare activated carbons for the adsorption of vitamin B12, *J. Anal. Appl. Pyrolysis.* 111 (2015) 247–253. doi:10.1016/j.jaap.2014.10.023.
- [38] M. Yang, B. Cheng, H. Song, X. Chen, Preparation and electrochemical performance of polyaniline-based carbon nanotubes as electrode material for supercapacitor, *Electrochim. Acta.* 55 (2010) 7021–7027. doi:10.1016/j.electacta.2010.06.077.

- [39] X. Xiang, E. Liu, Z. Huang, H. Shen, Y. Tian, C. Xiao et al., Preparation of activated carbon from polyaniline by zinc chloride activation as supercapacitor electrodes, *J. Solid State Electrochem.* 15 (2011) 2667–2674. doi:10.1007/s10008-010-1258-7.
- [40] K.S. Kim, S.J. Park, Easy synthesis of polyaniline-based mesoporous carbons and their high electrochemical performance, *Microporous Mesoporous Mater.* 163 (2012) 140–146. doi:10.1016/j.micromeso.2012.04.047.
- [41] M. Vujković, N. Gavrilov, I. Pašti, J. Krstić, J. Travas-Sejdic, G. Ćirić-Marjanović et al., Superior capacitive and electrocatalytic properties of carbonized nanostructured polyaniline upon a low-temperature hydrothermal treatment, *Carbon N. Y.* 64 (2013) 472–486. doi:10.1016/j.carbon.2013.07.100.
- [42] C. Long, D. Qi, T. Wei, J. Yan, L. Jiang, Z. Fan, Nitrogen-doped carbon networks for high energy density supercapacitors derived from polyaniline coated bacterial cellulose, *Adv. Funct. Mater.* 24 (2014) 3953–3961. doi:10.1002/adfm.201304269.
- [43] Z. Zhang, Z. Zhou, H. Peng, Y. Qin, G. Li, Nitrogen- and oxygen-containing hierarchical porous carbon frameworks for high-performance supercapacitors, *Electrochim. Acta.* 134 (2014) 471–477. doi:10.1016/j.electacta.2014.04.107.
- [44] T. Zhu, J. Zhou, Z. Li, S. Li, W. Si, S. Zhuo, Hierarchical porous and N-doped carbon nanotubes derived from polyaniline for electrode materials in supercapacitors, *J. Mater. Chem. A.* 2 (2014) 12545. doi:10.1039/C4TA01465K.
- [45] J.W.F. To, Z. Chen, H. Yao, J. He, K. Kim, H.-H. Chou et al., Ultrahigh Surface Area Three-Dimensional Porous Graphitic Carbon from Conjugated Polymeric Molecular Framework, *ACS Cent. Sci.* 1 (2015) 150518113247004. doi:10.1021/acscentsci.5b00149.
- [46] L. Sun, L. Wang, C. Tian, T. Tan, Y. Xie, K. Shi et al., Nitrogen-doped graphene with high nitrogen level via a one-step hydrothermal reaction of graphene oxide with urea for superior capacitive energy storage, *RSC Adv.* 2 (2012) 4498. doi:10.1039/c2ra01367c.
- [47] E.J. Jelmy, S. Ramakrishnan, S. Devanathan, M. Rangarajan, N.K. Kothurkar, Optimization of the conductivity and yield of chemically synthesized polyaniline using a design of experiments, *J. Appl. Polym. Sci.* 130 (2013) 1047–1057. doi:10.1002/app.39268.
- [48] S. Shreepathi, Dodecylbenzenesulfonic acid: a surfactant and dopant for the synthesis of processable polyaniline and its copolymers, Chemnitz University of Technology,

- PhD thesis, 2006.
- [49] T. Del Castillo-Castro, M.M. Castillo-Ortega, I. Villarreal, F. Brown, H. Grijalva, M. Pérez-Tello et al., Synthesis and characterization of composites of DBSA-doped polyaniline and polystyrene-based ionomers, *Compos. Part A Appl. Sci. Manuf.* 38 (2007) 639–645. doi:10.1016/j.compositesa.2006.02.001.
- [50] C.S. Stan, M. Popa, M. Olariu, M.S. Secula, Synthesis and Characterization of PSSA-Polyaniline Composite with an Enhanced Processability in Thin Films, *Open Chem.* 13 (2015) 467–476. doi:10.1515/chem-2015-0057.
- [51] A. John, P.J.P. Yadav, S. Palaniappan, Clean synthesis of 1,8-dioxo-dodecahydroxanthene derivatives catalyzed by polyaniline-p-toluenesulfonate salt in aqueous media, *J. Mol. Catal. A Chem.* 248 (2006) 121–125. doi:10.1016/j.molcata.2005.12.017.
- [52] A.K. A.M. Pharhad Hussain, Electrochemical synthesis and characterization of chloride doped polyaniline, *Bull. Mater. Sci.* 20 (2003) 329–344. doi:10.1007/BF02707455.
- [53] R.C. Rathod, V.K. Didolkar, S.S. Umare, B.H. Shambharkar, Synthesis of processable polyaniline and its anticorrosion performance on 316LN stainless steel, *Trans. Indian Inst. Met.* 64 (2011) 431–438. doi:10.1007/s12666-011-0099-0.
- [54] G. Neetika, K. D., T. S. K., Thermal Behaviour of Chemically Synthesized Polyanilines/Polystyrene Sulphonic Acid Composites, *Int. J. Mater. Chem.* 2 (2012) 79–85. doi:10.5923/j.ijmc.20120202.07.
- [55] R.C. Petterson, U. Grzeskowiak, L.H. Jules, N-Halogen Compounds. II. 1,2 The N—Cl Stretching Band in Some N-Chloroamides. The Structure of Trichloroisocyanuric Acid, *J. Org. Chem.* 25 (1960) 1595–1598. doi:10.1021/jo01079a030.
- [56] Z. Chen, Y. Sun, Applied Chemistry N -Halamine-Based Antimicrobial Additives for Polymers : Preparation , Characterization , and Antimicrobial Activity, (2006) 2634–2640. doi:10.1021/ie060088a.
- [57] S. Sinha, S. Bhadra, D. Khastgir, Effects of Dopant Type on the Properties of Polyaniline, *Polym. Polym. Compos.* 21 (2013) 449–456. doi:10.1002/app.
- [58] C.T. Hsieh, H. Teng, Influence of oxygen treatment on electric double-layer capacitance of activated carbon fabrics, *Carbon N. Y.* 40 (2002) 667–674. doi:10.1016/S0008-6223(01)00182-8.
- [59] X. Gao, A. Omosebi, J. Landon, K. Liu, Surface charge enhanced carbon electrodes for

- stable and efficient capacitive deionization using inverted adsorption–desorption behavior, *Energy Environ. Sci.* 8 (2015) 897. doi:10.1039/c4ee03172e.
- [60] L. Wei, G. Yushin, Nanostructured activated carbons from natural precursors for electrical double layer capacitors, *Nano Energy*. 1 (2012) 552–565. doi:10.1016/j.nanoen.2012.05.002.
- [61] J.J. Lado, R.L. Zornitta, F.A. Calvi, M.I. Tejedor-Tejedor, M.A. Anderson, L.A.M. Ruotolo, Study of sugar cane bagasse fly ash as electrode material for capacitive deionization, *J. Anal. Appl. Pyrolysis*. 120 (2016) 389–398. doi:10.1016/j.jaap.2016.06.009.
- [62] Y. Li, I. Hussain, J. Qi, C. Liu, J. Li, J. Shen et al., N-doped hierarchical porous carbon derived from hypercrosslinked diblock copolymer for capacitive deionization, *Sep. Purif. Technol.* 165 (2016) 190–198. doi:10.1016/j.seppur.2016.04.007.
- [63] K.S.W. Sing, Reporting physisorption data for gas/solid systems with special reference to the determination of surface area and porosity, *Pure Appl. Chem.* 54 (1982) 2201–2218. doi:10.1351/pac198557040603.
- [64] M. Aslan, M. Zeiger, N. Jackel, I. Grobelsek, D. Weingarth, V. Presser, Improved capacitive deionization performance of mixed hydrophobic / hydrophilic activated carbon electrodes, *J. Phys. Condens. Matter*. 28 (2016) 114003. doi:10.1088/0953-8984/28/11/114003.
- [65] Y. Qiu, J. Yu, G. Fang, H. Shi, X. Zhou, X. Bai, Synthesis of Carbon / Carbon Core / Shell Nanotubes with a High Specific Surface Area, *Society*. (2009) 61–68.
- [66] E. Frackowiak, Carbon materials for the electrochemical storage of energy in capacitors, 39 (2001) 937–950.
- [67] G. Rasines, P. Lavela, C. Macías, M.C. Zafra, J.L. Tirado, J.B. Parra et al., N-doped monolithic carbon aerogel electrodes with optimized features for the electrosorption of ions, *Carbon N. Y.* 83 (2015) 262–274. doi:10.1016/j.carbon.2014.11.015.
- [68] S. Zhao, T. Yan, H. Wang, G. Chen, L. Huang, J. Zhang et al., High capacity and high rate capability of nitrogen-doped porous hollow carbon spheres for capacitive deionization, *Appl. Surf. Sci.* 369 (2016) 460–469. doi:10.1016/j.apsusc.2016.02.085.
- [69] B.M. Asquith, J. Meier-Haack, B.P. Ladewig, Poly(arylene ether sulfone) copolymers as binders for capacitive deionization activated carbon electrodes, *Chem. Eng. Res. Des.* 104 (2015) 81–91. doi:10.1016/j.cherd.2015.07.020.
- [70] A.J. Bard, L.R. Faulkner, *Electrochemical Methods Fundamental and Applications*,

2001. doi:10.1038/nprot.2009.120.Multi-stage.
- [71] S. Xiong, F. Yang, H. Jiang, J. Ma, X. Lu, Covalently bonded polyaniline/fullerene hybrids with coral-like morphology for high-performance supercapacitor, *Electrochim. Acta.* 85 (2012) 235–242. doi:10.1016/j.electacta.2012.08.056.
- [72] R. Kötz, M. Carlen, Principles and applications of electrochemical capacitors, *Electrochim. Acta.* 45 (2000) 2483–2498. doi:DOI: 10.1016/S0013-4686(00)00354-6.
- [73] B. Hirschorn, M.E. Orazem, B. Tribollet, V. Vivier, I. Frateur, M. Musiani, Determination of effective capacitance and film thickness from constant-phase-element parameters, *Electrochim. Acta.* 55 (2010) 6218–6227. doi:10.1016/j.electacta.2009.10.065.
- [74] C.-W. Huang, H. Teng, Influence of Carbon Nanotube Grafting on the Impedance Behavior of Activated Carbon Capacitors, *J. Electrochem. Soc.* 155 (2008) A739. doi:10.1149/1.2965503.
- [75] J.B. Zang, Y.H. Wang, H. Huang, W.Q. Liu, Electrochemical characteristics of boron doped polycrystalline diamond electrode sintered by high pressure and high temperature, *J. Appl. Electrochem.* 39 (2009) 1545–1551. doi:10.1007/s10800-009-9838-x.
- [76] C.-M. Chen, *Surface Chemistry and Macroscopic Assembly of Graphene for Application in Energy Storage*, 2015. doi:10.1007/978-3-642-35133-4.
- [77] G. Xu, C. Zheng, Q. Zhang, J. Huang, M. Zhao, J. Nie et al., Binder-free activated carbon/carbon nanotube paper electrodes for use in supercapacitors, *Nano Res.* 4 (2011) 870–881. doi:10.1007/s12274-011-0143-8.
- [78] N.H. Basri, M. Deraman, M. Suleman, N.S.M. Nor, B.N.M. Dolah, M.I. Sahri et al., Energy and Power of Supercapacitor Using Carbon Electrode Deposited with Nanoparticles Nickel Oxide, *Int. J. Electrochem. Sci.* 11 (2016) 95–110.
- [79] J.H. Choi, Fabrication of a carbon electrode using activated carbon powder and application to the capacitive deionization process, *Sep. Purif. Technol.* 70 (2010) 362–366. doi:10.1016/j.seppur.2009.10.023.
- [80] K. Yang, T. Ying, S. Yiacoumi, C. Tsouris, Electrosorption of Ions from Aqueous Solutions by Carbon Aerogel : An Electrical Double-Layer Model, (2001) 1961–1969.
- [81] D. He, C.E. Wong, W. Tang, P. Kovalsky, T. David Waite, Faradaic Reactions in Water Desalination by Batch-Mode Capacitive Deionization, *Environ. Sci. Technol. Lett.* 3 (2016) 222–226. doi:10.1021/acs.estlett.6b00124.

- [82] T. Kim, J. Yu, C. Kim, J. Yoon, Hydrogen peroxide generation in flow-mode capacitive deionization, *J. Electroanal. Chem.* 776 (2016) 101–104. doi:10.1016/j.jelechem.2016.07.001.
- [83] F. Duan, X. Du, Y. Li, H. Cao, Y. Zhang, Desalination stability of capacitive deionization using ordered mesoporous carbon: Effect of oxygen-containing surface groups and pore properties, *Desalination*. 376 (2015) 17–24. doi:10.1016/j.desal.2015.08.009.
- [84] I. Cohen, E. Avraham, Y. Bouhadana, A. Soffer, D. Aurbach, Long term stability of capacitive de-ionization processes for water desalination: The challenge of positive electrodes corrosion, *Electrochim. Acta.* 106 (2013) 91–100. doi:10.1016/j.electacta.2013.05.029.
- [85] B. Shapira, E. Avraham, D. Aurbach, Side Reactions in Capacitive Deionization (CDI) Processes: The Role of Oxygen Reduction, *Electrochim. Acta.* 220 (2016) 285–295. doi:10.1016/j.electacta.2016.10.127.
- [86] J.J. Lado, R.E. Pérez-Roa, J.J. Wouters, M.I. Tejedor-Tejedor, C. Federspill, M.A. Anderson, Continuous cycling of an asymmetric capacitive deionization system: An evaluation of the electrode performance and stability, *J. Environ. Chem. Eng.* 3 (2015) 2358–2367. doi:10.1016/j.jece.2015.08.025.
- [87] J.J. Lado, R.E. Pérez-Roa, J.J. Wouters, M. Isabel Tejedor-Tejedor, M. A. Anderson, Evaluation of operational parameters for a capacitive deionization reactor employing asymmetric electrodes, *Sep. Purif. Technol.* 133 (2014) 236–245. doi:10.1016/j.seppur.2014.07.004.
- [88] P. Hojati-Talemi, L. Zou, M. Fabretto, R.D. Short, Using oxygen plasma treatment to improve the performance of electrodes for capacitive water deionization, *Electrochim. Acta.* 106 (2013) 494–499. doi:10.1016/j.electacta.2013.05.119.
- [89] T. Kim, J. Yoon, CDI ragone plot as a functional tool to evaluate desalination performance in capacitive deionization, *Rsc Adv.* 5 (2015) 1456–1461. doi:10.1039/c4ra11257a.
- [90] A. Yoshida, I. Tanahashi, A. Nishino, Effect of concentration of surface acidic functional groups on electric double-layer properties of activated carbon fibers, *Carbon N. Y.* 28 (1990) 611–615. doi:10.1016/0008-6223(90)90062-4.
- [91] A. Hemmatifar, J.W. Palko, M. Stadermann, J.G. Santiago, Energy breakdown in capacitive deionization, *Water Res.* 104 (2016) 303–311.



- doi:10.1016/j.watres.2016.08.020.
- [92] R. Zhao, P.M. Biesheuvel, A. van der Wal, Energy consumption and constant current operation in membrane capacitive deionization, *Energy Environ. Sci.* 5 (2012) 9520. doi:10.1039/c2ee21737f.
- [93] Y. Qu, P.G. Campbell, L. Gu, J.M. Knipe, E. Dzenitis, J.G. Santiago, M. Stadermann, Energy consumption analysis of constant voltage and constant current operations in capacitive deionization, *Desalination.* 400 (2016) 18–24. doi:10.1016/j.desal.2016.09.014.
- [94] T. Kim, J. Yoon, Relationship between capacitance of activated carbon composite electrodes measured at a low electrolyte concentration and their desalination performance in capacitive deionization, *J. Electroanal. Chem.* 704 (2013) 169–174. doi:10.1016/j.jelechem.2013.07.003.
- [95] Y. Liu, T. Chen, T. Lu, Z. Sun, D.H.C. Chua, L. Pan, Nitrogen-doped porous carbon spheres for highly efficient capacitive deionization, *Electrochim. Acta.* 158 (2015) 403–409. doi:10.1016/j.electacta.2015.01.179.
- [96] X. Xu, Z. Sun, D.H.C. Chua, L. Pan, Novel nitrogen doped graphene sponge with ultrahigh capacitive deionization performance., *Sci. Rep.* 5 (2015) 11225. doi:10.1038/srep11225.
- [97] X. Xu, L. Pan, Y. Liu, T. Lu, Z. Sun, D.H.C. Chua, Facile synthesis of novel graphene sponge for high performance capacitive deionization., *Sci. Rep.* 5 (2015) 8458. doi:10.1038/srep08458.
- [98] W. Shi, H. Li, X. Cao, Z.Y. Leong, J. Zhang, T. Chen et al., Ultrahigh Performance of Novel Capacitive Deionization Electrodes based on A Three-Dimensional Graphene Architecture with Nanopores, *Sci. Rep.* 6 (2016) 18966. doi:10.1038/srep18966.

## APPENDIX

**Table A3.1.** Polymerization yield for PANi doped with different anions

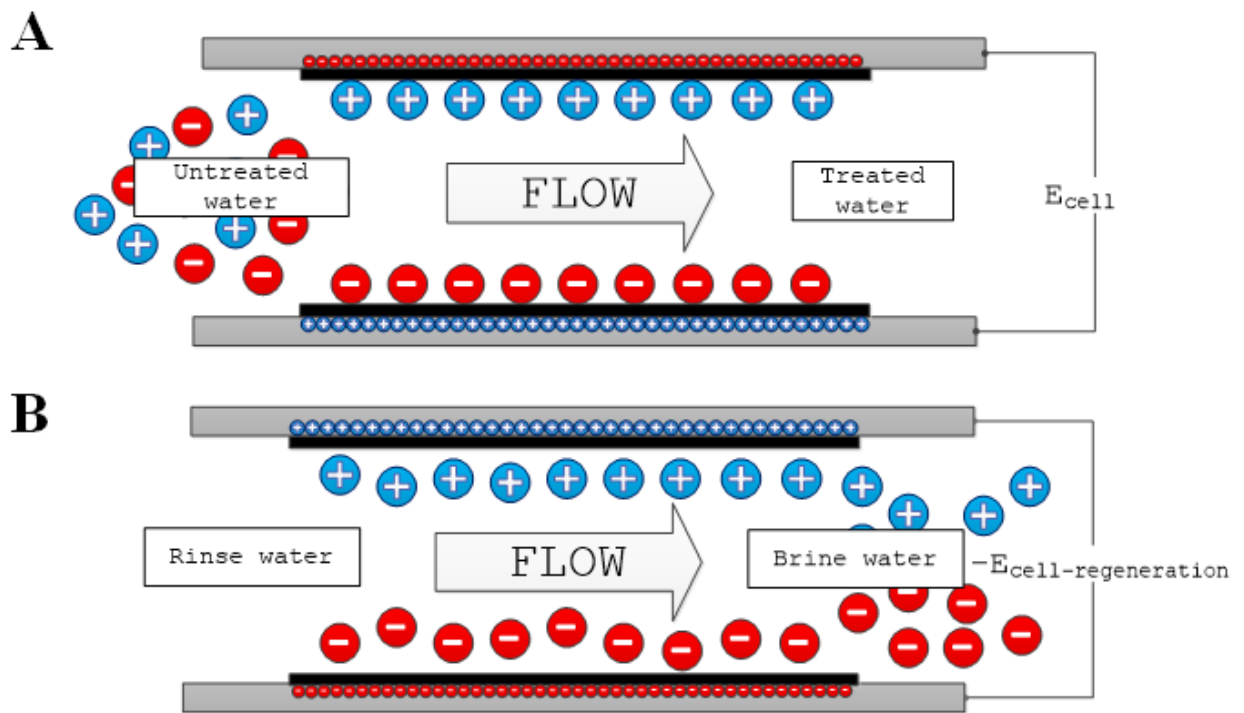
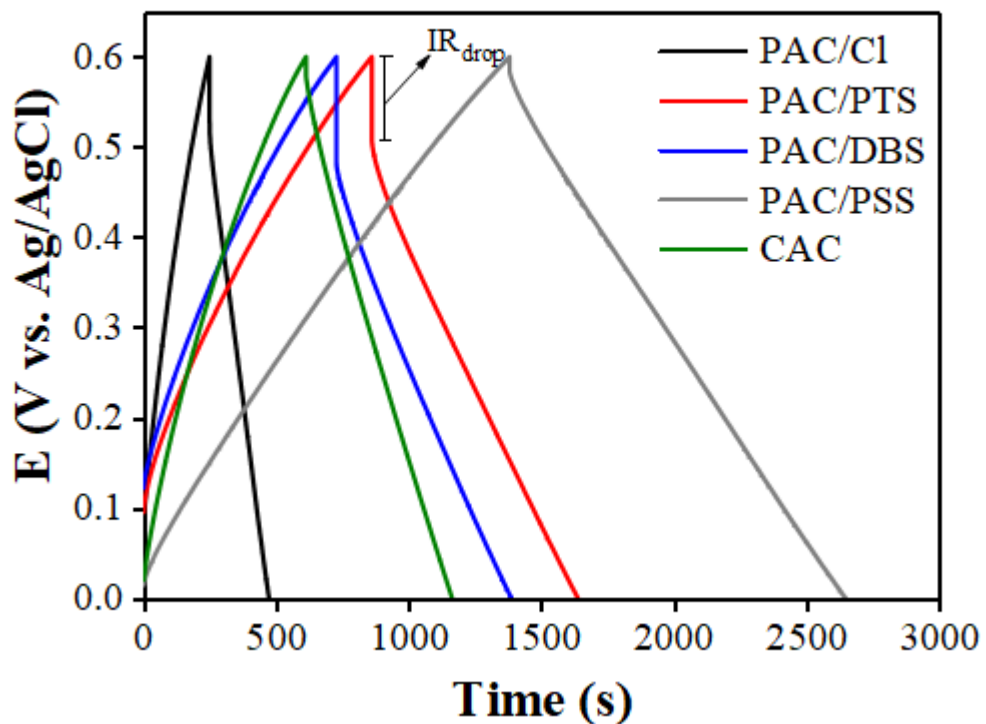
	$m_{\text{PANi}}$ (g)	$V_{\text{aniline}}$ (mL)	$Y_{\text{PANi}}$ (g <sub>PANi</sub> /mL aniline)
<b>PANi/Cl</b>	7.11	10	0.71
<b>PANi/PTS</b>	8.21	10	0.82
<b>PANi/DBS</b>	16.63	10	1.66
<b>PANi/PSS</b>	17.60	5	3.52

**Table A3.2.** Yield of pre-carbonization and activation of PANi doped with different anions

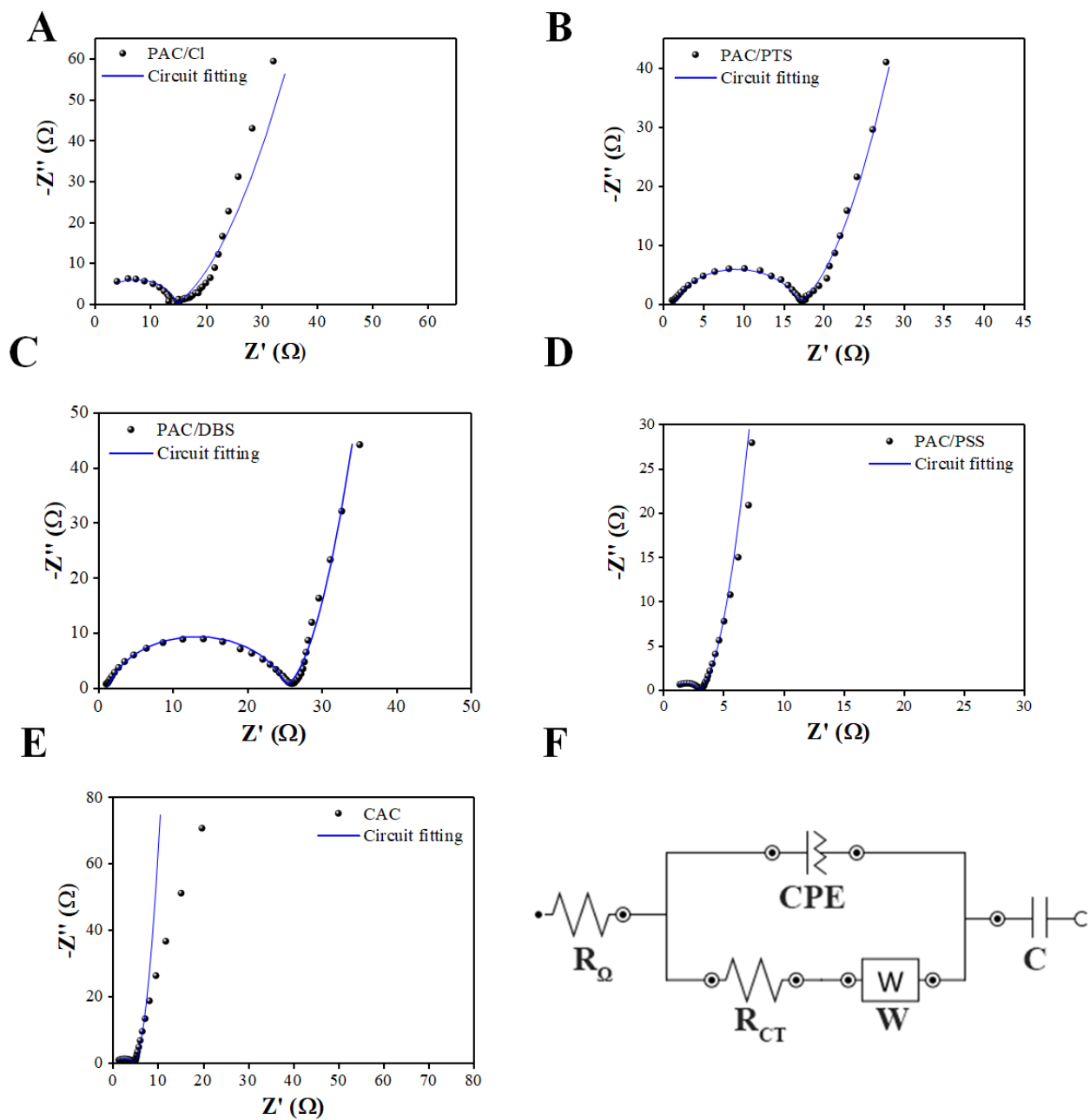
	$Y_C$ (%)	$Y_{AC}$ (%)	$Y_O$ (%)
<b>PAC/Cl</b>	32.7	48.0	15.7
<b>PAC/PTS</b>	37.9	32.3	12.3
<b>PAC/DBS</b>	31.3	29.9	9.4
<b>PAC/PSS</b>	23.4	31.4	7.4

**Table A3.3.**  $D_c$  based on the charge-discharge experiments

	$E_{\text{cell}}$	$C_{\text{CD}}$ (F/g)	$D_c$ (mg/g)	SAC (mg/g)	$\epsilon$ (%)
<b>PAC/Cl</b>	1.2	69.3	12.6	5.8	45.9
	1.4		14.7	5.1	34.6
<b>PAC/PTS</b>	1.2	121.0	22.0	14.3	64.9
	1.4		25.7	14.9	58.0
<b>PAC/DBS</b>	1.2	118.6	21.6	12.6	58.4
	1.4		25.2	11.7	46.4
<b>PAC/PSS</b>	1.2	108.4	19.7	13.1	66.4
	1.4		23.0	13.7	59.5
<b>CAC</b>	1.2	84.5	15.4	8.9	57.9
	1.4		17.9	10.9	60.7

**Figure A3.1.** Scheme of a CDI device: (A) electrosorption and (B) regeneration[1]**Figure A3.2.** Charge-discharge profiles obtained for the different carbon materials at a charge density of  $0.4 \text{ mA/cm}^2$ 

**Figure A3.3.** Circuit fitting for the PAC doped with  $\text{Cl}^-$  (A)  $\text{PTS}^-$  (B)  $\text{DBS}^-$  (C)  $\text{PSS}^-$  (D) CAC (E) and the equivalent circuit used for the fitting (F)



### Appendix references

- [1] R. L. Zornitta, J. J. Lado, M. A. Anderson and L. A. M. Ruotolo, *Sep. Purif. Technol.*, 2016, **158**, 39–52.

## CHAPTER 4

### SIMULTANEOUS ANALYSIS OF ELECTROSORPTION CAPACITY AND KINETICS FOR CDI DESALINATION USING DIFFERENT ELECTRODE CONFIGURATIONS

Capacitive deionization (CDI) offers an affordable technology for the reduction of salt concentrations in brackish water. However, there are still drawbacks concerning electrode capacity and energy consumption, compared to other well-established technologies such as reverse osmosis or electrodialysis. This study investigates high-adsorption electrodes based on polyaniline-activated carbon, applying different configurations (symmetric and asymmetric electrodes, and membrane CDI) to optimize electrosorption capacity and energy consumption. A new approach called *OSR* (optimized salt removal) is proposed, based on simultaneous analysis of the electrosorption capacity and the adsorption/desorption kinetics. This technique was used to evaluate different electrode configurations. The best performance was obtained using MCDI, which improved the electrode capacity from 14.9 to 20.0 mg/g, while reducing the specific energy consumption by 21%. It was demonstrated that the performance of the electrode depended on both the specific adsorption capacity (*SAC*) and the electrosorption/desorption kinetics. Fitting the electrosorption and desorption curves using a pseudo-first order kinetic model and applying the *OSR* method showed that the best desalination was achieved using MCDI at 1.2 V. This configuration did not present the highest *SAC* or the fastest electrosorption/desorption kinetics, but a good balance was obtained between these two variables.

#### 4.1. Introduction

Capacitive deionization is a low-cost technology that can be used for the desalination of brackish water (with salt concentration lower than 10 g/L). Recent advances in electrode materials and energy efficiency make CDI competitive with other well-established technologies such as reverse osmosis or reverse electrodialysis [1]. The main advantage of CDI is the low energy consumption resulting from the use of low cell voltages (1.2-1.4 V) for desalination [2]. This process employs the electric double layer (EDL) formed inside the pores of carbon electrodes for ion storage when a potential bias is applied. Therefore, properties of the material such as specific surface area (*SSA*), pore size distribution (*PSD*), and conductivity have important effects on desalination performance [3]. In addition, the electrode wettability, which

is highly dependent on the surface groups of the material, plays a crucial role in the electrode capacity, since greater hydrophilicity of the electrode enables easier access of water to the pores [4,5].

The development of new low-cost electrodes is still challenging. Several electrode materials have already been studied in attempts to increase desalination capacity and the kinetics of electrosorption, while reducing energy consumption. Nitrogen-doped activated carbons (N-doped AC) offer high performance electrode materials, due to the high specific adsorption capacity (*SAC*) attributed to surface nitrogen groups, which promotes pseudo-capacitance and increases conductivity [6]. For example, N-doped graphene and N-doped graphene sponge presented *SAC* values of 21.9 and 21.0 mg/g, respectively, while a value of 16.1 mg/g was obtained using N-doped carbon sponge derived from cotton [6–8]. Although these capacities are impressive, the cost of these electrodes, related to the high activation temperature and nitrogen doping with ammonia [8], means that they remain too expensive for large-scale applications. Another procedure to obtain N-doped AC is the use of precursors containing nitrogen atoms, avoiding the expense associated with doping using  $\text{NH}_3$ . To this end, glucosamine hydrochloride [9], polyacrylonitrile [10], polyaniline (PAni) [11–13], and polypyrrole [14] have been investigated as N-doping precursors.

Although the search for materials with high electrosorption capacity has intensified in the CDI field, the electrode kinetics has been little explored. Despite the paramount importance of the electrode *SAC*, the electrosorption and desorption kinetics can be decisive, since this influences the number of cycles possible in a given operational time. For instance, an inexpensive electrode with poor or moderate *SAC* can achieve good desalination performance if the electrosorption and desorption kinetics are sufficiently fast. Therefore, optimization of the electrosorption time could enable a greater number of adsorption/desorption cycles in the same operational time, resulting in the electrode performance being comparable to that of an electrode with higher *SAC*.

The modified Ragone plot proposed by Kim and Yoon [15] provides an important tool for simultaneous evaluation of the electrosorption capacity and the kinetics of the process, but it only considers the average salt adsorption rate (*ASAR*), without taking the desorption time into account. To the best of our knowledge, the present work is the first to describe a new approach, called *OSR* (optimized salt removal), for analysis of CDI electrode performance, simultaneously considering both the electrosorption capacity and the electrosorption and desorption kinetics. Instead of a plot, this method considers an optimized value for the mass of

salt removed during a given operational time. The *OSR* method was used to evaluate different electrode configurations, facilitating their comparison and providing an easy way to identify the most promising desalination process.

Desalination was carried out with an N-doped AC electrode previously prepared using a PANi precursor. The AC derived from PANi (PAC) was chosen due to the advantages of PANi as an AC precursor, including low monomer cost, ease of synthesis, and high nitrogen content (~15 wt.%), as well as the similarity of its structure to graphite, which facilitated the insertion of nitrogen into the carbon matrix. In a previous study,[16] Zornitta *et al.* successfully synthesized PAC derived from PANi doped with different anions (PAC) and obtained high-performance electrodes for CDI desalination. Using PANi doped with p-toluenesulfonate as precursor, the AC electrodes (PAC/PTS) showed high electrosorption capacity (14.9 mg/g at 1.4 V). The electrodes were modified by surface treatment and were used in symmetric and asymmetric configurations and in membrane CDI. The best electrode configuration was determined considering the desalination performance in terms of *OSR* per day.

Recent studies have found that the use of asymmetric electrodes improves desalination performance for two main reasons: (i) shift of the  $E_{pzc}$  of the electrodes, which maximizes the effective electrode potential used to adsorb ions [17,18]; and (ii) introduction of additional attractive forces that act to remove the ions from the electrolyte solution [19]. This strategy has been reported to optimize SAC, even in long-term experiments [18]. Another strategy widely employed to enhance CDI performance is the use of ion-selective membranes (MCDI) to improve charge efficiency [20]. In a typical CDI process, most of the electrosorption occurs within the carbon particles (in the micropores and mesopores), while the contribution of the macropores to the EDL is negligible [21]. During electrode polarization, co-ions (ions with the same charge as the polarized electrode) are repelled from the micropores, but are inhibited from leaving the electrode due to the presence of the membrane. Hence, these co-ions remain stored in the macropores in order to maintain electroneutrality, and more counter ions are removed from the electrolyte. Therefore, part of the charge that would be wasted in eliminating the co-ions is compensated by the use of the macropores as reservoirs of counter ions. Different to conventional CDI, in which the charge efficiency is far from unity due to the elimination of co-ions, MCDI usually presents high charge efficiency values [20,21].

In summary, in this study, symmetric and asymmetric CDI and MCDI were employed along with PAC electrodes in an attempt to maximize charge efficiency, increase electrode capacity, and reduce energy consumption. The different configurations were evaluated in a

desalination process, employing a new methodology for simultaneous analyses of *SAC*, electrosorption kinetics, and desorption kinetics.

### ***Simultaneous analysis of electrosorption capacity and kinetics***

In a CDI process operating under real conditions, both electrosorption and desorption processes must be considered when selecting the best electrodes for desalination, with the electrode kinetics and capacity being most important in terms of electrode performance. In the CDI field, electrode capacity is commonly evaluated using the salt adsorption capacity (*SAC*), which is the amount of salt removed per active mass of the carbon electrode. The kinetics of electrosorption can be evaluated using techniques such as the CDI Ragone plot [15] and pseudo-first or second order models [22–30]. The CDI Ragone plot provides information about *SAC*, *ASAR*, and the electrosorption time, with optimization of both parameters obtained from the top-right position in the plot. The fitting of electrosorption data using pseudo-first and second order kinetic models provides numeric information from the kinetic constant. It is widely accepted that this way of evaluating kinetics provides accurate information (high correlation coefficients) and is a straightforward technique for comparison of electrode kinetics.

Here, equations were developed in order to maximize electrode capacity by optimizing the electrosorption time, considering both capacity and kinetics. It has been widely reported that pseudo-first order kinetics provides good fits to CDI electrosorption data, so the development of the equations was based on fitting using the pseudo-first order kinetic model (Equation 4.1). Nevertheless, it is also possible to use other fittings, such as the pseudo-second order kinetic equation, as shown in the Appendix.

$$C_0 = C_0 \exp(-kt) \quad (4.1)$$

In order to describe both electrosorption and desorption using an exponential relationship, the variation of the electrode capacity in terms of *SAC* was modified using Equation 4.2:

$$SAC'(t) = SAC_m - SAC(t) \quad (4.2)$$

In this equation,  $SAC'(t)$  is the difference between the maximum *SAC* ( $SAC_m$ ) and *SAC* at a given time  $t$ .

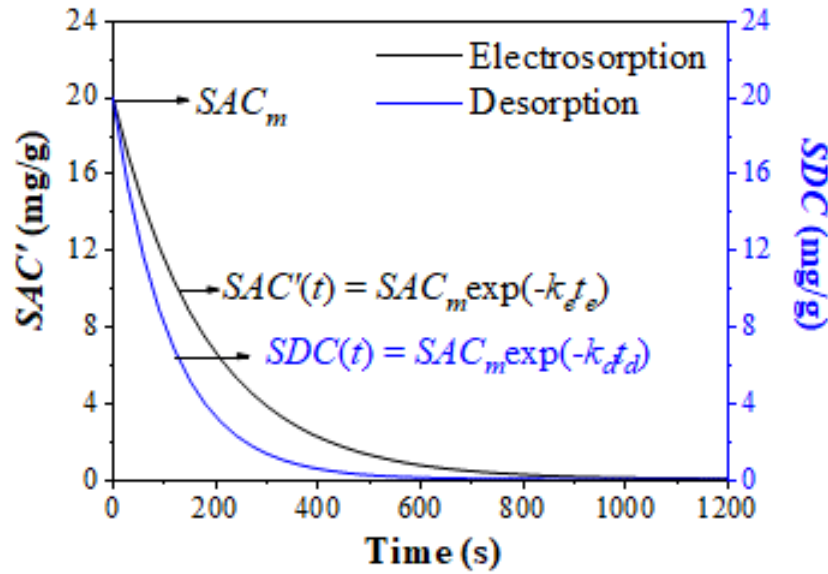
Figure 4.1 illustrates a typical  $SAC'(t)$  curve fitted to Equation 4.1. In order to provide both electrosorption and desorption curves in the same figure, Equation 4.1 was rewritten as Equations 4.3 and 4.4, where  $t(t)$  was replaced by  $SAC'(t)$  and  $SDC(t)$  (salt desorption concentration), respectively,  $C_0$  was replaced by  $SAC_m$ , and  $t_e$  and  $t_d$  are the electrosorption and desorption times, respectively.



$$SAC'(t) = SAC_m \exp(-k_e t_e) \quad (4.3)$$

$$SDC(t) = SAC_m \exp(-k_d t_d) \quad (4.4)$$

**Figure 4.1.** Electrosorption/desorption curves described by the pseudo-first order model for the PAC-PTS electrodes (20 mg/g  $SAC_m$  and pseudo-first order constants of  $k_e = 0.0055 \text{ s}^{-1}$  and  $k_d = 0.0090 \text{ s}^{-1}$  for electrosorption and desorption, respectively)



In order to properly compare the different materials and electrode configurations, an operational time ( $t_{op}$ ) was established for calculation of the amount of salt that could be removed. This was important, because CDI operates in cycles, and the more cycles performed in a given period of time, the greater the quantity of salt that can be removed. Calculation of the number of cycles ( $N_{cycles}$ ) considered both  $t_e$  and  $t_d$ , as shown in Equation 4.5:

$$N_{cycles} = \frac{t_{op}}{t_e + t_d} \quad (4.5)$$

where  $t_d$  can be calculated according to Equation 4.6, considering pseudo-first order kinetics:

$$t_d = \frac{-\ln\left(\frac{SDC(t)}{SAC_m}\right)}{k_d} \quad (4.6)$$

The numerator in Equation 4.6 can be estimated considering 99% desorption (Equation 4.7).

$$t_d = \frac{-\ln(0.01)}{k_d} \quad (4.7)$$

Considering that the amount of salt removed in a full cycle is the salt removed only in the electrosorption step (desorption does not contribute to salt removal), the mass adsorbed in one cycle ( $m_{oc}$ ) can be calculated using Equation 4.8.

$$m_{oc} = (SAC_m - SAC'(t)) \cdot m_E \quad (4.8)$$

Replacing  $SAC'(t)$  from Equation 4.3 in Equation 4.8, and  $t_d$  from Equation 4.6 in Equation 4.5, the amount of salt removed ( $SDC$ ) during time  $t_{op}$  can be calculated using Equation 4.9.

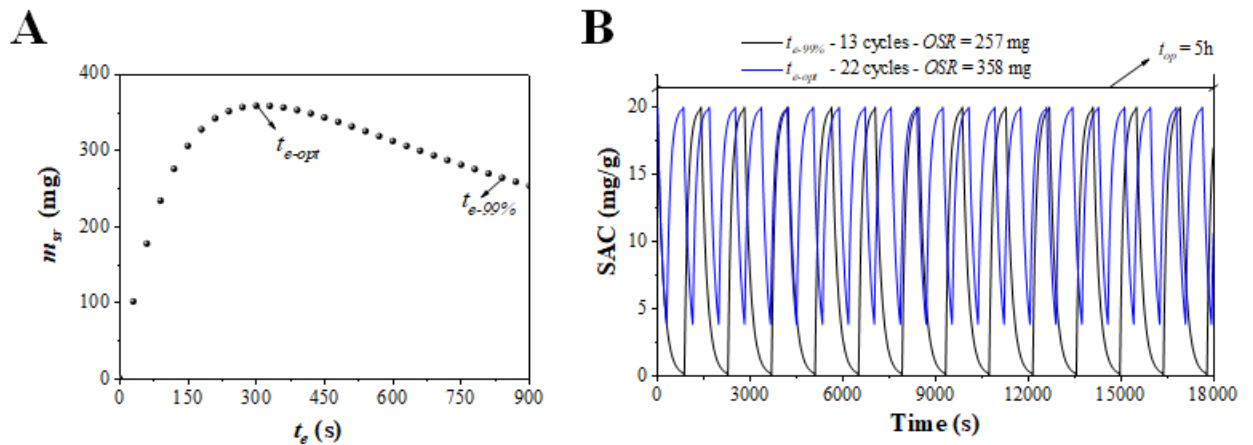
$$m_{sr} = N_{cycles} \cdot m_{oc} = \frac{t_{op}}{t_e \frac{\ln(0.01)}{k_d}} \cdot m_E SAC_m (1 - e^{-k_e t_e}) \quad (4.9)$$

Considering that in Equation 4.9, the only variable is  $t_e$ ,  $SDC$  may be maximized with respect to  $t_e$  by deriving Equation 4.9 and making it equal to zero (Equation 4.10).

$$\frac{e^{-k_e t_e - opt} - 1}{t_e - opt \frac{\ln(0.01)}{k_d}} + k_e e^{-k_e t_e - opt} = 0 \quad (4.10)$$

Equation 4.10 can be easily solved to obtain the optimized electro-sorption time ( $t_{e-opt}$ ), which is the time that maximizes  $SDC$ , thus giving the value of the optimized salt removal, called  $OSR$  (Fig. 4.2a). It is interesting to note that  $SAC_m$  does not appear in Equation 4.9, as expected since the number of cycles is only dependent on the electro-sorption/desorption kinetics. On the other hand,  $SAC$  depends on  $t_e$  (Equation 4.2), so consequently it is also optimized by Equation 4.9. Figure 4.2b compares the electro-sorption values obtained using  $t_{e-opt}$  and the electro-sorption time corresponding to 99% salt removal ( $t_{e-99\%}$ ). It can be seen that use of the optimized time ( $t_{e-opt}$ ) enabled many more cycles to be achieved, which, together with the  $SAC$ , provided the maximum value of  $m_{r-op}$ .

**Figure 4.2.** (A) Plot of  $m_{sr}$  against  $t_e$  ( $t_{op} = 5$  h), and (B)  $SAC$  comparison considering  $t_{e-99\%}$  and  $t_{e-opt}$  in a simulated CDI process lasting 5 h. Parameters:  $SAC_m = 20$  mg/g,  $k_e = 0.0055$  s<sup>-1</sup>, and  $k_d = 0.0090$  s<sup>-1</sup>



## 4.2. Experimental

### 4.2.1. Materials

Aniline monomer (99%, Sigma-Aldrich) was distilled prior to use for polymerization and was kept in an amber bottle at low temperature ( $<3\text{ }^{\circ}\text{C}$ ) to prevent oxidation. The anion source used as counterions for polyaniline was p-toluenesulfonic acid monohydrate, HPTS ( $\geq 98.5\%$ , Sigma-Aldrich). Ammonium persulfate (98%, Sigma-Aldrich) was used as oxidant to promote polymerization. Nitric acid (70%, Sigma-Aldrich) and ethylenediamine ( $\geq 99\%$ , Sigma-Aldrich) were used for surface treatment of the activated carbon in order to obtain asymmetric electrodes.

Polyvinylidene fluoride (PVDF, Sigma-Aldrich) and n-methylpyrrolidone (NMP, Synth) were used as binder and solvent, respectively, for electrode preparation. Cationic (CMI-7000S) and anionic (AMI-7001S) membranes were purchased from Membranes International Inc. and were maintained in 5% NaCl solution prior to use.

### 4.2.2. Polyaniline synthesis

Aniline (10 mL) was added at low temperature ( $\sim 3\text{ }^{\circ}\text{C}$ ), under constant stirring, to 500 mL of a solution containing 0.30 mol/L of HPTS. The polymerization process was started by adding 85.9 mL of the oxidant solution (1.0 mol/L), dripped slowly into the monomer solution. The mixture was left to react for 24 h. After polymerization, the precipitated PANi/PTS was filtered, washed with water, and dried in an oven at  $60\text{ }^{\circ}\text{C}$  for 24 h.

### 4.2.3. PAC/PTS preparation and surface treatment

A detailed description of the PAC preparation has already been provided in a previous paper.[16] Briefly, PANi was firstly carbonized in a tube furnace (Lindberg Blue M, Thermo Scientific) at  $850\text{ }^{\circ}\text{C}$ , with heating at a rate of  $10\text{ }^{\circ}\text{C}/\text{min}$ , for 2 h under an atmosphere of  $\text{N}_2$  (150 mL/min). After carbonization, the sample was activated with KOH, in a proportion of 1:4, followed by heating at  $850\text{ }^{\circ}\text{C}$  for 1.5 h, using the same heating rate and  $\text{N}_2$  flow conditions. The activated carbon was washed with 0.5 mol/L HCl, followed by washing with warm water until the pH of the wash solution approached neutral. The PAC was then dried at  $105\text{ }^{\circ}\text{C}$  for 24 h.

Surface treatment was carried out using a procedure adapted from Gao et al. [31]. Firstly, the PAC was mixed with  $\text{HNO}_3$  in a proportion of 1:13 (w/w) for 24 h, washed with plentiful warm water until the pH approached neutral, and dried in an oven at  $105\text{ }^{\circ}\text{C}$  for 24 h. The acid-treated PAC was then mixed with ethylenediamine in a proportion of 1:13 (w/w) in a

round bottom flask, heated to 105 °C using a thermal blanket, and maintained under reflux for 5 h. After that, the reflux system was removed and heating was continued until complete evaporation of the ethylenediamine. The surface-modified PAC (mPAC) was washed with warm water until the pH approached neutral, and was then dried in an oven at 105 °C for 24 h.

The PAC particles were large, smooth, and presented small cavities and a sponge-like shape. Textural analysis revealed that the PAC/PTS was predominantly microporous (the total, micropore, and mesopore volumes were 0.64, 0.59, and 0.05 cm<sup>3</sup>/g, respectively). The BET surface area was 1484 m<sup>2</sup>/g.[16]

The PAC and mPAC were further characterized in terms of zeta potential, using a Zetasizer Nano ZS system (Malvern Instruments).

#### 4.2.4. Electrode preparation and characterization

Carbon electrodes were prepared by mixing 10 wt.% of PVDF, previously dissolved in NMP, and 90 wt.% of activated carbon. The slurry was mixed and poured into a mold containing a graphite substrate. The mold was then placed in an oven at 80 °C for 12 h to remove all the solvent and form the carbon film.

Cyclic voltammetry (CV) and electrochemical impedance spectroscopy (EIS) evaluations of the electrodes prepared using PAC and mPAC were performed in 0.2 mol/L NaCl, using a three-electrode system with carbon electrodes as the working (2.5 cm x 1.0 cm) and counter (3.0 cm x 1.0 cm) electrodes. Two electrode configurations were used in the electrochemical characterizations: 1) symmetric electrodes, with the working and counter electrodes being composed of the same material (PAC<sup>-</sup> || PAC<sup>-</sup> and mPAC<sup>+</sup> || mPAC<sup>+</sup>); 2) asymmetric electrodes, with an mPAC working electrode and a PAC (mPAC<sup>+</sup> || PAC<sup>-</sup>) counter electrode. Ag/AgCl in saturated KCl was used as the reference electrode. An Autolab PGStat 204 potentiostat was used for all the measurements. CV was carried out at different scan rates ( $v$ ): 1, 5, 10, 50, and 100 mV/s, in a potential window between -0.2 V and 0.5 V, which was previously found to prevent redox reactions. The specific capacitance ( $C_S$ ) and the total specific capacitance ( $C_{CV}$ ) of the electrode (F/g) were calculated using Equations 4.11 and 4.12, respectively, where  $I$  is the current,  $m$  is the mass of the working electrode (g), and  $E_1$  and  $E_2$  are the lowest and highest values of the potential window.

$$C_S = \frac{I}{vm} \quad (4.11)$$

$$C_{CV} = \frac{\int_{E_1}^{E_2} IdE_{cell}}{vm(E_2 - E_1)} \quad (4.12)$$

#### 4.2.5. Electrosorption experiments

The electrosorption cell consisted of two acrylic plates, where carbon electrodes with dimensions of 10 cm x 5 cm were placed on titanium sheets employed as current collectors. Two plastic meshes placed between the carbon electrodes provided a gap of 1.8 mm necessary to ensure the flow of electrolyte and prevent short circuit. The cell was sealed with rubber gaskets, and all the components were assembled using nuts and bolts [2]. The nomenclature adopted for the symmetric and asymmetric electrodes was as follows: Electrode<sup>surface charge</sup> (cathode) || (anode) Electrode<sup>surface charge</sup>. Accordingly, the symmetric configuration using PAC electrodes was denoted PAC<sup>-</sup>(-) || (+)PAC<sup>-</sup>. For the asymmetric electrodes, two different configurations were evaluated: (1) PAC<sup>-</sup>(-) || (+)mPAC<sup>+</sup> and (2) mPAC<sup>+</sup>(-) || (+)PAC<sup>-</sup>. In the MCDI experiments, anionic and cationic membranes were placed on the positively and negatively charged electrodes, respectively, and a plastic mesh of 0.9 mm was used to ensure electrolyte flow.

During desalination, a 25 mL volume of 600 mg/L NaCl solution was pumped through the CDI cell using a peristaltic pump (Masterflex L/S, Cole-Parmer) at a constant flow rate (26 mL/min). An Autolab PGStat 204 potentiostat supplied constant cell potential (1.2 V or 1.4 V) during electrosorption and 0.0 V during desorption. In the MCDI experiments, desorption was performed at -0.3 V. Biesheuvel et al. demonstrated that the use of reverse potential during desorption improves the electrode capacity, due to the repulsion of co-ions [32]. The solution conductivity was measured online at the exit of the cell and was recorded every 30 s, using a conductivity meter (SevenCompact, Mettler Toledo). The conductivity was then converted to the salt concentration using a linear relationship obtained prior to the experiment. Each electrosorption/desorption experiment was performed until no conductivity variation was observed.

The salt adsorption capacity ( $SAC$ ), charge efficiency ( $Q_E$ ), and specific energy consumption ( $\eta$ ) were calculated according to Equations 4.13, 4.14, and 4.15, respectively, and were used to evaluate the performance of the electrode in the desalination process.

$$SAC = \frac{(C_0 - C)V}{m_E} \quad (4.13)$$

$$Q_E = 100 \frac{zFV\Delta C}{\int I_e dt} \quad (4.14)$$

$$\eta = \frac{E_{cell} \int I dt}{m_{rem}} \quad (4.15)$$

In these equations,  $C_0$  (mg/L) is the initial salt concentration,  $C$  (mg/L) is the salt concentration at time  $t$  (s),  $V$  (L) is the electrolyte volume,  $m_E$  is the mass of active material in

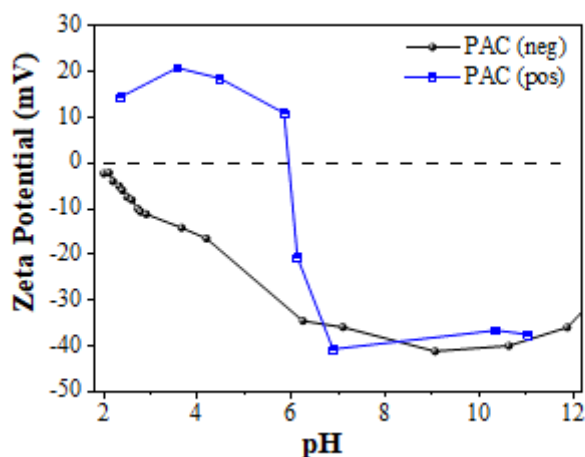
both electrodes,  $z$  is the ion charge,  $F$  is the Faraday constant (96485 C/mol),  $E_{cell}$  is the cell voltage applied for electrosorption (V), and  $m_{rem}$  is the mass of ions removed. The current  $I_e$  (Equation 4.14) is the effective current used for electrosorption (not considering the leakage current), while the current  $I$  (Equation 4.15) is the total current applied to the cell.

### 4.3. Results and Discussion

#### 4.3.1. Activated carbon characterization

Figure 4.3a shows the zeta potentials of the untreated and treated PAC in the pH range 2-12. The untreated PAC exhibited a negative net surface charge at all pH values, due to its high content of carboxylic groups, as previously found by Zornitta et al. [16]. Treatment with EDA [31] led to a positive charge, and mPAC showed both positive and negative net surface charges, with an isoelectric point at  $\text{pH} \approx 6$ .

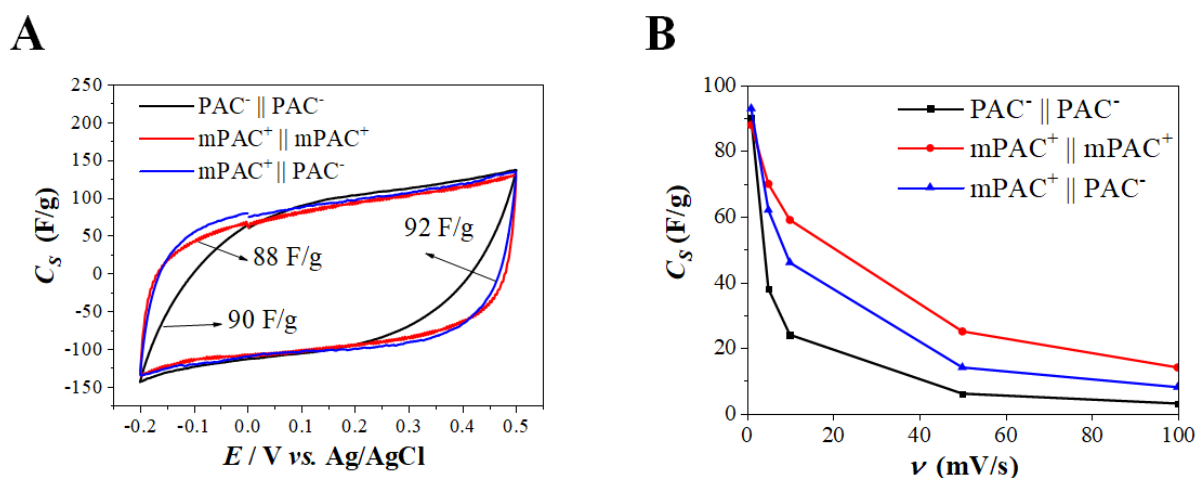
**Figure 4.3.** Zeta potential as a function of pH for PAC and mPAC



#### 4.3.2. Electrochemical characterization

Cyclic voltammetry characterization of the electrodes in different configurations was performed at different scan rates in order to analyze the electrode capacitance, resistivity, and mass transfer effects. The voltammograms obtained for the  $\text{mPAC}^+ \parallel \text{mPAC}^+$  and  $\text{PAC}^+ \parallel \text{PAC}^-$  configurations (Fig. 4.4a) showed quasi-rectangular shapes, characteristic of highly capacitive and conductive electrodes, while  $\text{PAC}^- \parallel \text{PAC}^-$  displayed some distortion, indicative of higher resistivity [33]. The specific capacitance calculated at 1 mV/s was similar for all electrodes and configurations, indicating that the capacitance was not affected by the surface treatment of the mPAC.

**Figure 4.4.** (A) Voltammograms for the  $\text{PAC}^-$  and  $\text{mPAC}^+$  electrodes at 1 mV/s, and (B) capacitance as a function of the scan rate. Electrolyte: 0.2 mol/L NaCl



In order to evaluate the electrode conductivity and mass transfer resistance, the capacitance values were calculated for different scan rates (Fig. 4.4b). For all the electrodes tested, higher capacitance values were obtained at the lowest scan rate, indicative of slow charging processes and resistance to penetration of the ions into the carbon structure at fast scan rates. The  $\text{mPAC}^+ \parallel \text{mPAC}^+$  combination presented the lowest mass transfer resistance, which could have been due to a combination of higher conductivity and a larger pore diameter, compared to  $\text{PAC}^- \parallel \text{PAC}^-$ . The quasi-rectangular shape of the curves (Fig. 4.4a) was indicative of higher conductivity of the  $\text{mPAC}^+ \parallel \text{mPAC}^+$  configuration [33]. It has been reported previously [34] that modification of PAC using EDA decreases the specific surface area and promotes pore enlargement, hence facilitating ion diffusion and EDL formation, even at high scan rates, and improving the charge storage capacity [35].

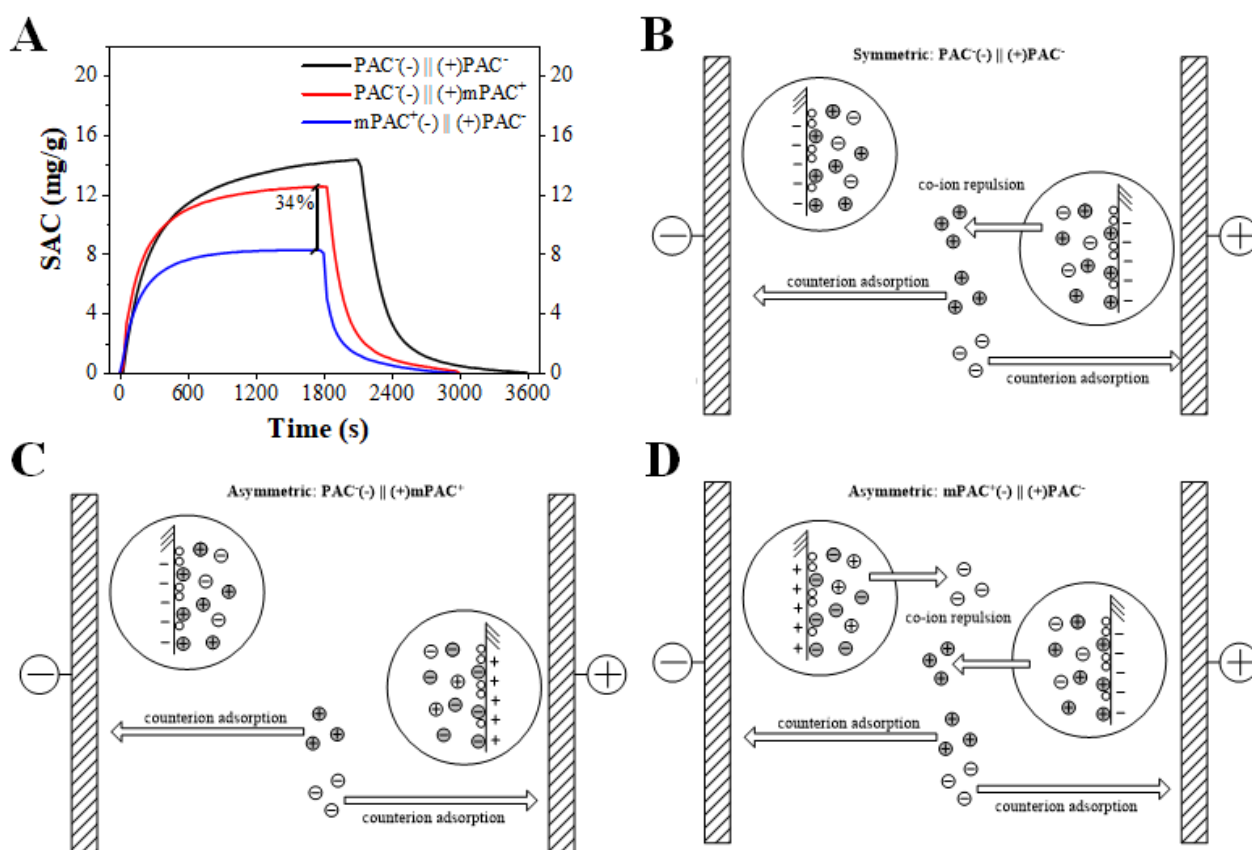
The fastest capacitance depletion rate was observed for  $\text{PAC}^- \parallel \text{PAC}^-$ , which could be explained by the narrow micropores of PAC,[16] which hindered ion diffusion, delayed EDL formation, and consequently reduced the capacitance. In the case of  $\text{mPAC}^+ \parallel \text{PAC}^-$ , intermediate behavior was observed for capacitance depletion according to scan rate, as expected since the limitations imposed by PAC and the improvements introduced using mPAC were still present.

### 4.3.3. Electrosorption

The desalination performances of the symmetric, asymmetric, and MCDI electrodes were compared in terms of electrosorption capacity, electrosorption kinetics, and energy

efficiency. The CDI performance achieved using asymmetric electrodes depends on the positions of the cathode and anode, related to the electrode surface charge. Figure 4.5 compares the electrosorption carried out using the symmetric and asymmetric electrodes. In the asymmetric configuration, the mPAC and PAC electrodes were positively and negatively polarized, respectively ( $\text{PAC}^-(-) \parallel (+)\text{mPAC}^+$ ). The opposite configuration ( $\text{mPAC}^+(-) \parallel (+)\text{PAC}^-$ ) was also evaluated, with the mPAC<sup>+</sup> and PAC<sup>-</sup> electrodes being negatively and positively polarized, respectively.

**Figure 4.5.** (A) Electrosorption and desorption performances of  $\text{PAC}^-(-) \parallel (+)\text{PAC}^-$ ,  $\text{PAC}^-(-) \parallel (+)\text{mPAC}^+$ , and  $\text{mPAC}^+(-) \parallel (+)\text{PAC}^-$  in 600 mg/L NaCl at 1.2 V, and schematic representations of co-ion repulsion and counterion adsorption for symmetric (B) and asymmetric configurations (C and D)



There was a clear influence of the surface charges of PAC and mPAC on SAC and the electrosorption kinetics of the asymmetric electrodes. The 34% higher SAC observed for the  $\text{mPAC}^+(-) \parallel (+)\text{PAC}^-$  configuration, compared to  $\text{PAC}^-(-) \parallel (+)\text{mPAC}^+$ , could be attributed to the less pronounced effect caused by repulsion of co-ions during the electrosorption process.



Prior to electrode polarization, the positively charged surface of mPAC promoted the repulsion of solution cations, while a repulsion of anions occurred at the negatively charged surface of PAC. As shown in Figure 4.5c, when the electrosorption started and a potential bias was applied, the greatest portion of the electrode potential was used for adsorption of cations and anions on the cathode (mPAC<sup>+</sup>(-)) and anode ((+)PAC<sup>-</sup>), respectively, instead of for the expulsion of co-ions from the EDL. Consequently, this type of asymmetry provided better ion removal. Using the opposite configuration (Fig. 4.5d), with PAC<sup>-</sup> and mPAC<sup>+</sup> as the cathode and anode, respectively, part of the charge applied for counterion adsorption was used to repel the co-ions from the PAC or mPAC EDL.[17] This becomes more evident considering the energy efficiency; while mPAC<sup>+</sup>(-) || (+)PAC<sup>-</sup> displayed a high  $Q_E$  (82%), a substantially lower  $Q_E$  (61%) was observed for the PAC<sup>-</sup>(-) || (+)mPAC<sup>+</sup> configuration, indicating that 39% of the charge supplied was probably used for repulsion of co-ions, instead of electrosorption. The same trend was observed for  $\eta$ , with the PAC<sup>-</sup>(-) || (+)mPAC<sup>+</sup> configuration presenting the worst energy efficiency among the electrode configurations analyzed, which could be explained by part of the applied  $E_{cell}$  being used to counterbalance the charge of the co-ions.

Figure 4.5a also provides a comparison of the asymmetric and symmetric configurations. Although the values of  $SAC$  for PAC<sup>-</sup>(-) || (+)PAC<sup>-</sup> were higher than for the asymmetric CDI, the electrosorption kinetics was slower. Table 4.1 displays the values of the pseudo-first order electrosorption kinetic constants. In all cases, the kinetic constants showed good fits to the electrosorption curves ( $R^2 > 95\%$ ). The faster kinetics observed for mPAC<sup>+</sup>(-) || (+)PAC<sup>-</sup> could be ascribed to faster electric double layer development, since co-ions repulsion was minimized and most of the charge provided to polarize the electrode surface was effectively used for electrosorption. In addition, the better electrode conductivity identified during the voltammetric characterization probably contributed to the faster kinetics. On the other hand, surface modification reduced the SSA and enlarged the pores [34], which also contributed to the faster kinetics of the asymmetric electrodes, but resulted in lower  $SAC_m$  values. It is also interesting to note that although the  $Q_E$  values obtained for PAC<sup>-</sup>(-) || (+)PAC<sup>-</sup> and mPAC<sup>+</sup>(-) || (+)PAC<sup>-</sup> were almost the same, the first configuration outperformed the second configuration in terms of  $\eta$ , which could be attributed to a lower leakage current (usually ascribed to faradaic reactions) in the case of PAC<sup>-</sup>(-) || (+)PAC<sup>-</sup>.

Chemical treatment of the PAC with EDA was used to provide surface charge in order to promote asymmetry between the electrodes, hence hindering co-ion repulsion during the electrosorption. The effect of co-ion repulsion during the electrosorption process is usually

responsible for loss of electrode capacity; hence, the minimization of this phenomenon is important for optimization of the CDI operation. Although the surface treatment acted to improve the electrode kinetics and conductivity, it probably had a deleterious effect on the SSA, as already reported elsewhere [34], hence leading to lower *SAC* values.

**Table 4.1.** *SAC*, kinetic constants,  $Q_E$ , and  $\eta$  for CDI carried out using different PAC and mPAC electrode configurations and applied voltages

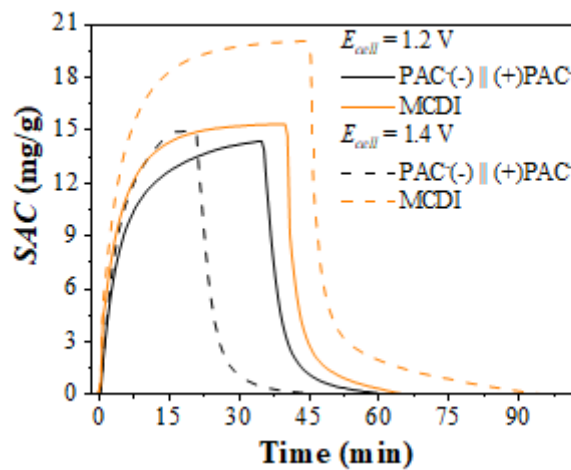
Configuration	$E_{cell}$ (V)	<i>SAC</i> (mg/g)	$k_e$ ( $\times 10^{-3}$ ) ( $s^{-1}$ )	$k_d$ ( $\times 10^{-3}$ ) ( $s^{-1}$ )	$Q_E$ (%)	$\eta$ (J/mg)
PAC <sup>-</sup> (-)    (+)PAC <sup>-</sup>	1.2	14.3	2.6	4.6	81	3.8
PAC <sup>-</sup> (-)    (+)PAC <sup>-</sup>	1.4	14.9	3.8	4.8	90	4.2
mPAC <sup>+</sup> (-)    (+)PAC <sup>-</sup>	1.2	12.5	3.9	5.2	82	4.1
PAC <sup>-</sup> (-)    (+)mPAC <sup>+</sup>	1.2	8.3	4.8	6.5	61	5.5
MCDI	1.2	15.3	3.4	5.6	81	2.8
MCDI	1.4	20.0	2.9	4.0	81	3.3

Another procedure widely employed to improve CDI by preventing co-ion repulsion is the use of ion-selective membranes. Figure 4.6 shows a comparison of the CDI and MCDI electrosorption processes carried out applying 1.2 V and 1.4 V. As expected, the selective membranes enhanced both *SAC* (by 7% at 1.2V and 34% at 1.4 V) and the energy efficiency of the electrodes (Table 4.1). The effect of the membranes on *SAC* could be ascribed to: (1) prevention of co-ion repulsion, which improved the electrode charge efficiency; (2) a high concentration of co-ions in the electrode macropores, which provided a driving force for attraction of counter ions; and (3) prevention of oxidation in the anode by reduction of the concentration of dissolved oxygen.[17,36,37] It is interesting to note that the membrane had a much greater influence on *SAC* improvement when 1.4 V was applied, rather than 1.2 V. This could be explained by the resistance introduced by the membrane (<40 ohm/cm<sup>2</sup>; Membranes International Inc.), resulting in a greater potential drop throughout the cell [17,24,37]. Considering that the membrane represented a series resistance within the cell, the effective potential used for electrosorption was lower than in a CDI process with application of the same  $E_{cell}$ .

The same trend was observed for energy efficiency. Although the *SAC* values were not significantly different for symmetric CDI and MCDI at 1.2 V, the values of  $\eta$  were lower (by

26%) for MCDI. As pointed out before, at the same applied  $E_{cell}$ , the electrode potential in MCDI is lower than in CDI [37], so the leakage current associated with faradaic reactions is consequently suppressed, resulting in lower values of  $\eta$  [38]. Accordingly, the value of  $\eta$  was higher at 1.4 V than at 1.2 V, because the greater electrode potential resulted in a higher leakage current. Nevertheless, the value of  $\eta$  for MCDI at 1.4 V was still the second lowest among all the electrodes. Therefore, the use of selective membranes seems to be promising for CDI, since it not only improves electrode capacity, but also reduces the energy requirement.

**Figure 4.6.** Plot of SAC against time for the MCDI and symmetric CDI, carried out at 1.2 V and 1.4 V in 600 mg/L NaCl



In summary, different strategies were studied in order to improve CDI desalination using PAC doped with PTS. The introduction of asymmetry in the electrodes only improved the electrosorption/desorption kinetics (Fig. 4.5a), while use of MCDI significantly improved the desalination capacity (Fig. 4.6). However, these results did not consider both electrosorption/desorption kinetics and capacity together, which will be analyzed below using the *OSR* method.

#### 4.3.4. Simultaneous analysis of SAC, $k_e$ , and $k_d$ using the OSR approach

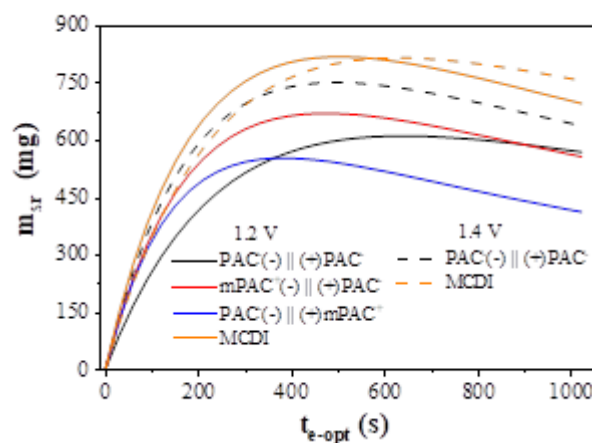
The previous sections present two important techniques employed to improve electrode capacity, preventing co-ion repulsion in order to maximize electrode performance for CDI. The highest SAC was obtained using MCDI at 1.4 V, while the fastest electrosorption kinetics was achieved using PAC<sup>-</sup>(-) || (+)mPAC<sup>+</sup> (Table 4.1). Although it is usually more intuitive to suppose that the electrode with the highest SAC is the best for the CDI operation,

the kinetics is also of great importance, since it determines the number of adsorption/desorption cycles. In this section, it is shown how these two electrode properties can be simultaneously evaluated using the *OSR* method, in order to determine the best electrode configuration for desalination. Equations 4.8 and 4.9 were used to calculate the values shown in Table 4.2 and Figure 4.7, illustrating the effects of the electrosorption capacity and kinetics on the final performance of the electrodes, considering an operational time of 24 h ( $t_{op} = 86400$  s or 1 day) and  $m_E = 1.0$  g.

**Table 4.2.** Parameters used to calculate *OSR* for the different electrode configurations, considering an operational time of one day

Electrode	$E_{cell}$ (V)	$t_{e-opt}$ (s)	$t_{d-99\%}$ (s)	$N_{cycles}$	$m_{e-opt}$ (mg)	<i>OSR</i> (mg/day)
PAC <sup>-</sup> (-)    (+)PAC <sup>-</sup>	1.2	639	1001	53	11.6	610
	1.4	493	959	60	12.6	750
mPAC <sup>+</sup> (-)    (+)PAC <sup>-</sup>	1.2	472	886	64	10.5	669
PAC <sup>-</sup> (-)    (+)mPAC <sup>+</sup>	1.2	381	708	79	7.0	552
MCDI	1.2	501	822	65	12.5	817
	1.4	626	1151	49	16.8	814

**Figure 4.7.** Plots of  $m_{sr}$  against  $t_{e-opt}$  for the symmetric and asymmetric CDI and MCDI



There are three different relations between capacity and kinetics that could be expected: i) the electrode with highest *SAC* would also have the highest *OSR*. This is usually true when the electrosorption/desorption kinetics of the electrodes are very similar and their *SAC* values are different. This was the case of the  $\text{mPAC}^{+(-)} \parallel (+)\text{PAC}^{-}$  and MCDI at 1.2 V, which showed almost the same numbers of cycles, but very different *SAC* values, with the MCDI outperforming the  $\text{mPAC}^{+(-)} \parallel (+)\text{PAC}^{-}$ ; ii) the electrosorption kinetics may enhance the electrode performance, even for low *SAC* values. For instance,  $\text{mPAC}^{+(-)} \parallel (+)\text{PAC}^{-}$  presented faster electrosorption than  $\text{PAC}^{-(-)} \parallel (+)\text{PAC}^{-}$  at 1.2 V, achieving 64 cycles, while the latter only achieved 53 cycles. Despite the higher *SAC* of  $\text{PAC}^{-(-)} \parallel (+)\text{PAC}^{-}$ , the faster kinetics of  $\text{mPAC}^{+(-)} \parallel (+)\text{PAC}^{-}$  enabled it to outperform  $\text{PAC}^{-(-)} \parallel (+)\text{PAC}^{-}$  in terms of *OSR*; and iii) an electrode with very high *SAC*, but slow kinetics. This was the case of MCDI at 1.4 V, which presented the highest *SAC* but the lowest electrosorption/desorption kinetics. Although the capacity played a very important role in maximizing the mass of salt removed, the slow kinetics of MCDI at 1.4 V resulted in lower *OSR*.

Evaluation of the desalination process in terms of *OSR* is very simple and provides valuable information about the electrode performance. Although few studies have provided data about desorption during CDI, Table 4.3 shows values of *OSR* estimated from different studies published in the literature. Under similar electrosorption/desorption conditions, the *OSR* obtained in this work was satisfactory, compared to previous work. Table 4.3 also shows situations in which the CDI electrodes presented very high *SAC* but very slow kinetics, such as in the case of the three-dimensional graphene, which achieved a capacity of 17.1 mg/g, with the electrosorption/desorption kinetics having the greatest influence on decreasing the *OSR* value.

In summary, comparison of all the electrodes evaluated in this study clearly demonstrated that the use of membranes enhanced electrode performance not only in terms of *SAC*, but also in terms of energy efficiency, resulting in the lowest values of  $\eta$  (Table 4.1). Although the use of asymmetric CDI improved the electrosorption/desorption kinetics, it was not sufficient to compensate for the loss of capacity caused by modification of the electrode surface. Therefore, although MCDI still faces challenges such as fouling and scaling, its high *SAC* (20 mg/g) and low energy consumption suggest MCDI as one of the best candidates for large-scale applications. The high *OSR* obtained using MCDI revealed that PAC electrodes are among the best electrodes for CDI. Moreover, although selective membranes add to the cost of CDI

equipment, the use of inexpensive PAC electrodes may make MCDI a competitive configuration for brackish water desalination.

**Table 4.3.** *OSR* values reported for different electrode materials.

Study	[NaCl] (mg/L)	$E_{cell}$ (V)	SAC (mg/g)	$k_e$ ( $\times 10^{-3}$ $\text{min}^{-1}$ )	$k_d$ ( $\times 10^{-3}$ $\text{min}^{-1}$ )	<i>OSR</i> (mg/day)
Rasines et al. [39]	1462.5	1.5	8.2	0.4	0.4	38
Rasines et al. [40]	1462.5	1.5	10.3	0.4	0.5	53
Li et al. [8]	500	1.2	16.1	4.2	5.7	939
Shi et al. [41]	500	1.6	17.1	1.6	0.7	163
Lado et al. [5]	600	1.2	5.3	1.7	1.4	86
Zhang et al. [42]	200	1.2	2.4	2.3	3.0	76
Ma et al. [43]	200	1.2	10.7	1.6	3.1	300
<b>This work</b>	600	1.2	15.3	3.4	5.5	817

#### 4.4. Conclusions

A novel approach called optimized salt removal (*OSR*) was employed to evaluate CDI electrodes, taking into account both capacity and kinetics. Different techniques were employed to enhance desalination performance by the reduction of co-ion repulsion and the use of asymmetric electrodes and MCDI, and this new method was evaluated for selection of the best electrode material and configuration.

Although the use of asymmetric electrodes improved the electrosorption/desorption kinetics, the electrode capacity decreased, relative to untreated electrodes. Nevertheless, application of the *OSR* method revealed that due to the enhanced kinetics, these electrodes outperformed symmetric electrodes (with non-treated material), since it was possible to perform many more cycles in the same operational time. In the case of MCDI, although the electrosorption/desorption kinetics became slower, the highest *SAC* value (up to 20 mg/g) was achieved using this configuration and applying 1.4 V. Hence, MCDI presented the highest *OSR* values among all the electrodes. However, comparison of the use of different cell voltages in MCDI showed that despite the lower *SAC* obtained at 1.2 V, the faster kinetics made this operational condition preferable to the use of higher cell voltages.

Application of the *OSR* approach revealed that an electrode exhibiting the highest *SAC* is not necessarily the best option for CDI, since kinetics can impose limitations. In the present case, use of MCDI at 1.2 V not only increased the *OSR* value, but also made the desalination process more energetically efficient. The findings showed that the *OSR* technique can be used for simple and straightforward evaluation of the performance of different CDI electrode configurations.

## References

- [1] M. a. Anderson, A.L. Cudero, J. Palma, Capacitive deionization as an electrochemical means of saving energy and delivering clean water. Comparison to present desalination practices: Will it compete?, *Electrochim. Acta.* 55 (2010) 3845–3856.  
doi:10.1016/j.electacta.2010.02.012.
- [2] R.L. Zornitta, J.J. Lado, M.A. Anderson, L.A.M. Ruotolo, Effect of electrode properties and operational parameters on capacitive deionization using low-cost commercial carbons, *Sep. Purif. Technol.* 158 (2016) 39–52.  
doi:10.1016/j.seppur.2015.11.043.
- [3] Y. Oren, Capacitive deionization (CDI) for desalination and water treatment — past, present and future (a review), *Desalination.* 228 (2008) 10–29.  
doi:10.1016/j.desal.2007.08.005.
- [4] C.T. Hsieh, H. Teng, Influence of oxygen treatment on electric double-layer capacitance of activated carbon fabrics, *Carbon N. Y.* 40 (2002) 667–674.  
doi:10.1016/S0008-6223(01)00182-8.
- [5] J.J. Lado, R.L. Zornitta, F.A. Calvi, M.I. Tejedor-Tejedor, M.A. Anderson, L.A.M.

- Ruotolo, Study of sugar cane bagasse fly ash as electrode material for capacitive deionization, *J. Anal. Appl. Pyrolysis*. 120 (2016) 389–398.  
doi:10.1016/j.jaap.2016.06.009.
- [6] X. Gu, Y. Yang, Y. Hu, M. Hu, J. Huang, C. Wang, Nitrogen-doped graphene composites as efficient electrodes with enhanced capacitive deionization performance, *RSC Adv.* 4 (2014) 63189–63199. doi:10.1039/C4RA11468J.
- [7] X. Xu, Z. Sun, D.H.C. Chua, L. Pan, Novel nitrogen doped graphene sponge with ultrahigh capacitive deionization performance., *Sci. Rep.* 5 (2015) 11225.  
doi:10.1038/srep11225.
- [8] G.X. Li, P.X. Hou, S.Y. Zhao, C. Liu, H.M. Cheng, A flexible cotton-derived carbon sponge for high-performance capacitive deionization, *Carbon N. Y.* 101 (2016) 1–8.  
doi:10.1016/j.carbon.2015.12.095.
- [9] S. Porada, F. Schipper, M. Aslan, M. Antonietti, V. Presser, T.P. Fellingner, Capacitive Deionization using Biomass-based Microporous Salt-Templated Heteroatom-Doped Carbons, *ChemSusChem*. 8 (2015) 1823. doi:10.1002/cssc.201500696.
- [10] X. Yang, D. Wu, X. Chen, R. Fu, Nitrogen-enriched nanocarbons with a 3-D continuous mesopore structure from polyacrylonitrile for supercapacitor application, *J. Phys. Chem. C*. 114 (2010) 8581–8586. doi:10.1021/jp101255d.
- [11] M. Trchová, E.N. Konyushenko, J. Stejskal, J. Kovářová, G. Ćirić-Marjanović, The conversion of polyaniline nanotubes to nitrogen-containing carbon nanotubes and their comparison with multi-walled carbon nanotubes, *Polym. Degrad. Stab.* 94 (2009) 929–938. doi:10.1016/j.polymdegradstab.2009.03.001.
- [12] J. Yan, T. Wei, W. Qiao, Z. Fan, L. Zhang, T. Li, Q. Zhao, A high-performance carbon derived from polyaniline for supercapacitors, *Electrochem. Commun.* 12 (2010) 1279–1282. doi:10.1016/j.elecom.2010.06.037.
- [13] L. Li, E. Liu, J. Li, Y. Yang, H. Shen, Z. Huang, X. Xiang, W. Li, A doped activated carbon prepared from polyaniline for high performance supercapacitors, *J. Power Sources*. 195 (2010) 1516–1521. doi:10.1016/j.jpowsour.2009.09.016.
- [14] A.B. Fuertes, T.A. Centeno, Mesoporous carbons with graphitic structures fabricated by using porous silica materials as templates and iron-impregnated polypyrrole as precursor, *J. Mater. Chem.* 15 (2005) 1079–1083. doi:10.1039/b416007j.
- [15] T. Kim, J. Yoon, CDI ragone plot as a functional tool to evaluate desalination performance in capacitive deionization, *Rsc Adv.* 5 (2015) 1456–1461.



- doi:10.1039/c4ra11257a.
- [16] R.L. Zornitta, F.J. García-Mateos, J.L. Lado, J. Rodríguez-Mirasol, T. Cordero, P. Hammer, L.A.M. Ruotolo, High-performance activated carbon from polyaniline for capacitive deionization, *Carbon N. Y.* 123 (2017) 318–333.
- [17] A. Omosebi, X. Gao, J. Landon, K. Liu, Asymmetric electrode configuration for enhanced membrane capacitive deionization, *ACS Appl. Mater. Interfaces.* 6 (2014) 12640–12649. doi:10.1021/am5026209.
- [18] X. Gao, A. Omosebi, J. Landon, K. Liu, Surface charge enhanced carbon electrodes for stable and efficient capacitive deionization using inverted adsorption–desorption behavior, *Energy Environ. Sci.* 8 (2015) 897. doi:10.1039/c4ee03172e.
- [19] K.C. Leonard, J.R. Genthe, J.L. Sanfilippo, W. a. Zeltner, M. a. Anderson, Synthesis and characterization of asymmetric electrochemical capacitive deionization materials using nanoporous silicon dioxide and magnesium doped aluminum oxide, *Electrochim. Acta.* 54 (2009) 5286–5291. doi:10.1016/j.electacta.2009.01.082.
- [20] Y.J. Kim, J.H. Choi, Enhanced desalination efficiency in capacitive deionization with an ion-selective membrane, *Sep. Purif. Technol.* 71 (2010) 70–75. doi:10.1016/j.seppur.2009.10.026.
- [21] R. Zhao, P.M. Biesheuvel, a. van der Wal, Energy consumption and constant current operation in membrane capacitive deionization, *Energy Environ. Sci.* 5 (2012) 9520. doi:10.1039/c2ee21737f.
- [22] H. Li, L. Zou, Ion-exchange membrane capacitive deionization: A new strategy for brackish water desalination, *Desalination.* 275 (2011) 62–66. doi:10.1016/j.desal.2011.02.027.
- [23] M. Mossad, L. Zou, A study of the capacitive deionisation performance under various operational conditions., *J. Hazard. Mater.* 213–214 (2012) 491–7. doi:10.1016/j.jhazmat.2012.02.036.
- [24] P. Hojati-Talemi, L. Zou, M. Fabretto, R.D. Short, Using oxygen plasma treatment to improve the performance of electrodes for capacitive water deionization, *Electrochim. Acta.* 106 (2013) 494–499. doi:10.1016/j.electacta.2013.05.119.
- [25] X. Xu, L. Pan, Y. Liu, T. Lu, Z. Sun, D.H.C. Chua, Facile synthesis of novel graphene sponge for high performance capacitive deionization., *Sci. Rep.* 5 (2015) 8458. doi:10.1038/srep08458.
- [26] Z. Chen, C. Song, X. Sun, H. Guo, G. Zhu, Kinetic and isotherm studies on the

- electrosorption of NaCl from aqueous solutions by activated carbon electrodes, *Desalination*. 267 (2011) 239–243. doi:10.1016/j.desal.2010.09.033.
- [27] X. Xu, Y. Liu, M. Wang, X. Yang, C. Zhu, T. Lu, R. Zhao, L. Pan, *Electrochimica Acta* Design and fabrication of mesoporous graphene via carbothermal reaction for highly efficient capacitive deionization, *Electrochim. Acta*. 188 (2016) 406–413. doi:10.1016/j.electacta.2015.12.028.
- [28] H. Li, L. Pan, Y. Zhang, L. Zou, C. Sun, Y. Zhan, Z. Sun, Kinetics and thermodynamics study for electrosorption of NaCl onto carbon nanotubes and carbon nanofibers electrodes, *Chem. Phys. Lett.* 485 (2010) 161–166. doi:10.1016/j.cplett.2009.12.031.
- [29] Y. Liu, L. Pan, T. Chen, X. Xu, T. Lu, Z. Sun, D.H.C. Chua, *Electrochimica Acta* Porous carbon spheres via microwave-assisted synthesis for capacitive deionization, *Electrochim. Acta*. 151 (2015) 489–496. doi:10.1016/j.electacta.2014.11.086.
- [30] H. Li, Y. Ma, R. Niu, Improved capacitive deionization performance by coupling TiO<sub>2</sub> nanoparticles with carbon nanotubes, *Sep. Purif. Technol.* 171 (2016) 93–100. doi:10.1016/j.seppur.2016.07.019.
- [31] X. Gao, S. Porada, A. Omosebi, K.L. Liu, P.M. Biesheuvel, J. Landon, Complementary surface charge for enhanced capacitive deionization, *Water Res.* 92 (2016) 275–282. doi:10.1016/j.watres.2016.01.048.
- [32] P.M. Biesheuvel, R. Zhao, S. Porada, A. van der Wal, Theory of membrane capacitive deionization including the effect of the electrode pore space, *J. Colloid Interface Sci.* 360 (2011) 239–248. doi:10.1016/j.jcis.2011.04.049.
- [33] E. Frackowiak, Carbon materials for the electrochemical storage of energy in capacitors, 39 (2001) 937–950.
- [34] G.D. Vuković, A.D. Marinković, M. Čolić, M.D. Ristić, R. Aleksić, A.A. Perić-Grujić, P.S. Uskoković, Removal of cadmium from aqueous solutions by oxidized and ethylenediamine-functionalized multi-walled carbon nanotubes, *Chem. Eng. J.* 157 (2010) 238–248. doi:10.1016/j.cej.2009.11.026.
- [35] L. Zou, L. Li, H. Song, G. Morris, Using mesoporous carbon electrodes for brackish water desalination, *Water Res.* 42 (2008) 2340–2348. doi:10.1016/j.watres.2007.12.022.
- [36] R. Zhao, O. Satpradit, H.H.M. Rijnaarts, P.M. Biesheuvel, A. van der Wal, Optimization of salt adsorption rate in membrane capacitive deionization, *Water Res.*

- 47 (2013) 1941–1952. doi:10.1016/j.watres.2013.01.025.
- [37] J.H. Choi, Determination of the electrode potential causing Faradaic reactions in membrane capacitive deionization, *Desalination*. 347 (2014) 224–229. doi:10.1016/j.desal.2014.06.004.
- [38] A. Hemmatifar, J.W. Palko, M. Stadermann, J.G. Santiago, Energy breakdown in capacitive deionization, *Water Res.* 104 (2016) 303–311. doi:10.1016/j.watres.2016.08.020.
- [39] G. Rasines, P. Lavela, C. Macías, M.C. Zafra, J.L. Tirado, J.B. Parra, C.O. Ania, N-doped monolithic carbon aerogel electrodes with optimized features for the electrosorption of ions, *Carbon N. Y.* 83 (2015) 262–274. doi:10.1016/j.carbon.2014.11.015.
- [40] G. Rasines, P. Lavela, C. Macías, M.C. Zafra, J.L. Tirado, C.O. Ania, Mesoporous carbon black-aerogel composites with optimized properties for the electro-assisted removal of sodium chloride from brackish water, *J. Electroanal. Chem.* 741 (2015) 42–50. doi:10.1016/j.jelechem.2015.01.016.
- [41] W. Shi, H. Li, X. Cao, Z.Y. Leong, J. Zhang, T. Chen, H. Zhang, H.Y. Yang, Ultrahigh Performance of Novel Capacitive Deionization Electrodes based on A Three-Dimensional Graphene Architecture with Nanopores, *Sci. Rep.* 6 (2016) 18966. doi:10.1038/srep18966.
- [42] H. Zhang, P. Liang, Y. Bian, Y. Jiang, X. Sun, C. Zhang, X. Huang, F. Wei, Moderately oxidized graphene–carbon nanotubes hybrid for high performance capacitive deionization, *RSC Adv.* 6 (2016) 58907–58915. doi:10.1039/C6RA10088K.
- [43] C. Ma, S. Huang, P. Chou, W. Den, C. Hou, Chemosphere Application of a multiwalled carbon nanotube-chitosan composite as an electrode in the electrosorption process for water purification, *Chemosphere*. 146 (2016) 113–120. doi:10.1016/j.chemosphere.2015.12.012.

## APPENDIX

The pseudo- $n$  order kinetics equation for  $n > 1$  (Equation A4.1) is shown adjusted for electrosorption and desorption in Equations A4.2 and A4.3, respectively.

$$\frac{1}{C_0^{n-1}} - \frac{1}{C(t)^{n-1}} = -k_n t \quad (\text{A4.1})$$

$$\frac{1}{SAC_m^{n-1}} - \frac{1}{SAC'(t)^{n-1}} = -k_{ne} t_e \quad (\text{A4.2})$$

$$\frac{1}{SAC_m^{n-1}} - \frac{1}{SDC(t)^{n-1}} = -k_{nd} t_d \quad (\text{A4.3})$$

Considering the number of cycles, calculated using Equation A4.4, and 99% desorption, Equation A4.3 may be rewritten as Equation A4.5.

$$N_{cycles} = \frac{t_{op}}{t_e + t_d} \quad (\text{A4.4})$$

$$t_{nd} = \frac{1}{k_{nd} SAC_m^{n-1}} (100^{n-1} - 1) \quad (\text{A4.5})$$

The mass of salt removed in one cycle is expressed by Equation A4.6.

$$m_{oc} = (SAC_m - SAC'(t)) \cdot m_E \quad (\text{A4.6})$$

Replacing  $t_{nd}$  in Equation A4.4, and inserting Equation A4.2 in Equation A4.6, the value of  $OSR$  for a pseudo- $n$  order process can be calculated using Equation A4.7.

$$m_{sr} = \frac{t_{op} m_E SAC_m}{t_e + \frac{1}{k_{nd} SAC_m^{n-1}} (100^{n-1} - 1)} \left( 1 - \frac{SAC_m^{n-2}}{1 + k_{ne} t_e SAC_m^{n-1}} \right) \quad (\text{A4.7})$$

Deriving Equation A4.7 in terms of  $t_e$ , and making it equal to zero, gives Equation A4.8.

$$k_d k_e t_e (SAC_m k_e t_e - 2) SAC_m^{2(n-1)} + (2k_d k_e t_e SAC_m - k_e 100^{n-1} - k_d + k_e) SAC_m^{n-1} + SAC_m k_d = 0 \quad (\text{A4.8})$$

Considering pseudo-first order kinetics, with  $n = 2$ , Equation A4.7 becomes:

$$OSR = \frac{t_{op} m_E}{t_e + \frac{99}{k_{2d} SAC_m}} \cdot \left( \frac{SAC_m k_{2e} t_e}{1 + SAC_m k_{2e} t_e} \right) \quad (\text{A4.9})$$

By deriving Equation A4.9 in terms of  $t_e$ , and making it equal to zero,  $t_{e-opt}$  is obtained according to Equation A4.10.

$$t_{e-opt} = \sqrt{\frac{99}{k_{2e}k_{2d}SAC_m^2}} \quad (A4.10)$$

## CHAPTER 5

# OPTIMIZED POLYANILINE-DERIVED CARBON ELECTRODES FOR CAPACITIVE DEIONIZATION

Capacitive deionization (CDI) emerged as new a water desalination technology in which ions are removed from brackish water by flowing between two polarized electrodes. Cations and anions move and are stored in the negatively and positively charged electric double layer (EDL), respectively. One of the most important components of the CDI cell is the electrode material, which affects other fundamental parameters such as the salt adsorption capacity (SAC), conductivity, desalination kinetics, and energy consumption. Typically, the CDI electrodes are carbon-based materials, fulfilling requirements as high specific surface area (SSA), chemical stability, and conductivity. Here, we make a comprehensive study of the variables involved in the polyaniline activated carbons (PAC) preparation. A new mechanism is proposed to explain how the carbonization/activation conditions have influence on textural properties (SSA and pore volume) of PAC. We found that carbonization at temperatures  $\leq 600$  °C are mandatory to provide more KOH-reactive carbon intermediates due to their turbostratic structure. After activation at 850 °C, remarkable pore volume (2.30 cm<sup>3</sup>/g) and SSA (~3600 m<sup>2</sup>/g) was achieved, which has direct influence on promoting high electrode capacitance (213 F/g, in 0.2 M NaCl), and SAC (22.2 mg/g, in 600 mg/L NaCl, 1.2 V). This SAC is among the highest values reported for CDI desalination using carbon electrodes. This work enlightens the mechanism to achieve high performance activated carbons, and provides a promising electrode material for CDI desalination.

### 5.1. Introduction

According to the United Nations, the access to potable water affects around 4 billion people living in areas of water scarcity, and this number could grow up to 6 billion until 2050.[1] In this context, water desalination is a feasible way to provide drinking water using well known technologies such as reverse osmosis,[2] electro dialysis,[3] and multistage flash distillation.[4]

In the last decade, capacitive deionization (CDI) has emerged as a promising technology for desalination. CDI is a low-cost technology employed mainly for brackish water desalination (salt concentration < 10000 mg/L). Based on the same principles of supercapacitors, the electric double layer (EDL) storages ions when the electrodes are polarized

at typical cell potentials ranging from 0.9 V to 1.2 V. In a simple CDI cell, the salt solution flows through a pair of charged electrodes, which attract and store the ions in the EDL. Once finished the electrosorption cycle, when the electrode saturates, a desorption cycle starts by short-circuiting the electrodes or inverting their polarization. In both cases, the ions are released back into a rinsing solution. This regeneration step can also be carried out before saturation in order to optimize the rate of salt removal in a full electrosorption/desorption cycle.[5]

Carbon has been widely studied as promising electrode material for CDI desalination since it encompasses desirable properties, such as: 1) high SSA and pore volume; 2) high conductivity; 3) easy polarization; 4) amphoteric behavior; 5) environmentally friendly material; 6) stability in different electrolytes.[6] Different forms of carbon with high salt adsorption capacity (SAC) and charge-efficiency have been investigated as electrode materials for CDI, such as: sponge,[7] cloth,[8] nanotubes,[9] graphene,[10,11] carbide-derived carbon[12], and activated[13,14]. However, despite of their good performance, most of these materials are still very expensive for an effective application.

Recently, we demonstrated that polyaniline-activated carbon (PAC) can be successfully applied as electrode for CDI desalination.[15] Besides the low-cost of the monomer, easy synthesis, and customization by varying the doping anion during the polymerization process, the high nitrogen content of polyaniline (PAni) (~15 wt%), may provide pyrrolic- and pyridinic-groups which enhances the carbon capacity and wettability due to their redox reactions.[16] It has also been observed changes in the PAC properties (conductivity, surface groups, and pore structure) when PAni had been doped with different anions. The highest SAC (14.3 mg/g) was achieved using the activated carbon derived from PAni doped with p-toluenesulfonic acid (PAni/PTS). The SAC was further improved by using ion selective membranes, reaching the value of 20.0 mg/g.[5,15] In these investigations, PAni was activated and carbonized at 850 °C, but we recently realized that the CDI performance improves as the carbonization temperature ( $T_C$ ) employed for PAC synthesis decreases, since  $T_C$  plays a very important role on the PAC properties. Therefore, in this work, we systematically investigate the effect of  $T_C$  on the electrode properties and CDI performance, along with the activation temperature ( $T_A$ ) and KOH/carbon PAni weight ratio ( $K/C$ ).

Few works explored the carbonization and activation temperature of PAni-activated carbons. Lin *et al.*[17] studied the carbonization, activation, and KOH/precursor ratio during the preparation of activated carbon used for CO<sub>2</sub> adsorption. These authors concluded that the carbonization and activation at 200 °C and 700 °C, respectively, and  $K/C$  2/1 provide the

highest specific surface area (*SSA*) ( $2720 \text{ m}^2/\text{g}$ ) and pore volume ( $1.68 \text{ cm}^3/\text{g}$ ). They state that the low carbonization temperature would not be enough to melt the KOH, and mix thoroughly with carbon, leading to a poor structure development. Zhang *et al.*[18] found that the carbonization and activation of PANi at  $200 \text{ }^\circ\text{C}$  and  $800 \text{ }^\circ\text{C}$ , respectively, and *K/C* 2/1 results in the highest *SSA* ( $3768 \text{ m}^2/\text{g}$ ), but the highest pore volume ( $2.85 \text{ cm}^3/\text{g}$ ) is achieved increasing *K/C* to 3/1. These authors suggest that PANi cross-linking at  $200 \text{ }^\circ\text{C}$  increases the *SSA* of the carbonized material, thus promoting a more homogeneous activation and leading to this high surface area. They also report that carbonization at temperatures higher than  $200 \text{ }^\circ\text{C}$  reduces the *SSA*, but the effect of the doping anion on the PANi cross-linking is not taken into account. On contrary, Silvestre-Ribeiro *et al.*[19], during their studies about the effect of  $T_A$  and  $T_C$  (*K/C* 3/1) using  $\text{SO}_3^{2-}$ -doped PANi, obtained the highest *SSA<sub>BET</sub>* ( $4240 \text{ m}^2/\text{g}$ ) after carbonization and activation at  $550 \text{ }^\circ\text{C}$  and  $800 \text{ }^\circ\text{C}$ , respectively. They suggest that the reactivity is ascribed to the amount of hydrogen on the carbon surface; however, they do not provide any evidence on this regard. In this scenario, the mechanisms of PANi carbonization and activation remains unclear, therefore demanding more experimental evidences to understand the role of  $T_A$  and  $T_C$  on the textural properties of the resulting activated carbon.

In this work, we present a comprehensive study about the influence of different activation conditions, bringing an insight on the role of carbonization/activation mechanism. PAC/PTS was chosen for this study since it is promising material for CDI. Here, we also present further evidences of the importance of PTS as doping anion on the properties of PAC. At first, the carbonization temperature was evaluated maintaining the same activation temperature and *K/C*. Then, the best carbonization temperature was applied to further investigate the activation temperature and *K/C*. All the materials were fully characterized by different techniques in order to provide the experimental background to understand the carbonization/activation mechanisms. The as obtained activated carbons were finally evaluated as electrodes for CDI. The desalination performance was evaluated in terms of SAC, electrosorption/desorption kinetics, and energy efficiency. Yet, a fully discussion on the role of the electrode properties and electrosorption behavior is provided in order to understand the entire process (from carbon properties up to desalination) and finishing with process optimization.

## 5.2. Experimental

### 5.2.1. Materials

The aniline monomer (99% Sigma-Aldrich) was distilled prior to polymerization and maintained in amber bottle at low temperature ( $< 3 \text{ }^\circ\text{C}$ ) to prevent oxidation. P-toluenesulfonic



acid monohydrate (HPTS,  $\geq 98.5\%$ , Sigma-Aldrich) was used as doping anion source. The oxidant used for polymerization was the ammonium persulfate (98%, Sigma-Aldrich).

Polyvinylidene fluoride (PVDF, Sigma-Aldrich) and n-methylpyrrolidone (NMP, 99.5%, Synth) were used as binder and solvent, respectively, for electrode preparation.

### 5.2.2. Polyaniline synthesis, activation, and electrode preparation

PAni was chemically synthesized using the best yield conditions adapted from Jelmi *et al.*[20]. Briefly, 10 mL of aniline was added at low temperature ( $\sim 3^\circ\text{C}$ ) and constant stirring to 500 mL solution containing 0.30 M HPTS. The polymerization started by adding 85.9 mL of the oxidant solution (1.0 M), dropped slowly into the monomer solution. The reaction was carried out for 2 h. After polymerization, the PTS<sup>-</sup>-doped PAni was filtered, washed with deionized water and dried in oven at  $60^\circ\text{C}$  for 24 h.[21] The polymer was labeled as PAni/PTS.

The PAni/PTS samples were carbonized at different temperatures ( $200^\circ\text{C}$ ,  $400^\circ\text{C}$ ,  $500^\circ\text{C}$ ,  $600^\circ\text{C}$ , and  $850^\circ\text{C}$ ) in a tubular furnace (Thermo Scientific Lindberg Blue M), at a heating rate of  $10^\circ\text{C}/\text{min}$  for 2 h, under  $\text{N}_2$  atmosphere ( $150\text{ mL}/\text{min}$ ). These samples were labeled as  $\text{C}_X$ , where X stands for the carbonization temperature divided by 100; for instance, the sample carbonized at  $500^\circ\text{C}$  was labeled as  $\text{C}_5$ . After carbonization, the samples were activated (PAC) using KOH pellets (Sigma-Aldrich) ( $K/C$  4/1), followed by heating at  $850^\circ\text{C}$  for 1.5 h using the same heating rate and  $\text{N}_2$  flow conditions as in the carbonization step. A non-carbonized PAni/PTS sample was activated under the same conditions. For a posterior study, samples carbonized at  $500^\circ\text{C}$  were activated varying the activation temperature ( $650^\circ\text{C}$ ,  $750^\circ\text{C}$ ,  $800^\circ\text{C}$ , and  $900^\circ\text{C}$ ). Two samples carbonized at  $500^\circ\text{C}$  were activated at  $750^\circ\text{C}$  and  $850^\circ\text{C}$ , using  $K/C$  2/1.

The as-obtained activated carbons were washed with HCl 0.5 M and warm water ( $60^\circ\text{C}$ ) until constant pH and then dried at  $105^\circ\text{C}$  for 24 h. The activated carbons were labeled as  $\text{C}_X\text{A}_Y\text{K}_Z$ , where X is the carbonization temperature divided by 100, Y the activation temperature divided by 10, and Z the  $K/C$ . For instance, the sample carbonized at  $500^\circ\text{C}$ , and activated at  $850^\circ\text{C}$  with  $K/C$  4/1 was labeled as  $\text{C}_5\text{A}_{85}\text{K}_4$ .

The carbon electrodes were prepared by mixing 10 wt.% of PVDF previously dissolved in NMP and 90 wt% of activated carbon. The slurry was kneaded and poured into a mold containing a graphite substrate. The mold was then placed into an oven at  $80^\circ\text{C}$  for 12 h to remove all the solvent and form the carbon film.[22]

### 5.2.3. Material Characterization

The carbon morphology was analyzed from images obtained in a scanning electron microscope (SEM, JEOL JSM-840) using high voltages (20-25 kV). SSA and pore size distribution (PSD) were determined from the N<sub>2</sub> adsorption/desorption isotherms at -196 °C using a Micrometics ASAP-2420. The samples were prior outgassed at 90 °C for 30 min, and then 300 °C for 240 min. The specific surface area was calculated using Brunauer-Emmett-Teller (BET) equation ( $SSA_{BET}$ ) in the linear regime between 0.01-0.30 P/P<sub>0</sub>, following the criteria proposed by Rouquerol *et al.*[23] The 2D-NLDFT Heterogeneous surface model was employed to calculate the pore size distribution,[24] total pore volume ( $V_{total}$ ), and DFT specific surface area ( $SSA_{DFT}$ ) using the SAIEUS (Solution Adsorption Integral Equation Using Splines) software. The pore size corresponding to the half of  $V_{total}$  was assumed as the average pore size ( $d_{50}$ ). The mesopore volume was determined by the difference between the total pore volume of N<sub>2</sub> adsorbed at P/P<sub>0</sub> > 0.95 and the micropore volume (pores ≤ 2 nm). The structure of the synthesized materials was characterized by X-ray diffraction (XRD) with CuK $\alpha$  = 1.5406 Å radiation and scanned for 2 $\theta$  values from 5-70 ° using Shimadzu XRD-6000 diffractometer.

The carbon composition was determined from thermogravimetric analysis (TGA) and its derivative (DTG) using a TA Instrument, model TGA Q500. The measurements were performed in a platinum pan in temperatures up to 900 °C, heating rate of 10 °C/min, in N<sub>2</sub> atmosphere (60 mL/min). The surface functional groups were identified by Fourier transform infrared spectroscopy FTIR (Bruker Vertex 70 spectrophotometer) using the KBr pellet technique and quantified using X-ray photoelectron spectroscopy analysis (XPS) using a Thermo Scientific instrument, model K-Alpha, with Al K $\alpha$  radiation source (1486.6 eV). Elemental analysis (CHNS) was performed with a Fisons – EA-1108 CHNS Element Analyzer (Thermo Scientific) at 1020 °C, calibrated with BBOT. The oxygen content was calculated by difference.

#### 5.2.4. Electrochemical characterization

Cyclic voltammetry (CV) was recorded at different scan-rates in 200 mM NaCl using a three-electrode cell with carbon electrodes as working (1.0 cm x 1.0 cm) and counter electrodes (1.0 cm x 2.5 cm), and Ag/AgCl in saturated KCl as reference electrode. The potential window between -0.2 V and 0.5 V vs. Ag/AgCl was previously determined to prevent redox reactions. A potentiostat Autolab PGStat 204 was used for all measurements.

The specific capacitance ( $C_s$ ) and the average specific capacitance ( $C_{cv}$ ) of the electrodes (F/g) were calculated using Eqs. 1 and 2, respectively, where  $I$  is the current,  $m$  the

mass of carbon in the working electrode (g), and  $E_1$  and  $E_2$  are the low and high values of the potential window.

$$C_S = \frac{I}{v.m} \quad (5.1)$$

$$C_{CV} = \frac{\int_{E_1}^{E_2} IdV}{v.m.(E_2-E_1)} \quad (5.2)$$

The converted deionization capacity ( $D_c$ ) was calculated using Eq. 3, in which  $E_{cell}$  is the applied cell potential (V),  $F$  the faraday constant (96485 C/mol), and  $M_w$  the molecular weight of NaCl (58.5 g/mol).

$$D_c = 1000.C_{CV}.E_{cell} \frac{M_w}{4.F} \quad (5.3)$$

The potential of zero charge ( $E_{PZC}$ ) was determined by electrochemical impedance spectroscopy (EIS) in 10 mM NaCl, applying an amplitude of 10 mHz and step potential (100 mV) starting from -0.3 V up to +0.6 V vs. Ag/AgCl. The capacitance ( $C_{EIS}$ ) was calculated using Eq. 4, in which  $\omega$  is the angular frequency and  $Z''$  the imaginary component of the EIS spectrum.  $C_{EIS}$  was normalized considering the lowest value of capacitance.

$$C_{EIS} = \frac{1}{|\omega Z''|} \quad (5.4)$$

### 5.2.5. Electrosorption

The desalination performance was evaluated using a recirculating batch setup previously described in Zornitta *et al.*[22] Briefly, the cell consisted of two acrylic plates with two titanium sheets (current collectors) in contact with the carbon electrodes (5 cm x 5 cm). A plastic mesh separated the electrodes providing a gap of 1.8 mm for the electrolyte to flow. Rubber gaskets sealed up the cell and all the components were assembled by nuts and bolts.

During desalination, an aqueous solution containing 600 mg/L NaCl (35 mL) recirculated through the CDI cell at a constant flow-rate (26 mL/min) using a peristaltic pump (Masterflex L/S Cole-Parmer). A potentiostat Autolab PGStat 204 applied a constant cell potential of 1.2 V (electrosorption) and 0 V (desorption). The solution conductivity was measured online at the exit of the cell and recorded every 30 s using a conductivity meter (Mettler Toledo SevenCompact Conductivity). The conductivity was converted to salt concentration using a linear relationship obtained prior to the experiment.

Salt adsorption capacity (SAC), charge efficiency ( $Q_E$ ) and specific energy consumption ( $\eta$ ) were calculated using Eqs. 5-7, respectively, and used to evaluate the performance of the electrode in the desalination process.

$$SAC = \frac{(C_0 - C_t).V}{m_E} \quad (5.5)$$

$$Q_E = 100 \times \frac{z.F.V.\Delta C}{\int I_e dt} \quad (5.6)$$

$$\eta = \frac{E_{cell} \cdot \int I dt}{m_{rem}} \quad (5.7)$$

In these Equations,  $C_0$  is the initial salt concentration (mg/L),  $C_t$  (mg/L) the salt concentration at time  $t$ ,  $V$  the volume of electrolyte (L),  $m_E$  the mass of active material in both electrodes,  $z$  the ion charge, and  $m_{rem}$  the mass of ions removed. The current ( $I_e$ ) in Eq. 6 is the effective current used for electrosorption (subtracting the leakage current) while the current ( $I$ ) in Eq. 7 is the total current.

The electrosorption and desorption kinetics were investigated through the optimized salt removal (*OSR*) technique, adapted from our previous work.[5] The electrosorption kinetics was fitted according to a pseudo first (Eq. 8) or pseudo second (Eq. 9) order models. The desorption kinetics was evaluated using the desorption time corresponding to the full regeneration of the electrode. The optimized electrosorption time ( $t_{e-opt}$ ) was calculated by deriving the amount of salt removed ( $m_{sr}$ ) (Eqs. 10 and 11 for pseudo 1<sup>st</sup> and 2<sup>nd</sup> order, respectively) and making it equal to zero. Replacing  $t_{e-opt}$  in Eq. 10 or 11 provides the *OSR* (mg/day).

$$SAC' = mSAC \cdot \exp(-k_1 \cdot t) \quad (5.8)$$

$$SAC' = \frac{mSAC}{1 + mSAC \cdot k_2 \cdot t_e} \quad (5.9)$$

$$m_{sr1} = \frac{t_{op} \cdot m_E \cdot mSAC}{t_e + t_d} (1 - e^{-k_e \cdot t_e}) \quad (5.10)$$

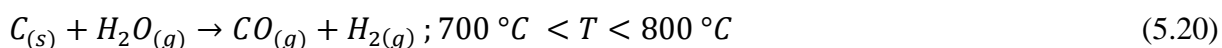
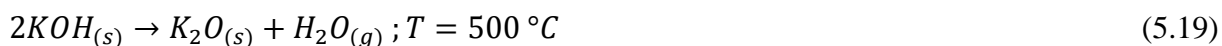
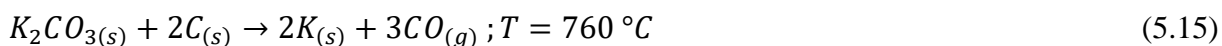
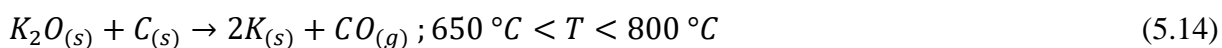
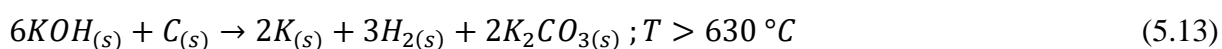
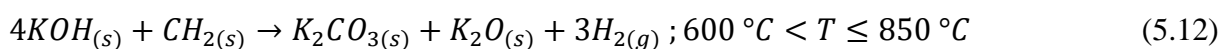
$$m_{sr2} = \frac{t_{op} \cdot m_E \cdot mSAC}{t_e + t_d} \left( 1 - \frac{mSAC^{n-2}}{1 + k_{ne} \cdot t_e \cdot mSAC^{n-1}} \right) \quad (5.11)$$

In these equations,  $mSAC$  is the highest value of SAC (mg/g),  $SAC' = mSAC - SAC(t)$ ,  $t_{op}$  the operational time (day),  $m_E$  the mass of both electrodes (g),  $t_e$  the electrosorption time,  $t_d$  the desorption time, and  $k_{ne}$  is the pseudo  $n$ -order electrosorption kinetics.

### 5.3. Results and Discussion

Table 5.1 displays the yield of carbonized PANi ( $Y_{CP}$ ) and PAC ( $Y_{PAC}$ ) obtained under different carbonization and activation conditions. Raising  $T_C$ ,  $Y_{CP}$  decreases since more volatiles are released. Accordingly, the lowest carbonization yield (35.2%) is obtained applying 850 °C. Surprisingly, the activation of the PANi carbonized at temperatures  $\leq 400$  °C led to the full consumption (reaction) of the precursor ( $Y_T = 0$ ), thus indicating its high reactivity with KOH. Considering the same activation condition, it is interesting to notice that the higher  $T_C$  the higher the  $Y_T$ , evidencing that KOH is more reactive with PANi carbonized at low temperatures.

Maintaining  $T_C$  at 500 °C and  $K/C$  at 4/1, the higher  $T_A$  the lower  $Y_T$  since more carbon reacts with KOH, which can be explained by the fact that most of the activation reactions displayed in Eqs. 12-20 occur only at high temperatures.[25–27] Therefore, at low  $T_A$  (e.g. 650 °C), the activation is less effective since the reactions involving  $CO_2$  (Eq. 18) and  $H_2O$  (Eq. 20) do not occur and, consequently, the values of  $Y_T$  are higher (24.8 wt.%). On the other hand, at high  $T_A$ , such as 900 °C, all the reactions in Eqs. 12-20 occur simultaneously, leading to a reduction of  $Y_T$  (11.4 wt.%).



The activation process was further investigated varying  $T_A$  from 750 °C to 850 °C, but maintaining  $T_C$  at 500 °C and  $K/C$  at 2/1. As  $T_A$  increases,  $Y_T$  diminishes, but this trend is more sensitive using  $K/C$  2/1. Besides, the low values of  $Y_{PAC}$  at high  $T_A$  is an indicative of high SSA development since the activation is more effective and the reaction products removal is facilitated. On the other hand, the use of high temperatures also have a deleterious effect on the SSA, such as pore collapsing and shrink.[28]

According to Eqs. 12-17, activation with KOH is mostly influenced by the presence of potassium. In order to compare its influence on the activation,  $C_5$  was activated at 850 °C using  $K_2CO_3$  (sample  $C_5A_{85}KC$ ). The weight ratio of  $K_2CO_3$  to carbon (4.95:1) was chosen to provide the same KOH/carbonized PANi ratio used to obtain  $C_5A_{85}K_4$ . The highest  $Y_T$  observed for this sample (34 wt.%) is attributed to the less effective reaction between carbon and potassium due to the reduction of  $K_2O$  and  $K_{(s)}$  (Eqs. 12 and 13), and the lack of carbon reaction with  $H_2O$ , since reactions in Eqs. 19 and 20 do not occur.

### 5.3.1. Characterizations

Figure 5.1a displays a micrograph of PANi/PTS after the chemical synthesis, revealing the typical coral-like morphology with interconnected rods with diameters ranging from 200-300 nm.[29] After carbonization at 500 °C ( $C_5$ ) (Fig. 5.1b) the rods melted (melting point of PANi  $\approx$  330 °C), but the coral-like morphology is preserved. The rod diameters grow up to 450-850 nm. The same morphology is observed for  $C_4$  and  $C_{8.5}$ , but the rod size is larger when  $T_C$  increases (Fig. A5.1a and b).

After activation, the morphologies are completely distinct, *e.g.*  $C_5A_{85}K_4$  (Fig. 5.1c) has a smooth surface which results from the complete melting of  $C_5$ . The large cavities (0.8-2  $\mu$ m) probably results from the strong reaction between the precursor and KOH, which releases large amounts of volatiles during the activation. The surface becomes smoother, compact, and with few cavities when  $T_C$  is higher than 850 °C, *e.g.*  $C_{8.5}A_{85}K_4$  (Fig. 5.1d).

The XRD pattern of PANi/PTS and carbonized samples are shown in Figure 5.2a. The reflections for PANi/PTS refers to the typical PANi structure.[30] After carbonization, the diffraction profiles for  $C_4$  and  $C_5$  exhibit a broad band centered at 20.7 °, which is assigned to the amorphous carbon structure composed of microcrystalline carbon fragments (turbostratic structure) (Fig. 5.2b).[31] The disordered arrangement of the graphite basal planes in the turbostratic structure provides an open framework with more spaces between the planes. Yet, the surface groups formed at the edges of the carbon structure provide higher chemical reactivity, when compared to graphitic carbon.[32] Interestingly,  $C_{8.5}$  shows two broad diffraction bands at 25° and 43° assigned to graphitic structure (Fig. 5.2c), indicating that this carbon has a more developed and organized structure than the carbonized at low temperatures. In addition, the formation of the graphitic structure decreases the mesopore volume and promotes a change in morphology, as confirmed by the SEM images (Figs. 5.1 and A5.1), and TEM micrographs (Fig. A5.2).[33,34]

In order to further understand the reactivity of the carbonized PANi with KOH, the carbons were characterized by elemental analysis, TGA, and FTIR. Table 5.2 shows the elemental composition of PANi/PTS and the carbonized and activated materials. Considering that PANi is composed only by carbon, nitrogen and hydrogen, the presence of sulfur in the samples is assigned solely to the presence of the doping anion PTS. Based on the sulfur and nitrogen content, the later present in the in the polymer backbone, the oxidation state of PANi was estimated by atomic balance. The doping level was calculated as 43.4 wt.%, giving an

oxidation state of 0.47, which means that almost half of the polymer is formed by quinone units, which corresponds to the protonated emeraldine salt.[35]

**Figure 5.1.** SEM images of the PAni/PTS (A), C<sub>5</sub> (B), C<sub>5</sub>A<sub>85</sub>K<sub>4</sub> (C), and C<sub>8.5</sub>A<sub>85</sub>K<sub>4</sub>

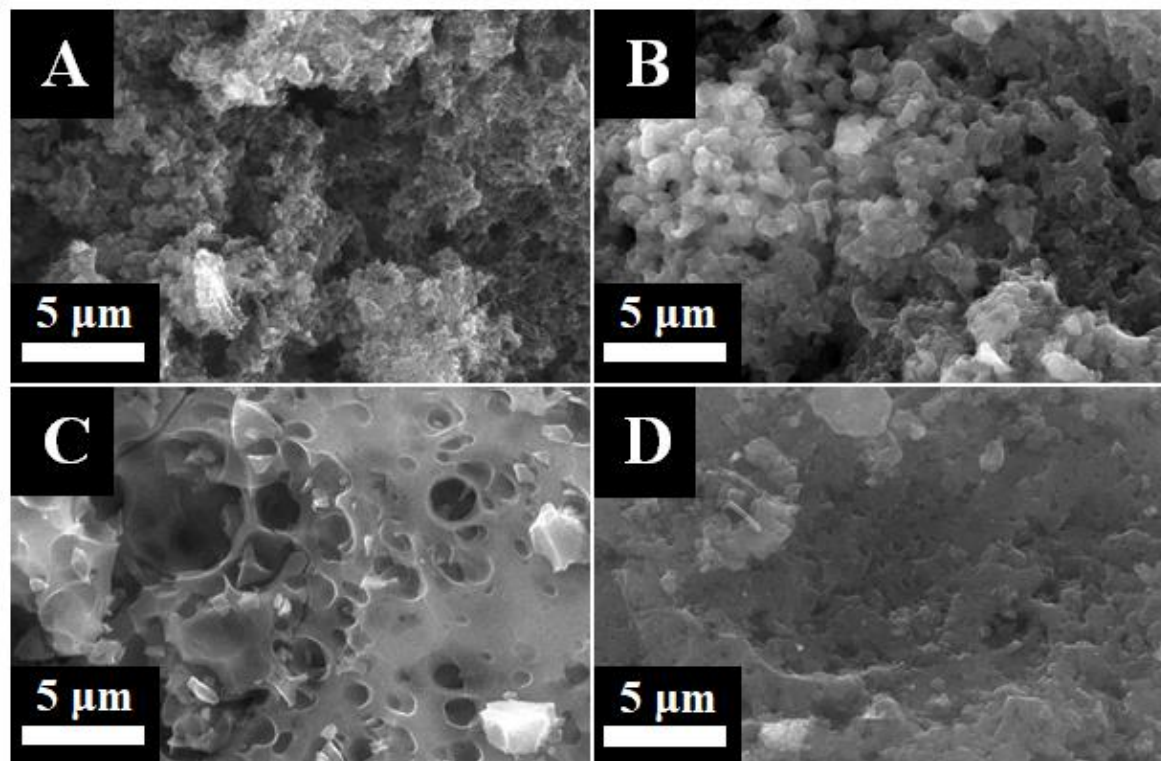


**Figure 5.2.** (A) XRD patterns for PAni/PTS, C<sub>4</sub>, C<sub>5</sub> and C<sub>8.5</sub> samples, (B) turbostratic structure, and (C) graphitic structure

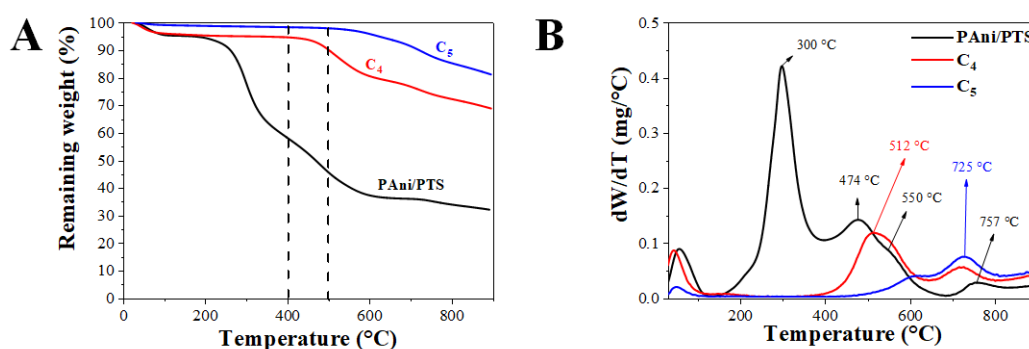
**Table 5.2.** Elemental analysis of PAni/PTS and their carbonization and activation products, weight percentage of PTS, and ratio between the oxygen from PTS and total oxygen content (O<sub>PTS</sub>/O)

	C	H	N	S	O	O <sub>PTS</sub> /O
	wt. %					
PAni/PTS	56.3	4.6	7.5	8.1	23.5	0.53
C <sub>4</sub>	64.2	4.1	10.1	2.2	19.5	0.17
C <sub>5</sub>	66.5	4.1	10.0	1.7	17.8	0.14
C <sub>8.5</sub>	78.3	3.2	6.4	2.0	10.1	0.30
C <sub>5</sub> A <sub>65</sub> K <sub>4</sub>	78.3	4.5	5.2	0	12.0	0
C <sub>5</sub> A <sub>85</sub> K <sub>4</sub>	87.7	3.7	1.6	0	7.0	0
C <sub>5</sub> A <sub>75</sub> K <sub>2</sub>	83.6	3.8	2.1	0	10.5	0
C <sub>5</sub> A <sub>85</sub> KC	71.6	1.8	1.3	1.0	24.3	0.06

Figures 5.3a and b show the TGA and dTGA, respectively, for PAni/PTS, C<sub>4</sub>, and C<sub>5</sub>. In the range between 50 °C and 105 °C, all samples presented a small mass loss (~5 wt.%) due

to the release of physisorbed water. The presence of water explains the oxygen content not assigned to the dopant in PAni/PTS (7.7 wt.%). From 280-320 °C there is an expressive mass loss for PAni/PTS, commonly attributed to the release of carboxylic, lactone and/or anhydride groups.[36] Considering that non-doped PAni is oxygen-free, the weight loss rate observed at 300 °C confirms the release of oxygen from the PTS. This trend agrees well with other studies.[37] As expected, no mass loss at 300 °C is observed for C<sub>4</sub> and C<sub>5</sub> since both samples have been carbonized at high temperatures. The elemental analysis also reveals that the sulfur content decreases 5.9 wt.% when PAni/PTS is carbonized at 400 °C. On the other hand, not all oxygen released during the carbonization comes from the dopant, as estimated by the O<sub>PTS</sub>/O ratio.

**Figure 5.3.** TGA (A), and dTGA (B) of PAni and their carbonization products



Since the PAni decomposition occurs between 450-600 °C,[37] two thermal events in this regard are identified in the dTGA of PAni/PTS at 474 °C and 550 °C, while only one is observed for C<sub>4</sub> at 512 °C and C<sub>5</sub> at 600 °C. This difference is attributed to the partial decomposition of the carbon during the carbonization step prior to the TGA analysis. Although the elemental analysis revealed that the oxygen content decreases as  $T_A$  increases, the amount of oxygen released assigned to PTS (O<sub>PTS</sub>) is different for samples C<sub>4</sub> and C<sub>5</sub> and, consequently, the ratio O<sub>PTS</sub>/O decreases (Table 5.2). These results suggest that although some compounds assigned to PTS decomposition have been released, other compounds still remain in the C<sub>8.5</sub> structure. Therefore, carbonization at high temperature (C<sub>8.5</sub>) increases the content of carbon. Taking into account the elemental analysis, the thermal events at 725 °C (C<sub>4</sub> and C<sub>5</sub>) and 757 °C (PAni/PTS) were ascribed to the elimination of some nitrogen groups at high-temperatures, which reduces the content of nitrogen, while the percentage of sulfur remains practically the same, indicating that the content of sulfur in the carbon structure is stabilized at 500 °C. No evident trend between  $T_C$  and the hydrogen content in the samples is observed. After reaching



850 °C, the remaining mass of PANi is ~32 wt.%, which is in good agreement with  $Y_{CP}$  for  $C_{8.5}A_{85}K_4$  (Table 5.1) and aligns well to other values found in literature.[37,38]

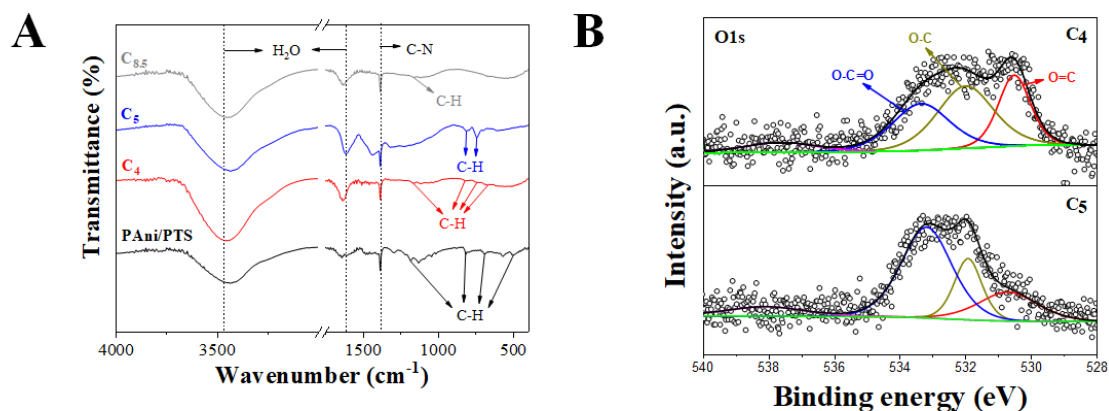
The absence of sulfur in the activated carbons is due to desulfurization reaction promoted by the KOH, as already demonstrated elsewhere.[39] Low carbonization and activation temperatures led to a high nitrogen content (5.2 wt.% for  $C_5A_{65}K_4$ ), but even at high activation temperatures the nitrogen content is not negligible (1.6 wt.% for  $C_5A_{85}K_4$ ). The presence of nitrogen in some surface groups is important for electrochemical applications, since they can carry out redox reactions. Activation using  $K_2CO_3$  led to an oxygen-rich material, indicating a more oxidized surface.

FTIR analysis was carried out to obtain information about the surface groups in PANi/PTS and their carbonization products. According to Figure 5.4a 4A, all samples present absorbance at  $3470\text{ cm}^{-1}$ ,  $1630\text{ cm}^{-1}$ , and  $1384\text{ cm}^{-1}$ , characteristic of the stretching and deformation vibrations of water and C-N stretching, respectively.[40–42] The absorbance bands observed for PANi/PTS at  $491\text{ cm}^{-1}$ ,  $685\text{ cm}^{-1}$ ,  $815\text{ cm}^{-1}$ , and  $1182\text{ cm}^{-1}$  are assigned to out-of-plane C-H bending of the benzenoid ring. For the carbonized samples, the C-H bending are slightly displaced to different positions:  $669\text{ cm}^{-1}$ ,  $741\text{ cm}^{-1}$ ,  $810\text{ cm}^{-1}$ , and  $1163\text{ cm}^{-1}$  for  $C_4$ , and  $695\text{ cm}^{-1}$ ,  $745\text{ cm}^{-1}$ , and  $813\text{ cm}^{-1}$  for  $C_5$ . Only a very weak band at  $1163\text{ cm}^{-1}$  is observed for  $C_{8.5}$ . [43–47] For PANi/PTS, the bands at  $1041\text{ cm}^{-1}$  and  $1130\text{ cm}^{-1}$  are ascribed to the presence of  $HSO_4^-/SO_3^-$  in the sulfonated aromatic ring due to  $PTS^-$ , while the vibrations at  $1298\text{ cm}^{-1}$  and  $1479\text{ cm}^{-1}$  are assigned to C-N and C=C ring vibration of the benzenoid ring, respectively.[42,48] The band at  $1444\text{ cm}^{-1}$  for  $C_5$  is ascribed to the C=C bending vibration.[49]

FTIR reveals the diminution of surface groups as  $T_C$  increases. Groups assigned to C-H bonds are present in all samples, with a slightly decrease in the samples carbonized at higher temperatures. This aligns well with the elemental analysis, in which the variation of the hydrogen content in the carbonized is negligible, and shows that the amount of hydrogen *per se* does not explain the higher reactivity of the  $C_5$  with KOH than  $C_{8.5}$  as suggested by other authors.[19] To further understand the higher reactivity of  $C_4$  compared with  $C_5$ , both materials were characterized by XPS (Fig. 5.4b). Although the carbon content is higher in  $C_5$ , the nitrogen content decreases as  $T_C$  increases (Table A5.1). The N-groups in both materials are assigned to pyridinic (~398.1 eV) and pyrrolic (~399.8 eV) groups (Fig. A5.3). Although similar oxygen content has been determined for  $C_4$  and  $C_5$ , there are differences in oxygen bonding groups. The O1s spectra for  $C_4$  reveals the presence of C=O (~530.5 eV), and C-O (~532.0 eV) groups (63.0 at.%), while  $C_5$  is mainly composed by the O-C=O (~533.2 eV) (52.4 at.%). The sulfur

content is negligible in both cases. These results evidence the influence of the carbonized temperature on the carbon surface properties and suggest that the presence of different oxygen surface groups can induce to different reactivity during the carbonization step.

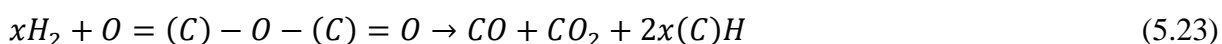
**Figure 5.4.** FTIR of PANi and their carbonization products (A), and high resolution deconvoluted O1s XPS spectra of C<sub>4</sub> and C<sub>5</sub> (B)



Indeed, oxygen surface groups such as aldehydes/ketones (C=O), alcohol/phenol/epoxy (C-O), and carboxylic acid/ester (O=C-O) reacts with KOH before and throughout the activation; however, at room temperature, aldehyde undergo nucleophilic substitution reaction (Cannizzaro Reaction) in concentrated KOH (Eq. 21), forming carboxylic potassium salt and alcohol.[50] Other reaction involving alcohol dehydration in basic media (Eq. 22), have also been reported.[51] Reactions of KOH with the precursor may also play an important role on the mechanism of carbon activation. Chunlan *et al.*[52] suggested a mechanism in which KOH reacts with surface groups forming C-O-K intermediates which react at high temperature with the carbon surface to form K<sub>2</sub>CO<sub>3</sub> and K<sub>2</sub>O (Eqs. 12, 13, 17, and 19). Posteriorly, the potassium compounds are deoxidized forming metallic K, which intercalates in the *d*-space of the carbon layers. Therefore, the reactions in Eqs. 21 and 22 represent intermediate steps in the activation mechanism. Other authors also suggested that potassium and oxygen present in the surface groups might cause the lamellae separation by oxidation of the crosslinking carbon atoms during activation.[53]



As the mixture of the carbon precursor and KOH are heated up during the activation step, H<sub>2</sub> is formed according to reactions in Eqs. 12, 13, and 20. During the activation, the oxygen content diminishes due to the reaction of hydrogen with oxygen groups, such as the carboxylic acid anhydride, according to Eq. 23.[56-58] Despite of the low oxygen content on the C<sub>4</sub> and C<sub>5</sub> surfaces (Table A5.1), the elemental analysis has evidenced a greater amount in the bulk (Table 5.2). Comparing the elemental analysis for C<sub>5</sub> before and after activation (C<sub>5</sub>A<sub>65</sub>K<sub>4</sub>, C<sub>5</sub>A<sub>85</sub>K<sub>4</sub>, and C<sub>5</sub>A<sub>75</sub>K<sub>2</sub>), the oxygen content decreases due to carbon conversion to CO and CO<sub>2</sub>, according to Eq. 23.



### 5.3.2. Mechanism of activation of the carbonized precursors

Based on the characterization results, we propose a new mechanism for the KOH activation of the carbonized PANi/PTS precursor obtained at different temperatures. The mechanisms proposed in prior studies[18,19] does not explain our results since no activation occurs for the samples carbonized at  $T_C \leq 400$  °C (the precursor is totally consumed in the reaction with KOH) and no variation on the hydrogen content is detected. According to our experimental evidences, the role of  $T_A$  on the activated carbon is based on two mechanisms occurring simultaneously: Facilitated-K intercalation and surface groups reactivity.

We propose that the reactions expressed by Eqs. 21 and 22 take place prior the activation process, forming –C-O-K as intermediary. Considering the commonly accepted activation mechanism for KOH activation, as the carbon precursor and the activating agent are continuously heated up during the activation step, K<sub>2</sub>CO<sub>3</sub> and K<sub>2</sub>O are formed according to Eqs. 12, 13, 17, and 19. Simultaneously, the hydrogen released during activation (Eqs. 12, 13, and 20) reacts with the oxygen groups according to Eq. 23, and the potassium oxides are deoxidized to form metallic K, which intercalates in the carbon structure.

According to our X-ray analysis (Fig. 5.2), the turbostratic structure is formed when PANi is carbonized at 400 °C or 500 °C. The open framework of this structure facilitates the K intercalation, thus promoting more effective activation, resulting in the C<sub>5</sub>A<sub>85</sub>K<sub>4</sub> morphology (Fig. 5.1c). The turbostratic structure is also characterized by many functional groups at the edges of the basal planes which further improves the reactivity of C<sub>4</sub> and C<sub>5</sub> with KOH. According to the XPS analysis (Table A5.1), these groups are mainly composed by oxygen (C=O, C-O, and O=C-O). This trend also explains why C<sub>4</sub> activation did not result in any activated carbon. In this case, the partial decomposition of PANi during the carbonization step

(Fig. 5.3a and b), the turbostratic structure and the oxygen-rich precursor (Table A5.1) promoted a remarkable reactivity with KOH, leading to the total carbon consumption, consequently,  $Y_T = 0$ .

On contrary, when PANi is carbonized at 850°C, the graphitic structure (Fig. 5.2) hinders the access of the metallic potassium, reducing its reactivity with carbon. Simultaneously, the reactivity decreases due the minor content of oxygen surface groups (Table A5.1), which are volatilized at high temperatures, thus preventing the intermediate reactions in Eqs. 21-23. This trend is also corroborated by the more compact morphology exhibited by  $C_{8.5}A_{85}K_4$  (Fig. 5.1d).

The comprehension of these mechanisms of carbonization/activation is extremely important since they influence the textural and electrochemical properties and, consequently, affects the electrosorption/desorption kinetics and ion storage capacity of the activated carbon used for CDI purposes.

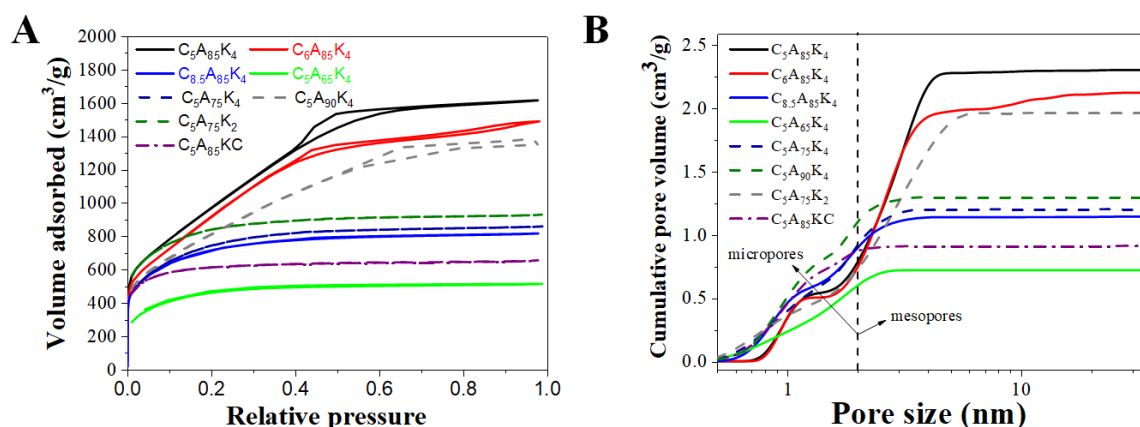
### 5.3.3. Textural properties

Figure 5.5a displays the  $N_2$  adsorption/desorption isotherms for the carbons prepared under different activation conditions.  $C_5A_{85}K_4$  and  $C_6A_{85}K_4$  present type II isotherms while the other activated carbons present type I isotherm according to IUPAC classification.[56] The high  $N_2$  uptake at low pressures ( $P/P_0 < 0.01$ ) for all carbons indicates the presence of micropores (pore width  $< 2$  nm). The steady increase in the  $N_2$  uptake for  $C_5A_{85}K_4$ ,  $C_6A_{85}K_4$ , and  $C_5A_{90}K_4$  up to  $P/P_0 = 0.5$  and the less pronounced H4-type hysteresis loop are attributed to mesoporosity (pore width  $> 2$  nm). The PSD (Fig. 5.5b) determined from the isotherms confirmed the presence of mesopores occupying 66%, 65%, and 63% of the total pore volume for  $C_5A_{85}K_4$ ,  $C_5A_{85}K_4$ , and  $C_5A_{90}K_4$  respectively (Table 5.3). It is important to notice the remarkable values of  $SSA_{BET}$  for  $C_5A_{85}K_4$  and  $C_6A_{85}K_4$ : 3653  $m^2/g$  and 3539  $m^2/g$ , respectively. More realistic values of specific surface area were calculated using the 2D-NLDFT method ( $SSA_{DFT}$ ) and are compared with  $SSA_{BET}$  in Table 5.3.[24,56] Notwithstanding the values of  $SSA_{DFT}$  are lower than  $SSA_{BET}$ , they are still very high compared to other activated carbons found in literature.

As seen in Table 5.3, the activation process is mandatory to obtain high SSA, but  $T_C$  has an expressive influence on the textural properties of the activated carbons. Accordingly, when  $T_C$  raises from 500 °C ( $C_5A_{85}K_4$ ) to 600 °C ( $C_6A_{85}K_4$ ) or 850 °C ( $C_{8.5}A_{85}K_4$ ), maintaining the same activation conditions, the  $SSA_{DFT}$  decreases 7.2% and 20.0%, respectively. This trend aligns well with the observed for  $Y_{PAC}$  ( $C_{8.5}A_{85}K_4 \geq C_5A_{85}K_4 \geq C_6A_{85}K_4$ ). Indeed, this reinforces our hypothesis which states that higher reactivity between the precursor and KOH occurs when

PAni is carbonized at low  $T_C$ . Furthermore, as  $T_C$  decreases from 850 °C to 500 °C, the total pore volume of the activated carbon increases 45% due to the pore enlargement (Table 5.3). It is noteworthy that in our previous study,[15] the  $SSA_{BET}$  of the sample  $C_{8.5}A_{85}K_4$  was 59% lower than the obtained in this work, just because the KOH-impregnation method was different. In our previous work, the carbonized material was mixed with KOH and immediately activated at 850 °C. In this work, the impregnation lasted 24 h, suggesting that the contact between the carbonized material and the KOH play an important role on the pore development, especially on the light of the proposed carbonization/activation mechanism.

**Figure 5.5.** Nitrogen adsorption-desorption isotherms (A), and PSD (B) of polyaniline activated carbon obtained under different activation conditions. The isotherms and PSD for  $C_5$  and  $C_{8.5}$  are shown in **Figure A5.3**



**Table 5.3.**  $SSA_{BET}$ ,  $SSA_{DFT}$ , total volume of pores ( $V_{total}$ ), volume of micropores ( $V_{mic}$ ), percentage of mesopores ( $\%V_{mes}$ ), and average pore diameter ( $d_{50}$ ) obtained from the  $N_2$  adsorption/desorption isotherms

Material	$SSA_{BET}$ (m <sup>2</sup> /g)	$SSA_{DFT}$ (m <sup>2</sup> /g)	$V_{total}$ (cm <sup>3</sup> /g)	$V_{mic}$ (cm <sup>3</sup> /g)	$\%V_{mes}$	$d_{50}$ (nm)
$C_5$	158	106	0.08	0.07	20	1.6
$C_{8.5}$	332	467	0.16	0.16	0	0.7
$C_5A_{85}K_4$	3649	2470	2.30	0.78	66	2.5
$C_6A_{85}K_4$	3539	2291	2.12	0.74	65	2.4
$C_{8.5}A_{85}K_4$	2617	1978	1.14	0.90	21	1.2
$C_5A_{65}K_4$	1687	1175	0.71	0.59	17	1.3
$C_5A_{75}K_4$	2725	2059	1.21	0.92	24	1.4
$C_5A_{90}K_4$	2945	2361	1.96	0.72	63	2.5
$C_5A_{75}K_2$	3063	2353	1.30	1.10	15	1.1
$C_5A_{85}KC$	2329	1881	0.93	0.87	6	1.0
$C_{8.5}A_{85}K_4^*$	1484	-	0.64	0.59	8	-

\* $C_{8.5}A_{85}K_4$  obtained for immediate contact of KOH with precursor.[15]

The reduction of the activation temperature from 850 °C to 650 °C decreases dramatically the  $SSA_{DFT}$  (48%), impacts the PSD, and increases  $Y_{PAC}$  (27%) for  $C_5A_{65}K_4$ . At 650 °C, the temperature is not enough to promote all the activation reactions between the carbon precursor and KOH.  $C_5A_{65}K_4$  is mostly microporous due to the lack of physical activation reactions involving  $CO_2$  and  $H_2O$  (Eqs. 18 and 20), which are known to promote pore enlargement.[28,57] Although activation at 750 °C ensures pore development ( $C_5A_{75}K_4$ ), it is not as effective as the activation at 850 °C. Comparing activations at 750 °C and 850 °C at the same  $T_C$  and  $K/C$ , the  $SSA_{DFT}$  decreases ~17 % (decreasing  $T_A$ ) and an expressive reduction of mesoporosity (42%) is observed, thus indicating that pore enlargement takes place at temperatures higher than 750 °C, probably promoted by the reactions involving  $CO_2$  (Eq. 6). A further increase of  $T_A$  to values up to 900 °C reduces both,  $SSA_{DFT}$  and pore volume, but the mesoporosity remains, probably due to the pore collapsing. As  $K/C$  reduces to 2/1 ( $C_5A_{75}K_2$ ), the  $SSA_{DFT}$  increases ~14%, while the mesopore volume reduces 9% compared to  $C_5A_{75}K_4$ . This trend is well aligned to other works in literature,[58,59] and is attributed to the over-activation caused by the higher KOH weight ratio.[60]

Activation using  $K_2CO_3$  promotes mainly the development of micropores in  $C_5A_{85}KC$  (94%), with negligible presence of mesopores. Furthermore, the  $SSA_{DFT}$  of  $C_5A_{85}KC$  is 23% lower than  $C_5A_{85}K_4$ , evidencing the mild reactivity between  $K_2CO_3$  and the precursor.

#### 5.3.4. Electrochemical characterization

CV experiments were carried out to evaluate the conductivity and capacitance of the electrodes in 200 mM NaCl. This concentration was employed to prevent limitations imposed by mass transfer. Figure 5.6a displays the voltammograms run at 1 mV/s for the electrodes prepared using the activated carbons carbonized at different temperatures. The quasi-rectangular shape is characteristic of capacitive materials with low resistivity.[61] The CVs for the other carbon electrodes show the same pattern (Fig. A5.5). The highest capacitance (213 F/g) calculated by Eq. 2 is achieved for  $C_5A_{85}K_4$ . Although this value is very high, it is still lower than the capacitance obtained using expensive materials, such as N-doped graphene (~287 F/g).[7] As shown in Table 5.4, the high capacitance observed for PANi activated carbons are very dependent on the carbonization and activation conditions.

**Figure 5.6.** (A) Cyclic voltammeteries recorded at 1 mV/s and (B) capacitance at different scan-rates. Electrolyte concentration: 200 mM NaCl

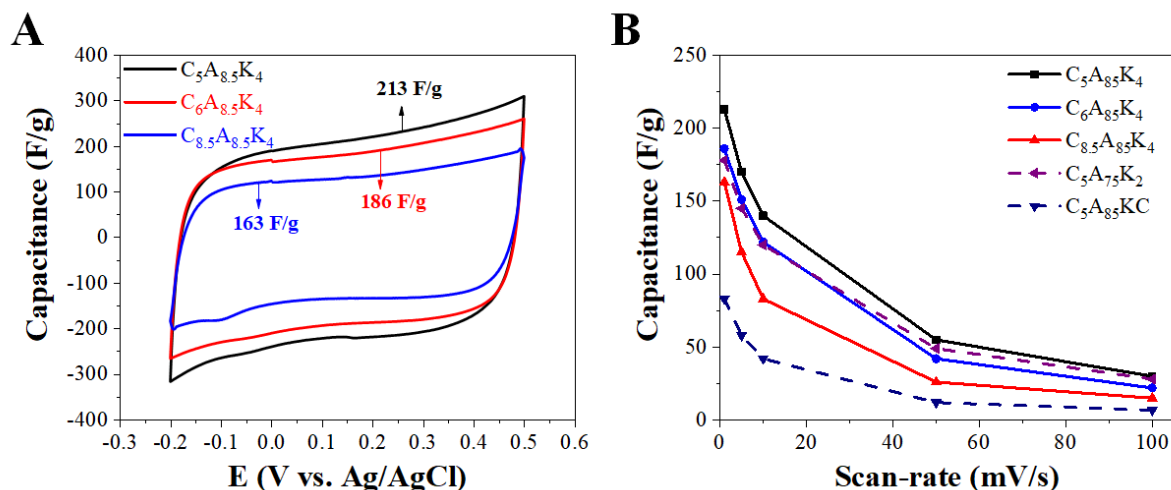


**Table 5.4.** Capacitance calculated from the cyclic voltammograms at 1 mV/s in 200 mM NaCl, and converted deionization capacity ( $D_c$ ).

	$C$ (F/g)	$D_c$ (mg/g)
$C_5A_{85}K_4$	213	38.7
$C_6A_{85}K_4$	186	33.8
$C_{8.5}A_{85}K_4$	162	29.5
$C_5A_{65}K_4$	88	16.0
$C_5A_{75}K_4$	142	25.8
$C_5A_8K_4$	132	24.0
$C_5A_9K_4$	211	38.4
$C_5A_{75}K_2$	178	32.4
$C_5A_{85}K_2$	181	32.9
$C_5A_{85}KC$	83	15.1

An evident trend is observed between the capacitances and the textural properties shown in Table 5.3, since the higher the SSA the higher the capacitance. The values of  $D_c$  calculated by Eq. 3 indicate that if the capacitance is completely converted in SAC, remarkable values of salt electrosorption, among the highest already reported for CDI, would be achieved (Table A5.3). However, in diluted solutions, the SAC seldom matches  $D_c$  due to ohmic losses, faradaic reactions, and ion transport limitations. Nevertheless, it has been reported that SAC usually corresponds to 50-60% of  $D_c$ , [62] which is, for most of the materials shown in Table 5.4, a high value of predicted SAC.

The trend between capacitance and scan-rate shown in Figure 5.6b is an indicative of the ion diffusion kinetics in the electrode. As the scan-rate increases, the capacitance decreases due to the sluggishness of ion diffusion, thus affecting the EDL formation. The capacitance drop is usually less sensitive for mesoporous materials since the mesopores behave as large avenues for ion diffusion, thus facilitating the access to the pores.[63] However, despite of the mesoporosity observed for C<sub>5</sub>A<sub>85</sub>K<sub>4</sub>, (Table 5.3), no evident kinetics improvement has been achieved compared with the microporous carbons, e.g. C<sub>5</sub>A<sub>85</sub>KC.

### 5.3.5. Desalination

#### 5.3.5.1. Influence of carbonization conditions

Electrosorption experiments were carried out to evaluate the performance of PAC electrodes for desalination. The performance of the carbonized samples (C<sub>4</sub>, C<sub>6</sub>, and C<sub>8.5</sub>) were also investigated, but negligible salt removal was achieved (Fig. A5.5) due to the poor pore structure development.

The SAC kinetics of electrosorption and desorption shown in Figure 5.7a reveals the influence of the  $T_C$  on the desalination performance. The maximum value of SAC ( $mSAC$ ) was achieved using C<sub>5</sub>A<sub>85</sub>K<sub>4</sub> and C<sub>6</sub>A<sub>85</sub>K<sub>4</sub> after ~15 min, and C<sub>8.5</sub>A<sub>85</sub>K<sub>4</sub> after ~19 min, indicating that the open pore structure of the PANi carbonized at low temperatures (Table 5.3) enhances the desalination kinetics. The remarkable  $mSAC$  achieved using C<sub>5</sub>A<sub>85</sub>K<sub>4</sub> is among the highest values reported for CDI using carbon electrodes (Table A5.3). According to Tables 5.3 and 5.5, as  $T_C$  increases,  $mSAC$  decreases due to the small pore volume and less favorable PSD (e.g. C<sub>8.5</sub>A<sub>85</sub>K<sub>4</sub>). The values of  $mSAC$  in Figure 5.7a aligns well with those of capacitance and correspond to 50-60% of  $D_c$  (Table 5.4).

A linear trend between the  $mSAC$  and  $SSA_{BET}$  is observed in Figure A5.7, except for C<sub>5</sub>A<sub>75</sub>K<sub>4</sub>, demonstrating that, in this case, high  $SSA_{BET}$  is mandatory in order to achieve high electrosorption uptake, although it has been reported that the most important variable determining  $mSAC$  is the pore volume distribution.[64] In this regard, the results obtained using C<sub>5</sub>A<sub>85</sub>K<sub>4</sub> and C<sub>6</sub>A<sub>85</sub>K<sub>4</sub> also aligns well to literature since they present the highest pore volume, mainly associated to mesopores (Table 5.3), which improves the electrosorption kinetics according to Table A5.2.

Theoretical SAC values ( $tSAC$ ) were calculated from a model taking into account the pore size distribution of the carbon material.[64] Despite the different values of  $mSAC$  and  $tSAC$  (Table 5.5), they follow the same trend for C<sub>5</sub>A<sub>85</sub>K<sub>4</sub>, C<sub>6</sub>A<sub>85</sub>K<sub>4</sub>, and C<sub>8.5</sub>A<sub>85</sub>K<sub>4</sub>, in which the values of  $tSAC$  correspond to ~82% of the experimental. Furthermore, the nitrogen content of



$C_5A_{85}K_4$  (Table 5.2) probably is associated to pyrrolic and pyridinic surface groups, which are recognized to provide pseudocapacitance and enhance electrosorption.[16]

**Figure 5.7.** SAC (A) and  $m_{sr}$  (B) against time obtained using the electrode materials prepared at different values of  $T_C$ . Desalination conditions: 600 mg/L NaCl, 1.2 V

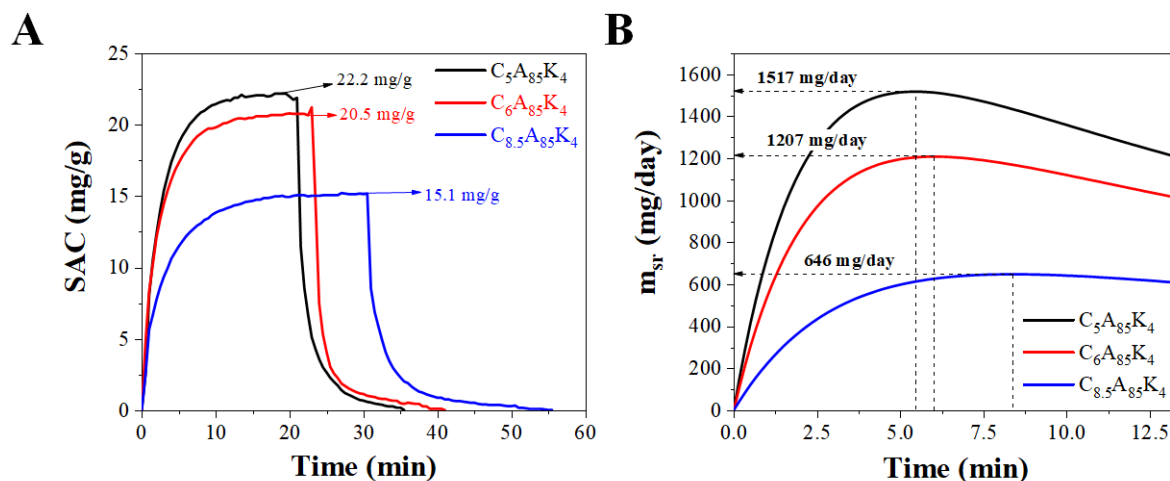


**Table 5.5.**  $mSAC$ ,  $OSR$ , charge-efficiency and specific energy consumption for the activated carbon electrodes in 600 ppm NaCl.  $E_{cell} = 1.2$  V.  $tSAC$  was calculated for 5 mM NaCl

Electrode	$mSAC$ (mg/g)	$OSR$ (mg/day)	$Q_E$ (%)	$\eta$ (J/mg)	$tSAC$ (mg/g)
$C_5A_{85}K_4$	22.2	1517	81	4.2	18.4
$C_6A_{85}K_4$	20.6	1207	88	3.9	16.9
$C_{8.5}A_{85}K_4$	15.1	646	78	5.0	12.6
$C_5A_{75}K_4$	7.2	1136	38	8.4	12.2
$C_5A_{80}K_4$	17.3	1235	70	4.2	-
$C_5A_{90}K_4$	19.3	1501	77	4.5	16.4
$C_5A_{75}K_2$	19.6	1503	84	4.0	14.4
$C_5A_{85}K_2$	17.6	1418	82	4.4	-
$C_5A_{85}KC$	12.0	1137	74	5.4	11.3

Figure 5.7b shows the optimal salt removal (*OSR*) for the activated carbon electrodes prepared at different  $T_C$ . The *OSR* combines simultaneously the effects of *mSAC* and electrode kinetics (adsorption and desorption) and has been proposed by Zornitta and Ruotolo[5] as an attempt for an overall evaluation of the electrode used in the desalination process. The electrosorption kinetics and desorption times used for the *OSR* calculations are presented in Table A5.2. The effect of the carbonization temperature on the *OSR* desalination performance is clear. According to Table 5.5, C<sub>8.5</sub>A<sub>85</sub>K<sub>4</sub> has less than half of the *OSR* of C<sub>5</sub>A<sub>85</sub>K<sub>4</sub> and C<sub>6</sub>A<sub>85</sub>K<sub>4</sub>, despite of its *mSAC* be slightly low. The superior *OSR* for C<sub>5</sub>A<sub>85</sub>K<sub>4</sub> is attributed to the faster kinetics promoted by the large pore volume, which improves the ion diffusion in the pores.

Among the electrodes in Table 5.5, the highest  $Q_E$  and lowest  $\eta$  are achieved using C<sub>6</sub>A<sub>85</sub>K<sub>4</sub>, suggesting a minor effect of co-ion repulsion in the micropores, as already evidenced in our previous work.[65] Interestingly, although lower  $Q_E$  is observed for C<sub>5</sub>A<sub>85</sub>K<sub>4</sub> compared to C<sub>6</sub>A<sub>85</sub>K<sub>4</sub>, the values of  $\eta$  are very similar due to the fact that for  $\eta$  calculation the leakage current is taken into account, *i.e.*, the ohmic drop and faradaic reactions are considered. In the case of the electrodes C<sub>8.5</sub>A<sub>85</sub>K<sub>4</sub> and C<sub>5</sub>A<sub>85</sub>K<sub>4</sub>, although they have similar  $Q_E$ , the first one has higher  $\eta$  due to the lower *mSAC*, despite of the leakage current observed for this electrode be lower (not shown).

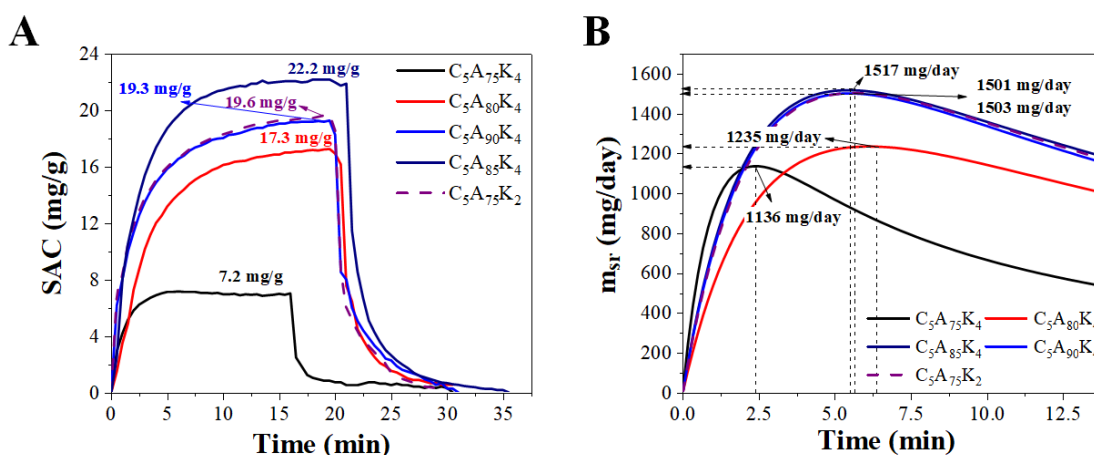
### 5.3.5.2. Influence of the activation conditions

The effect of different activation conditions ( $T_A$  and  $K/C$ ) on the electrode performance are displayed in Figure 5.8. High *mSAC* is achieved using C<sub>5</sub>A<sub>75</sub>K<sub>2</sub> and C<sub>5</sub>A<sub>90</sub>K<sub>4</sub>, with practically the same electrosorption/desorption performance. However, the *mSAC* for these materials is still lower than the C<sub>5</sub>A<sub>85</sub>K<sub>4</sub> (Table 5.5). On the other hand, the fast electrosorption/desorption kinetics observed for C<sub>5</sub>A<sub>75</sub>K<sub>2</sub> and C<sub>5</sub>A<sub>90</sub>K<sub>4</sub> led to practically the same *OSR* for C<sub>5</sub>A<sub>85</sub>K<sub>4</sub> (Fig. 5.8b).

Interestingly, using C<sub>5</sub>A<sub>65</sub>K<sub>4</sub> (Fig. A5.8) and C<sub>5</sub>A<sub>75</sub>K<sub>4</sub> a different desalination trend is observed. While C<sub>5</sub>A<sub>65</sub>K<sub>4</sub> behaves as inverse CDI (iCDI),[66] the *mSAC* for C<sub>5</sub>A<sub>75</sub>K<sub>4</sub> is much lower than the other electrodes. These trends cannot be explained by the textural properties, since the *tSAC* calculated from the PSD predicts a value higher than the experimental and *mSAC* for C<sub>5</sub>A<sub>75</sub>K<sub>4</sub> is out of the linear trend shown in Figure A5.7. Therefore, the unexpected performances of these electrodes was ascribed to the presence of functional surface groups.

The effect of the surface groups can be indirectly estimated from the potential of zero charge ( $E_{PZC}$ ) of the electrode,[65] which was determined from the differential capacitance obtained by EIS for the activated carbons prepared at different values of  $T_A$  (Fig. A5.9a). The  $E_{PZC}$  decreases from 0.4 V to 0.3 V and 0.2 V vs. Ag/AgCl as the activation temperature increases from 650 °C to 750 °C and 800 °C, respectively. This trend indicates that the surface of  $C_5A_{65}K_4$  is more acid than the other electrodes, which means that the electrode surface is negatively charged.[65,67] As  $T_A$  increases, the surface groups responsible for the negative chemical charge are released during activation, thus reducing  $E_{PZC}$  for  $C_5A_{75}K_4$ , and stabilizing at 0.2 V at temperatures higher than 800 °C.

**Figure 5.8.** SAC (A) and  $m_{sr}$  (B) against time for the electrodes prepared with carbons activated at different conditions. 600 mg/L NaCl, 1.2 V



Another important variable required to analyze the effect of co-ion repulsion is the short circuit potential ( $E_0$ ), usually employed as the electrode potential during the regeneration step. For the positive electrode, the higher the difference between the values of  $E_0$  and the positive  $E_{PZC}$ , the stronger the effect of co-ion repulsion.[5] Table A5.4 reveals that as  $T_A$  increases,  $E_0$  remains at 0.12-0.19 V vs. Ag/AgCl. The highest  $E_{PZC} - E_0$  differences are justly observed for  $C_5A_{65}K_4$ , followed by  $C_5A_{75}K_4$ . Thus, the effect of  $E_{PZC}$  on the co-ion repulsion explains the low values of  $mSAC$  and  $Q_E$ , and the high  $\eta$  observed for  $C_5A_{75}K_4$ . Indeed,  $D_c$  and  $tSAC$  predictions based on the capacitance and PSD for  $C_5A_{75}K_4$  by far overestimates the real value of  $mSAC$ .

Interestingly, although the  $mSAC$  for  $C_5A_{80}K_4$  is much higher than that for  $C_5A_{75}K_4$  (140%), the  $OSR$  is only ~9% superior due to its slow electrosorption and desorption kinetics (Fig. 5.8b). A similar trend has already been reported in our previous work,[5] and highlight the importance of taking into account not only the sorption capacity, but also the kinetics to

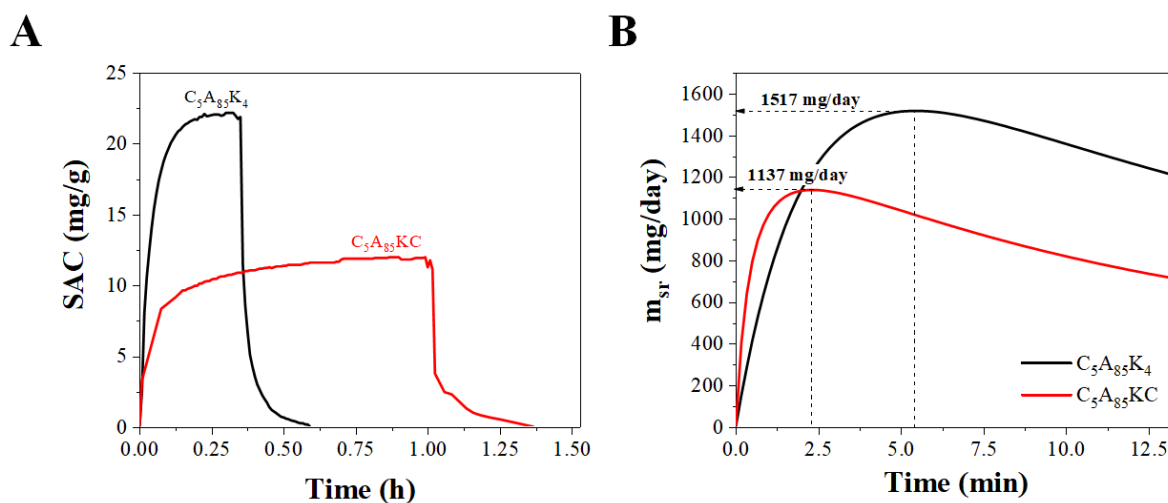
evaluate the electrode performance. The highest value of  $mSAC$  is obtained for  $C_5A_{85}K_4$  and, despite its slow electrosorption and desorption kinetic (Table A5.2), it has the highest  $OSR$  among the studied electrodes. As  $T_A$  increases to 900 °C ( $C_5A_{90}K_4$ ),  $mSAC$  decreases, although its  $OSR$  remains similar to the obtained using  $C_5A_{85}K_4$ . This  $mSAC$  agrees well with the values predicted by capacitance and PSD *i.e.*,  $\sim 83\%$   $tSAC$  and  $D_c$  between 50-60%.

Higher  $mSAC$  is achieved reducing  $K/C$ , but maintaining  $T_A$  at 750 °C ( $C_5A_{75}K_2$ ), compared with  $C_5A_{75}K_4$ . This trend is explained by the higher SSA and large pore volume. On the other hand, the narrow pore size ( $d_{50}$ ) of  $C_5A_{75}K_2$  is responsible by the poor electrosorption and desorption kinetics observed for this electrode, which results in low  $OSR$ . Activating at 850 °C, the opposite trend is observed, *i.e.*, the  $mSAC$  for  $C_5A_{85}K_2$  is lower than for  $C_5A_{85}K_4$ , and the kinetics is slower as well. This result suggests a synergetic effect between  $K/C$  and  $T_A$  on the electrode properties and, consequently, on the desalination performance.

### 5.3.5.3. Influence of the activating agent

The desalination performance of the electrodes prepared with carbons activated with KOH and  $K_2CO_3$  ( $C_5A_{85}KC$ ) are compared in Figure 5.9a. The superior performance of  $C_5A_{85}K_4$  is evident and well aligned with its the pore structure (Table 5.3) and electrochemical characterization (Table 5.4). KOH activation provides activated carbons with higher SSA, pore volume, and electrosorption capacity (Table 5.5). The electrosorption and desorption kinetics for  $C_5A_{85}KC$  are very fast (Fig. 5.9b) and fits well to the pseudo second order model (Table A5.2), thus having a strong impact on the  $OSR$  calculation. The  $OSR$  is high, despite its low  $mSAC$ , but still inferior than the observed for  $C_5A_{85}K_4$ . Interestingly, the  $mSAC$  for  $C_5A_{85}KC$  aligns well with  $tSAC$  and achieves  $\sim 80\%$  of  $D_c$  due to the predominance of micropores. Considering that  $K_2CO_3$  is easier to handle than KOH, and the treatment after activation is facilitated, activation using  $K_2CO_3$  could be a feasible alternative to provide activated carbon electrodes for CDI.

**Figure 5.9.** SAC (A) and OSR (B) against time for  $C_5A_{85}K_4$  and  $C_5A_{85}KC$ . 600 mg/L NaCl,  $E_{cell} = 1.2$  V



#### 5.4. Conclusion

Capacitive deionization is a promising technology typically used for water desalination. The achievement of a material with high desalination capacity, low energy consumption, and fast desalination kinetics is still one of the challenging issues for the effective use of CDI. In this work, we presented an optimized activated carbon, PAC/PTS, with remarkable properties such as very high specific surface area, large pore volume, and high nitrogen content, which provided high capacitance and desalination capacity.

A new mechanism for PTS-doped polyaniline (PAni/PTS) carbonization/activation was proposed, enlightening how the preparation conditions affects the pore development of the activated carbon. Low carbonization temperatures ( $500\text{ }^{\circ}\text{C} \leq T_C \leq 600\text{ }^{\circ}\text{C}$ ) provides oxygen-rich carbons with a turbostratic structure which improves their reactivity with KOH during activation at temperatures higher than  $700\text{ }^{\circ}\text{C}$ , leading to remarkable values of SSA ( $3649\text{ m}^2/\text{g}$ ) and pore volume ( $2.30\text{ cm}^3/\text{g}$ ) at optimized conditions ( $T_C = 500\text{ }^{\circ}\text{C}$ ,  $T_A = 850\text{ }^{\circ}\text{C}$ , and  $K/C$  4/1 -  $C_5A_{85}K_4$ ). Activation at  $T_A \leq 650\text{ }^{\circ}\text{C}$  lead to a poor pore structure PAC, with high oxygen and nitrogen content which indicates the presence of surface groups. Although activation at high  $T_A$  ( $900\text{ }^{\circ}\text{C}$ ) resulted in a well-developed pore structure, pore shrinkage and collapsing diminish the pore volume and SSA.

$C_5A_{85}K_4$  electrode provided the highest capacitance ( $213\text{ F/g}$ ) and SAC ( $22.2\text{ mg/g}$ ), which is ascribed not only to its textural properties, but also to the pseudocapacitive effect

ascribed to the presence of nitrogen heteroatoms. This SAC is among the highest values reported for CDI desalination using carbon electrodes.

### References:

- [1] WWAP (United Nations World Water Assessment Programme)/UN-Water. 2018. The United Nations World Water Development Report 2018: Nature-based solutions for water, UNESCO, Paris, 2018. [www.unesco.org/open-access/](http://www.unesco.org/open-access/).
- [2] E. García-Quismondo, C. Santos, J. Palma, M.A. Anderson, On the challenge of developing wastewater treatment processes: capacitive deionization, *Desalin. Water Treat.* (2014) 1–10. doi:10.1080/19443994.2014.984929.
- [3] R.K. McGovern, A.M. Weiner, L. Sun, C.G. Chambers, S.M. Zubair, J.H. Lienhard V, On the cost of electrodialysis for the desalination of high salinity feeds, *Appl. Energy*. 136 (2014) 649–661. doi:10.1016/j.apenergy.2014.09.050.
- [4] A.D. Khawaji, I.K. Kutubkhanah, J.-M. Wie, Advances in seawater desalination technologies, *Desalination*. 221 (2008) 47–69. doi:10.1016/j.desal.2007.01.067.
- [5] R.L. Zornitta, L.A.M. Ruotolo, Simultaneous analysis of electrosorption capacity and kinetics for CDI desalination using different electrode configurations, *Chem. Eng. J.* 332 (2018). doi:10.1016/j.cej.2017.09.067.
- [6] Y. Oren, Capacitive deionization (CDI) for desalination and water treatment — past, present and future (a review), *Desalination*. 228 (2008) 10–29. doi:10.1016/j.desal.2007.08.005.
- [7] X. Xu, Z. Sun, D.H.C. Chua, L. Pan, Novel nitrogen doped graphene sponge with ultrahigh capacitive deionization performance., *Sci. Rep.* 5 (2015) 11225. doi:10.1038/srep11225.
- [8] C. Kim, P. Srimuk, J. Lee, S. Fleischmann, M. Aslan, V. Presser, Influence of pore structure and cell voltage of activated carbon cloth as a versatile electrode material for capacitive deionization, *Carbon N. Y.* 122 (2017) 329–335. doi:10.1016/j.carbon.2017.06.077.
- [9] H. Li, L. Pan, T. Lu, Y. Zhan, C. Nie, Z. Sun, A comparative study on electrosorptive behavior of carbon nanotubes and graphene for capacitive deionization, *J. Electroanal. Chem.* 653 (2011) 40–44. doi:10.1016/j.jelechem.2011.01.012.

- [10] H. Li, L. Zou, L. Pan, Z. Sun, Novel graphene-like electrodes for capacitive deionization., *Environ. Sci. Technol.* 44 (2010) 8692–7. doi:10.1021/es101888j.
- [11] A.G. El-Deen, R.M. Boom, H.Y. Kim, H. Duan, M.B. Chan-Park, J.H. Choi, Flexible 3D Nanoporous Graphene for Desalination and Bio-decontamination of Brackish Water via Asymmetric Capacitive Deionization, *ACS Appl. Mater. Interfaces.* 8 (2016) 25313–25325. doi:10.1021/acsami.6b08658.
- [12] S. Porada, L. Weinstein, R. Dash, a van der Wal, M. Bryjak, Y. Gogotsi, P.M. Biesheuvel, Water desalination using capacitive deionization with microporous carbon electrodes., *ACS Appl. Mater. Interfaces.* 4 (2012) 1194–9. doi:10.1021/am201683j.
- [13] M. Aslan, M. Zeiger, N. Jackel, I. Grobelsek, D. Weingarth, V. Presser, Improved capacitive deionization performance of mixed hydrophobic / hydrophilic activated carbon electrodes, *J. Phys. Condens. Matter.* 28 (2016) 114003. doi:10.1088/0953-8984/28/11/114003.
- [14] J.J. Lado, R.L. Zornitta, F.A. Calvi, M. Martins, M.A. Anderson, F.G.E. Nogueira, L.A.M. Ruotolo, Enhanced capacitive deionization desalination provided by chemical activation of sugar cane bagasse fly ash electrodes, *J. Anal. Appl. Pyrolysis.* 126 (2017). doi:10.1016/j.jaap.2017.06.014.
- [15] R.L. Zornitta, F.J. García-Mateos, J.L. Lado, J. Rodríguez-Mirasol, T. Cordero, P. Hammer, L.A.M. Ruotolo, High-performance activated carbon from polyaniline for capacitive deionization, *Carbon N. Y.* 123 (2017) 318–333.
- [16] X. Xu, L. Pan, Y. Liu, T. Lu, Z. Sun, Enhanced capacitive deionization performance of graphene by nitrogen doping, *J. Colloid Interface Sci.* 445 (2015) 143–150. doi:10.1016/j.jcis.2015.01.003.
- [17] D. Lin, X. Zhang, X. Cui, W. Chen, Highly porous carbons with superior performance for CO<sub>2</sub> capture through hydrogen-bonding interactions, *RSC Adv.* 4 (2014) 27414–27421. doi:10.1039/c4ra04545a.
- [18] X. Zhang, X. Cui, W. Chen, A comprehensive study of polyaniline-derived porous carbons via KOH activation, *RSC Adv.* 5 (2015) 77629–77636. doi:10.1039/c5ra13515j.
- [19] A. Silvestre-albero, J. Silvestre-albero, M. Mart, F. Rodr, *Micro / Mesoporous*

- Activated Carbons Derived from Polyaniline : Promising Candidates for CO<sub>2</sub> Adsorption, *Ind. Eng. Chem. Res.* 53 (2014) 15398–15405.
- [20] E.J. Jelmy, S. Ramakrishnan, S. Devanathan, M. Rangarajan, N.K. Kothurkar, Optimization of the conductivity and yield of chemically synthesized polyaniline using a design of experiments, *J. Appl. Polym. Sci.* 130 (2013) 1047–1057. doi:10.1002/app.39268.
- [21] Z. Zhang, Z. Zhou, H. Peng, Y. Qin, G. Li, Nitrogen- and oxygen-containing hierarchical porous carbon frameworks for high-performance supercapacitors, *Electrochim. Acta.* 134 (2014) 471–477. doi:10.1016/j.electacta.2014.04.107.
- [22] R.L. Zornitta, J.J. Lado, M.A. Anderson, L.A.M. Ruotolo, Effect of electrode properties and operational parameters on capacitive deionization using low-cost commercial carbons, *Sep. Purif. Technol.* 158 (2016) 39–52. doi:10.1016/j.seppur.2015.11.043.
- [23] F. Rouquerol, J. Rouquerol, K.S.W.S.W.K. Sing, P. Llewellyn, G. Maurin, J. Rouquerol, P. Llewellyn, K.S.W.S.W.K. Sing, *Adsorption by Powders and Porous Solids*, 2014. doi:10.1016/B978-0-08-097035-6.00012-7.
- [24] J. Jagiello, J.P. Olivier, 2D-NLDFT adsorption models for carbon slit-shaped pores with surface energetical heterogeneity and geometrical corrugation, *Carbon N. Y.* 55 (2013) 70–80. doi:10.1016/j.carbon.2012.12.011.
- [25] J. Díaz-Terán, D.M. Nevskaja, J.L.G. Fierro, A.J. López-Peinado, A. Jerez, Study of chemical activation process of a lignocellulosic material with KOH by XPS and XRD, *Microporous Mesoporous Mater.* 60 (2003) 173–181. doi:10.1016/S1387-1811(03)00338-X.
- [26] J. Zhang, J. Gao, Y. Chen, X. Hao, X. Jin, Characterization, preparation, and reaction mechanism of hemp stem based activated carbon, *Results Phys.* 7 (2017) 1628–1633. doi:10.1016/j.rinp.2017.04.028.
- [27] M.A. Lillo-Ródenas, D. Cazorla-Amorós, A. Linares-Solano, Understanding chemical reactions between carbons and NaOH and KOH An insight into the chemical activation mechanism, *Carbon N. Y.* 41 (2003) 267–275.
- [28] S. Guo, J. Peng, W. Li, K. Yang, L. Zhang, S. Zhang, H. Xia, Effects of CO<sub>2</sub> activation



- on porous structures of coconut shell-based activated carbons, *Appl. Surf. Sci.* 255 (2009) 8443–8449. doi:10.1016/j.apsusc.2009.05.150.
- [29] J. He, J.W.F. To, P.C. Psarras, H. Yan, T. Atkinson, R.T. Holmes, D. Nordlund, Z. Bao, J. Wilcox, Tunable Polyaniline-Based Porous Carbon with Ultrahigh Surface Area for CO<sub>2</sub> Capture at Elevated Pressure, *Adv. Energy Mater.* 6 (2016). doi:10.1002/aenm.201502491.
- [30] J.P. Pouget, M.E. Jozefowicz, A.J. Epstein, X. Tang, A.G. MacDiarmid, X-ray Structure of Polyaniline, *Macromolecules.* (1991) 779–789. doi:10.1021/ma00003a022.
- [31] H.-M. Lee, H.-R. Kang, K.-H. An, H.-G. Kim, B.-J. Kim, Comparative studies of porous carbon nanofibers by various activation methods, *Carbon Lett.* 14 (2013) 180–185. doi:10.5714/CL.2013.14.3.180.
- [32] S. Schimmelpfennig, B. Glaser, One Step Forward toward Characterization: Some Important Material Properties to Distinguish Biochars, *J. Environ. Qual.* 41 (2012) 1001. doi:10.2134/jeq2011.0146.
- [33] C.S. Yang, Y.S. Jang, H.K. Jeong, Bamboo-based activated carbon for supercapacitor applications, *Curr. Appl. Phys.* 14 (2014) 1616–1620. doi:10.1016/j.cap.2014.09.021.
- [34] B.S. Girgis, Y.M. Temerk, M.M. Gadelrab, I.D. Abdullah, X-ray Diffraction Patterns of Activated Carbons Prepared under Various Conditions, *Carbon Lett.* 8 (2007) 95–100. doi:10.5714/CL.2007.8.2.095.
- [35] I.Y. Sapurina, M.A. Shishov, Oxidative Polymerization of Aniline: Molecular Synthesis of Polyaniline and the Formation of Supramolecular Structures, *New Polym. Spec. Appl.* (2012). doi:10.5772/48758.
- [36] W. Shen, Z. Li, Y. Liu, Surface Chemical Functional Groups Modification of Porous Carbon, *Recent Patents Chem. Eng.* 1 (2008) 27–40. doi:10.2174/1874478810801010027.
- [37] B. Sreedhar, M. Sairam, D.K. Chattopadhyay, P.P. Mitra, D. V. Mohan Rao, Thermal and XPS studies on polyaniline salts prepared by inverted emulsion polymerization, *J. Appl. Polym. Sci.* 101 (2006) 499–508. doi:10.1002/app.23301.
- [38] M. Trchová, E.N. Konyushenko, J. Stejskal, J. Kovářová, G. Čirić-Marjanović, The

- conversion of polyaniline nanotubes to nitrogen-containing carbon nanotubes and their comparison with multi-walled carbon nanotubes, *Polym. Degrad. Stab.* 94 (2009) 929–938. doi:10.1016/j.polymdegradstab.2009.03.001.
- [39] S. Ratanakandilok, S. Ngamprasertsith, P. Prasassarakich, Coal desulfurization with methanol/water and methanol/KOH, *Fuel*. 80 (2001) 1937–1942. doi:10.1016/S0016-2361(01)00047-3.
- [40] Y. Zhao, H. Liu, F. Wang, J. Liu, K. Chul Park, M. Endo, A simple route to synthesize carbon-nanotube/cadmium-sulfide hybrid heterostructures and their optical properties, *J. Solid State Chem.* 182 (2009) 875–880. doi:10.1016/j.jssc.2009.01.001.
- [41] G.M. Neelgund, E. Hrehorova, M. Joyce, V. Bliznyuk, Synthesis and characterization of polyaniline derivative and silver nanoparticle composites, *Polym. Int.* 57 (2008) 1083–1089. doi:10.1002/pi.2445.
- [42] M. Trchová, J. Stejskal, Polyaniline: The infrared spectroscopy of conducting polymer nanotubes (IUPAC Technical Report), *Pure Appl. Chem.* 83 (2011) 1803–1817. doi:10.1351/PAC-REP-10-02-01.
- [43] M. Cochet, G. Louarn, S. Quillard, M.I. Boyer, J.P. Buisson, S. Lefrant, Theoretical and experimental vibrational study of polyaniline in base forms: Non-planar analysis. Part I, *J. Raman Spectrosc.* 31 (2000) 1029–1039. doi:10.1002/1097-4555(200011)31:11<1029::AID-JRS640>3.0.CO;2-A.
- [44] T. Remyamol, P. Gopinath, H. John, Phenylenediamine functionalized reduced graphene oxide/polyaniline hybrid: Synthesis, characterization, improved conductivity and photocurrent generation, *RSC Adv.* 4 (2014) 29901–29908. doi:10.1039/c4ra03155e.
- [45] V.G. Phadnis, K.R. Jagdeo, Mn doped Polyaniline for Supercapacitor Application, *Int. J. Allied Pract. Res. Rev.* II (2015) 28–34.
- [46] D.S. Vicentini, R. V. Salvatierra, A.J.G. Zarbin, L.G. Dutrac, M.M. Sá, Synthesis and characterization of carboxyl-substituted polyanilines doped with halogenated acids: Combining conductivity with solubility, *J. Braz. Chem. Soc.* 25 (2014) 1939–1947. doi:10.5935/0103-5053.20140173.
- [47] D.C. Schnitzler, A.J.G. Zarbin, Organic/inorganic hybrid materials formed from TiO<sub>2</sub>

- nanoparticles and polyaniline, *J. Braz. Chem. Soc.* 15 (2004) 378–384.  
doi:10.1590/S0103-50532004000300007.
- [48] G. Neetika, K. D., T. S. K., Thermal Behaviour of Chemically Synthesized Polyanilines/Polystyrene Sulphonic Acid Composites, *Int. J. Mater. Chem.* 2 (2012) 79–85. doi:10.5923/j.ijmc.20120202.07.
- [49] A. A. Jatratar, J. B. Yadav, R. R. Deshmukh, H. C. Barshilia, V. Puri, R. K. Puri, Glow discharge plasma polymerized nanostructured polyaniline thin film optical waveguide, *Adv. Mater. Lett.* 8 (2016) 180–184. doi:10.5185/amlett.2017.6409.
- [50] S. Phonchaiya, B. Panijpan, S. Rajviroongit, T. Wright, J.T. Blanchfield, A Facile Solvent-Free Cannizzaro Reaction An Instructional Model for Introductory Organic Chemistry Laboratory, *J. Chem. Educ.* 86 (2009) 85–86. doi:10.1021/ed086p85.
- [51] W. Reusch, Elimination reactions of Alcohols,  
<https://www2.chemistry.msu.edu/faculty/reusch/virttxtjml/Alcohol11.htm> (Accessed Jan. 7, 2019). (n.d.).  
<https://www2.chemistry.msu.edu/faculty/reusch/virttxtjml/alcohol11.htm> (accessed July 1, 2019).
- [52] L. Chunlan, X. Shaoping, G. Yixiong, L. Shuqin, L. Changhou, Effect of pre-carbonization of petroleum cokes on chemical activation process with KOH, *Carbon N. Y.* 43 (2005) 2295–2301. doi:10.1016/j.carbon.2005.04.009.
- [53] H. Marsh, D.S. Yan, T.M. O’Grady, A. Wennerberg, Formation of active carbons from cokes using potassium hydroxide, *Carbon N. Y.* 22 (1984) 603–611. doi:10.1016/0008-6223(84)90096-4.
- [54] D. Lozano-Castelló, J.M. Calo, D. Cazorla-Amorós, A. Linares-Solano, Carbon activation with KOH as explored by temperature programmed techniques, and the effects of hydrogen, *Carbon N. Y.* 45 (2007) 2529–2536.  
doi:10.1016/j.carbon.2007.08.021.
- [55] J.M. Calo, D. Cazorla-Amorós, A. Linares-Solano, M.C. Román-Martínez, C. Salinas-Martínez De Lecea, The effects of hydrogen on thermal desorption of oxygen surface complexes, *Carbon N. Y.* 35 (1997) 543–554. doi:10.1016/S0008-6223(96)00173-X.
- [56] M. Thommes, K.A. Cychosz, Physical adsorption characterization of nanoporous

- materials: Progress and challenges, *Adsorption*. 20 (2014) 233–250.  
doi:10.1007/s10450-014-9606-z.
- [57] F. Rodríguez-Reinoso, M. Molina-Sabio, M.T. González, The Use of Steam and CO<sub>2</sub> as Activating Agents in the Preparation of Activated Carbons, *Carbon N. Y.* 33 (1995) 15–23.
- [58] A.A. El-Hendawy, An insight into KOH activation mechanism via production of microporous activated carbon for heavy metal removal, *Egypt. J. Chem.* 51 (2008) 681–700. doi:10.1016/j.apsusc.2008.10.034.
- [59] W. Zhang, M. Zhao, R. Liu, X. Wang, H. Lin, Colloids and Surfaces A : Physicochemical and Engineering Aspects Hierarchical porous carbon derived from lignin for high performance supercapacitor, *Colloids Surfaces A Physicochem. Eng. Asp.* 484 (2015) 518–527. doi:10.1016/j.colsurfa.2015.08.030.
- [60] J. Wang, I. Senkowska, S. Kaskel, Q. Liu, Chemically activated fungi-based porous carbons for hydrogen storage, *Carbon N. Y.* 75 (2014) 372–380.  
doi:10.1016/j.carbon.2014.04.016.
- [61] E. Frackowiak, Carbon materials for the electrochemical storage of energy in capacitors, 39 (2001) 937–950.
- [62] T. Kim, J. Yoon, Relationship between capacitance of activated carbon composite electrodes measured at a low electrolyte concentration and their desalination performance in capacitive deionization, *J. Electroanal. Chem.* 704 (2013) 169–174.  
doi:10.1016/j.jelechem.2013.07.003.
- [63] L. Zou, L. Li, H. Song, G. Morris, Using mesoporous carbon electrodes for brackish water desalination, *Water Res.* 42 (2008) 2340–2348.  
doi:10.1016/j.watres.2007.12.022.
- [64] S. Porada, L. Borchardt, M. Oschatz, M. Bryjak, J.S. Atchison, K.J. Keesman, S. Kaskel, P.M. Biesheuvel, V. Presser, Direct prediction of the desalination performance of porous carbon electrodes for capacitive deionization, *Energy Environ. Sci.* 6 (2013) 3700–3712. doi:10.1039/c3ee42209g.
- [65] R.L. Zornitta, P. Srimuk, J. Lee, B. Krüner, M. Aslan, L.A.M. Ruotolo, V. Presser, Charge and potential balancing for optimized capacitive deionization using lignin-

- derived, low-cost activated carbon electrodes, *ChemSusChem*. 11 (2018) 2101–2113. doi:10.1002/cssc.201800689.
- [66] P.M. Biesheuvel, H.V.M. Hamelers, M.E. Suss, Theory of Water Desalination by Porous Electrodes with Immobile Chemical Charge, *Colloids Interface Sci. Commun.* 9 (2015) 1–5. doi:10.1016/j.colcom.2015.12.001.
- [67] X. Gao, S. Porada, A. Omosebi, K.L. Liu, P.M. Biesheuvel, J. Landon, Complementary surface charge for enhanced capacitive deionization, *Water Res.* 92 (2016) 275–282. doi:10.1016/j.watres.2016.01.048.
- [68] Y. Liu, X. Xu, M. Wang, T. Lu, Z. Sun, L. Pan, Nitrogen-doped carbon nanorods with excellent capacitive deionization ability, *J. Mater. Chem. A*. 00 (2015) 1–8. doi:10.1039/C5TA03663A.
- [69] X. Xu, H. Tang, M. Wang, Y. Liu, Y. Li, T. Lu, L. Pan, Carbon spheres with hierarchical micro/mesopores for water desalination by capacitive deionization, *J. Mater. Chem. A*. 4 (2016) 16094–16100. doi:10.1039/C6TA07616E.
- [70] T. Wu, G. Wang, Q. Dong, F. Zhan, X. Zhang, S. Li, H. Qiao, J. Qiu, Starch Derived Porous Carbon Nanosheets for High-Performance Photovoltaic Capacitive Deionization, *Environ. Sci. Technol.* 51 (2017) 9244–9251. doi:10.1021/acs.est.7b01629.
- [71] C.-L. Yeh, H.-C. Hsi, K.-C. Li, C.-H. Hou, Improved performance in capacitive deionization of activated carbon electrodes with a tunable mesopore and micropore ratio, *Desalination*. 367 (2015) 60–68. doi:10.1016/j.desal.2015.03.035.
- [72] R.L. Zornitta, P. Srimuk, J. Lee, B. Krüner, Charge and Potential Balancing for Optimized Capacitive Deionization Using Lignin-Derived , Low-Cost Activated Carbon Electrodes, (2018) 1–14. doi:10.1002/cssc.201800689.
- [73] X. Xu, A. Enaiet Allah, C. Wang, H. Tan, A.A. Farghali, M. Hamdy Khedr, V. Malgras, T. Yang, Y. Yamauchi, Capacitive deionization using nitrogen-doped mesostructured carbons for highly efficient brackish water desalination, *Chem. Eng. J.* (2019). doi:10.1016/j.cej.2019.01.098.

## APPENDIX

**Table A5.1.** Surface elemental composition obtained from the XPS survey and surface groups determined from the deconvoluted O1s high resolution XPS

	C1s	O1s	N1s	S2p	C-O	C=O	O-C=O	H <sub>2</sub> O
	at. %				at. %			
C <sub>4</sub>	84.6	4.6	10.1	0.7	1.8	1.1	1.3	0.4
C <sub>5</sub>	87.2	4.2	8.3	0.3	0.8	0.8	2.2	0.4

**Table A5.2.** Electrosorption kinetics constant and desorption time ( $t_D$ )

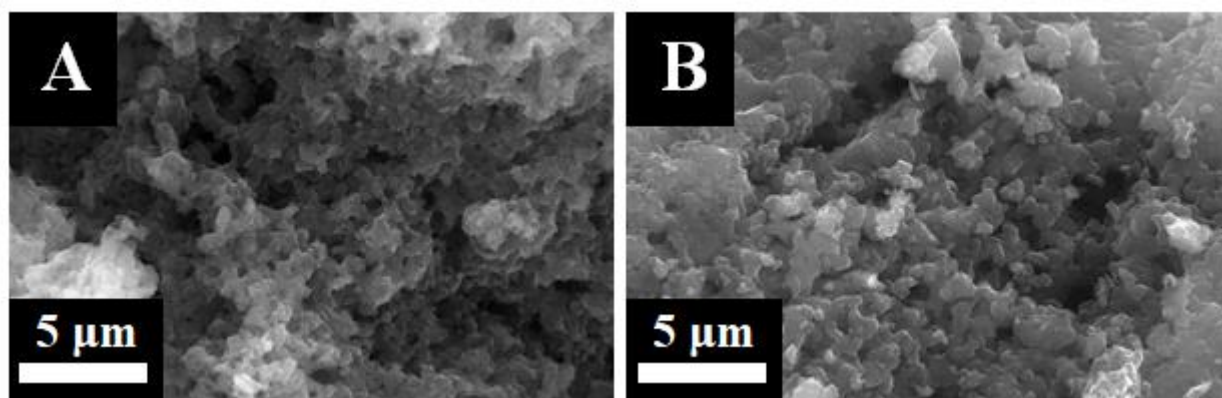
Material	$k_{e1} \times 10^{-3} (s^{-1})$	$k_{e2} \times 10^{-3} (L/s g)$	$t_D (s)$
C <sub>5</sub> A <sub>85</sub> K <sub>4</sub>	6.4	-	780
C <sub>6</sub> A <sub>85</sub> K <sub>4</sub>	6.1	-	960
C <sub>8.5</sub> A <sub>85</sub> K <sub>4</sub>	4.3	-	1290
C <sub>5</sub> A <sub>75</sub> K <sub>4</sub>	14.2	-	330
C <sub>5</sub> A <sub>80</sub> K <sub>4</sub>	4.8	-	630
C <sub>5</sub> A <sub>90</sub> K <sub>4</sub>	5.5	-	600
C <sub>5</sub> A <sub>75</sub> K <sub>2</sub>	5.3	-	600
C <sub>5</sub> A <sub>85</sub> K <sub>2</sub>	5.5	-	570
C <sub>5</sub> A <sub>85</sub> KC	-	8.1	600

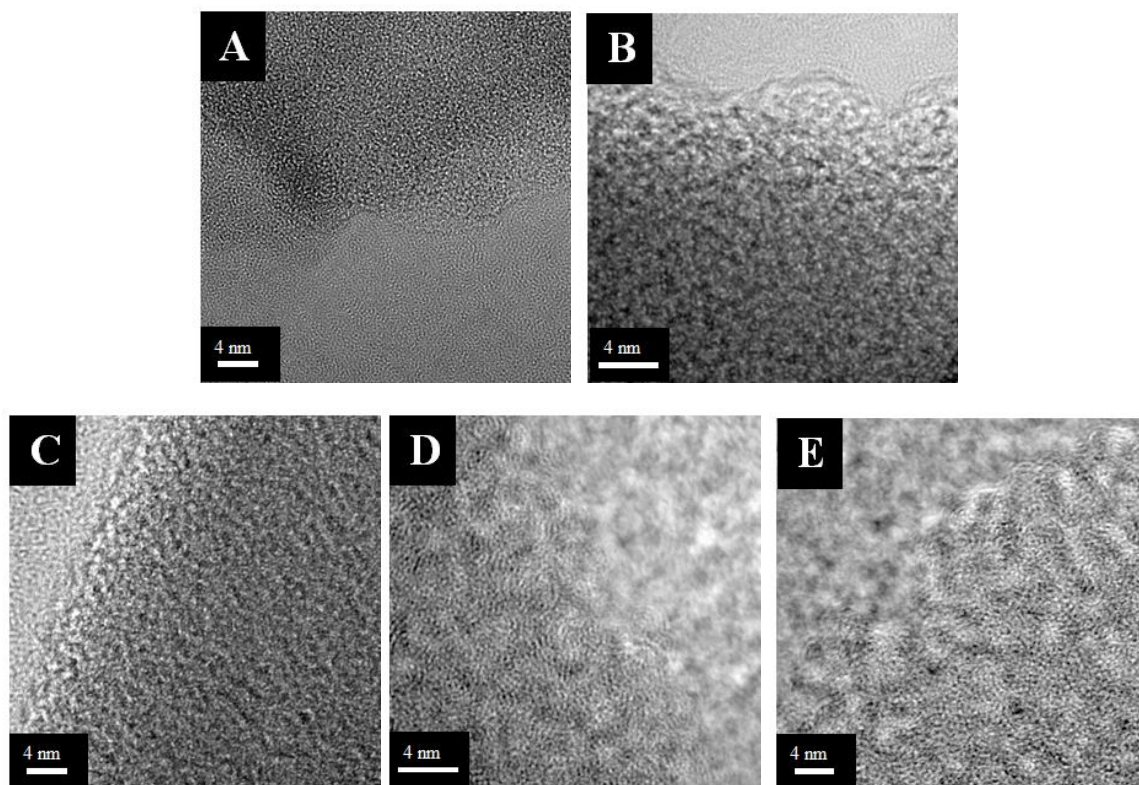
**Table A5.3.** *mSAC* of different electrode materials for water desalination using CDI

Material	<i>mSAC</i> (mg/g)	NaCl concentration (mg/L)	$E_{cell}$ (V)	Reference
N-doped carbon nanorods	17.6	500	1.2	[1]
N-doped graphene sponge	21.0	500	1.5	[2]
Carbon spheres	15.8	500	1.2	[3]
Commercial activated carbon	13.1	300	1.2	[4]
Activated carbon cloth	16.0	300	1.2	[5]
Porous carbon nanosheets	15.6	500	1.1	[6]
Coconut shell derived carbon	20.9	585	1.0	[7]
Lignin activated carbon	18.5	585	1.0	[8]
N-doped mesostructured carbon	20.6	585	1.2	[9]
Polyaniline activated carbon	22.2	600	1.2	This work

**Table A5.4.** Values of  $E_0$  and  $E_{PZC}$  for the activated carbon electrodes

<b>Material</b>	$E_0$	$E_{PZC}$
	<b>(V vs. Ag/AgCl)</b>	
<b>C<sub>5</sub>A<sub>65</sub>K<sub>4</sub></b>	0.18	0.4
<b>C<sub>5</sub>A<sub>75</sub>K<sub>4</sub></b>	0.19	0.3
<b>C<sub>5</sub>A<sub>80</sub>K<sub>4</sub></b>	0.12	0.2
<b>C<sub>5</sub>A<sub>85</sub>K<sub>4</sub></b>	0.14	0.2
<b>C<sub>5</sub>A<sub>90</sub>K<sub>4</sub></b>	0.18	0.2
<b>C<sub>5</sub>A<sub>75</sub>K<sub>2</sub></b>	0.15	0.2
<b>C<sub>5</sub>A<sub>85</sub>K<sub>2</sub></b>	0.14	0.2

**Figure A5.1.** SEM images of C<sub>4</sub> (A) and C<sub>8.5</sub> (B)

**Figure A5.2.** TEM micrographs of C<sub>4</sub> (A), C<sub>5</sub> (B), C<sub>8.5</sub> (C), C<sub>5</sub>A<sub>85</sub>K<sub>4</sub> (D), and C<sub>8.5</sub>A<sub>85</sub>K<sub>4</sub> (E)



**Figure A5.3.** XPS survey spectrum for C<sub>4</sub> (A) and C<sub>5</sub> (B), deconvoluted high resolution XPS C1s for C<sub>4</sub> (C) and C<sub>5</sub> (E), and N1s for C<sub>4</sub> (D) and C<sub>5</sub> (F)

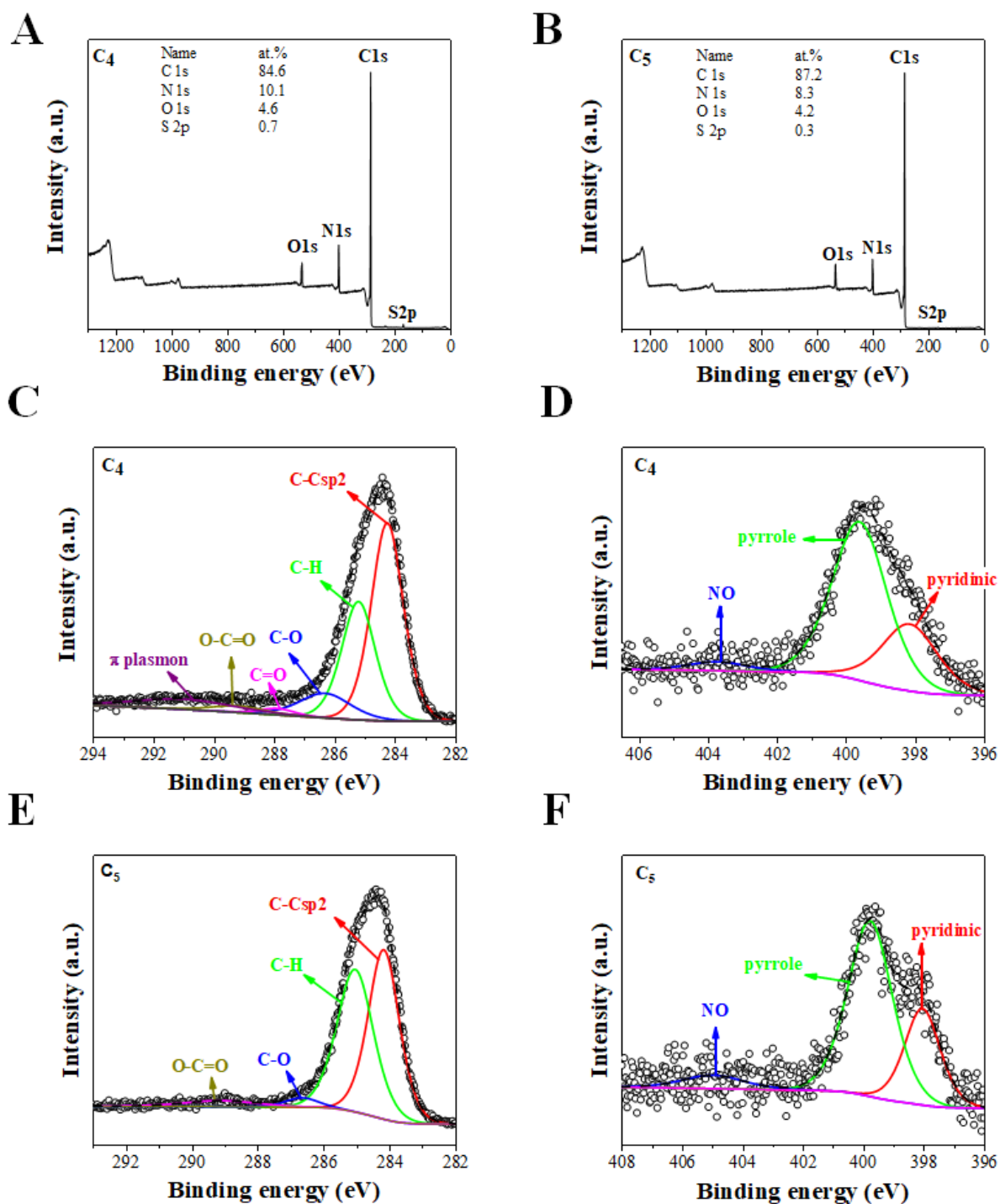


**Figure A5.4.** Nitrogen adsorption-desorption isotherms (A), and PSD (B) for C<sub>5</sub> and C<sub>8.5</sub>. Observation: The open isotherm observed for C<sub>5</sub> was reproducible, including using different equipment, and was ascribed to the presence of very narrow slit pores or bottle shaped pores. In this case, N<sub>2</sub> molecules at 77 K move very slowly that the adsorption is kinetically limited

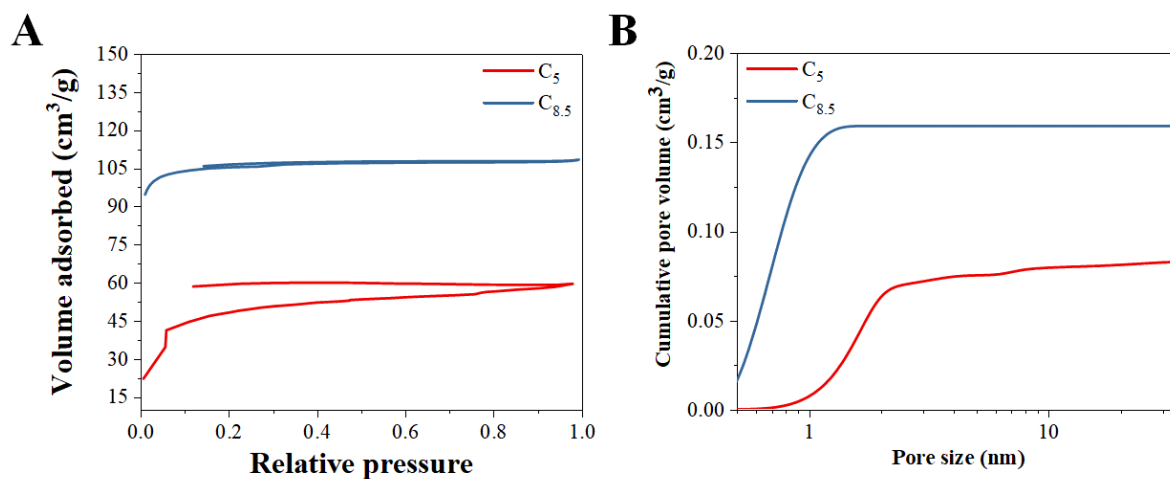


**Figure A5.5.** CVs recorded at 1 mV/s in 200 mM NaCl for the electrodes prepared with the activated carbons obtained under different activation conditions

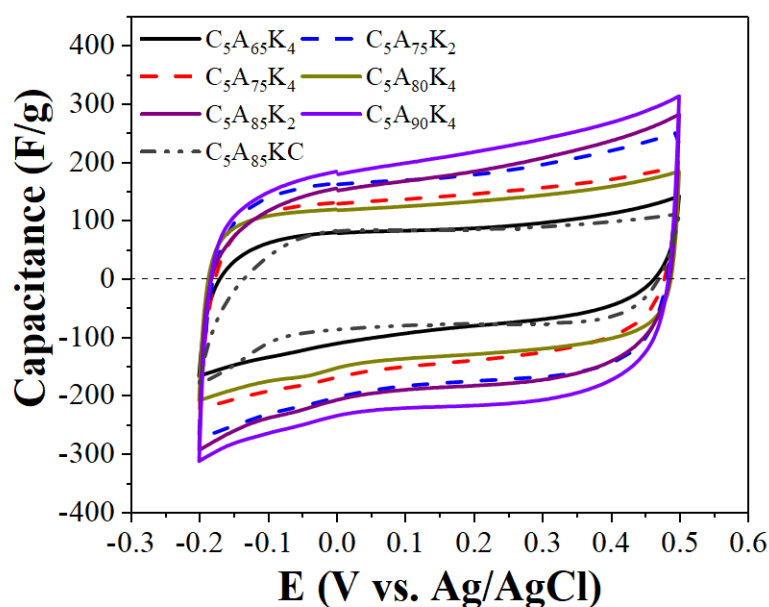


**Figure A5.6.** Conductivity profile for the electrodes prepared with PANi carbonized at different temperatures

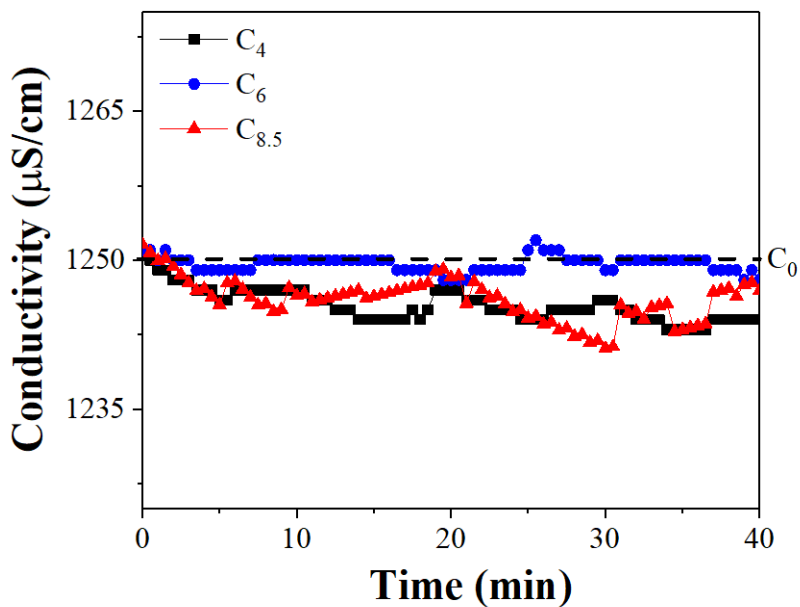


**Figure A5.7.**  $mSAC$  vs.  $SSA_{BET}$  for PAC electrodes. Experimental conditions: 1.2 V, 600 mg/L NaCl

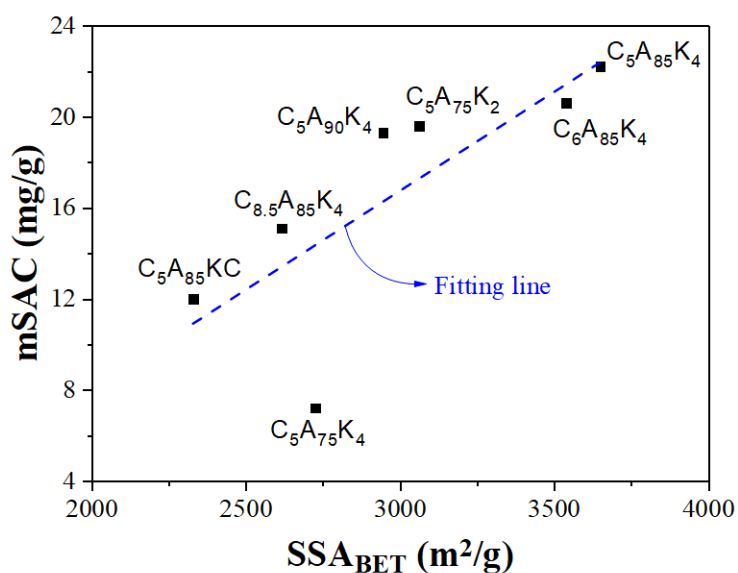


**Figure A5.8.** Conductivity profile and  $E_{cell}$  vs. time for  $C_5A_{6.5}K_4$ . Concentration: 600 mg/L NaCl

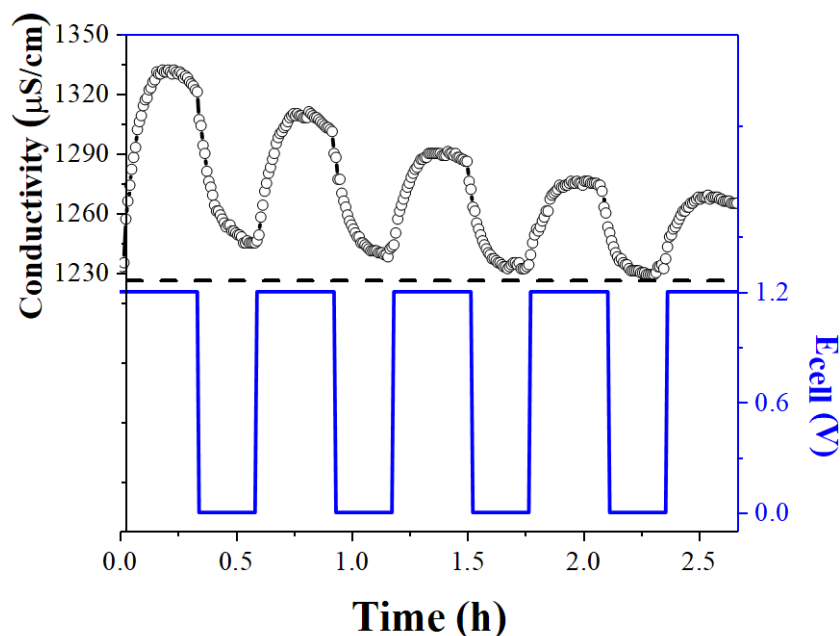
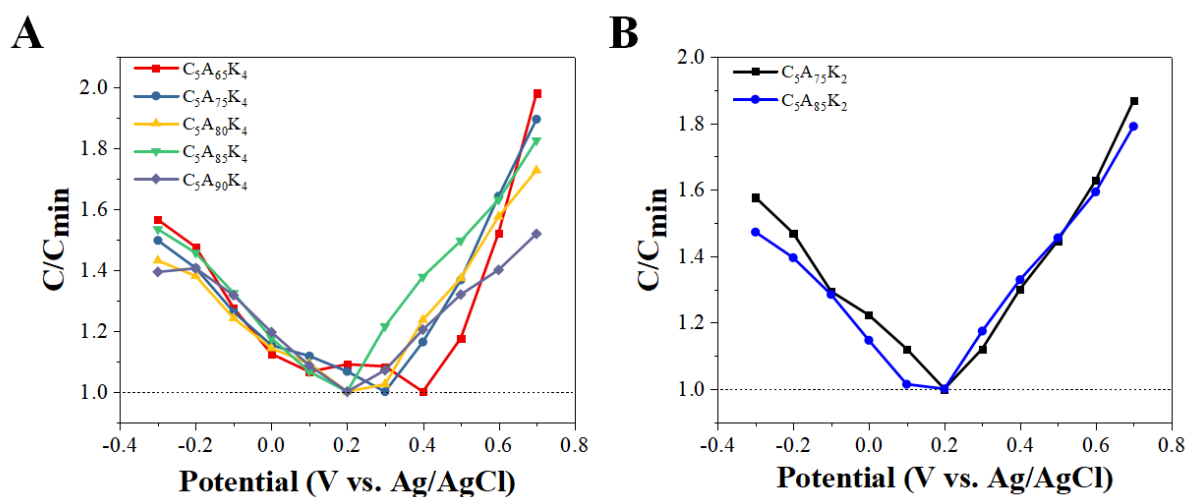


**Figure A5.9.** Normalized capacitance vs. electrode potential for PAC electrodes obtained at different activation temperatures (A), and low  $K/C$  (B). The values of capacitance were measure in 600 mg/L NaCl by EIS at 0.01 Hz



#### References:

- [1] Y. Liu, X. Xu, M. Wang, T. Lu, Z. Sun, L. Pan, Nitrogen-doped carbon nanorods with excellent capacitive deionization ability, *J. Mater. Chem. A*. 00 (2015) 1–8. doi:10.1039/C5TA03663A.

- [2] X. Xu, Z. Sun, D.H.C. Chua, L. Pan, Novel nitrogen doped graphene sponge with ultrahigh capacitive deionization performance., *Sci. Rep.* 5 (2015) 11225. doi:10.1038/srep11225.
- [3] X. Xu, H. Tang, M. Wang, Y. Liu, Y. Li, T. Lu, L. Pan, Carbon spheres with hierarchical micro/mesopores for water desalination by capacitive deionization, *J. Mater. Chem. A.* 4 (2016) 16094–16100. doi:10.1039/C6TA07616E.
- [4] M. Aslan, M. Zeiger, N. Jackel, I. Grobelsek, D. Weingarth, V. Presser, Improved capacitive deionization performance of mixed hydrophobic / hydrophilic activated carbon electrodes, *J. Phys. Condens. Matter.* 28 (2016) 114003. doi:10.1088/0953-8984/28/11/114003.
- [5] C. Kim, P. Srimuk, J. Lee, S. Fleischmann, M. Aslan, V. Presser, Influence of pore structure and cell voltage of activated carbon cloth as a versatile electrode material for capacitive deionization, *Carbon N. Y.* 122 (2017) 329–335. doi:10.1016/j.carbon.2017.06.077.
- [6] T. Wu, G. Wang, Q. Dong, F. Zhan, X. Zhang, S. Li, H. Qiao, J. Qiu, Starch Derived Porous Carbon Nanosheets for High-Performance Photovoltaic Capacitive Deionization, *Environ. Sci. Technol.* 51 (2017) 9244–9251. doi:10.1021/acs.est.7b01629.
- [7] C.-L. Yeh, H.-C. Hsi, K.-C. Li, C.-H. Hou, Improved performance in capacitive deionization of activated carbon electrodes with a tunable mesopore and micropore ratio, *Desalination.* 367 (2015) 60–68. doi:10.1016/j.desal.2015.03.035.
- [8] R.L. Zornitta, P. Srimuk, J. Lee, B. Krüner, Charge and Potential Balancing for Optimized Capacitive Deionization Using Lignin-Derived , Low-Cost Activated Carbon Electrodes, (2018) 1–14. doi:10.1002/cssc.201800689.
- [9] X. Xu, A. Enaiet Allah, C. Wang, H. Tan, A.A. Farghali, M. Hamdy Khedr, V. Malgras, T. Yang, Y. Yamauchi, Capacitive deionization using nitrogen-doped mesostructured carbons for highly efficient brackish water desalination, *Chem. Eng. J.* (2019). doi:10.1016/j.cej.2019.01.098.

## CHAPTER 6

### GENERAL DISCUSSION, CONCLUSIONS, AND SUGGESTIONS FOR FUTURE WORKS

In this work, it was demonstrated how different types of activated carbons may be employed as electrodes for water desalination through CDI technology. In this chapter, it is discussed the main remarks of the materials investigated.

#### 6.1. Specific surface area, pore volume, and pore size distribution

Considering that the EDL formation is a surface phenomenon, it would be expected that the higher the SSA the higher the SAC. However, this trend is not always true. It has been demonstrated that low values of SAC even for materials with low SSA, as in the case of PAC/Cl, in which the most important role is played by functional surface groups on the electrode surface.

An improvement is obtained by correlating SAC and pore volume, which is directly determined from the N<sub>2</sub> isotherm at high relative pressures, but it should be considered that there is a lack of information about the contribution of micropores or mesopores to the total pore volume. The EDL is more effectively developed in the micropores rather than in the mesopores. This trend is observed for the C<sub>5</sub>A<sub>75</sub>K<sub>2</sub> and C<sub>5</sub>A<sub>90</sub>K<sub>4</sub> (Chapter 5, Table 3), in which the latter presents higher pore volume, despite of its low micropore volume. Therefore, the SAC of both materials was practically the same.

In this context, it seems that the most reasonable way to correlate the SAC with the textural properties is using the PSD. In this fashion, both information concerning to the total pore volume and the contribution of differential pore size, which accounts the micro and mesopores, are considered in the analysis. A model considering these aspects is found in the CDI literature to predict SAC and agrees well with our experimental data.[1] However, one should be careful using this a model since the surface groups present on the carbon surface are not accounted and may change the electrochemical behavior of the electrode, as in the case of C<sub>5</sub>A<sub>75</sub>K<sub>4</sub>, in which, despite of its good pore structure, it presents poor desalination performance.

## 6.2. Surface groups

Importantly, the stability of the electrode material must be taken into account, as in the case of the LK electrode. Using symmetric electrodes, despite of the suitable SSA and PSD of LK, the  $mSAC$  decreases after 5 cycles due to the loss of oxygen surface groups.

The presence of functional surface groups is as important as PSD, or even more, to determine the electrode performance in terms of  $mSAC$  and charge efficiency. Most of the models reported in literature was developed considering carbon materials without any chemical surface charge and perfect surface distribution of the ionic charge. This is usually true for activated carbons with a very high carbon content (>97 wt.%) in which heteroatoms and surface groups are negligible. However, carbons with high content of oxygen, nitrogen, phosphorous, sulfur, and other heteroatoms, may shift the potential of zero charge of the electrode in neutral solution (e.g. NaCl solution) causing the co-ion repulsion effect in symmetrical electrode configuration. Furthermore, usually the surface groups reduce the electrode stability, e.g. LK electrode, and may also reduce the overpotential for water splitting.

On the other hand, in asymmetrical electrode configuration, these surface groups introduce surface charges that may enhance the electrode electrosorption capacity due to introduction of pseudocapacitance (ascribed to nitrogen and oxygen surface groups), and reducing the co-ion repulsion. We demonstrated that using LK electrode and low  $E_{cell}$  (1.0 V) it is possible to achieve high SAC (18.5 mg/g) and charge efficiency (88%) when the appropriate electrode configuration is used.

## 6.3. Asymmetry vs. MCDI

Ion selective membranes have similar effect as modifying the electrode surface ( $E_{PZC}$ ) regarding to hinder the co-ion repulsion phenomena. The use of membranes implies in positive and negative aspects. Besides the effect on co-ion repulsion, MCDI also avoids electrode degradation due to dissolved oxygen, but increases in ohmic drop and  $E_{cell}$  are introduced. Additionally, fouling issues still remains.

Instead using membranes, co-ion repulsion can be avoided by changing the chemical surface charge of the carbon electrode. For instance, the insertion of amide groups (positively charged) was presented in Chapter 4 to avoid cations repulsion on the positive electrode. Although the chemical treatment introduces surface charge, it also has a deleterious effect on the specific surface area and PSD, as observed for mPAC<sup>+</sup>.

In summary, ion selective membrane still seems more effective enhancing the CDI performance, since it does not affect the electrode material. Nevertheless, two electrodes with

different surface charges and desired textural properties may consist in an alternative to membranes since their electrochemical stability have been proven, which was the case of using LK and MSP-20 as negative and positive electrodes, respectively (Chapter 2).

#### 6.4. Materials development

The materials developed in this work were exclusively tested as electrodes for CDI, but their textural and electrochemical properties qualify them for many other applications in which high SSA, micro/mesoporosity, high conductivity, and presence of functional surface groups are desired.

As examples of such applications, C<sub>5</sub>A<sub>85</sub>KC (Chapter 5) can be used for CO<sub>2</sub> adsorption due to its predominant microporosity.[2] Although desirable, CDI usually does not require a high conductive electrode since the electrolyte conductivity is limited by the dilute concentration of salt, which limits the electrosorption.[3] However, the conductivity of PAC e LK electrodes, besides their high capacitances, meets the desirable values for applications in EDL supercapacitors, in which the ionic strength of the electrolyte is high. Additionally, for this application, the electrode conductivity is usually improved using additives such as acetylene black, graphite, or graphene. In this regard, the PAC/PSS electrode (Chapter 3) is a promising candidate due to its high conductivity and capacitance.

#### 6.5. Metrics for CDI evaluation

Although *mSAC* is commonly used to evaluate the electrode performance for CDI, this information is not complete since it does not provide information about the electrosorption/desorption kinetic. As CDI is an intermittent process, the faster the electrosorption/desorption kinetic, more cycles are performed and, consequently, more salt can be removed considering the same time interval.

In this sense, in Chapter 4 we introduced a new method to evaluate the electrode performance, called optimized salt removal (OSR), which takes into account the electrosorption capacity and kinetics. We observed that electrodes with high *mSAC* but slow electrosorption/desorption kinetic could be overcome by electrodes with lower *mSAC* but very fast sorption kinetics. This method was further successfully employed in Chapter 5 for other electrode materials.

#### 6.6. Summary

This thesis enlightened some important aspects of CDI desalination. It was demonstrated that low-cost materials can reach high desalination performance when correctly



employed. Therefore, even an initially undesirable activated carbon can be improved using simple techniques such as increasing electrode mass, or using different electrode materials as positive and negative electrodes. Furthermore, it was demonstrated that using a simple activation technique, such as KOH activation, it is possible to obtain activated carbons with functional surface groups able to enhance the electrosorption capacity.

In terms of textural properties, remarkable SSA ( $\sim 3600 \text{ m}^2/\text{g}$ ) and pore volume ( $2.30 \text{ cm}^3/\text{g}$ ) were achieved only by controlling the carbonization/activation temperature during PAC preparation. A new mechanism of activation using KOH, specific for PANi doped with PTS, was proposed taking into account the structure of the carbon and the presence of surface groups. This high SSA and pore volume translated into one of the highest SAC values ( $\sim 22 \text{ mg/g}$ ) reported in the CDI literature for symmetric electrodes using activated carbons. This high SAC value is promising for large-scale applications. The materials developed in this thesis can also find applications in other fields in which high SSA and conductivity, and nitrogen or oxygen functional surface groups are required.

### 6.7. Suggestions for future works

One more step towards the achievement of high performance materials has been achieved in this thesis. However, further searches must be carried out to improve and optimize the desalination capacity and performance for long-term and large-scale experiments. On this regard, the following suggestions are proposed for future works:

- LK electrode showed remarkable performance for a low-cost electrode in long-term experiments. It is suggested to employ this electrode for desalination of more concentrated solutions, and evaluate its performance in multicomponent solutions. These will provide good insight about energetic demand on a real system using this electrode;
- PAC electrodes showed very high SAC, along with high SSA and pore volume. The performance of this electrode must be evaluated in long-term experiments. In case of lack of performance, the same techniques (asymmetry and  $E_{cell}$  reduction) employed for LK could be applied.;
- Nowadays, one of the major drawbacks to be overcome to make CDI effective for application is related to the effect of co-ions repulsion and degradation of the positive electrode. The development of new strategies to stabilize the positive electrode using

low-cost electrodes is probably the most exciting area to be explored in capacitive deionization.

## References

- [1] S. Porada, L. Borchardt, M. Oschatz, M. Bryjak, J.S. Atchison, K.J. Keesman, S. Kaskel, P.M. Biesheuvel, V. Presser, Direct prediction of the desalination performance of porous carbon electrodes for capacitive deionization, *Energy Environ. Sci.* 6 (2013) 3700–3712. doi:10.1039/c3ee42209g.
- [2] A. Silvestre-albero, J. Silvestre-albero, M. Mart, F. Rodr, Micro / Mesoporous Activated Carbons Derived from Polyaniline : Promising Candidates for CO<sub>2</sub> Adsorption, *Ind. Eng. Chem. Res.* 53 (2014) 15398–15405.
- [3] R.L. Zornitta, J.J. Lado, M.A. Anderson, L.A.M. Ruotolo, Effect of electrode properties and operational parameters on capacitive deionization using low-cost commercial carbons, *Sep. Purif. Technol.* 158 (2016) 39–52. doi:10.1016/j.seppur.2015.11.043.

## CHAPTER 7

### ACADEMIC PRODUCTION

#### 7.1. Publications

##### 7.1.1. First author

**ZORNITTA, RAFAEL LINZMEYER**; SRIMUK, PATTARACHAI ; LEE, JUHAN ; KRÜNER, BENJAMIN ; ASLAN, MESUT ; RUOTOLO, LUIS AUGUSTO MARTINS ; PRESSER, VOLKER . **Charge and potential balancing for optimized capacitive deionization using lignin-derived, low-cost activated carbon electrodes.** *ChemSusChem*, v. 11, p. 2101-2113, **2018**.

**ZORNITTA, RAFAEL L.**; GARCIA-MATEOS, FRANCISCO J. ; LADO, JULIO J. ; RODRÍGUEZ-MIRASOL, JOSÉ ; CORDERO, TOMÁS ; HAMMER, PETER ; RUOTOLO, LUIS A.M. **High-performance activated carbon from polyaniline for capacitive deionization.** *Carbon*, v. 123, p. 318-333, **2017**.

**ZORNITTA, RAFAEL L.**; RUOTOLO, LUÍS A.M. **Simultaneous analysis of electrosorption capacity and kinetics for CDI desalination using different electrode configurations.** *Chemical Engineering Journal*, v. 332, p. 33-41, **2017**.

**ZORNITTA, RAFAEL L.**; LADO, JULIO J. ; ANDERSON, MARC A. ; RUOTOLO, LUÍS A.M. **Effect of Electrode Properties and Operational Parameters On Capacitive Deionization Using Low-cost Commercial Carbons.** *Separation and Purification Technology (Print)*, v. 158, p. 39-52, **2016**.

**ZORNITTA, R. L.**; PINCELLI, G. ; **RUOTOLO, L. A. M.** **Modification of the Conducting Polymer Polyaniline for enabling cation exchange.** *Química Nova*, v. 37, p. 1459-1464, **2014**.

##### 7.1.2. Co-author

LEE, JUHAN ; SRIMUK, PATTARACHAI ; ZWINGELSTEIN, ROSE ; **ZORNITTA, RAFAEL LINZMEYER** ; CHOI, JAEHOON ; KIM, CHOONSOO ; PRESSER, VOLKER . **Sodium ion removal by hydrated vanadyl phosphate for**

**electrochemical water desalination. Journal of Materials Chemistry A**, (Online published), **2019**.

LEE, JUHAN ; SRIMUK, PATTARACHAI ; CARPIER, SIDONIE ; CHOI, JAEHOON ; **ZORNITTA, RAFAEL LINZMEYER** ; KIM, CHOONSOO ; ASLAN, MESUT ; PRESSER, VOLKER . **Confined redox reactions of iodide in carbon nanopores for fast and energy-efficient desalination of brackish water and seawater. ChemSusChem**, **2018**.

LADO, JULIO J. ; **ZORNITTA, RAFAEL L.** ; CALVI, FELIPE A. ; MARTINS, MARIANA ; ANDERSON, MARC A. ; NOGUEIRA, FRANCISCO G.E. ; RUOTOLO, LUÍS A.M. . **Enhanced capacitive deionization desalination provided by chemical activation of sugar cane bagasse fly ash electrodes. Journal of Analytical and Applied Pyrolysis**, v. 126, p. 143-153, **2017**.

FARINOS, ROSIMEIRE M. ; **ZORNITTA, RAFAEL L.** ; RUOTOLO, LUÍS A. M. . **Development of Three-Dimensional Electrodes of PbO Electrodeposited on Reticulated Vitreous Carbon for Organic Electrooxidation. Journal of the Brazilian Chemical Society**, v. 28, p. 187-196, **2016**.

LADO, JULIO J. ; **ZORNITTA, RAFAEL L.** ; CALVI, FELIPE A. ; TEJEDOR-TEJEDOR, M.ISABEL ; ANDERSON, MARC A. ; RUOTOLO, LUÍS A.M. . **Study of Sugar Cane Bagasse Fly Ash as Electrode Material for Capacitive Deionization. Journal of Analytical and Applied Pyrolysis**, v. 120, p. 389-398, **2016**.

## **7.2. Conferences**

### **7.2.1. Presenter**

**ZORNITTA, RAFAEL L.**; NOGUEIRA, FRANCISCO G.E. ; RUOTOLO, LUIS A.M. . **Enhanced Performance of Polyaniline-derived Activated Carbon by Controlling the Carbonization Temperature**. In: ElecNano 8, 2018, Nancy. Electrochemistry for Nano & Nano for Electrochemistry. Nancy, France, p. 146-146, **2018**.

**ZORNITTA, R. L.; GARRIDO, J. J. L. ; RUOTOLO, L. A. M. . **Analysis of Parameters and Operational Conditions of Low-Cost Electrodes for Capacitive Deionization.** In: International Conference on Capacitive Deionization and Electrosorption, CDI&E 2015, INM Leibniz Institute for New Materials, Saarbrücken, Germany, p. 102-103, **2015.****

**ZORNITTA, R. L.; RUOTOLO, L. A. M. . **Dessalinização de água utilizando tecnologia de deionização capacitiva: análise de diferentes eletrodos.** In: XX Congresso Brasileiro de Engenharia Química, 2014, Florianópolis, Brazil. Proceedings of XX COBEQ, **2014****

PINCELLI, G. ; **ZORNITTA, R. L.** ; RUOTOLO, L. A. M. . **Modificação de polímeros condutores para uso como trocadores iônicos.** In: 10º Encontro Brasileiro sobre Adsorção – Federal University of São Paulo, 2014, Guarujá, SP, Brazil, Proceedings of X EBA, **2014.**

### 7.2.2. Published in the proceedings

**ZORNITTA, R. L.**; GARCIA-MATEOS, FRANCISCO J. ; LADO, JULIO J. ; RODRÍGUEZ-MIRASOL, JOSÉ ; CORDERO, TOMÁS ; HAMMER, PETER ; RUOTOLO, LUIS A.M. . **High-Performance Activated Carbon from Polyaniline Doped with Different Anions for Capacitive Deionization.** In: 10th World Congress of Chemical Engineering, 2017, Barcelona, Spain. Proceedings of the 10th WCCE, **2017.**

**ZORNITTA, R. L.**; RUOTOLO, L. A. M. . **Brackish Water Desalination by Capacitive Deionization.** In: 65th Annual Meeting of the International Electrochemical Society, 2014, Lausanne - Switzerland. Proceedings of 65th Annual Meeting ISE, **2014.**

LADO, J. J. ; **ZORNITTA, R. L.** ; CALVI, F. A. ; RUOTOLO, L. A. M. ; TEJEDOR-TEJEDOR, I. ; ANDERSON, M. A. . **Effect of Thermal Treatment on Sugar Cane Bagasse Fly Ash Electrodes for Capacitive Deionization.** In: International Conference on Capacitive Deionization and Electrosorption, 2015, Saarbrücken.

CDI&E 2015 International Conference on Capacitive Deionization and Electrosorption. Saarbrücken: INM Leibniz Institute for New Materials, Germany, p. 100-101, **2015**.

**ZORNITTA, R.L.**; GARRIDO, J. J. L. ; RUOTOLO, L. A. M. . Influence of Activated Carbon Film Thickness on the Electrode Performance in Capacitive Deionization. In: ECS 227th Meeting, 2015, Chicago. Proceedings of the ECS 227th Meeting, **2015**.

### **7.3. Patents**

**ZORNITTA, R.L.**; RUOTOLO, L.A.M; *High-performance activated carbon from conducting polymers for different applications*, Patent application BR10201701045, INPI – Instituto Nacional da Propriedade Intelectual, Patent pending, **2017**